The Structure of Molecular Clouds

by

Jonathan H. Rowles

A thesis submitted for the degree of
Doctor of Philosophy

Centre for Astrophysics and Planetary Science

School of Physical Sciences
University of Kent
Canterbury, England

December 2010

DECLARATION

This thesis has not been submitted as an exercise for a degree at any other university. Except where stated, the work described therein was carried out by me alone.

I give permission for the Library to lend or copy this thesis upon request.

SIGNED: 

Dedicated to my lovely wife, Michelle.

If there is something very slightly wrong in our definition of the theories, then the full mathematical rigor may convert these errors into ridiculous conclusions.

Richard P. Feynman, 1918-1988.

49 stars to the centre of each pixel

& for me
the pleasure was
in cloud selection
in mapping by fixed grid spatial resolution
by nearest neighbour noise

& when fitting functions
to extinction free regions
rebinned
filtered
masked
& splined with knots at every degree
there was that fantastic finding of median colour
& near infrared excess

job done
the knowledge now edges away
into the cosmos
no longer just mine
& yet for all time
I was here
& this the irrefutable evidence
of my 49 stars.

Poem written for Jonathan Rowles in celebration of the award of PhD

Summary

The physics and turbulent properties responsible for shaping the structure in molecular clouds are analysed.

Data from the Two-Micron All-Sky Survey are used to determine all-sky median near-infrared extinction maps. Two types of map are made: maps with a near-constant noise in each pixel and maps with a constant resolution. The standard map has a resolution as high as 1′ along the Galactic plane. The resolution and depth of optical extinction are significantly better than those achieved in previous large-scale studies.

The maps are used to examine the column density and mass distributions of 30 nearby molecular clouds. The low column density (i.e. turbulence dominated) parts of the clouds could be well fit by a log-normal distribution. A universal extinction threshold of $A_V = 5.6 \pm 1.2$ mag is found, above which there is an excess of material when compared to a log-normal distribution. Gravity is implied as the dominant factor in structure shaping above this threshold, as the column density and mass distributions are similar for all clouds. Below this threshold, the structure is determined by turbulence and the environment of the cloud. Two groups of clouds with distinct column density/mass distributions are identified, that correspond to 'star forming' and 'non-star forming' groups.

Structure function and Δ-variance analyses are performed on the same nearby molecular clouds. Average values are calculated for the structure function parameters Δ, intermittency, codimension and fractal dimension. The results imply a mixture of solenoidal and compressive forcing in the turbulence dominated regions of the clouds.

An average value for the mass index scaling exponent is calculated which is close to the value expected for clouds where turbulence is driven/governed by solenoidal forcing. For the 'star forming' clouds the average value implies a mixture of solenoidal and compressive forcing, while the value for the 'non-star forming' group implies exclusively solenoidal forcing. It is concluded from this that compressive forcing is associated with the presence of clustered star formation.

Acknowledgements

Firstly and foremostly I thank my supervisor Dirk Froebrich, for his expert tutelage over the past three (and a bit) years. Always willing to give advice and instruction, for which I am hugely grateful. Thank you, Dirk!

Thanks also to Michael Smith, my associate supervisor, for his input and help.

Special thanks and love to my wonderful wife, Michelle, especially for bearing with me as I put my thesis together.

A big thank you to my parents, Stuart and Jane, and my in-laws, Bob and Jean, for the parts you've played in looking after me and feeding me when I've visited.

Thanks also to my friends in Ashford, Norwich and elsewhere whose friendship has blessed me over the last few years since I moved to Kent.

Thank you to the guys in the Postgrad (formerly CAPS) office, for the many conversations that were sometimes even about physics! Special thanks to Mark Price, for always promptly sorting out any IT issues.

As a side-project to this thesis, research was conducted into the behaviour of quasi-spherical objects on quasi-planar surfaces. These were impacted with pseudo-2D rods with the intention of depositing the quasi-spheroids into gravitational wells. Dirk's experiments were consistently more accurate than mine. However, my experiments were consistently more accurate than those by Andrew Lightwing and Ryan Laird. I thank my participants in this research.

This publication makes use of data products from the 2MASS, which is a joint project of the University of Massachusetts and the Infrared Processing and Analysis Center/California Institute of Technology, funded by the National Aeronautics and Space Administration and the National Science Foundation.

Publications

A list of publications resulting from work presented in this thesis is given below.

Refereed Publications

1. **The Structure of Molecular Clouds: Paper I - An All Sky Near Infrared Extinction Map**
   Rowles, J. H., Froebrich, D., 2009, Monthly Notices of the Royal Astronomical Society, 395 1640

2. **The Structure of Molecular Clouds: Paper II - Analysis of Nearby Giant Molecular Clouds**
   Froebrich, D., Rowles, J. H., 2010, Monthly Notices of the Royal Astronomical Society, 406 1305

Submitted

1. **The Structure of Molecular Clouds: Paper III - Structure Functions of Nearby Giant Molecular Clouds**
   Rowles, J. H., Froebrich, D., 2010,

Table of Contents

List of Tables

List of Figures

Chapter 1

Introduction and Theory

This chapter sets the context for the basis of this thesis. Firstly, the motivation behind the research is given. Then molecular clouds, the sites of star formation are discussed. The following section briefly outlines the current theory of star formation with relevance to the specific area of study in this thesis. Then the topics of interstellar dust and extinction are presented. The latter is followed by a section discussing some of the methods of measuring extinction. The next section discusses turbulence in the interstellar medium (ISM). This is followed by a review of some methods to analyse the structure of molecular clouds. Lastly, an outline is given of some of the remaining problems to be solved.

1.1 Motivation

Stars are important for several reasons. Firstly, they are the main source of radiation in the Universe, either directly or indirectly. Dust in the interstellar medium absorbs starlight and re-radiates it at longer wavelengths - this alone accounts for ~30% of observed radiation (Bernstein et al., 2002). Secondly, all elements heavier than H, He and Li originate from stars, hence we are literally made from star dust. All of the heavy elements (heavier than Fe) that exist on Earth were created in supernova caused by the death of massive stars.

Thirdly, stars provide us with our main source of information about the Galaxy and Universe in which we live. Both in the daytime and night-time, all of the natural light we see in the sky originates from stars. By using observations at optical and other wavelengths, much information can be gleaned. This information includes: the constituting elements of stars, their temperature, size, age etc. Studying the life cycles of stars is important; for example, life on earth depends on our nearest star, the Sun. Over the last hundred years or so astronomers have studied many different types of stars in the Universe, each at different stages in their life cycle. Star formation is ongoing at the present time and occurs exclusively in molecular clouds.

Molecular clouds are observed as dark patches in the starry sky. They are especially prevalent along the Milky Way. As an example, Figure 1.1 shows the Pipe Nebula, the

Prancing Horse Nebula, and part of the Galactic plane towards the Galactic centre. As the name suggests molecular clouds are made from molecules - hydrogen and other elements. The collapse of fragments of molecular clouds is the precursor to star formation and is subject to several factors including turbulence, magnetic fields, gravity and thermodynamics.

The mass of the stars that are formed depends on the conditions in the molecular cloud at the collapse. Knowing the mass of stars is important as this parameter determines the life and death of the star. Therefore, elucidating the conditions in molecular clouds prior to the collapse is important. This thesis investigates the structure of molecular clouds using all-sky *median* near-infrared extinction maps. The column density and mass distributions of molecular clouds are analysed along with the structure functions of the clouds.

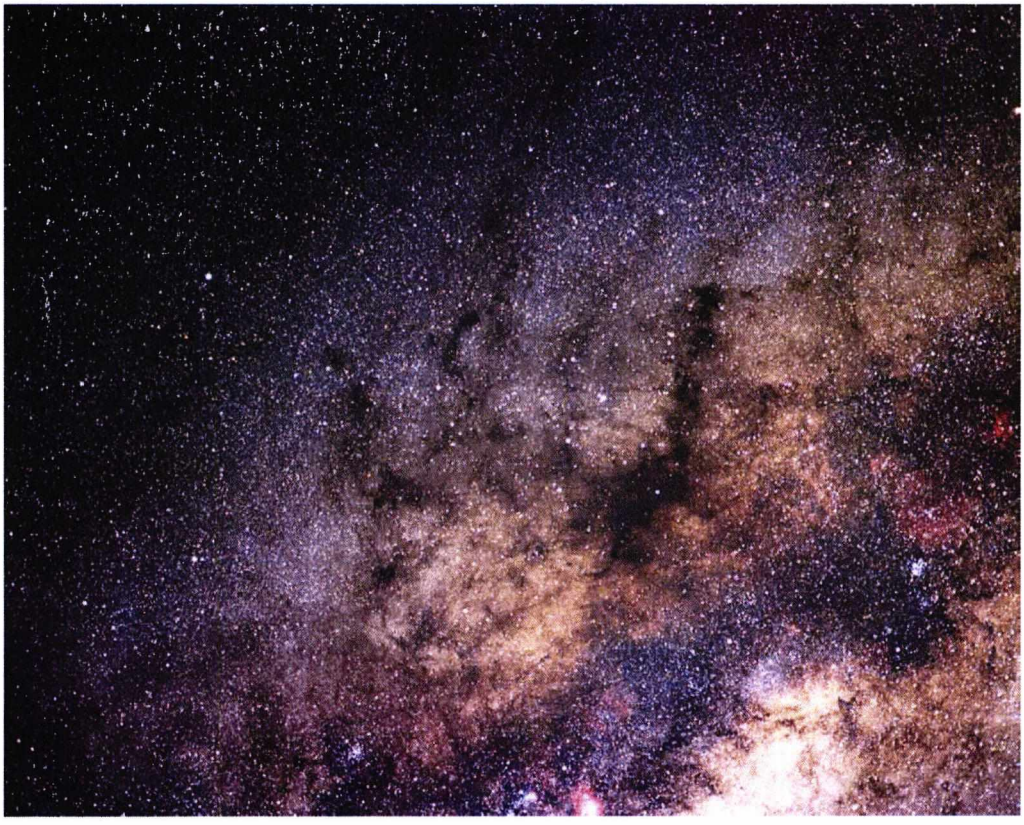

Figure 1.1: An example of molecular clouds, the Pipe Nebula (centre right) and the Prancing Horse Nebula (centre left - optical image © Chris Cook and Jim Janusz). The Galactic centre is at the lower right of the image.

This thesis is presented in the following order. After this chapter, which sets out the context and background, the second chapter outlines the data analysis method. The third

chapter presents the results, and the fourth chapter gives the interpretation of the results. The fifth and final chapter is the conclusion of the thesis.

It should be noted that while the research in this thesis was being carried out, some of the works cited were published (i.e. in the years 2007-2010). In some cases it was possible to incorporate the published findings in this work; in other cases it was not. One example of the latter was the work by Knude (2010), which gave revised distances to nearby molecular clouds. This work was published after the majority of the analysis for this thesis had been performed, therefore the revised distances were not used, but only referenced.

1.2 Molecular Clouds

This section outlines the role of molecular clouds as the birthplace of stars. The important attributes of molecular clouds are outlined, followed by a discussion on the evolution of clouds.

1.2.1 The Birthplace of Stars

Molecular clouds range in size from as small as $\leq$ 0.1 pc to 100 pc and have masses of $\sim M_\odot$ up to 10^6 $M_\odot$ (Mac Low & Klessen, 2004). Within the clouds there are smaller scale structures of a few parsecs and masses of around a few thousand solar masses (Larson, 2003a). These may form clusters of stars. Smaller structures on the scale of 0.1 pc and with a mass of approximately 1 $M_\odot$ may form isolated or small multiple systems (e.g. Visser et al. (2002)).

Some aspects of the structure of molecular clouds may be modelled by using fractal type structures (e.g. Elmegreen et al. (2000)). The boundaries of molecular clouds especially have fractal-like structures which suggest the presence of turbulent flows (e.g. Falgarone et al. (1991)). Therefore, turbulence is strongly believed to be responsible for the structure of molecular clouds. Like terrestrial clouds, molecular clouds are dynamic and do not exist in a state of equilibrium. Furthermore, virtually all molecular clouds are

observed to be forming stars (Mac Low & Klessen, 2004). Hence, there cannot be any 'dead time' between the formation of the cloud and the commencement of star formation.

The molecules in the clouds are formed on dust grains (discussed later in Section 1.4), and the rate of formation of molecules depends on the density of dust. Higher rates of formation occur in denser regions (Larson, 2003a). A minimum column density is required in molecular clouds to shield the molecules from being dissociated by interstellar UV radiation. This threshold is approximately 10-20 $M_\odot$ pc^{-2} ($N_H \simeq 1 - 2 \cdot 10^{21}$, corresponding to a visual extinction of about 0.5-1 mag A_V (Hartmann et al., 2001)). Typical column densities are higher than this and are about 100 $M_\odot$ pc^{-2}. Molecular clouds are surrounded by regions of less dense material in the form of atomic gas. The mass of interstellar gas in our Galaxy is divided roughly equally between molecular hydrogen and atomic hydrogen (e.g. Draine (2009)).

The densities of gas in molecular clouds can be as least high as 10^5 cm^{-3} in the cores; clumps may have a density around 10^3 cm^{-3} (Larson, 2003a). However, the typical density of the whole cloud is of the order of 20 cm^{-3}. In the densest parts of the cloud, the gas is thermally coupled to the dust. The dust controls the temperature due to its thermal emission properties. Therefore, the temperature is kept low, and of the order of 10 K over the range of densities found (e.g. Masunaga & Inutsuka (2000)). Gravity is a dominant force over thermal pressure except in the smallest clumps. However, the clouds form stars quite inefficiently (star formation efficiencies are typically less than 5%), which implies that the collapse of clouds is impeded - the most likely mechanisms for this being turbulence or magnetic fields (Klessen et al., 2000; Brandenburg & Nordlund, 2009).

The observed motions within molecular clouds are supersonic. The velocities greatly exceed the typical sound speeds of 0.2 km s^{-1}. The motions observed tend to be random small-scale and these are referred to as turbulence. See Section 1.7 for further discussion on this topic. Magnetic fields also have an effect on the structure of molecular clouds. These are difficult to measure directly. However, using simulations of magnetohydrodynamic (MHD) waves it has been found that the MHD wave motions decay on a timescale of the order of the crossing time of the cloud (e.g. Mac Low et al. (1998)). Therefore, the

MHD turbulence requires a source of energy to continually regenerate it.

1.2.2 Evolution of Molecular Clouds

Molecular clouds in the ISM are transient features which exist over a relatively short timescale of the order of millions of years or less (e.g. Elmegreen (2000)). This corresponds to the order of the crossing time of the turbulent motion across the cloud (Elmegreen, 2000; Hartmann, 2003). For GMCs a typical lifetime is quoted as 17±4 Myr by Murray (2010). A review of the evolution of molecular clouds is given in Vázquez-Semadeni (2010), in which developments in the study of molecular clouds over the last couple of decades are reported. These developments are included in the remainder of this section.

Using observations of the galaxy M33, Engargiola et al. (2003) have found that GMCs are assembled rapidly from swept-up HI, with star formation commencing promptly. Furthermore, Kawamura et al. (2009) suggest that clouds undergo an evolutionary process whereby the mass and star formation rates increase with time. Using observations of GMCs in the Large Magellanic Cloud (LMC) they postulated that the mass of GMCs increases from $10^{4.5-5} M_{\odot}$ to $10^{6.5-6} M_{\odot}$ in approximately 25 Myr. After this time the GMCs have also produced clusters and HII regions. The material is available for such clouds to grow since they are not isolated entities and lack any discernible boundary or discontinuity (Ballesteros-Paredes et al., 1999). So the cloud forms once material swept up from the cold neutral medium (CNM) reaches a sufficient density to allow the formation of hydrogen molecules (Vázquez-Semadeni, 2010).

Once a cloud forms and begins to grow, it rapidly becomes molecular, magnetically supercritical and gravitationally unstable (Vázquez-Semadeni, 2010). This indicates that the cloud should contract immediately. However, theory indicates the cloud is a mixture of cold and warm gas (Vázquez-Semadeni et al., 2006), and that the turbulence inherent in the cloud at formation has an important role in the early development of the cloud. When collapse does occur, it is thought to occur locally at first with only a small fraction of the cloud mass involved and the bulk of the cloud remaining at low density (referred to as *hierarchical gravitational collapse* by Vázquez-Semadeni et al. (2007)). The density

fluctuations are non-linear hence the free-fall timescales of local collapses are shorter than those of the cloud. Typical timescales for local collapses are of the order of 10 Myr (Vázquez-Semadeni, 2010).

The first stars to be formed in a cloud result from the collapse of low mass structures in the cloud and these are the most numerous sites of star formation within the cloud (as implied by Vázquez-Semadeni (1994)). Of course most of the mass involved in star formation in the cloud goes into the formation of clusters of stars (Lada & Lada, 2003). Numerical modelling of this configuration in clouds has been performed (Vázquez-Semadeni et al., 2007) and is found to be consistent with observations (Vázquez-Semadeni et al., 2009). In the latter it was found that they were able to successfully model the attributes (e.g. masses, sizes, velocity dispersions etc.) of both low mass and high mass star forming regions.

Subsequent star formation in clouds may be driven by feedback from existing stars in the cloud, or outflows from stars, or by supernovae (by high-mass, short lived stars). In the first case, it is not known whether the feedback from existing stars in a cloud actually disperses the cloud or allows the cloud to survive in some short-term equilibrium. More observations, modelling and analysis need to be done to provide a conclusive answer (Vázquez-Semadeni, 2010). Certainly the feedback only disperses the cloud locally.

Secondly, simulations have suggested that outflows may be sufficient to sustain turbulence in clouds on parsec scales (Carroll et al., 2009). The energy and momentum from the outflows is converted into turbulent motion in the clouds, and can provide this energy for several crossing times (Matzner, 2007). Thirdly, the energy input from supernova explosions was simulated by Joung & Mac Low (2007). They found that although supernovae produce compressed clouds and hence local star formation, global star formation across the cloud is actually hindered.

Finally, molecular clouds are dispersed by such factors as UV radiation, stellar winds and supernovae (Baumgardt & Kroupa, 2007). As mentioned earlier, the typical lifetime for a GMC is of the order of 17±4 Myr (Murray, 2010). Any clusters of stars contained within the cloud are also affected with three probable final stages - either complete dis-

persal, or only a loose association remaining, or a compact core (Chen & Ko, 2009).

1.2.3 The Larson Relations

An important result was published by Larson (1981), finding that the densities, internal velocities and size of molecular clouds could be described by a power-law relation. The measurement of internal velocities was particularly important as it showed that the motions in molecular clouds resulted from supersonic turbulence.

The three relations for linewidth (velocity dispersion) and size (e.g. Myers (1983); Solomon et al. (1987)), virial equilibrium, followed by density and size are given by,

$$\sigma \propto r^{\beta}; \beta \approx 0.5 \pm 0.05, \tag{1.1}$$

$$\frac{2GM}{\sigma^2 r} \simeq 1, \tag{1.2}$$

and

$$\rho \propto r^{\alpha}; \alpha \approx -1.1. \tag{1.3}$$

Only two of the Equations 1.1, 1.2 and 1.3 are independent. Furthermore, only one of these relations may be real in 3D data - namely Equation 1.1. A typical velocity for σ is of the order of 0.72±0.07 km s^{-1} (Solomon et al., 1987).

The significance of Equation 1.2 is that it implies that molecular clouds are gravitationally bound (i.e. $2\ E_{kinetic} = E_{potential}$). For clouds with values of $\alpha > 1$, they are unbound and are either in the process of expanding or prevented from doing so by an external pressure.

The behaviour suggested by Equation 1.3 is only observed due to the limited dynamic range of the tracer molecules, therefore is unlikely to be real (Scalo, 1990). The equation implies constant column densities between clouds. It also implies that the mass M contained within the radius r should scale as $M(r) \propto r^2$, as discussed later in this section.

The original published form of Equation 1.1 had $\beta \simeq 0.38$ (Larson, 1981), which is close to that expected by Kolmogorov type turbulence, i.e. $\beta = 1/3$ (see Section 1.8.1.1). However, Passot et al. (1988) found that $\beta \simeq 0.5$ (e.g. Myers (1983)), which is closer to the result expected from Burger's type turbulence (see Section 1.8.1.3), for the observed strongly turbulent conditions.

An equation relating the column density to the size of the cloud was derived by Solomon et al. (1987),

$$\langle H_2 \rangle = (1.5 \pm 0.3) \cdot 10^{22} cm^{-2} (R/pc)^{0.0 \pm 0.1}. \tag{1.4}$$

This equation is dependent on the relation between the mass of the cloud and the radius being of the order $M(r) \propto r^2$; however, for lower mass cloud the relation is more like $M \propto R^{1.9}$ (e.g. Kauffmann et al. (2010b)), altering the exponent in Equation 1.4 to -0.1 ± 0.1. In single clouds, with $0.1 \leq r \leq 1.0$ pc, Lombardi et al. (2010a) found that $M(r) \propto r^{1.6}$. The lack of consensus for a value of the exponent indicates that more data is needed to ascertain the true value. For further discussion on this topic, relating to the practical use of the mass-size relation, see Section 1.8.3.

1.3 Star Formation

In this section the standard picture of star formation is discussed, with emphasis on the natal clouds. Also discussed are relevant topics such as the Initial Mass Function (IMF), the formation of binary systems, multiple systems and clusters. Then Star Formation Efficiency (SFE) and Star Formation Rate (SFR) are discussed. Finally, recent observations in the area of star formation are discussed along with some ongoing projects.

1.3.1 The Standard Picture

The majority of star formation in our Galaxy happens in the spiral arms, where there are concentrations of interstellar gas in the form of molecular clouds (Larson, 2003a). Some star formation also occurs at the centre of the Galaxy, but can only be inferred

indirectly due to obscuration by dust. The interstellar gas from which stars form consists predominantly of molecules (e.g. H_2, CO, NH_3 etc), hence the name molecular clouds (see Section 1.2).

The 'standard picture' proposes that star formation occurs in molecular clouds in the following way. Density fluctuations in an almost stable uniform medium become amplified by gravity. This process is known as 'gravitational instability' (Jeans, 1928). This 'classical' view does not take into account the effects of rotation, magnetic fields or turbulence. The fluctuations fall into two categories; firstly, short-wavelength perturbations which are pressure dominated and propagate as sound waves. Secondly, perturbations with a longer wavelength exceeding a critical value propagate and grow exponentially. These waves are gravity dominated. Their wavelength exceeds the 'Jeans length' given by e.g. Larson (2003a),

$$\lambda_J = \pi^{\frac{1}{2}} c (G\rho)^{-\frac{1}{2}}, \tag{1.5}$$

where ρ is the density, c is the isothermal sound speed, and G is the gravitational constant. A minimum mass - above which the cloud becomes gravitationally unstable - can be derived, assuming the density fluctuations have similar dimensions in all three coordinates. This minimum mass, termed the 'Jeans mass' is given by (Spitzer, 1978),

$$M_J = \frac{5.57 c^3}{G^{\frac{3}{2}} \rho^{\frac{1}{2}}}. \tag{1.6}$$

The factor of 5.57 assumes that the density perturbations are plane wave; for spherical perturbations the factor becomes 8.53 (Larson, 1985). However, the Jeans analysis does not take account of the fact that collapse of the background medium may overwhelm the local density fluctuations (Larson, 2003a). But, results from numerical simulations suggest that using the Jeans analysis as an approximation is still useful.

One may consider a stable situation with an isothermal sphere in equilibrium, with a finite size, fixed temperature and boundary pressure. The density of this sphere is not constant (as for the 'Jeans mass' analysis) but increases towards the centre of the sphere.

This condition may exist in a prestellar core in a near equilibrium state. Such a sphere is known as a Bonner-Ebert sphere. It would be liable to collapse if its radius exceeds a critical value (e.g. Spitzer (1968)),

$$R_{BE} = \frac{0.48c^2}{G^{\frac{1}{2}}P^{\frac{1}{2}}}, \tag{1.7}$$

or its mass exceeds the value,

$$M_{BE} = \frac{1.18c^4}{G^{\frac{3}{2}}P^{\frac{1}{2}}}. \tag{1.8}$$

Here, P is the boundary pressure. In an isothermal medium the pressure and density are related by $P = \rho c^2$, therefore Equations 1.7 and 1.8 are related to Equations 1.5 and 1.6 but with smaller coefficients. This is expected since for the Bonner-Ebert sphere contains only matter where the density is higher than the background density.

Once the cloud has fragmented, the collapse of prestellar cores can be considered. Two different types of model exist which place limits on how the collapse may be initiated. One model is that the collapse occurs when gravity overcomes the thermal pressure in a marginally stable clump of gas. The initial state is assumed to be similar to that of a Bonner-Ebert sphere considered earlier.

The other type of model assumes that the prestellar cores are supported by magnetic fields and condense gradually by *ambipolar diffusion* (Shu, 1977). The gas contracts slowly across the field lines and charged particles (such as electrons and ions) are only able to move along the field lines and hence inhibit the movement of uncharged particles. The core should then collapse only once enough mass has accumulated to overcome the magnetic support. However, Nakano (1998) state that it is highly implausible that ambipolar diffusion is the mechanism responsible for the formation of cloud cores, due to the turbulent velocity profiles observed. This implies that turbulence may have a greater role in supporting cloud cores against gravity, and that the collapse may be due to the dissipation of turbulence rather than by ambipolar diffusion (Nakano, 1998).

The thermal behaviour of the gas is important to the collapse. The temperature of

the gas is able to fall at increasing gas density, but only if the density is low initially. This is due to the increasing efficiency of atomic and molecular line cooling. At higher densities, the gas becomes thermally coupled to the dust, which controls the temperature through thermal emission. In this way the temperature rises only slowly. Overall the temperature remains in the range 6 K to 12 K while the density increases by a couple of orders of magnitude (Larson, 2003a). This occurs where the core is optically thin to thermal emission from the dust, at densities below 10^{10} cm^{-3}.

The collapse of a uniform sphere of gas (in the absence of a pressure gradient) occurs in the timescale,

$$t_{ff} = \left(\frac{3\pi}{32G\rho}\right)^{\frac{1}{2}}, \tag{1.9}$$

known as the free-fall time (Spitzer, 1978). Here, ρ is the density of the gas and G is the gravitational constant. In reality a finite outward pressure gradient would slightly decelerate the collapse. However the time for each radial mass shell to collapse, using the average interior density of the shell, is still close to the free-fall time. So the denser inner regions of the sphere collapse at a faster rate than the outer less dense regions.

Once the initial core has formed, the central region becomes opaque to thermal dust emission and the temperature begins to rise. A second collapse then occurs which raises the central density to what would be expected for a star. However, the central mass is still rather small with a mass of approximately 10^{-2} M$_\odot$ (Larson, 2003a). The remaining mass of the star is acquired through accretion. A disk of rotating material forms around the protostar and material falls into the centre. In the model by Shu (1977), the accretion rate is given by,

$$\dot{M} = \frac{0.975c^3}{G}, \tag{1.10}$$

where c is the isothermal sound speed. This would lead to the formation of a solar mass star in approximately 6.5×10^5 years (Larson, 2003a). The actual accretion rate is higher than this, one possible solution gives a rate of 46.9 c^3/G, known as the 'Larson-Penston-

Hunter' solution (e.g. derived from Hunter (1977)).

As part of the accretion process angular momentum must be conserved, which may be through the presence of jets and outflows, or by angular momentum being lost to the outer reaches of the disk. This leads to longer than expected accretion timescales (Larson, 2002); a more likely solution is given later in Section 1.3.3). The rotation rate of the protostar increases through this process. Once accretion has finished then the central protostar becomes visible to optical observations. Sources within clouds that are only visible to far-infrared and millimetre wavelength observations are defined as *Class 0* sources (André et al., 2000).

To quantify a measure of stellar youth, the infrared excess of a young source can be derived from its infrared spectral index,

$$\alpha_{IR} \equiv \frac{d\log(\lambda F_\lambda)}{d\log\lambda}, \tag{1.11}$$

where λ is the wavelength and F_λ is the measured flux density at that wavelength (Stahler & Palla, 2005). Objects with $\alpha_{IR} > 0$ are defined as *Class I* sources. These are found in dense cores using emission from NH_3 for example. Objects for which $-1.5 < \alpha_{IR} < 0$ are defined as *Class II* sources. *Class III* sources have $\alpha_{IR} < -1.5$ (Stahler & Palla (2005), following the original classifications given in Lada (1987)).

1.3.2 The Initial Mass Function

Knowing the distribution of stellar masses *at birth* from the molecular clouds is important. This is known as the initial mass function (IMF - Salpeter (1955)). The IMF gives the relative number of stars produced per unit mass interval (Kroupa, 2002). Ultimately, the amount of material that can accrete onto a prestellar core is determined by several factors; the amount of mass available, the temperature/density of the cloud, magnetic fields, turbulence. Therefore, a fully deterministic theory for the IMF is unlikely to exist (Mac Low & Klessen, 2004). However, much research has been done to understand what can be observed. Salpeter derived the following relation (Salpeter, 1955),

$$\frac{dN}{d\log M} \propto M^{-\alpha}, \tag{1.12}$$

with a value for α of ~1.35. However, plotting the IMF against $\log M$ for even solar neighbourhood stars shows a deviation from this value, especially at lower masses. For example, as M approaches 0.08 $M_\odot$, the smallest amount of mass for a which an object is able to undergo nuclear fusion, the value of α seems to approach 0. In dense cores, a similar relation exists as for the IMF, called the dense core mass function (DCMF - Alves et al. (2007). In their paper, Alves et al. (2007) conjecture that the origin of the IMF is linked to the DCMF, perhaps originating from a thermal, 'Jeans-like', fragmentation process in the molecular gas.

In recent work, a more complex value for α has been derived. For self-gravitating structures, Hennebelle & Chabrier (2008) found that $\alpha = (n-1)/(2n-4)$ where n is $\simeq 3.8$ (the spectral index for the velocity power spectrum). For non self-gravitating structures they found that $\alpha = 2 - n'/3$, where n' is the power spectrum index of $\log\rho$.

1.3.3 Formation of Binary Systems

One difficulty in explaining how stars accrete mass arises from the issue of angular momentum conservation. The rotation velocity of the system will increase dramatically as the system becomes more compact, resulting in such high speeds that the system would break apart. A solution might be that stars (of mass <10 $M_\odot$) form in pairs or multiple systems, thereby some of the angular momentum goes into the orbital motions of the stars. Of course solitary stars are also observed, and their presence could perhaps be explained if stars form in a triple system and one star is ejected (Larson, 1972; Reipurth, 2000), leaving a binary system. Isolated star formation may also occur in molecular clouds where the turbulence causes local collapse, but upholds the cloud at larger scales (Klessen et al., 2000). In this case, the star formation rate is lower and the protostars are thinly spread out in the cloud. Returning to angular momentum, most is actually lost due to the braking effect of magnetic fields, both in individual and multiple systems (e.g. Mouschovias

(1991)).

Fragmentation occurs due to excessive rotation during the isothermal phase of collapse (Larson, 2003a). The presence of a ring or bar structure in the disk will also lead to the formation of binaries and multiple systems. Interactions with other nearby cores will increase the likelihood of binary systems (Whitworth, 2001). If the structure of the cloud is filamentary then the initial conditions for collapse are non-axisymmetric and this will increase the possibility of binary formation. The removal of angular momentum through jets was discussed earlier; it turns out that more than 85% of jet sources are in binary or triple systems, suggesting that the jets are triggered by the close companions (Reipurth, 2000, 2001).

1.3.4 Formation of Multiple Stars and Clusters

There is strong evidence that stars more massive than 10 $M_{\odot}$ form in clusters (such as in the constellation of Orion, shown in Figure 1.2. Three of the molecular clouds analysed in this thesis are found in Orion). Clusters form in more massive molecular clouds where the densities and temperatures are much higher than for low mass star formation ($n > 10^7 cm^{-3}$ and T > 100 K, Evans (1999)). These clouds do not tend to be long-lived entities (of the order of 1 Myr - Vázquez-Semadeni et al. (2005)). However, there is still debate as to the exact mechanism of massive star formation. Some evidence suggests that high-mass star formation is simply a scaled-up analogue of low-mass star formation (Molinari et al., 2008).

Massive cloud cores tend to generate large density fluctuations and clumpy substructure (Larson, 1981). This leads to the creation of clusters of stars. These may in turn merge early on to form more massive stars. Within clusters, there is a powerlaw relation between the most massive star in the cluster, and the mass of the remaining stars (e.g. $M_{star} \sim 1.2\ M_{cluster}^{0.45}$, Larson (2003b), also see Johnston et al. (2009)).

Figure 1.2: The constellation of Orion, containing sites of star formation in which clusters are formed (optical image © Rogelio Bernal Andreo). Three of the molecular clouds analysed in this thesis are found in Orion; λ-Ori (associated with the nebulosity on the left), Orion A (located middle right of the image) and Orion B (below the centre of image). This optical image shows 'Barnard's loop' (large circular structure on the right) together with many other famous nebulae including M42/3, and the Horsehead nebula etc.

1.3.5 Star Formation Efficiency and Star Formation Rate

An important question to consider is what is the efficiency of star formation, i.e. what percentage of a molecular cloud is converted in stars? Without any kind of support GMCs could be expected to collapse on a timescale of 1-2 free-fall times (Goldreich & Kwan, 1974). Ignoring the effects of stellar feedback within the cloud, this would lead to most of the material being converted into stars and hence a high star forming efficiency (SFE), a fact that was disputed soon after the former supposition (Zuckerman & Evans, 1974). Evidence suggests that once the fraction of material used to make stars in a cloud reaches $\epsilon_{GMC} \approx 0.08$ then stellar feedback disrupts the collapse of further material (e.g. Murray (2010)). This fraction may also be defined by Equation 1.13,

$$\epsilon_{GMC} \equiv \frac{M_*}{M_{GMC} + M_*}, \tag{1.13}$$

where M_* is an estimate of the mass contained in young (< 3.9 Myr) stars and M_{GMC} is the mass of the cloud (Murray, 2010). An upper limit on the value of ϵ_{GMC} is given by

Alves et al. (2007) of 30%±10% for the dense cores of clouds (hence this relates to the self-gravitating parts of clouds). However, Murray (2010) found a range of values for ϵ_{GMC} from 0.2% to 20%. They measured a typical lifetime for a cloud with average mass in their sample of 17±4 Myr, using WMAP data of 13 bright free-free emission sources in the Galaxy (Murray & Rahman, 2010). This corresponds to approximately 2 free-fall times. They concluded that the star formation rate in molecular clouds increases with age until the feedback from stars in the cloud disrupts the process. Thus, the star formation rate is unlikely to be determined by turbulence. Star formation efficiency and the lifetime of GMCs are discussed in Feldmann & Gnedin (2010). Using models they find there is insufficient observational evidence to prove whether a varying rate of star formation exists in molecular clouds.

In a recent paper, Lada et al. (2010) investigated the star formation activity for a selection of nearby molecular clouds. They found that the star formation rate varies between different clouds. In particular, they found that the rate of star formation SFR is related to the mass of the cloud $M_{0.8}$ above an extinction threshold of 0.8 mag A_K, by the relation Equation 1.14,

$$SFR(M_{\odot}yr^{-1}) = 4.6 \pm 2.6 \times 10^{-8} M_{0.8}(M_{\odot}). \tag{1.14}$$

They also found that Equation 1.14 agrees with observations of star formation rates in both Galactic and extragalactic star formation sites.

1.3.6 Observations of Star Formation

This section outlines the nature of relevant observations, firstly giving an overview of the COMPLETE Survey as an example.

1.3.6.1 The COMPLETE Survey

The COordinated Molecular Probe Line Extinction Thermal Emission (COMPLETE, Ridge et al. (2006)) Survey of Star Forming Regions is an attempt to provide a compre-

hensive database of data useful for understanding star formation. The survey combines a whole variety of data, including

- Extinction maps derived from 2MASS data using the NICER algorithm (explained in Section 1.6.6.2).
- Extinction and temperature maps derived from *IRAS* 60 μm and 100μm emission.
- H I maps of atomic gas.
- ^{12}CO and ^{13}CO maps of molecular gas.
- Submillimeter continuum images of emission from dust in dense cores.

The COMPLETE survey was executed in two phases; Phase I to gather observations at scales from 0.1 pc to 10 pc (i.e. a more 'macroscopic' view of the star formation process), and Phase II to focus more on star-forming cores where the scale is < 0.1 pc. Phase I of the COMPLETE survey presented data on the Ophiuchus and Perseus molecular clouds (Ridge et al., 2006). Numerous publications have been released since this first work. The material published in respect of the COMPLETE survey may be accessed via links on the COMPLETE webpage[1].

1.3.6.2 Observing the Column Density Distribution

In order to better understand the processes involved in star formation, it is necessary to probe the structure of the molecular clouds in which they form. In an ideal situation one would want to know the volume density distribution of the molecules in the cloud. At this point there are two problems. Firstly, it is not possible to ascertain the volume distribution, due in part to the fact that only one view of the cloud is presented to the observer due to the extreme distance (though recently a method has been outlined by Brunt et al. (2010) to recover the 3D PDF from 2D column density data). Any assumptions that could be made would be heavily dependent on the model(s) used. Secondly, molecular hydrogen cannot be observed in emission at low temperature due to its configuration. As it does not

[1] http://www.cfa.harvard.edu/COMPLETE.

possess a permanent dipole moment, the lowest possible transition (rotational, $J = 2 \rightarrow 0$) requires an ambient temperature of around 510 K; however molecular clouds have a typical temperature of only 20 K or less.

Therefore, it is necessary to consider what methods can be used to trace the molecular hydrogen (column density) distribution in molecular clouds. An excellent comparison of some methods of cloud structure analysis are given in Goodman et al. (2009). An overview of their COMPLETE survey (Ridge et al. (2006) - data from which was used to make the comparison) was given in Section 1.3.6.1. The three methods of cloud structure analysis compared were near-infrared extinction mapping, thermal emission mapping in the far-infrared, and mapping the intensity of CO isotopologues (i.e. tracing the gas in the cloud rather than tracing the dust as in the first two methods).

The near-infrared extinction maps used by Ridge et al. (2006) were derived using data from the Two Micron All-Sky Survey (2MASS). The maps had a resolution of approximately 5′ and measured visual extinction from 0 mag to 10 mag with a reliability of ~0.25 mag. The far-infrared maps used data from the IRIS (Improved Reprocessing of the IRAS Survey) database (Miville-Deschênes & Lagache, 2005). They used the IRIS flux maps at 60μm and 100μm to derive dust temperature and far-infrared optical depth maps, which are converted to column density maps by using a calibrated conversion from far-infrared optical depth to near-infrared extinction (see also Pineda et al. (2008)). Lastly, the molecular line emission maps (^{13}CO and ^{12}CO) were made for the COMPLETE Survey (Section 1.3.6.1), with the data smoothed to 5′ to match the other maps. The ^{12}CO data was used to calibrate by estimating the excitation temperature, and a constant abundance of H_2 is assumed relative to ^{13}CO. A conversion procedure is used to give the A_V from the ^{13}CO maps.

On comparing the results from these three methods, Goodman et al. (2009) found that the maps made using molecular line mapping do not give column densities that resemble those made from the maps using the dust based methods. Therefore, the ^{13}CO maps are of limited use. They also found that the correct calibration of the maps in all three cases is crucial. They concluded that extinction maps made using data in the near infrared

represent the least biased way to measure column density in molecular clouds, assuming the near constancy of the gas to dust ratio (Hildebrand, 1983).

As mentioned earlier, gases such as CO may be used to trace the molecular hydrogen in a cloud. This is less straightforward than with using dust as a tracer, due to the abundance of CO changing with the density of the cloud (e.g. Glover & Mac Low (2010)). Firstly, there is the likelihood that CO emission attributed to molecular clouds may in fact be from diffuse molecular gas in the ISM (Liszt et al., 2010). The diffuse molecular gas emission is observed along lines of sight away from dark clouds but is also likely to interfere with measurements in dark clouds too.

Secondly, the existence of CO is dependent on being shielded from photodissociation and there is a sharp cut-off in the abundance in CO at $A_V \leq 3$. (This is confirmed in Pineda et al. (2010), who find that the relationship between A_V and N(CO) is linear between $A_V \simeq 3-10$, and that the fractional abundance of CO below $A_V = 3$ is lower by two orders of magnitude). When shielded from ultraviolet radiation, all available *gaseous* carbon is found in CO. Despite the variation in the ratio of CO to H_2 throughout molecular clouds, the integrated intensity measured from the $J = 1 \rightarrow 0$ rotational transition line in ^{12}CO and the H_2 column density appear to show a good correlation.

1.4 Interstellar Dust

This section discusses the dust found in the interstellar medium, including background information and theory. Beforehand, some theory is given on molecular hydrogen and carbon monoxide, both of which are important molecules associated with interstellar dust.

1.4.1 Molecular Hydrogen

The chief constituent of molecular clouds is the hydrogen molecule (e.g. Shull & Beckwith (1982)). Unfortunately, it is difficult to detect as even the lowest excited energy levels (corresponding to rotation of the molecule) are too far above the ground state to be sufficiently populated at low temperature. Furthermore, as the molecule consists of two

identical atoms it lacks a permanent dipole moment. Radiation from a rotationally excited molecule is possible through the slower quadrupole transition. The vibrational and rotational states are denoted by v and J respectively. The rotational quantum number J can only change by 0 or ±2, with $J = 0 \rightarrow 0$ not allowed. These changes are denoted O, Q and S for $\Delta J = +2, 0, -2$ respectively. There are no selection rules for the vibrational quantum number v for electric quadrupole transitions.

The lowest possible rotational transition is the 0-0S(0) line (i.e. $J = 2 \rightarrow 0$, within the $v = 0$ state) transition which has an energy change of over 500 K. This is detectable at a wavelength of 28.2μm in the far-infrared. This line is only observed in warm molecular hydrogen, i.e. not in cold molecular clouds.

Another useful line, due to it's high brightness, is the 1-0S(1) line which is observed in the near-infrared at 2.12μm. This arises from the $J = 3 \rightarrow 1$ ro-vibrational transition, with v changing from 1 to 0. However, the ambient temperature required is in excess of 6000 K, therefore this line is usually observed as a result of shocks or energetic collisions in high density regions.

1.4.2 Carbon Monoxide

The CO molecule is less abundant in molecular clouds than H_2, but is also self-shielding against ambient ultraviolet radiation. Hence, it can be used to as a tracer of molecular gas. Unlike H_2, it does have a permanent dipole moment, therefore J can change by ±1. These changes are denoted by O, P, Q, R, S for $\Delta J = +2, +1, 0, -1, -2$ respectively.

The lowest energy transition is the 0-0R(0) line (i.e. $J = 1 \rightarrow 0$, within the $v = 0$ state) which requires an ambient temperature of 5.5 K. It emits strongly at radio frequencies, for example the photon emitted by the $J = 1 \rightarrow 0$ transition has a wavelength of 2.6mm. Beyond a critical density, the emissivity decreases as more molecules are excited to states with $J > 1$. At this point the molecule is ineffective as a gauge of it's density. Other isotopes of CO are useful, such as ^{13}CO, which remains optically thin even in high density clouds (due to lower abundance) and has a near-constant abundance except in cold (T <15 K) cores (Goodman et al., 2009).

1.4.3 Background and Theory of Interstellar Dust

Dust is an important tracer of molecular hydrogen in molecular clouds. The existence of dust in the interstellar medium was first implied in the 1920s, when a technique for measuring the extinction of starlight using the dimming of stars by dark clouds was published by Wolf (1923). Then Trumpler (1931) postulated that these dark clouds were caused by the presence of 'free atoms or fine cosmic dust'. Photographic catalogues of dark 'nebulae' had been made by Barnard from around 1910 to 1927. Much work was done by Bok in the 1960s onwards in categorising these clouds (e.g. Bok (1956)). Studies have shown that dust grains condense out of the dense, warm winds of evolved stars, or are formed from supernova explosions (e.g. Rho et al. (2009)).

The composition of dust in the ISM can only be determined indirectly as it is not yet possible to collect samples from outside of our solar system. Studies of dust within our Solar system are useful, but show a population of dust that cannot be compatible with the wider ISM (e.g. Draine (2008)). Dust grains consist predominantly of carbon, silicon, hydrogen, magnesium and iron (e.g. Draine (2003, 2009). Dust along the line of sight attenuates (and reddens) starlight, and this allows the properties of the dust to be investigated.

The decrease in observed extinction with wavelength, as shown in Figure 1.3 (from Draine (2009)), is known as the *extinction curve*. A broad bump in the extinction curve at 2175 Å is likely due (Weingartner & Draine, 2001) to clusters of Polycyclic Aromatic Hydrocarbons (PAHs). PAHs consist of linked carbon rings arranged in planar form (Stahler & Palla, 2005). For example, excess emission in the infrared due to PAHs is observed in planetary nebulae (Cohen & Barlow, 2005). Silicate features are also observed in the spectra.

A less prominent feature in the extinction curve are the Diffuse Interstellar Bands (DIBs). Over 150 spikes in the range 0.38-0.868 μm have been identified (Jenniskens & Desert, 1994). The origin of DIBs is believed to be the presence of protonated PAHs in the grains (Pathak & Sarre, 2008). Spectroscopic analysis of dust reveals other features such as the presence of silicates, chain-like hydrocarbon bonds, ice features and other

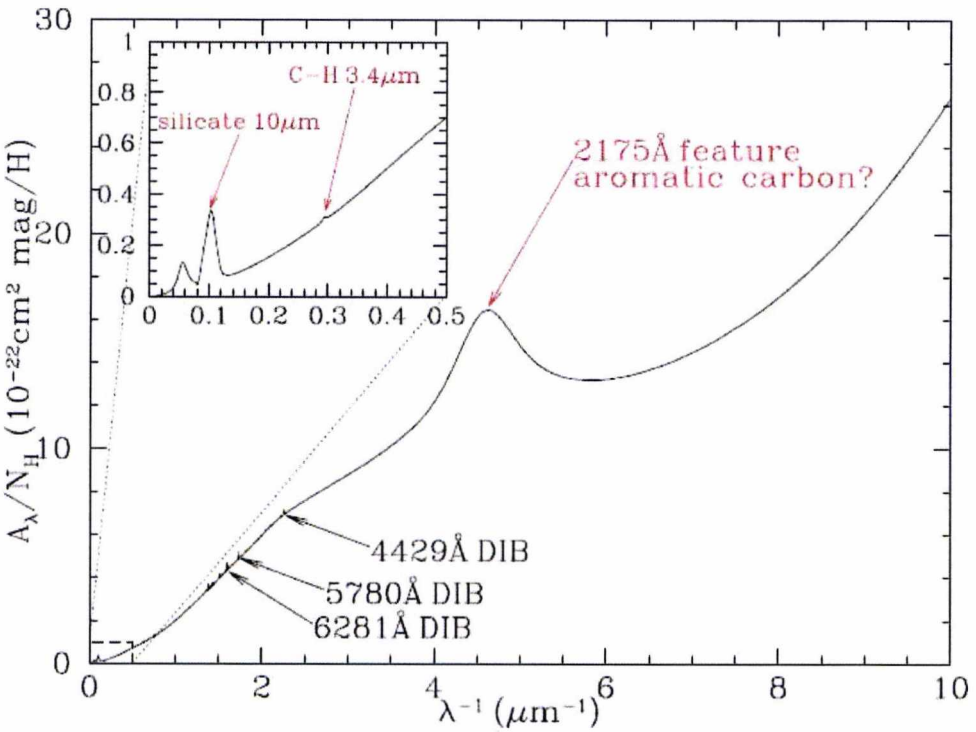

Figure 1.3: An extinction curve showing the variation in extinction with wavelength over the range 10,000 Å to 1250 Å. The bump at 2175 Å is clearly visible. Also shown are the wavelengths of some Diffuse Interstellar Bands (DIBs). Figure taken from Draine (2009).

species including CO_2, NH_3, CO, CH_3OH, CH_4 and others (Draine, 2003). Even H_2O is postulated to form on dust grains (Mokrane et al., 2009) in the presence of ozone. Other elements including O, Mg, Si and Fe have been inferred from X-ray observations due to the absorption of X-rays (Schulz et al., 2002). Another feature which gives some insight into the composition of dust grains is Extended Red Emission (ERE). This consists of a broad emission between ~5400 Å and ~9000 Å peaking between 6100 Å and 8200 Å (Draine, 2003). The exact cause of ERE is uncertain but several sources such as PAHs and quenched carbonaceous composites have been suggested (Wada et al., 2008).

Dust is responsible for obscuring much radiation at visual and ultraviolet wavelengths, except that emitted by relatively nearby sources (e.g. Mathis (1990), Draine (2003)). It also determines the wavelengths at which other galaxies may be observed. The energy absorbed by dust is re-radiated at far infrared wavelengths, and this makes up 30% of the luminosity of the Galaxy Bernstein et al. (2002). Dust controls the behaviour of the

ISM, and the process of star formation. The gas-to-dust ratio in molecular clouds is a near constant (100 to 1, from e.g. Hildebrand (1983)), due to the heavy processing of dust in the ISM (Mathis, 1990). The star formation efficiency (SFE) is determined by the distribution of gas and dust in the Galaxy. In regions of high dust concentration, such as star forming cores, the SFE found using models can be as high as 50% (Clark & Bonnell, 2004). Typical rates of star formation in clusters, again using models, yield a SFE of 5-10% (Clark et al., 2005).

The shape and alignment of grains has an important effect of the polarisation and reddening of starlight. Light from reddened stars tends to be linearly polarised due to differential extinction by dust grains aligned by a local magnetic field (Draine, 2003, 2009). The dust grains must be sufficiently non-spherical for extinction in one polarisation mode to be sufficiently different from the extinction measured in the other polarisation mode (Draine, 2003). Grains may also be aligned by radiative torques (Lazarian & Hoang, 2009; Lazarian, 2009). These are caused by the grains exhibiting a different cross-section to left-handed and right-handed photons. In the first instance this should result in the spin-up of grains. However, gaseous bombardment and infrared emission reduce the spin rates and allow alignment with the magnetic field. A model for the treatment of spinning grains is given by Ali-Haïmoud et al. (2009). Dust grains are also responsible for the scattering of incident starlight (e.g. Li (2008)). The scattering can be forward or back-scattering depending on the position of the illuminating source.

The primary method of heating of dust grains in the ISM is by the absorption of incident radiation from stars. The density of dust grains in the ISM is sufficiently low so that there is little collisional heating. Dust grains cool by emission of infrared radiation, occuring over a typical timespan of 24 hours (Draine, 2003). Grain temperatures vary along each line-of-sight, and between different grain types and sizes throughout a molecular cloud (e.g. Schnee et al. (2006)). Larger grains with a radius of $\geq$200 Å are better able to retain a constant temperature, whereas smaller grains with a radius of $\leq$50 Å vary wildly in temperature. It is difficult to derive an average temperature for smaller grains due to these fluctuations. In smaller grains the infrared emission happens soon after heat-

ing by a photon, while the grain temperature is at a peak (Draine, 2003). Over the smaller size scales, the larger grains are more frequently hit by photons so are more constant in temperature.

The radiation absorbed by grains is subsequently re-emitted at longer wavelengths. Therefore, observations in far-infrared and sub-millimetre wavelengths are required to probe the dust emission. The exact wavelength depends on the temperature of each grain. Treating each grain as a *blackbody*, the peak wavelength of the emission can be determined from *Wien's displacement law* (e.g. Stahler & Palla (2005)),

$$\lambda_{max} = \frac{2.9 \cdot 10^{-3}}{T}. \tag{1.15}$$

Therefore, at 240μm, the corresponding temperature is approximately 12 K, for example.

Emission is also observed from diffuse dust, which exceeds that expected from thermal emission. The strongest bands are in the wavelength range 3.3-11.3μm. These bands closely correspond to C-C or C-H bond vibrations in molecules such as PAHs, and are caused by vibration in the outer bonds of the PAH molecules.

Observations show that most of the dust in the Galaxy lies along the Galactic plane. The actual distribution of dust is found to be asymmetrically warped about the plane. Marshall et al. (2006) used data from 2MASS to measure the extinction along 64,000 individual lines of sight in the Galactic centre (l within 100° of the Galactic centre; $|b| \leq 10°$) to determine the distribution of dust. They compared the results with existing extinction maps and CO surveys, and found the same large scale structures in each map. In terms of the warping, which is most pronounced at distances of around 8 kpc, the material warps towards the north at values of $|l| \approx 60$ to 80° and warps towards the south at values of $|l| \approx 280$ to 300°.

Dust grains may be destroyed or broken-up by grain-grain collisions in interstellar shock waves, e.g. caused by supernovae (Draine, 2003). In such regions, the size distribution of the dust is altered and the small-to-large size ratio is increased (Mazzei & Barbaro, 2010). This explains the presence of anomalous extinction curves which cannot be explained by a simple relation (see Section 1.5.1).

1.5 Extinction

Extinction of starlight is caused by the presence of dust along the line of sight. Dust causes the starlight to be attenuated and reddened. As previously discussed, the level of attenuation varies with wavelength. The term reddening derives from the fact that the level of attenuation is greater at shorter (bluer) wavelengths. A reliable way to measure extinction is to compare two identical stars (at an identical distance), one exhibiting extinction, and the other in a region free from extinction. This is known as the 'pair-method'. The extinction may obtained by using the observed flux of each star, F_λ and F_λ^0 respectively, together with Equation 1.16,

$$A_\lambda \equiv 2.5 \log_{10}\left(\frac{F_\lambda^0}{F_\lambda}\right). \tag{1.16}$$

A drawback of this method is having to calculate the extinction along every line of sight, i.e. for every star in the field. This makes the method computationally expensive and restricts the area that can be investigated. It also relies on the accurate determination of the type of each star, and the fact that each star needs to be compared with an identical star in an extinction-free field, at the same distance.

1.5.1 Reddening Law

To determine how starlight is affected when it has passed through a molecular cloud, a 'reddening law' is used (Rieke & Lebofsky, 1985). This can be determined by taking a field of stars, and calculating the colour-excess $\langle\rangle$ of three wavebands (J, H and K, for example). Therefore, the reddening is the difference between the observed star colour and the true colour given the star's spectral type. The intrinsic (tr) colour is deducted from each star's measured colour and the results are plotted, one waveband against the other, i.e. plotting $[J-H]-[J-H]_{tr}$ against $[H-K]-[H-K]_{tr}$. If the data conform to the reddening law, then the plotted points lie roughly along a straight line.

One can define the ratio of total to selective extinction $R_V = A_V/E(B-V) = 3.09$ (Rieke & Lebofsky, 1985). The quantity R_V is dimensionless and may be determined by

extrapolating near-infrared extinction out to infinite wavelength (e.g. Mathis (1990)). For the diffuse ISM a typical value of R_V is approximately 3.1, but this varies for different lines of sight. In the Taurus and Ophiuchus molecular clouds the value of R_V may be as high as 4 to 6 due to the density of these clouds (Mathis, 1990). A reddening law similar to that of Rieke & Lebofsky (1985) was derived using 2MASS data (Indebetouw et al., 2005). Their data (showing $\langle[J-H]\rangle$ as a function of $\langle[H-K]\rangle$) are quoted in Figure 11 of Lombardi et al. (2008a).

1.5.2 Optical Extinction

Extinction may be measured at optical wavelengths, giving good sensitivity at low values of A_V (e.g. $A_V < 5$), (Dobashi et al., 2005). However, a major drawback is poor penetration into clouds. Visual extinction can be measured for values of A_V as high as 20 (Cambrésy et al., 2002), but generally will give lower values of A_V compared to methods which are better able to penetrate clouds (e.g. at longer wavelengths).

Visual extinction is proportional to the column density of material along the line of sight. The column density can be expressed as

$$N(H) = 6.83 \times 10^{21} cm^{-2} \cdot \frac{A_V}{R_V}. \tag{1.17}$$

The extinctions at three wavelengths (say, at the B-band, V-band and an arbitrary wavelength λ) are related by (e.g. Stahler & Palla (2005)),

$$\frac{E(\lambda - V)}{E(B-V)} = \frac{A_\lambda}{E(B-V)} - \frac{A_V}{E(B-V)}, \tag{1.18}$$

with $E(\lambda - V) = A_\lambda - A_V$ and $E(B-V) = A_B - A_V$ and $A_V/E(B-V) = R_V$. The quantities $E(\lambda - V)$ and $E(B-V)$ represent the colour excess. It is preferable to use longer wavelengths than V, as the extinction law becomes less dependent on the line of sight (Mathis, 1990). Hence, near-infrared (NIR) wavelengths are useful for calculating extinction.

1.5.3 Near-infrared Extinction

At near-infrared wavelengths (~0.9μm and ~5.0μm) the extinction curve can be expressed as a power-law (Mathis, 1990), such that,

$$A_\lambda \propto \lambda^{-\beta}. \tag{1.19}$$

The value of β varies in the literature and is around 1.6-1.8 (e.g. Draine (2003), Froebrich et al. (2007), Stead & Hoare (2009) found $\beta \simeq 2.14$, using a combination of UKIDSS Galactic Plane Survey data and a synthetic model). The value varies for different clouds and in regions of high extinction may be slightly higher. The factor β was found to depend on the column density of the cloud being measured (Froebrich & del Burgo, 2006).

1.6 Techniques to Measure Extinction

This section outlines different methods that can be used to measure extinction, such as the star count method, extinction from reddening, using reflection from clouds and colour excess methods.

1.6.1 Star Count Method

Extinction may be measured using the Star Count method. The number of stars in a small area of sky are compared to a control area of the same size in a region free from extinction (e.g. Wolf (1923); Bok (1956); Froebrich et al. (2005); Dobashi et al. (2005)). This method can be visualised by plotting the log of the cumulative number of stars at increasing magnitude, from the two areas. Such a plot is known as a Wolf diagram (see Figure 1.4). This method assumes that extinction reduces the magnitudes of all the stars in the region affected by extinction, except those brighter than a certain magnitude. The brighter, unaffected stars are therefore in the foreground. The extinction can then be calculated along the line of sight by subtracting the difference in magnitudes between the two fields.

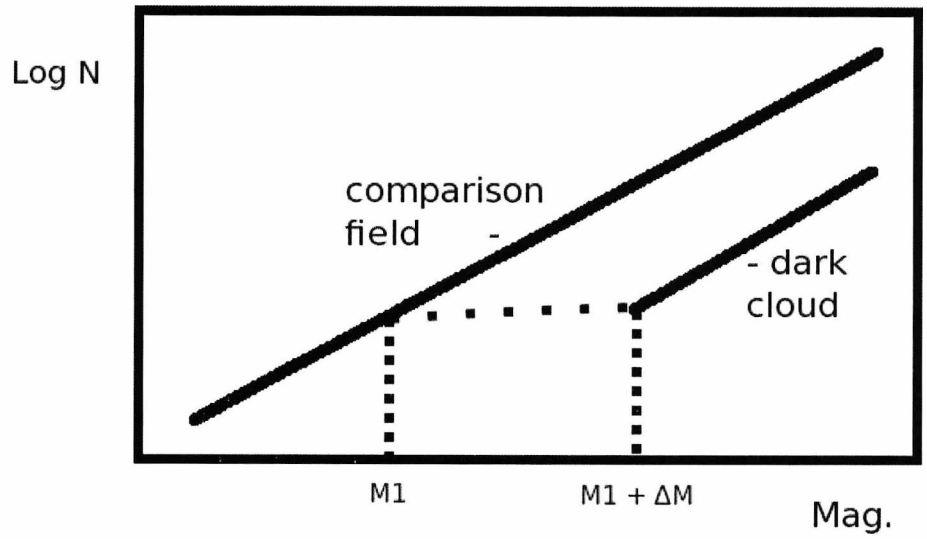

Figure 1.4: A Wolf diagram, showing the shift in magnitude (ΔM) above a certain threshold (M1) for a dark cloud when compared to a comparison field. The offset in magnitude gives the extinction value for the dark cloud.

There are several major disadvantages of this method. One drawback of this method is the assumption that the absolute magnitude of each star counted is identical. Another drawback is that the stars counted are distributed evenly in space. Both assumptions are in practise not correct. This method also gives a high noise compared to other methods, as the noise is inversely proportional to the root of the number of stars. This method only produces a meaningful result if a sufficient number of stars can be counted (Froebrich et al., 2005). This places a lower limit on the size of the area where extinction can be measured and hence the resolution attainable. Furthermore, the maximum visual extinction which can be measured is limited by the fraction of foreground to background stars in the field (Cambrésy et al., 2002). Of course, the number of background stars detected varies with the amount of material along the line of sight. Hence, the suppression of foreground stars is critical to obtaining the correct extinction.

Using an optical star count method, Cambrésy (1999) published extinction maps of several well known molecular clouds. The following giant molecular clouds were surveyed: Lupus, ρ Ophiuchus, Scorpius, the Coalsack, Taurus, Chamaeleon, Musca, Corona

Australis, Serpens, IC 5146, Vela, Orion, Monoceros R1 and R2, the Rosette nebula and Carina. An adaptive grid method was utilised which used a fixed number of stars per cell (20 stars per cell), rather than a fixed cell size. In this way the noise per pixel was kept more-or-less constant. The maximum extinction values found are approximately 10 mag. Analysis of the data gave estimates for the masses of the individual clouds.

A catalogue and atlas of dark clouds was published by Dobashi et al. (2005), using data from the Digitised Sky Survey. The survey covered the sky for the region where $|b| \leq 40°$. The data were obtained in three wavebands, (B, V, and R). Two different map resolutions were produced, the high resolution map having a resolution of 6′, the lower resolution being 18′. The survey identified 2448 dark clouds with 2841 clumps within them. Physical parameters of the clouds and clumps, such as position, size and A_V are given. A comparison with the maps of Schlegel et al. (1998) (see Section 1.6.3) is given in the paper, finding that their A_V values are a few times lower than the A_V (derived from the $E(B-V)$ given by Schlegel et al. (1998)). The explanation for this, in the Galactic plane region, is given as being due to the dust temperature assumed by Schlegel et al. (1998) not being appropriate to measure the A_V correctly. At higher latitudes the discrepancy is attributed to enhancement of dust emissivity at infrared wavelengths.

1.6.2 Extinction from Reddening

As discussed in Section 1.5.1, the ratio of the total extinction in a given waveband (A_λ) to the selective extinction ($E(B-V)$, for example) is generalised by (e.g. Mathis (1990)),

$$R_\lambda = \frac{A_\lambda}{E(B-V)}. \tag{1.20}$$

However, the ratio R_λ is not constant and varies according to the Spectral Energy Distribution (SED) of the source. The SED of a source is affected by the composition of the source and by dust along the line of sight. A method of correcting photometry at any wavelength for extinction is outlined in McCall (2004). Any measure of reddening for a target should first be converted into an optical depth at a standard wavelength. The

recommended standard wavelength is 1 μm (McCall, 2004), due to the lower sensitivity of reddening laws to environment in the near-infrared.

A combination of the star count method with reddening (utilising the colours of stars) was published by Cambrésy et al. (2002). Data from 2MASS was used to make an extinction map of the North America and Pelican Nebula region. Visual extinctions with up to values of 35 mag were measured. When combining the star count method with reddening, correct calibration of the two methods is important. For example, the same cell size was used for each method. They also found that less than 3% of the mass of any given molecular cloud is found at A_V values of higher than 20 mag.

1.6.3 Emission from Dust

A full sky map of $E(B-V)$ was produced by Schlegel et al. (1998), intended as a new estimator of Galactic extinction. Data from the *COBE*/DIRBE and *IRAS*/ISSA maps were used. The $E(B-V)$ map, using observations at 100μm, shows dust temperature. Diffuse emission from dust in the infrared can be used as a measure of column density. The $E(B-V)$ values may be converted to extinction, A_V, by assuming an R_V value of 3.1. The resolution of the final $E(B-V)$ map is 6.1′. The removal of zodiacal light was a major factor in producing the map, this was achieved by modelling the interplanetary dust with measurements at 25μm (as interplanetary dust is prevalent in this wavelength), and extending this model to the actual (longer) wavelength used. Normalisation of the maps was achieved by using the colours of background galaxies as calibration.

Regarding the dust temperature, a variation of approximately 4 K (between 17 K to 21 K) is present, giving rise to a variation of a factor of 5 in terms of column density. In the paper the authors state that the accuracy of the maps for $|b|$ <10° requires further investigation. However, the temperature in cores is lower, e.g. $T \simeq 10.6K$ in the star forming Bok globule CB244 (Stutz et al., 2010). Furthermore, the line of sight temperature distribution is not known, leading to inaccuracies when converting the dust-continuum emission into column density. The dust emissivity is not well understood at the wavelengths of 100μm. Subsequent to the publication of the Schlegel et al. (1998)

maps, Arce & Goodman (1999) and Yasuda et al. (2007) found that their extinction values differed from those derived using the $E(B-V)$ values by a factor of ~1.4. They attribute this to a departure in the relationship assumed by Schlegel et al. (1998) between dust emissivity and $E(B-V)$ above values of $E(B-V) > 0.15$ (0.47 mag A_V).

1.6.4 Reflection from Clouds

One technique to analyse the structure in molecular clouds is to study the scattering of ambient starlight (termed 'cloudshine' e.g. Nakajima et al. (2003); Foster & Goodman (2006)). This method works as the reflected radiation is a function of the mass distribution in the cloud. The reflected emission can be observed at infrared wavelengths as these allow deeper probing of the structure compared with optical wavelengths (Padoan et al., 2006). This method of measuring the density structure of clouds does not suffer from problems that afflict other methods (e.g. problems due to dust temperature and dust emissivity that affect emission methods), but does rely on the isotropic illumination of the cloud by ambient starlight. In this respect, the method relies on the cloud being uniformly distant from the illuminating stars.

1.6.5 Molecular Line Emission

Due to the temperatures and densities found in molecular clouds, emission lines from the molecules are present in sub-mm and radio wavelengths. To be useful as a tracer of molecular hydrogen, the abundances of molecules need to be known. The abundances are typically small, but high enough in the denser parts of clouds to be useful. Therefore, molecular line emission is not useful for tracing low column density regions. Furthermore, the abundances may vary due to chemical evolution, or the molecules may freeze-out onto dust grains - making the method unreliable where this occurs. Another difficulty with this technique is that the line fluxes are also temperature dependent and lines may be optically thick. Nonetheless, an example of a survey using this technique is described in Section 1.3.6.1.

1.6.6 Colour Excess Methods

1.6.6.1 Near Infrared Colour Excess

A new way to calculate extinction was developed to utilise near-infrared data. The Near Infrared Colour Excess method was presented by Lada et al. (1994). The dependence of extinction on wavelength in the near-infrared range (around 0.9μm to 5.0μm) means that the additional colour of a star attributable to extinction (called the *colour excess*) can be derived as

$$< \lambda_1 - \lambda_2 >= (m_{\lambda_1} - m_{\lambda_2}) - (m^{int}_{\lambda_1} - m^{int}_{\lambda_2}) = A_{\lambda_1} - A_{\lambda_2}. \tag{1.21}$$

Here m_{λ_1} and m_{λ_2} are the observed magnitudes, and m^{int}_{λ} are the intrinsic, or true, magnitudes at λ_1 and λ_2.

Using Equation 1.19 to obtain the ratio of extinctions at two wavelengths gives

$$\frac{A_{\lambda_1}}{A_{\lambda_2}} = \left(\frac{\lambda_1}{\lambda_2}\right)^{-\beta}. \tag{1.22}$$

Rearranging Equations 1.21 and 1.22 gives,

$$A_{\lambda_2} = \frac{< \lambda_1 - \lambda_2 >}{\left(\frac{\lambda_2}{\lambda_1}\right)^{\beta} - 1}, \tag{1.23}$$

where β is the near-infrared power law index. For a third wavelength, λ_3, where $\lambda_1 < \lambda_2 < \lambda_3$, a similar relation can be found,

$$A_{\lambda_2} = \frac{< \lambda_2 - \lambda_3 >}{1 - \left(\frac{\lambda_3}{\lambda_2}\right)^{-\beta}}. \tag{1.24}$$

The relationship between the power law factor β and colour excess can be better understood by the use of a colour-colour diagram (see Figure 1.5). Plotting the $E(J-H)$ magnitudes against the $E(H-K)$ magnitudes for a sample of stars in a region with extinction shows a general linear relationship. The gradient, R, is the colour excess ratio (e.g. Froebrich & del Burgo (2006)). The factor β can then be estimated using, for example,

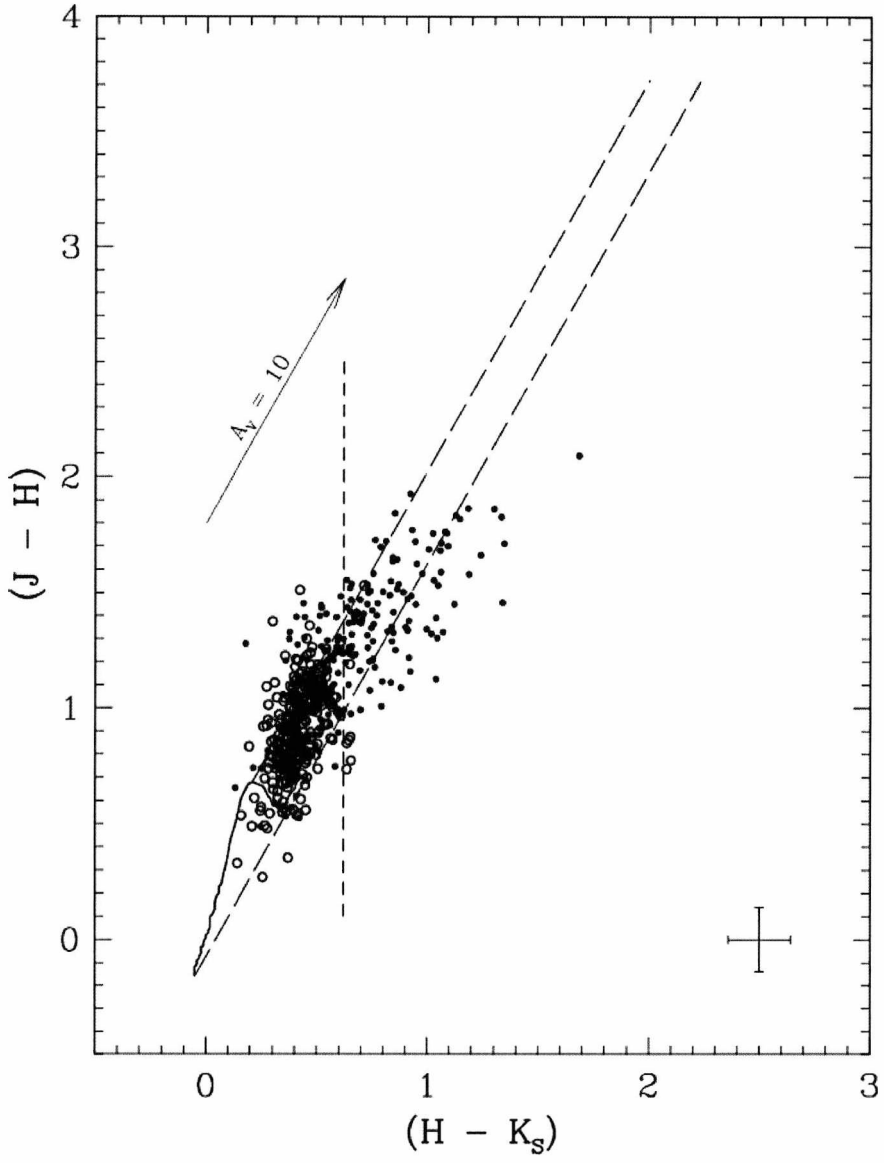

Figure 1.5: An example colour-colour diagram for stars in the molecular cloud [MAB97]250.63-3.63 towards IRAS 07527-3446 in our Galaxy (from Yun et al. (2009)). Here the data are being used to classify whether or not stars belong to a cluster. Filled circles denote sources inside the expected limits of the cluster, while open circle denotes those stars outside of this area. The vertical dashed line at $(H - K_s) = 0.62$ mag denotes the cut-off colour for cluster membership. A typical error bar is represented by the cross on the lower right.

Equation 10 in Froebrich & del Burgo (2006).

The NICE method relies on the intrinsic (H–K) colours of normal main sequence stars being distributed over a small range (see Table 3 in Koornneef (1983)). The average (H – K) colour is assumed to be 0.15 mag. If the intrinsic colours of the background stars are known, then the accuracy of the extinction measurements can be improved. Calibration

using stars in a nearby control field will allow this, providing the control field is free from extinction (Lada et al., 1994).

An extinction map covering major clouds in the Galactic anticentre region was published by Froebrich et al. (2007). The extinction map was made using the NICE method of Lada et al. (1994). The map has an oversampling of 2 with pixel sizes of 2′. Using their map the power-law index of the reddening law ($\beta = 1.8 \pm 0.2$) was found for molecular clouds in the anticentre region. Additionally, the column density distributions (CDDs) were analysed for major molecular clouds in the region. Plots of $\log N$ (where N is the number of pixels) against A_V were produced. A linear polynomial was fitted to each of the $\log N$ against A_V plots. They found the slope of the column density distributions became steeper with at greater distances. This was attributed either to a change in the physical laws in molecular clouds at a threshold scale of 1 pc, or to the dilution of A_V values with distance.

1.6.6.2 The NICER Method

A generalised version of the NICE method was later developed by Lombardi & Alves (2001). They called their method NICER (Near Infrared Colour Excess Revisited). This method can utilise data from three bands (i.e. the J, H and K bands), by combining two ways of calculating extinction,

$$\hat{A}_V = 15.846 \cdot \left[\frac{1}{N} \sum_{n=1}^{N} (H-K)^{obs} - \langle (H-K)^{int} \rangle \right], \tag{1.25}$$

and

$$\hat{A}_V = 9.35 \cdot \left[\frac{1}{N} \sum_{n=1}^{N} (J-H)^{obs} - \langle (J-H)^{int} \rangle \right]. \tag{1.26}$$

Both Equation 1.25 and 1.26 give some uncertainty in the estimate of A_V. The uncertainty in A_V depends on three factors,

1. The scatter in intrinsic colour is larger for $[J-H]$ than for $[H-K]$,

2. The photometric errors for the J-band are smaller then those for the K-band (unless viewing along the line-of-sight for high extinction clouds),

3. The numerical coefficient in Equation 1.26 (i.e. 9.35) is smaller than the numerical coefficient in Equation 1.25.

Therefore there are advantages and disadvantages to using either Equation 1.25 or 1.26 when calculating extinction. Lombardi & Alves (2001) combine these estimators to give an 'optimal estimator' for the extinction,

$$\hat{A}_V = b_1 \left[c_1^{obs} - \langle c_1^{tr} \rangle \right] + b_2 \left[c_2^{obs} - \langle c_2^{tr} \rangle \right]. \tag{1.27}$$

Here, c_1 and c_2 represent the chosen colours, i.e. $[J - H]$ and $[H - K]$, b_1 and b_2 are determined from Equations 1.28 and 1.29,

$$b_1 k_1 + b_2 k_2 = 1; \tag{1.28}$$

$$a + b_1 \langle c_1^{tr} \rangle + b_2 \langle c_2^{tr} \rangle = 0, \tag{1.29}$$

where k_1 and k_2 are the coefficients from Equations 1.25 and 1.26 (i.e. 1/9.35 and 1/15.846). The variance for this method is given in Equation 1.30,

$$Var(\hat{A}_V) = \Sigma_{i,j} b_i b_j Cov_{i,j}(c^{tr}) + \Sigma_{i,j} b_i b_j Cov_{i,j}(\epsilon). \tag{1.30}$$

In Equation 1.30, the covariances of the intrinsic colours ($Cov_{i,j}(c^{tr})$) and the covariance of the photometric errors ($Cov_{i,j}(\epsilon)$) are used. The index i denotes the colour used (e.g. $[J - H]$, $[H - K]$), and j originates with the covariance matrix.

In the case where more than one star is used to calculate an extinction, the NICER method applies a spatial smoothing to stars that are angularly close together. This allows a smooth extinction map to be made with a high signal-to-noise ratio. The improvement of signal-to-noise compared with the NICE method is a factor of two on the noise variance (Lombardi & Alves, 2001). This means that with 2MASS data, clouds with an A_V of 0.5 mag can be detected with a signal-to-noise of 3σ.

Data from the 2MASS point source catalogue were used to make wide field extinction maps (Lombardi et al., 2006, 2008a). In Paper I, Lombardi et al. (2006), an extinction map was produced of the Pipe Nebula covering 48 square degrees. Using the NICER technique their map is sensitive down to 0.5 A_V at a 3-σ detection limit and has a resolution of 1′. A normal reddening law for the Pipe Nebula was found, that is $E(J-H) = (1.85\pm0.15)E(H-K)$. A more accurate relationship was derived between the near-infrared extinction and the ^{12}CO column density. It was found that CO measurements are insensitive for low column densities corresponding to an A_V of up to 2 magnitudes.

In Paper II, Lombardi et al. (2008a), the NICER technique was applied to the Ophiuchus and Lupus clouds. A larger area of 1 672 square degrees was covered, with sensitivity down to A_K = 0.05 mag (corresponding to an A_V of 0.46 mag). The resolution quoted is 3′. They used the data to derive structure functions for the two clouds, finding that the Lupus cloud exhibited a structure function plot that would be expected from the theoretical work of She & Leveque (1994), while Ophiuchus could not be fit satisfactorily to any existing theoretical model.

1.6.6.3 The NICEST Method

In order to overcome problems with the NICE and NICER methods, a revised method called NICEST was proposed by Lombardi (2009). The former methods suffer from small scale inhomogeneities arising from either sub-structures or unresolved filaments in clouds, or from foreground stars. These problems are dealt with in the NICEST method by introducing a smoothing technique which does not bias the extinction estimate. An new estimator for the extinction at some point in the sky is,

$$\hat{A}_V = \frac{\Sigma_n w_n \hat{A}_n}{\Sigma_n w_n} - \beta \frac{\Sigma_n w_n \sigma_n^2}{\Sigma_n w_n}. \tag{1.31}$$

In Equation 1.31, w_n denotes the weighting for the stars around the point of interest, equivalent to $w(x';x)10^{\alpha k_1 \hat{A}_n}$. This is a function of the position and displacement from the position (x and x'), α is the slope of number counts, and k_1 is the extinction law for the waveband utilised. The term β is equivalent to $\alpha k_1 \ln 10$.

An adjustment for the presence of foreground stars, involves calculating the fraction of foreground stars to background stars in an extinction free region, f_0. Due to the weightings used in the overall estimator, this fraction should not change in extincted regions. Therefore, the estimator can be adjusted to by a factor of $1/(1\text{-}f_0)$. This factor will be close to 1 for nearby molecular clouds.

The NICEST method was used to make 23 near-infrared extinction maps by Kainulainen et al. (2009). For nearby clouds ($d \approx 170$ pc) they were able to attain a resolution of 2′ with a 3σ-error of between 0.5-1.5 mag A_V. They used the maps to show that the column density PDFs could be fit by a log-normal relationship at low A_V values. At higher column densities they found that power-law-like 'wings' formed, indicative of active star-forming clouds. They also conjectured that turbulence plays a major role only in the early stages of the cloud formation and that other factors such as gravitational forces tend to become more prevalent.

1.7 Turbulence in the ISM

In this section a definition is given of turbulence in the astrophysical sense. This is followed by the theory of the energy spectra in turbulence. Finally, a discussion is presented of recent attempts to model astrophysical turbulence using simulations.

1.7.1 Definition of Turbulence

In the context of the ISM, 'turbulence' refers to the random, chaotic motion of material within a molecular cloud. The study of turbulence and its impact on astrophysical processes is a vast subject which may only be summarised here. There are several useful reviews, such as Elmegreen & Scalo (2004), Scalo & Elmegreen (2004) and Brandenburg & Nordlund (2009). The role of turbulence in controlling star formation is reviewed by Mac Low & Klessen (2004) and Ballesteros-Paredes et al. (2007).

In turbulent motion energy is distributed over a large range of length scales (i.e. from small to large) with the bulk of the energy held in the larger scale motions. For example,

turbulence driven accretion is postulated to operate over a wide range of astrophysical scales (Klessen & Hennebelle, 2010). The energy is cascaded down from larger scales into smaller scales, at which viscosity becomes important. At these small scales the motion becomes random and isotropic, hence statistical methods provide the best way to study turbulence.

Though the turbulence observed in molecular clouds may not exactly resemble the 'classical' eddy turbulence seen in a terrestrial setting, classical theory is still useful. A flow of material/fluid may be classified as laminar or turbulent according to a dimensionless quantity known as the Reynolds number (see Equation 1.32). This is calculated by the ratio of inertial force to viscous force in the flow. A fully turbulent flow is generally defined as one having a Reynolds number of around 2000 and above, though this is only approximate. The Reynolds number is,

$$Re = \frac{\rho V^2}{\frac{\mu V}{L}} = \frac{\rho V L}{\mu}, \tag{1.32}$$

where ρ is the density, V is the mean velocity of the fluid, L is the length scale and μ is the dynamic viscosity.

The energy supplied to drive the turbulence in the ISM can come from several sources, including on larger scales, Galactic shear, supernova explosions, gravitational instability within spiral arms and stellar winds/radiation (Brunt et al., 2009). Small scale sources such as outflows from young stars also contribute but do not provide the velocity fluctuations provided by larger scale sources (Brunt et al., 2009). Interstellar turbulence is found to decay with a timescale around that of the gravitational free-fall time for a collapsing cloud , hence the need for a constant driving source (Mac Low et al., 1998; Ostriker et al., 2001).

1.7.2 Simulations of Turbulence

1.7.2.1 Limitations of Modelling

Much work has been done to model the effects of turbulence to attempt to match what is observed in molecular clouds. Firstly, consideration needs to made of the limitations that are imposed on simulations. A major limitation is the number of 'particles' included in the calculation (i.e. the performance of the machines used in the calculations limits the scope of the simulations). Including too many 'particles' in the simulation, either because they are too small or the area/volume too large, will mean that the simulation cannot be run in a reasonable timescale. Therefore, the 'particles' are typically not actually individual molecules but much larger units, hence the size of these units places a limit on the resolution that can be attained.

Other limitations are caused by the assumptions made prior to the simulation. Usually not all physical influences are taken into account (e.g. they may be deemed to have a negligible effect) so may not be included. For example, Federrath et al. (2009) assume the gas in molecular clouds is isothermal in their simulations, as a rough approximation. In practice there *are* variations in the temperature of gas in molecular clouds (e.g. Lehtinen et al. (2007)). Other effects may be ignored altogether if they are deemed to have a minimal effect, such as stellar feedback in the simulations by Cho & Kim (2010). Finally, any defects in physical laws used in the modelling (e.g. using Jean's mass as the threshold for collapse of material) will affect the results, potentially rendering them unrealistic. Therefore, simulations can only ever provide a rough approximation of physical processes.

1.7.2.2 Recent Work in Turbulence Modelling

The advent of modern computers has allowed the simulation of physical conditions found in molecular clouds (Klessen et al., 2009). Many different scenarios can be modelled, with an emphasis on matching the results to actual observations. The entire process from the assembly of the molecular cloud, to the formation of fragments, cores and protostars

can all be modelled.

For example, simulations have been used to find that probability density functions (PDFs) for volume and column density distributions (with an isothermal equation of state) in turbulent clouds can be fitted with a log-normal function (e.g. Passot & Vázquez-Semadeni (1998); Padoan et al. (1997)). Observations indicate that clouds which are forming stars have column density PDFs which show an extended tail at high extinctions (when fitted by a log-normal function), whereas non-star forming clouds do not (Kainulainen et al., 2009). The extended tail in the PDF is formed by self-gravity (Cho & Kim, 2010), which increases the core formation rate.

The 3D structure of molecular clouds is modelled and examined in Audit & Hennebelle (2010). They performed high-resolution numerical simulations of converging flows. They found that the thermal behaviour of the gas has a major effect on the density PDFs. In the isothermal case, the resulting PDF can be well fit by a log-normal relation. However, using a 2-phase scenario, only the high density component of molecular clouds could be well fit by a log-normal function. The low density component (in the range 10-300 cm^{-3}) produced a PDF which deviated significantly from a log-normal type distribution, raising a doubt as to whether a log-normal density distribution is appropriate for molecular clouds. But they propose no better distribution. Furthermore, using models of three molecular clouds formed in different ways, Tassis et al. (2010) found that log-normal type distributions are common to all generic molecular cloud types, rather than a particular indicator of supersonic turbulence in the cloud.

Using simulations, it is possible to separately treat the solenoidal and compressive forcings that are drivers of the turbulence in the ISM, and also model combinations of them both. Observations of solenoidal forcing (see Equation 1.33) will show vortex-like, filamentary structures (Elmegreen & Scalo, 2004). These have a fractal dimension of one (denoted $D = 1$).

Compressive forcing (see Equation 1.34) is caused by the action of shocks and large scale flows on a molecular cloud (Elmegreen & Scalo, 2004). Therefore, the motion is longitudinal and results in sheetlike structures. Hence, the structures have a fractal

dimension $D = 2$. Theoretical results indicate that turbulence in the ISM arises from a mixture of solenoidal and compressive forcing (Federrath et al., 2010). These can be expressed as solenoidal modes u_{sol} and compressive modes u_{comp} respectively (Elmegreen & Scalo, 2004),

$$\nabla \cdot \mathbf{u}_{sol} = 0, \tag{1.33}$$

$$\nabla \times \mathbf{u}_{comp} = 0. \tag{1.34}$$

Federrath et al. (2010) assume that the gas is isothermal in their simulations, as a rough approximation. Work by Kirk et al. (2009a) analyses the interplay between turbulence and magnetic fields in molecular clouds using simulations. They test which simulations bear similarities to real molecular clouds, using a 'thin sheet geometry' for the simulations. This results in reasonably quick (when compared with true 3-D) simulations allowing the testing of many input parameters. They find that magnetic fields dampen turbulence on both small and large scales, thus some mechanism is required to inject further energy on the larger scales to overcome the dampening. Kirk et al. (2009a) conclude that further simulations should be performed at higher resolutions to assess the implications of their result.

Simulations of turbulence have been used to describe the nature of protostellar cores. The predominant force acting on cores is self-gravity. Ballesteros-Paredes et al. (2007) postulated that the self-gravitating, turbulent gas found in cores is unlikely to be shaped by magnetic fields, which have only a minor effect. In models of turbulent magnetised clouds the cores do not align with the magnetic field (Ballesteros-Paredes & Mac Low, 2002). Girichidis et al. (2010) produced adaptive-mesh hydrodynamical simulations of collapsing turbulent cloud cores. They found that the initial density profile in collapsing cores is mostly responsible for determining the cloud evolution and formation of clusters.

However, Smith et al. (2009) found that the environment around the core must also be important in it's evolution, since the initial density profile alone does not entirely account

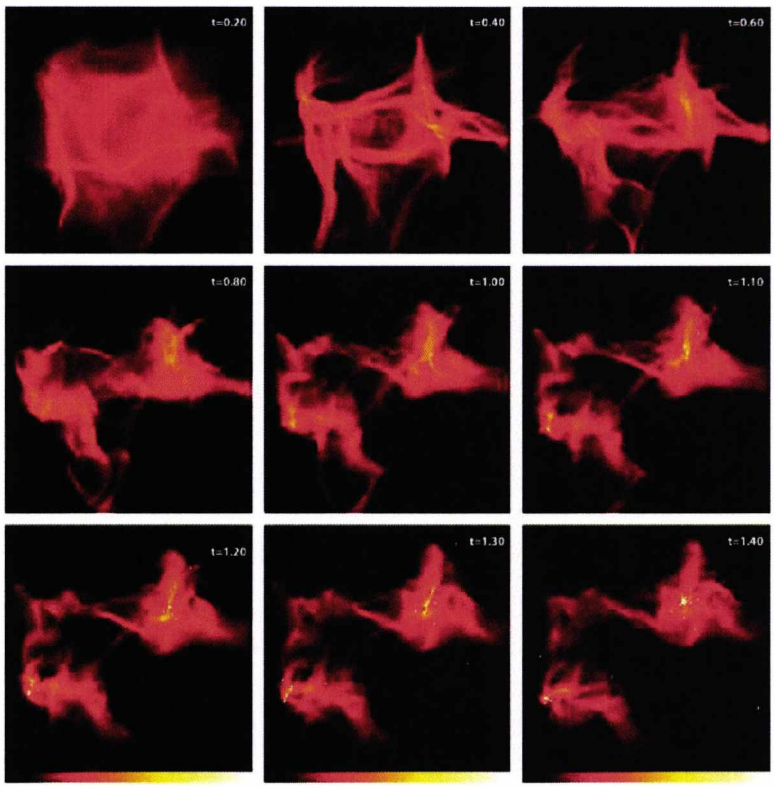

Figure 1.6: An example simulation of a molecular cloud forming two dense cores, from Bate (2009). The time units are given in free-fall times (1.90×10^5 Yrs). Each panel shows the log of the column density N, from $-1.7 < \log N < 1.5$ g cm^{-2}.

for behaviour seen in their simulations. A similar result was found by Bate (2009), who found that changing the initial power spectrum in a star forming molecular cloud had little or no effect on the stars produced, in their simulations. An example of one of their simulations is shown in Figure 1.6.

Another application of modelling is to simulate the abundances of molecules in molecular clouds. Work by Glover et al. (2010) models the formation of CO and H_2 in molecular clouds. They found that H_2 is a good tracer of the gas distribution, but that CO does not correlate well with the density of the gas n or visual extinction A_V. They also found that the temperature of the gas in clouds is not constant, with some gas at temperatures of $T > 20K$ in less dense parts of the clouds. In a later paper, Glover & Mac Low (2010) found that H_2 abundance is a function mainly of the available formation time, and is relatively insensitive to photodissociation. They found that only a few tenths of a magnitude of visual extinction is required to shield the molecular hydrogen from being destroyed.

1.8 Structural Analysis of Molecular Clouds

In this section the definition of structure functions is given, followed by a brief summary of some of the previously published models of turbulence in the literature. Finally, the Δ-variance technique for analysing structure in images, and the mass-size relation analysis technique are discussed.

1.8.1 Definition of Structure Functions

Differences in velocity between two distant points in a turbulent medium are expected to be uncorrelated, whereas the velocity difference between two points in close proximity should be highly correlated. Reconciling these relations of velocity differences leads us to determine structure functions for the medium. These are of the form (e.g. Elmegreen & Scalo (2004), Lombardi et al. (2008a)),

$$S_p(\phi) = \langle |A_V(\theta) - A_V(\theta + \phi)|^p \rangle , \tag{1.35}$$

where ϕ represents the distance between points, θ represents all positions in the cloud, and p is the order of the structure function. Here the observable is the visual extinction, A_V. A power-law can be fitted to the resulting structure function, of the form,

$$S_p(\phi) \propto \phi^{\eta(p)}, \tag{1.36}$$

which gives a slope $\eta(p)$. This can be used to compare the structure functions of different clouds against those predicted by theoretical models (see following Sections 1.8.1.1, 1.8.1.2 and 1.8.1.3).

1.8.1.1 The Kolmogorov Model

Due to the instantaneous and chaotic nature of turbulence, a statistical approach must be considered for analysis. Kolmogorov (1941) (hereafter K41) carried out this kind of analysis and derived the following result for the energy spectrum function,

$$E(k) = C_K \epsilon^{\frac{2}{3}} k^{-\frac{5}{3}}, \tag{1.37}$$

where C_K is called the Kolmogorov constant, ϵ is the viscous dissipation rate and k is the wave number. The exponents are derived using standard dimensional analysis. C_K tends to deviate for higher-orders in the structure function (explained in Section 1.8.1). In physical space, Kolmogorov predicts the longitudinal velocity structure functions S_p, of order p, such that,

$$S_p(\phi) = C_p (\epsilon\phi)^{\frac{p}{3}} \propto \phi^{\eta(p)}. \tag{1.38}$$

Here, ϕ is the distance between points, C_p is some constant which depends only on the order p, and ϵ is the viscous dissipation rate. In the general case, S_p is proportional to ϕ to the power the scaling exponent $\eta(p)$. For Kolmogorov type turbulence one finds the ratio of scaling exponents normalised to the third order is,

$$\frac{\eta(p)}{\eta(3)} = \frac{p}{3}. \tag{1.39}$$

Kolmogorov found a relation between the length scale L and the mean rate of energy dissipation $\dot{E}$,

$$\dot{E} = \frac{\eta v^3}{L}, \tag{1.40}$$

where η is an empirically determined constant and v is the velocity is the medium. Turbulent viscosity, ν, is defined as,

$$\nu = \lambda v. \tag{1.41}$$

This approach assumes that the turbulence is driven on large scale (L), forming eddies at that scale, and that the energy is then cascaded down into smaller eddies and scales. To be in equilibrium the energy flow must be constant from one scale to the next, and eventually dissipated according to Equation 1.40. In practice this is not valid for any

scale of motion, mainly due to other, non-local, interactions affecting the medium. The Kolmogorov wave number is defined, k_d, above which viscosity will dampen the velocity perturbations. This leads to the relation

$$k_d = \left(\frac{\epsilon}{\nu^3}\right)^{\frac{1}{4}}, \tag{1.42}$$

which defines the dissipation range.

1.8.1.2 The She-Leveque Model

Experimental measurements for the scaling exponents show a deviation from the Kolmogorov relation for turbulence, for increasing orders of p. In this case the flow is said to be intermittent and the Kolmogorov relation Equation 1.39 no longer holds. This is due to the scaling of velocity differences over fixed distances being different in different locations (Brandenburg & Nordlund, 2009). She & Leveque (1994) (hereafter SL92) derived the following relation for the velocity scaling function (as displayed in Padoan et al. (2003)),

$$\frac{\zeta(p)}{\zeta(3)} = \gamma p + C(1 - \beta^p), \tag{1.43}$$

where the factor C is the codimension,

$$C = \frac{1 - 3\gamma}{1 - \beta^3}, \tag{1.44}$$

and β is the intermittency parameter and γ is a scaling factor. This relation works for structures that are not influenced by magnetic fields. For incompressible (or weakly compressible) turbulence it was shown that $C = 2$, $\gamma = 1/9$ and $\beta^3 = 2/3$ so we have (She & Leveque, 1994),

$$\frac{\zeta(p)}{\zeta(3)} = \frac{p}{9} + 2\left[1 - \left(\frac{2}{3}\right)^{\frac{p}{3}}\right]. \tag{1.45}$$

The most intense dissipative structures have a filamentary or vortical structure, hence

the theoretical fractal dimension is $D = 1$. In practice, the vorticity structures do not have a one dimensional structure on the smallest scales (Elmegreen & Scalo, 2004), and the fractal dimension is greater than one.

1.8.1.3 The Kolmogorov-Burgers Model

Boldyrev (2002) (hereafter B02; see also Boldyrev et al. (2002)) extended the She-Leveque relation to model supersonic turbulence. They found that while turbulence obeys the Kolmogorov law in the inertial range, the behaviour deviates in the dissipative range (i.e. as the turbulence decays) due to the development of shock singularities. Revised values for the parameters were derived, so that $C = 1$, $\gamma = 1/9$ and $\beta^3 = 1/3$, leading to a revision of Equation 1.45,

$$\frac{\zeta(p)}{\zeta(3)} = \frac{p}{9} + 1 - \left(\frac{1}{3}\right)^{\frac{p}{3}}. \tag{1.46}$$

Equation 1.46 shows good agreement with simulations of highly supersonic turbulence. Whilst interstellar turbulence is most likely solenoidal, the most dissipative structures are shocks or sheetlike structures (Elmegreen & Scalo, 2004). These have a fractal dimension of $D = 2$.

1.8.2 The Δ-variance Technique

A method for analysing astronomical images containing molecular cloud structures, called the Δ-variance technique, was introduced by Stutzki et al. (1998) (and improved on by Ossenkopf et al. (2008a)). It was noted that the structure in molecular clouds bore similarities to *fractional Brownian motion* (fBm) fractals (Stutzki et al., 1998). A phenomenon of fBm is similar to classical Brownian motion except that the increments in fBm are dependent - i.e. if the pattern at any point in fBm is increasing, it will tend to increase in the next step. The structure resulting from fBm may be characterised by a power law spectrum and power spectral index. By using the power spectral index the Δ-variance technique can be used to quantify the structural scaling behaviour of e.g. molecular clouds (Bensch et al.,

2001).

The Δ-variance technique is an adaptation of a method used for measuring drift characteristics of electronic devices and instrumentation known as *Allan-variance*. The *Allan-variance* is the variance of the differences of subsequent averages over time t in a random time series. This is usually performed on a 1-dimensional array in electronics, however, for analysis of images a 2-dimensional approach is required. With images it is necessary to analyse the variance between differences of averages, over adjacent areas with spatial separation l. The technique works by measuring the quantity of structure on a particular length scale (e.g. Δr) and filtering the data $f(\Delta r)$ with a spherically symmetric 'down-up-down' type function. The Δ-variance is defined as Equation 1.47 (Ossenkopf et al., 2008a),

$$\sigma_{\Delta}^{2}(l) = 2\pi \int_{0}^{\infty} P(|k|) \left| \tilde{\bigodot}_{l}(|k|) \right|^{2} |k| d|k|. \tag{1.47}$$

In Equation 1.47, $\tilde{\bigodot}_{l}$ denotes the Fourier transform of the filter function with size l and wavenumber k. The choice of filter function is important, and two specific filter types were found to satisfactorily probe the structure in molecular clouds, a French hat filter and a Mexican hat filter (Ossenkopf et al., 2008a). Both filters are spherically symmetric composite functions with separate functions for the core and the annulus. The French hat filter is a spherical 'down-up-down' type function while the Mexican hat is composed of two Gaussian functions to give a smoother transition from the core to the annulus. The optimal filter function for molecular clouds was found to be either a Mexican hat filter with a diameter ratio of 1.50, or a French hat filter with a diameter ratio of 2.30 (Ossenkopf et al., 2008b).

The French hat filter is defined using Equations 1.49 and 1.50,

$$\bigodot_{l}(\Delta r) = \bigodot_{l,core}(\Delta r) - \bigodot_{l,ann}(\Delta r), \tag{1.48}$$

$$\underset{l,core}{\odot}(\Delta r) = \frac{4}{\pi l^2} \begin{cases} 1 : |\Delta r| \leq l/2, \\ 0 : |\Delta r| > l/2, \end{cases} \tag{1.49}$$

$$\underset{l,ann}{\odot}(\Delta r) = \frac{4}{\pi l^2} \begin{cases} 1/(\nu^2 - 1) & : l/2 < |\Delta r| \leq \nu \times l/2, \\ 0 & : |\Delta r| \leq l/2, |\Delta r| > \nu \times l/2. \end{cases} \tag{1.50}$$

The Mexican hat filter is defined using Equations 1.51 and 1.52,

$$\underset{l,core}{\odot}(\Delta r) = \frac{4}{\pi l^2} \exp\left(\frac{\Delta r^2}{(l/2)^2}\right), \tag{1.51}$$

$$\underset{l,ann}{\odot}(\Delta r) = \frac{4}{\pi l^2(\nu^2 - 1)} \left[\exp\left(\frac{\Delta r^2}{(\nu l/2)^2}\right) - \exp\left(\frac{\Delta r^2}{(l/2)^2}\right)\right]. \tag{1.52}$$

In a comparison of the results obtained using the French hat filter compared with those obtained using the Mexican hat filter, it was found that both filters were equally good for analysing molecular clouds. Therefore, the Mexican hat filter was arbitrarily chosen for this analysis, rather than generating similar results twice. To obtain reliable Δ-variance values, the parameter $l \times \nu$ must not exceed 2/3 of the image size, when using the Mexican hat filter (Ossenkopf et al., 2008a).

A draw-back of the Δ-variance method is that it has a high sensitivity to the noise originating with the photometric errors in the observations (Ossenkopf & Mac Low, 2002). This results in large uncertainties associated with the σ_Δ^2 values, especially in images with large 'empty' areas.

A quantitative measure of the slope of σ_Δ^2 against r is given by the mass index scaling exponent α, as $\sigma_\Delta^2(r) \propto r^\alpha$. The mass index scaling exponent must firstly be determined over the correct dynamic range, otherwise the correct slope is not determined (Ossenkopf et al., 2008a). The lower limit of the range is determined by the level of noise, the size of oversampled pixels (if oversampled), and the size of the smallest structure in the image. The upper limit is determined by the largest size of structure in the image.

1.8.3 The Mass-Size Relation in Molecular Clouds

The Mass-Size relation method is a contour-based map analysis technique developed by Kauffmann et al. (2010a) (building on work by Rosolowsky et al. (2008)). It is known that the mass contained within a radius r is proportional to r^2 (McKee & Ostriker, 2007). The Mass-Size method utilises extinction maps to identify regions of similar column density (denoted visually by contours) and calculating the mass within them. The effective radius is measured for each contour. The Mass-Size relation can be seen by plotting a log-log diagram of mass against effective radius. Using this method, Kauffmann et al. (2010a) find agreement with mass-size measurements derived using the CLUMPFIND technique, however little correlation was found at a detailed level when compared to CLUMPFIND results. This is expected as molecular clouds show smooth, large-scale profiles which cause problems for an automated routine analysing for thresholds in the data (e.g. Froebrich et al. (2007)).

In their second paper, Kauffmann et al. (2010b) used the technique to analysis local molecular clouds. They found a revision of the mass-size law $m(r) = 460 M_{\odot}(r/\mathrm{pc})^{1.9}$ (i.e. from *Larson's third law*, - Larson (1981) and McKee & Ostriker (2007)) for several local GMCs of $m(r) \propto r^{1.27}$. The exponent is stated as being highly approximate for a particular cloud, but less than 1.5. They found a limiting case for the mass range of structure as $m(r) \leq 870 M_{\odot}(r/\mathrm{pc})^{1.33}$, i.e. that fragments in clouds not forming massive stars have mass less than this in a range of radius $0.01 \leq (r/\mathrm{pc}) \leq 10$ (Kauffmann & Pillai, 2010). Therefore, the majority of clouds fall short of this threshold for massive star and cluster formation.

At larger scales ($1 \leq r/\mathrm{pc} \leq 4$) they found a limiting relation for the most massive fractions of $m(r) = 400 M_{\odot}(r/\mathrm{pc})^{1.7}$ Kauffmann et al. (2010b). Examples of clouds containing such fragments include Taurus, Perseus, Ophiuchus and the Pipe Nebula. The relation compares well with that obtained by Lombardi et al. (2010a), that $m(r) = 380 M_{\odot}(r/\mathrm{pc})^{1.6}$.

1.9 Remaining Problems to be Solved

Having briefly discussed the topics of molecular clouds and star formation, this section outlines remaining problems and questions, which this thesis will address.

Are there any correlations between the physical attributes of GMCs and the parameters that can be determined observationally? Does the star formation rate or mode of star formation depend on such factors as the column density/mass distribution in the cloud, or can analysis of the structure functions reveal a correlation? For example, in their paper analysing the Taurus, Perseus and California cloud complexes, Lombardi et al. (2010b) found that these three diverse clouds (in terms of the mode of star formation) cannot be fit by one model to explain the internal structures. However, is there, for example, a correlation between the star formation mode and any of the observable parameters (e.g. structure functions, Δ-variance peaks etc.)?

Are there observable differences between clouds that are forming clouds and those that are not or have a low star formation rate? There are few clouds which have no star formation ongoing within them (Kainulainen et al., 2009) and these tend to be of lower mass than GMCs (which generally have a mass of at least $1 \cdot 10^4 M_\odot$ (McKee & Ostriker, 2007)). Larger clouds form stars either in clusters (Lada & Lada, 2003), or in isolation (such as in the Taurus molecular cloud (Mizuno et al., 1995)). Does the star formation mode result from the environment in which the cloud is situated?

Is there a cut off threshold of column density between turbulence dominated material and that which is self-gravitating? For example, using 850μm continuum emission data, 2MASS and R-band data, Johnstone et al. (2004) found candidate protostellar cores in the Ophiuchus cloud. They associated these cores exclusively with high extinction regions in the cloud using an extinction map. They found that no candidate objects were observed at extinctions of less than 7 mag A_V, hence this could be a cut-off threshold between the star forming and non-star forming parts of the cloud. This analysis will be carried out for many clouds in this thesis to see if there is a common threshold between clouds or not.

Chapter 2

Data Analysis Method

This chapter outlines the methods used. Firstly, an overview of the 2MASS project is given, including the details relevant to this thesis. Then the extinction maps and extinction determination methods are described, including the calculation of the uncertainties. The sample clouds selected for analysis are presented, with relevant details, along with the Galactic plane region which was also analysed. The cloud structure analysis and structure function determination methods are then described. Finally, there is a brief overview of the methods used for testing correlations.

2.1 The 2MASS Project

The extinction maps made for this research used data from the Two Micron All Sky Survey (2MASS). 2MASS was a survey of the entire sky at three near-infrared wavelengths (the following specifications for 2MASS come from Skrutskie et al. (2006), or from the 2MASS website[1]). These were the J, H and K_s bands (see Table 2.1).

Table 2.1: A Table showing wavebands used in by 2MASS.

Waveband	Wavelength μm	Bandwidth μm	Signal-to-noise greater than 10 at magnitudes brighter than
J	1.235	0.162	15.8
H	1.662	0.251	15.1
K_s	2.159	0.262	14.3

Two highly automated 1.3m telescopes were used for the observations, one in the northern hemisphere, the other in the southern hemisphere, in order to cover the whole sky. The northern telescope was at the Mount Hopkins observatory in Arizona, USA (coordinates N 31° 40′ 50″8, W 110° 52′ 41″0). The southern telescope was at the Cerro Tololo Inter-American Observatory (CTIO) in Chile (coordinates S 30° 10′ 3″7, W 70° 48′ 18″0). The domes for the two telescopes are shown in Figure 2.1, with the northern facility on the left and the southern facility on the right. The survey began in June 1997 at the northern observatory and March 1998 at the southern observatory. The survey was completed on 15th February 2001. In terms of weather restrictions, the survey was carried out on clear nights with no threat of rain.

[1] http://www.ipac.caltech.edu/2mass/overview/about2mass.html

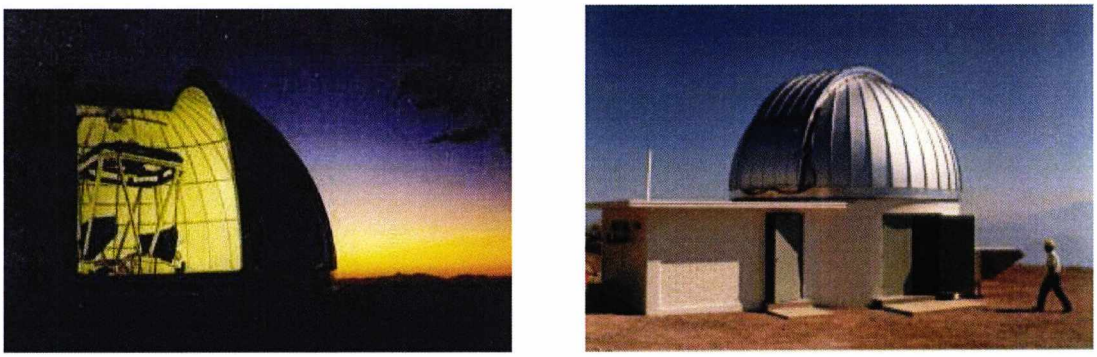

Figure 2.1: The left image shows the dome and telescope of the northern facility at the Mount Hopkins observatory in Arizona, USA, while the right image shows the dome and building of the southern facility at the Cerro Tololo Inter-American Observatory (CTIO) in Chile.

2MASS represented a considerable improvement on previous surveys (e.g. the Two Micron Sky Survey (TMSS) which surveyed ~70% of the sky (Neugebauer & Leighton, 1969)). For example, the improvement in sensitivity of 2MASS compared with TMSS was a factor of 80,000. 2MASS could detect objects around 100 million times fainter than TMSS. A pixel size of 2.0" square was used. Sources brighter than 1 mJy were detected. Each frame in the observations comprised of six 1.3s exposures leading to a total integration time of 7.8s.

A problem affecting the J and H-band observations was the detection of airglow in the earth's atmosphere. The K_s band observations suffered from the effects of seasonal variation (i.e. weather), in that fainter objects could be detected in better conditions. This effect causes the appearance of 'stripes' in any (e.g.) extinction maps compiled using 2MASS data.

The following data products were released by the 2MASS project.

1. A digital atlas of the sky comprising of small (8′ by 16′) images.
2. A point source catalogue containing accurate positions and fluxes for around 471 million objects.
3. An extended source catalogue containing positions and magnitudes for galaxies and nebulous objects.

The second item - the point source catalogue - was used to make the extinction maps for this thesis.

2.2 The Extinction Maps

As discussed earlier (in Section 2.1), data were extracted from the 2MASS Point Source catalogue (Skrutskie et al., 2006). The required data were: the stellar coordinates (in RA and Dec), the J, H, and K magnitudes, and the photometric uncertainties for the J, H, and K magnitudes. Good photometric quality was ensured by only using stars with a quality flag of 'AAA'. Therefore, the signal-to-noise ratio for the J, H, and K bands was greater than 5.

Using only stars with quality flag 'AAA' meant that, without oversampling, a star density of at least one star per pixel could be attained. This applies in the areas of highest extinction (i.e. in the Galactic plane region) with $|b| < 20$, and a pixel size of 30′. Including sources with a lower quality flag would increase the number of stars available and allow the possibility of higher resolutions to be attained, but at the cost of increased noise.

The coordinates were then converted into the Galactic coordinate system (Blaauw et al., 1960) using the IRAF CONVERT utility and these were prepended to the data files. The data files were then split into smaller, more manageable .txt files each containing sources in a horizontal strip 2° high by 360° wide. These strips were further split into blocks depending on the density of stars at that latitude, i.e. smaller files for higher density regions. For example, in the higher latitudes above $|b| > 70°$ the full width of 360° was used, whereas at the Galactic Plane the strips were only 1° wide. The strip width was varied accordingly in between, as shown in Table 2.2, so that each file contained roughly the same number of stars.

Each file/block contained extra data within an overlap (in l and b) to allow for oversampling and ensure that there were enough nearby stars in order to find, say, the nearest 100 stars to the centre of a pixel on the edge of the block. The overlaps were an extra 0.1° for $|b| < 20°$ and 0.25° at $|b| > 20°$. This gives a total of 3088 input files covering

Table 2.2: A Table showing the width (in l) of the $2°b$ strip files and the number of files created.

$\|b\|$ °	Width (l °) in file	No. of files
0 – 4	1	1440
4 – 8	2	720
8 – 10	3	240
10 – 14	8	180
14 – 18	12	120
18 – 22	20	72
22 – 28	24	90
28 – 36	36	80
36 – 48	72	60
48 – 70	120	66
70 – 90	360	20

the whole sky. Additionally, files corresponding to each data file were created specifying the parameters for that block (minimum and maximum coordinates with pixel size). This allowed the parameters of the data to be known before the data was read, so that the correct dimensions of arrays could be declared in advance.

The pixel size was varied from 0.5′ at $b = 0°$ and 2′ at $b = 90°$. The variation with Galactic latitude is shown in Table 2.4. The final maps are available via the internet[2]. The maps are presented in the Mercator projection, in 360° by 20° strips to keep the maximum size of individual files to under an acceptable amount of 200 Mb.

2.2.1 The Types of Map

This section describes the types of map made for the analysis. Firstly, one must consider whether the data is to be oversampled. In the simplest case, the map is divided into square pixels and only the data (stars) in each pixel are analysed. In this instance there is no oversampling of the data. However, if the data outside of a particular pixel is included in the calculation then the data is said to be *oversampled.* Oversampling gives smoother results for an image, especially where there are few data items in some of the pixels. Oversampling is disadvantageous if one is interested only in the data in each pixel, i.e. if estimating the mass of a molecular cloud.

[2]http://astro.kent.ac.uk/extinction

Table 2.3: The different maps created for the project. A brief description is given together with the type of map (*con-noise* or *con-res*). The oversampling status is specified together with the shape of the resolution element.

No.	Description	Map Type	Oversampling (y/n)	Resolution element
1	A_V - 25 stars	Con-noise	y	Circle
2	A_V - 49 stars	Con-noise	y	Circle
3	A_V - 100 stars	Con-noise	y	Circle
4	σ_{A_V} - 25 stars	Con-noise	y	Circle
5	σ_{A_V} - 49 stars	Con-noise	y	Circle
6	σ_{A_V} - 100 stars	Con-noise	y	Circle
7	Distance to 25^{th} neighbour	Con-noise	y	Circle
8	Distance to 49^{th} neighbour	Con-noise	y	Circle
9	Distance to 100^{th} neighbour	Con-noise	y	Circle
10	A_V	Con-res	y	Circle
11	σ_{A_V}	Con-res	y	Circle
12	A_V - 0.5′	Con-res	n	Box
13	A_V - 1′	Con-res	n	Box
14	A_V - 2′	Con-res	n	Box
15	A_V - 4′	Con-res	n	Box
16	σ_{A_V} - 0.5′	Con-res	n	Box
17	σ_{A_V} - 1′	Con-res	n	Box
18	σ_{A_V} - 2′	Con-res	n	Box
19	σ_{A_V} - 4′	Con-res	n	Box
20	No. of stars in each 0.5′ box	Con-res	n	Box
21	No. of stars in each 1′ box	Con-res	n	Box
22	No. of stars in each 2′ box	Con-res	n	Box
23	No. of stars in each 4′ box	Con-res	n	Box

Table 2.4: Pixel sizes and spatial resolution of the maps depending on Galactic latitude $|b|$. For the *Con-noise-maps* the spatial resolution depends on the number of stars (25, 49, or 100) used and also varies with position.

$\|b\|$ range	Pixel size [′]	Spatial resolution of *Cons-res maps* [′]
90° – 50°	2.0	6.8
50° – 40°	1.5	5.1
40° – 20°	1.0	3.4
20° – 0°	0.5	1.7

If the data used is within a radius, r, of the centre of the pixel, then the sampling rate can be calculated as Equation 2.1,

$$r = \sqrt{\frac{rate^2}{\pi}}. \tag{2.1}$$

Here, *rate* is the oversampling rate, r is the resulting radius. If square resolution elements are used which are larger than the map pixels, then the oversampling rate is simply the size of the square divided by the size of the pixel. If the resolution elements are smaller than the pixel size then the data is said to be *undersampled.*

2.2.1.1 Constant Noise Maps

When using 2MASS data, the photometric uncertainties of stars are generally similar in each region, due to the observing conditions when the data was taken (see Section 2.1). Therefore, using the same number of stars in the calculation for each pixel will give a near-constant noise for that pixel as the noise depends on $1/N$ (where N is the number of stars. See Section 2.4.1 for further details). So a fixed number of stars from the centre of each pixel was chosen - 25, 49 and 100. As the noise is near-constant these maps are hence named *Con-noise maps*. The distribution of individual statistical uncertainties can be seen later in Figure 3.8 (see Section 3.2.1). This type of map will have a variable spatial resolution, as the distance to the 'Nth' star and the amount of oversampling is variable and depends on the star density in that area.

2.2.1.2 Constant Resolution Maps

Other extinction maps were determined using only stars within a fixed distance of the centre of each pixel. Hence, these maps are known as *con-res maps*. For maps 10 and 11 (see Table 2.3), the radius was chosen as 1.7 times the pixel size to give an oversampling of three (see Equation 2.1). The maps created are shown in Table 2.3. As the resolution is fixed, the noise therefore varies from one pixel to another, as each pixel contains a different number of stars. The distribution of the individual statistical uncertainties for these maps is shown in Figure 3.9 in Section 3.2.2.

In order to investigate the structure of GMCs additional *con-res maps* were created where the values in each pixel are independent of neighbouring pixels, i.e. no oversampling. Therefore, constant resolution maps were made with no oversampling; these are the maps used for the analysis of column density and mass distribution. These maps are

Table 2.5: The pixel sizes of *con-res maps* 12-23.

$\|b\|$ range	Pixel size of maps 12, 16, 20 [′]	Pixel size of maps 13, 17, 21 [′]	Pixel size of maps 14, 18, 22 [′]	Pixel size of maps 15, 19, 23 [′]
90° – 50°	2.0	4.0	8.0	12.0
50° – 40°	1.5	3.0	6.0	12.0
40° – 20°	1.0	2.0	4.0	8.0
20° – 0°	0.5	1.0	2.0	4.0

also shown in Table 2.3, and are numbered maps 12 through 23.

It should be noted that each resolution element in these maps is a box shape rather than a circle. The differences caused between these two pixel shapes were analysed. A grid containing 10,000 randomly distributed values (between 0 and 1) was created. The median values were found for each *square* in the grid, and also for a *circle* (of radius 0.5, therefore undersampled) centred on each pixel. A histogram of the differences between the two median value grids was found to be a Gaussian distribution with parameters σ=2.6 · 10^{-4} and μ=−7.7 · 10^{-3}. Therefore, the effect is negligible due to the small value of σ.

In the additional *con-res maps* maps (12-23), the size of each pixel was varied (e.g. from 0.5′ to 4′ for $|b|$ <20) in multiples of two, to determine whether any observed trends are the same at different spatial scales. The pixel sizes (and the dependence on Galactic latitude) for the *con-res maps* 12-23 are as shown in Table 2.5. These additional *con-res maps* were produced using the method described above in Section 2.2. As discussed, the pixels consist of square boxes rather than selecting stars within a certain radius of the pixel centre. This allows the use of all available sources without oversampling. The same pixel sizes apply for the variance (σ_{A_V}) maps and star density maps.

2.3 Extinction Determination

In this section the methods used to determine the extinction are discussed, using the data extracted from the 2MASS point source catalogue as described in Section 2.2.

2.3.1 Median Colours

For the next stage of making the maps, the median colour (e.g. J-H, H-K and J-K) is determined in each pixel using the stars contained in that pixel. This gives a map which can be used to create the colour excess maps. Using the J and H band data (for example) the median colour was then calculated for each pixel,

$$[J-H] = Median(m_{\rm J}^i - m_{\rm H}^i). \tag{2.2}$$

Here, i represents the index of each star contained in the pixel. The data was processed using an IDL script, which output FITS files of each block. The calculations for the *con-noise* (variable resolution) maps used the nearest N number of stars to the centre of each pixel. As discussed in Section 2.2.1.1 values of 25, 49 and 100 were used for N. The calculation of distance to the centre of the pixel included a correction (of $\cos b$) to eliminate the effect of stretching with latitude due to the choice of projection, which becomes more significant at higher latitudes.

The *median* colour was used rather than the *mean* for the following reasons:

1. The effect of young (i.e. with a disk), intrinsically red stars which would influence the mean is eliminated.

2. The effect of clusters with colours different from the foreground/background colours is eliminated.

3. The correct colour excess is measured, or else the cloud is not detected.

The first two points are valid as long as there are more foreground and background stars than young or red stars. In our maps only two clusters with intrinsic redness dominate over the extinction. These objects are the Orion Nebula Cluster and the cluster in the L 1688 cloud in Ophiuchus.

To measure the unbiased colour excess/extinction, the third point is the most important consideration. As long as there are more background stars to the cloud then using the median ensures that the colour of the background stars is measured which leads to the

correct value of the extinction. If there are more foreground stars than background stars then the cloud is not detected at all. If one was to use the mean instead of the median one would only measure part of the extinction, and the result would vary for similar clouds at different distances (see Froebrich & del Burgo (2006) for further comparison between the use of the mean (with a star counting method) or median (colour excess)).

2.3.2 Colour Excess

The maps of median colour are converted into maps of colour excess. An adjustment needs to be made in respect of the various stellar populations in different parts of the Galaxy, which give rise to differing median colours. An iterative method to deal with this was developed. The steps are:

1. The median colour maps were re-binned to a larger pixel size of 10′, then median filtered with a filter size of one degree.

2. Regions influenced by dust clouds were masked out. Firstly, dust clouds were identified using the maps by Schlegel et al. (1998). Data with $E(B-V) > 0.125$ mag (i.e. $A_V > 0.39$ mag) were identified as clouds and masked. In subsequent iterations this stage was completed using a preliminary version of our map. Data with an extinction of $A_V > 0.5$ mag were identified and masked. This area mask was then extended by 40′ into unmasked regions to ensure all major clouds were adequately masked out.

3. Spline functions were then fitted to the unmasked (i.e. extinction free) regions, along every 10′ column of constant Galactic longitude with knots at every degree. This allowed the estimation of the background colour values in regions with dust clouds present (i.e. with no available extinction free data).

4. Spline functions were then fitted to the unmasked regions along 10′ rows, to the results from the previous stage. The result of this stage was then expanded to the size of the desired map and smoothed to 5′.

5. This resulting colour background map is subtracted from the original median colour map, giving the colour excess map (see Equation 2.3).

6. Subsequent iterations are repeated from stage 2.

The colour excess is derived by subtracting the colour background map from the original median colour map,

$$\langle J-H\rangle_{(l,b)} = [J-H]_{(l,b)} - fit[J-H]_{(l,b)}. \tag{2.3}$$

Here, (l, b) denotes the position in the map, from Galactic l and b coordinates.

Since three wavelengths were utilised one can in principle calculate three colour excess maps for a given waveband. However the $\langle J-K\rangle$ colour excess is not used as the data is not independent of the other two colours. Using the H-band, there are two independent ways of deriving the extinction A_H, i.e. Equations 1.23 and 1.24 from Section 1.6.6.1. In these equations the bands J, H and K are represented by λ_1, λ_2 and λ_3 respectively. β is the near-infrared power law index. See Section 2.4.2 for a discussion on the effect of changes in β. The extinction calculated using the two bands was averaged and converted to visual extinction,

$$A_V = \frac{5.689}{2} \cdot (A_{H,\langle J-H\rangle} + A_{H,\langle H-K\rangle}) \tag{2.4}$$

The factor of 5.689 is used to convert the H-band extinction into A_V (Mathis, 1990).

2.3.3 Calibration Offsets

Before the extinction maps could be used, we needed to take account of differences arising from the different colour excesses. Giant and dwarf stars of the same spectral type have different colours. This was an issue in the H-band extinction map created using the $\langle J-H\rangle$ colour excess data. In general, giants will have redder $[J-H]$ and $[J-K]$ colours than dwarfs. The fitted function however, determines the median colour of dwarf stars, as it was not possible to use data from around the central Galactic plane (where giants

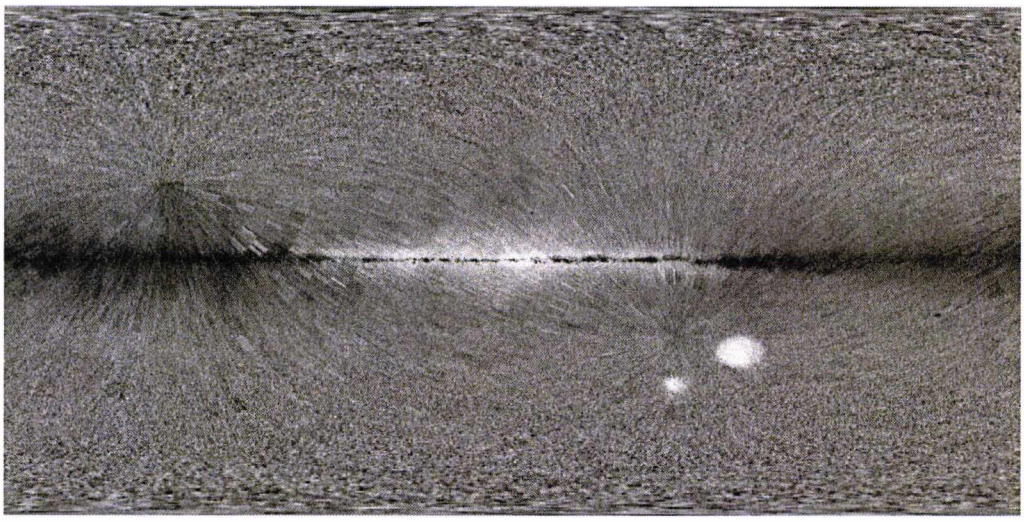

Figure 2.2: Gray scale representation of the difference map calculated as $D_{A_V} = 5.689 \cdot (A_{H,\langle J-H\rangle} - A_{H,\langle H-K\rangle})$ (see text for details). A_V values are scaled linearly from -1.5 mag (black) to $+1.5$ mag (white). The image size is $360° \times 180°$ with the Galactic Centre (bulge) in the middle. The ρ Ophiuchus complex appears just above and to the right of the centre. The two white patches to the lower right of the centre are the Large and Small Magellanic Clouds.

dominate) due to the over-abundance of dust clouds. It turns out that the $\langle H-K\rangle$ colour excess maps do not suffer as much from this problem, hence they were used as a control field.

A differences map D_{A_V} was determined using the extinction maps created from the two colour excess maps $\langle J-H\rangle$ and $\langle H-K\rangle$, using the relation

$$D_{A_V} = 5.689 \cdot (A_{H,\langle J-H\rangle} - A_{H,\langle H-K\rangle}) . \tag{2.5}$$

Clearly, systematic residuals were found (see Figure 2.2). An offset of nearly 2 mag A_V is found in the regions close to the Galactic centre (shown by the central white area in Figure 2.2), caused by giants. This region extends by approximately 120° in l.

As shown in Figure 2.2, there are also negative offsets along the Galactic plane, away from the Galactic centre. The likely cause is a greater fraction of higher mass stars contained in this region of spectral types O to F. These stars have a $[J-H]$ colour smaller than that of the low mass dwarfs found away from the Galactic plane which were used

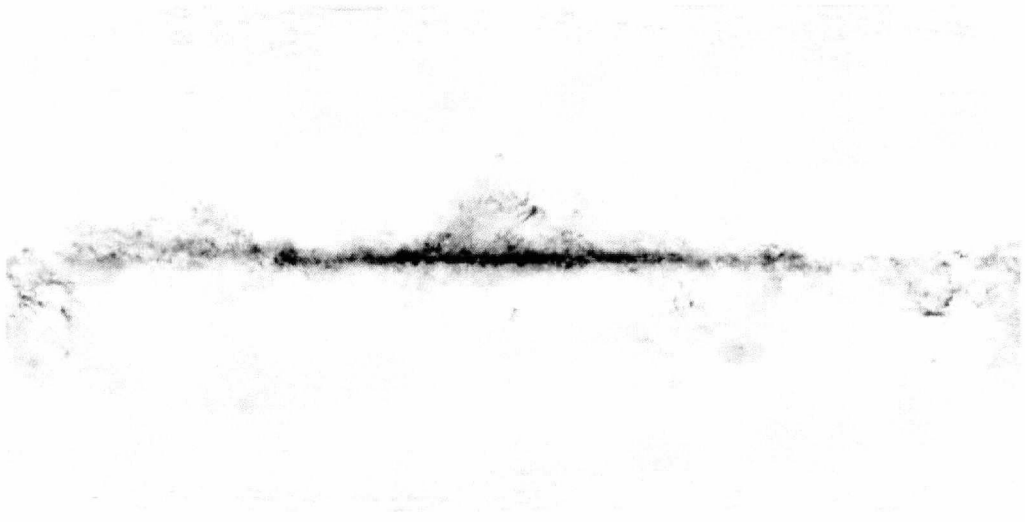

Figure 2.3: The all sky extinction map using the nearest 49 stars. The image size is $360° \times 180°$ with the Galactic Centre in the middle. Optical extinction values are scaled linearly from −1 mag (white) to +7 mag (black).

for the fitting of the background. This effect is not so pronounced in the $[H - K]$ colour and therefore gives rise to the observed difference. Another explanation could be due to objects with an $[H - K]$ excess due to the presence of a disk. This is true for the Orion Nebula Cluster and L 1688 but cannot be true for such a large region shown in Figure 2.2. Therefore, the former explanation is most likely.

The difference image D_{A_V} was filtered to correct for these large scale offsets. The filtering size was 4.5° in l and 0.3° in b. The difference image was then subtracted from the $[J - H]$ map before the final extinction map (shown in Figure 2.3) was created using Equation 2.4. If the subtraction of differences was not done correctly, this would lead to incorrect A_V values in the maps. This in turn would lead to incorrect analysis of the column density and mass distributions. However, there would be little effect on the analysis of structure. The maps obtained from $[H - K]$ were compared with the maps of Dobashi et al. (2005) and no deviations are found greater than one sigma in uncertainty.

There are smaller variations in the maps due to changes in the observing conditions - these were discussed in Section 2.1.

2.4 Calculation of the Uncertainties

This section describes the calculation of the uncertainties, both statistical and systematic.

2.4.1 Statistical Uncertainties

Maps of the uncertainties (or variances) in extinction were produced corresponding to each extinction map. To create these the photometric errors extracted from the 2MASS catalogue were propagated using the following formulae. For the median colours the uncertainties in a given pixel were calculated by

$$\sigma_{[J-H]} = \frac{1.253}{N} \cdot \sqrt{\sum_{i=1}^{N} (\sigma_J^i)^2 + \sum_{i=1}^{N} (\sigma_H^i)^2}. \tag{2.6}$$

Here, N is the number of stars in the pixel, σ_J^i and σ_H^i are the J and H-band uncertainties in the photometry of each star in the pixel. The factor of 1.253 comes from using the median to calculate the final uncertainty rather than using the mean (from Kenney & Keeping (1962), page 211). The efficiency of the median is the ratio of the variance of the mean over the variance of the median, i.e. $4N/\pi$ $(2N+1)$. For large values of N this tends to $2/\pi \approx 0.637$. The factor by which the uncertainty in the *median* is larger than the uncertainty in the *mean* is the root of the reciprocal of this,

$$\sqrt{\frac{\pi}{2}} \simeq 1.253. \tag{2.7}$$

Therefore, the uncertainty by using the median is larger by a factor of 1.253 than using the mean, for large samples and a normal distribution.

To calculate the uncertainties in colour excess, the uncertainties derived using Equation 2.6 were used. It was assumed that during the conversion from colour maps into colour excess maps only systematic and not statistical uncertainties were introduced, i.e.,

$$\sigma_{\langle J-H \rangle} = \sigma_{[J-H]}. \tag{2.8}$$

The errors in the H-band extinction determined from the colour excess are

$$\sigma_{A_{H,\langle J-H\rangle}} = \frac{\sigma_{\langle J-H\rangle}}{\left(\frac{\lambda_H}{\lambda_J}\right)^{\beta} - 1}, \tag{2.9}$$

and

$$\sigma_{A_{H,\langle H-K\rangle}} = \frac{\sigma_{\langle H-K\rangle}}{1 - \left(\frac{\lambda_K}{\lambda_H}\right)^{-\beta}}. \tag{2.10}$$

These variances were combined to ascertain the overall variance in the final A_V map, in Equation 2.11,

$$\sigma^2_{A_V} = \left(\frac{5.689}{2}\right)^2 \cdot \left(\sigma^2_{A_{H,\langle J-H\rangle}} + \sigma^2_{A_{H,\langle H-K\rangle}} + 2 \cdot \sigma_{cov}\right). \tag{2.11}$$

The covariance of the two extinction maps, σ_{cov}, is introduced (compare Equation 2.11 to Equation 2.4), as the terms are not independent of each other (see Froebrich & del Burgo (2006) for example). The σ_{cov} value was calculated in the following way. Firstly, a histogram was produced of the extinction values in a cloud-free area in the final extinction map. Secondly, the FWHM of this distribution was measured, giving a value for $\sigma^2_{A_V}$. Then σ_{cov} was calculated by using the known contributions from the $\sigma_{\langle J-H\rangle}$ and $\sigma_{\langle H-K\rangle}$ maps (i.e. see Equations 2.9 and 2.10).

An alternative method to calculate σ_{cov} (but only using data from extinction-free regions) would be to use the relation

$$\sigma_{cov} = \frac{1}{N} \cdot \sum_{j=1}^{N} \left(\left(A_{H,\langle J-H\rangle}\right)_j \cdot \left(A_{H,\langle H-K\rangle}\right)_j \right), \tag{2.12}$$

which is summed over all pixels, j. Note that because the H-band extinction values are not independent of each other this method yields too small a value for σ_{cov} - typical values are σ_{cov} $\approx$0.0015 mag^2. Therefore, this method was rejected in favour of the process described above. The actual values for the covariance are shown in Section 3.3 in the Results chapter.

Using the *con-noise maps* for the nearest 25, 49 and 100 stars, it was found empirically that the average covariance values can be calculated using Equation 2.13,

$$\sigma_{cov}(N) \propto N^{-0.8}. \tag{2.13}$$

This formula can be applied when calculating the uncertainties for the *con-res maps*, as we know the star density for each pixel. The method used for the *con-noise maps* is not valid here as the number of stars in each pixel varies.

2.4.2 Systematic Uncertainties

Systematic uncertainties introduced during the making of the extinction maps need to be taken into account. These may arise from stages such as fitting the background median colours (due to imperfections in the fit), or from variations in the extinction law in different areas of the maps. Such uncertainties could be included in Equation 2.11, however, due to the different sizes and scales of the uncertainties it is not possible to add them numerically. The magnitude and likely impacts are discussed here.

- Any imperfections in the fit of the background colours will introduce systematic uncertainties. The scale of these offsets will be larger than the filter size of 4.5° in l and 0.3° in b used in the fitting process. Therefore, any systematic uncertainty here will not influence the observed structure or CDD in any particular cloud, but may affect the extinction, A_V. However, the magnitude of the offsets is found to be small in comparison with the maps of Schlegel et al. (1998) and Dobashi et al. (2005). See Sections 3.1.3.2 and 3.1.3.3 for further discussion.

- Small scale systematic offsets caused by the 2MASS observing procedure, which may appear as stripes on any maps using 2MASS data. This is a local issue occuring over scales of around ~14′ by ~6′. These stripes are caused by the observing conditions leading to varied completeness limits on different nights observations. Under darker conditions more redder stars are detected, so the median colour of stars changes. The $[H-K]$ observations are more affected as deeper observations at these wavelengths pick out more dwarfs which tend to be redder; the $[J-H]$ observations are not affected as much. Apart from the use of Quality flag 'AAA'

stars, no other restrictions were placed on the stars included in determining the extinction maps so as not to reduce the achievable spatial resolution. The magnitudes of these offsets amount to 1 mag A_V in the maps determined from $[H-K]$ colours and 0.5 mag A_V in the those determined from $[J-H]$. Therefore, the maps determined from $[J-H]$ colours are less affected by this issue. In the final maps the magnitude of this effect can be as high as double the systematic uncertainty. Hence, care should be taken especially with any cloud structures that are aligned with the sweep direction of the 2MASS observations.

- Any variations in the extinction law with spatial scale will introduce small scale systematic uncertainties. The extinction law is expected to change in regions of high column density. The optical properties of the dust may be altered by coagulation of grains or the formation of ice mantles (see Ossenkopf (1993), Preibisch et al. (1993), Larson & Whittet (2005)). A change in our value of β=1.70 of $\pm$0.2 leads to a change in A_V of ~10%. Given an example uncertainty of 0.28 mag (for the *con-noise map* of the nearest 49 stars - see Table 3.4 in the Results chapter), such variations in the extinction law would only be measurable at A_V values greater than 8 mag, i.e. three sigma detections. This justifies the use of a constant value (of 1.70) for β.

2.5 Cloud Selection

This section gives details about the individual clouds selected for analysis. Only clouds with a reliably known distance were selected. The clouds were chosen to be relatively nearby - all are less than 1 kpc in distance, with the exception of the Rosette Nebula. Clouds close to the Galactic centre (and along the plane towards the Galactic centre) were avoided due to the likelihood of having two (or more) clouds along the line of sight, which would invalidate the analysis.

The 30 sample clouds are shown in Table 2.6. The l and b ranges shown in the table denote the rectangles extracted from the *con-res maps*. The table also shows the distance

Table 2.6: Summary table of the clouds analysed. The table shows the area analysed for each cloud in Galactic coordinates, the distance and the source of the distance data.

Name	l range [°]	b range [°]	Dist. (pc)	Dist. reference
Aquila Rift	32.5 – 25.5	2.0 – 6.0	225	Straižys et al. (2003)
Auriga 1	156.0 – 173.0	-12.0 – -3.0	450	Lada et al. (2009)
Auriga 2	175.0 – 186.0	-11.0 – -2.0	140	Kenyon et al. (2008)
Cepheus Flare	100.0 – 117.0	10.0 – 20.0	390	Kun et al. (2008)
Chamaeleon I	295.5 – 298.0	-17.5 – -14.0	160	Whittet et al. (1997)
Chamaeleon II	302.0 – 304.5	-15.5 – -13.0	178	Whittet et al. (1997)
Chamaeleon III	300.5 – 304.0	-19.0 – -15.5	150	Whittet et al. (1997)
Circinus	316.0 – 319.0	-6.0 – -3.0	700	Bally et al. (1999)
Corona Australis	1.0 – 359.0	-20.0 – -17.0	170	Knude & Høg (1998)
Cygnus OB7	88.0 – 95.0	1.0 – 5.5	770	Uyanıker et al. (2001)
λ Ori	188.0 – 201.0	-18.0 – -6.0	400	Muench et al. (2008)
Lupus 1	337.0 – 340.0	14.0 – 18.0	155	Lombardi et al. (2008b)
Lupus 2	338.0 – 340.0	11.0 – 12.5	155	Lombardi et al. (2008b)
Lupus 3	338.0 – 340.5	8.5 – 10.5	155	Lombardi et al. (2008b)
Lupus 4	335.0 – 339.0	6.0 – 9.0	155	Lombardi et al. (2008b)
Lupus 5	340.5 – 344.0	7.0 – 11.0	155	Lombardi et al. (2008b)
Lupus 6	339.0 – 344.0	5.0 – 7.0	155	Lombardi et al. (2008b)
Lupus 7	336.0 – 338.0	4.0 – 5.5	155	Lombardi et al. (2008b)
Lupus 8	334.0 – 338.0	2.0 – 4.0	155	Lombardi et al. (2008b)
Lupus 9	345.0 – 349.0	5.0 – 8.0	155	Lombardi et al. (2008b)
Monoceros	212.0 – 222.0	-13.0 – -7.0	830	Carpenter & Hodapp (2008)
Musca	300.0 – 303.0	-10.0 – -6.0	150	Knude & Høg (1998)
Ophiuchus	350.0 – 360.0	12.0 – 19.0	119	Lombardi et al. (2008b)
Orion A	208.0 – 219.0	-21.0 – -16.0	410	Muench et al. (2008)
Orion B	201.0 – 211.0	-17.0 – -8.0	410	Muench et al. (2008)
Perseus	156.0 – 163.0	-25.0 – -15.0	310	Motte & André (2001)
Rosette Nebula	204.5 – 210.0	-3.5 – -0.5	1650	Román-Zúñiga & Lada (2008)
Scorpius	357.0 – 6.0	16.0 – 20.0	120	Cambrésy (1999)
Serpens	30.0 – 32.0	4.0 – 6.0	260	Straižys et al. (1996)
Taurus	164.0 – 178.0	-19.0 – -10.0	140	Kenyon et al. (2008)

and the reference for the distance data.

A representation of the positions of the clouds relative to the solar system and Galactic centre is shown in Figures 2.4 and 2.5. The data are shown over two separate figures for clarity. The axes units are in parsecs.

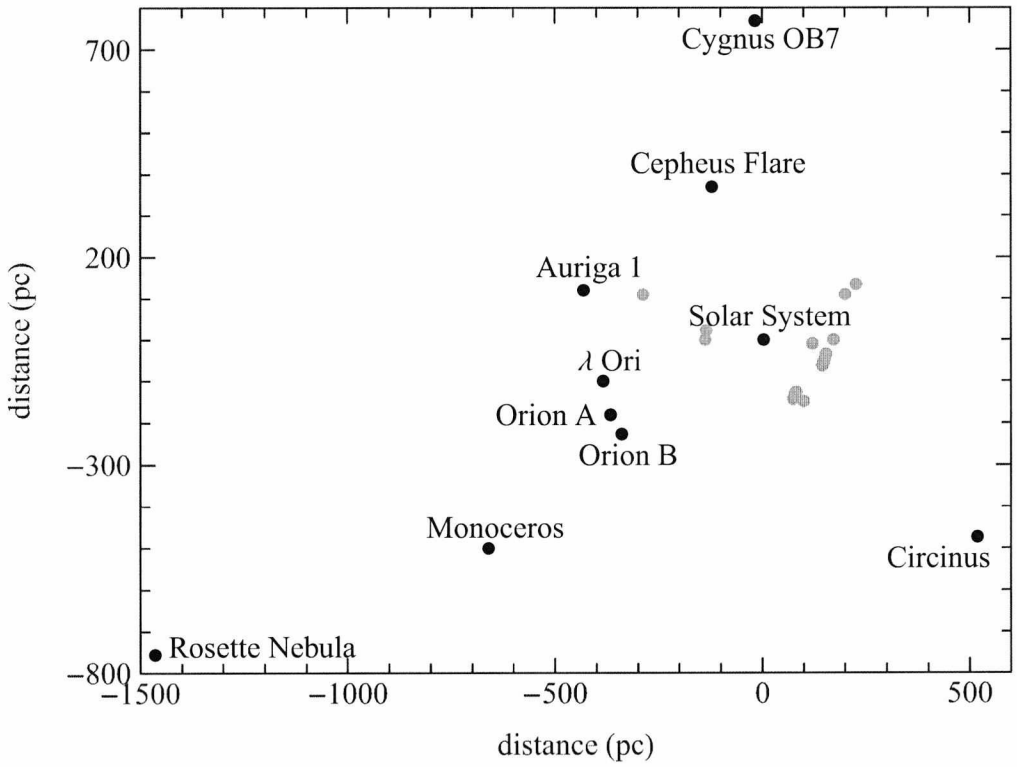

Figure 2.4: The cloud positions relative to the solar system (origin) and Galactic centre (8.33±0.35kpc to the right). The axes units are in parsecs. The grey circles show the positions of the clouds detailed in Figure 2.5.

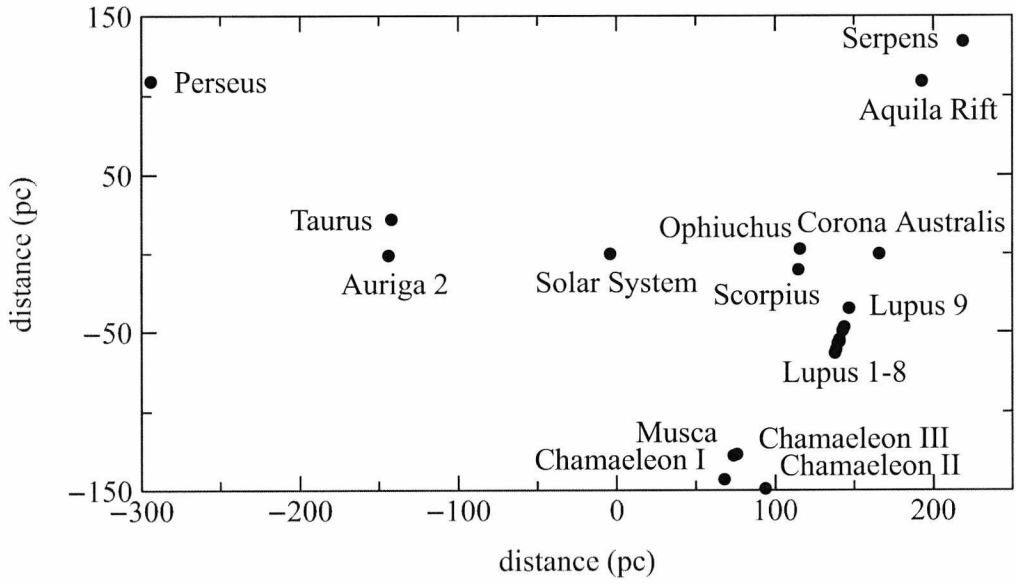

Figure 2.5: The cloud positions relative to the solar system (origin) and Galactic centre (8.33±0.35kpc to the right). The axes units are in parsecs.

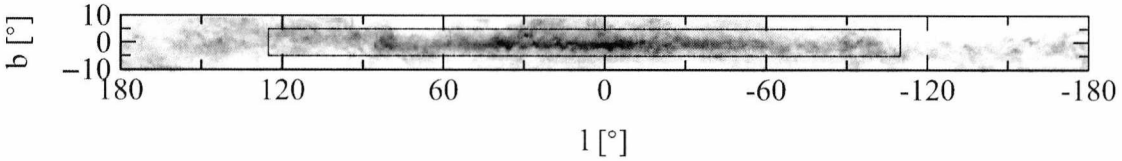

Figure 2.6: Grey scale representation of a detail of the *con-noise* extinction map based on the nearest 49 stars, used for the Galactic plane analysis (inner boxed area). Extinction values are square root scaled from 0 mag (white) to 15 mag (black) of optical extinction.

2.6 Galactic Plane Analysis

This section describes the part of the Galactic plane that was also selected for analysis. The area, in the region $125° < l < 250°$, $|b| < 5°$, contains at least one or more molecular cloud. Therefore, it is of interest to apply the techniques used in this thesis to this area, to analyse how the CDDs and structure function parameters vary with position. The whole region was split into individual regions of $5° \times 5°$ (see Figure 2.6). Each individual region contains material above 1 mag A_V in each part. The fundamental difference of these regions compared to the selected GMCs is that the distance to each 'cloud' is not known. In fact there may be two or more clouds along the line of sight.

2.7 Cloud Structure Analysis Methods

This section describes the methods used to analyse the CDDs of the selected molecular clouds. The CDDs can be investigated at different spatial scales using A_V maps with different sized pixels. Previously published methods of analysing the CDDs were discussed in Sections 1.6.6.1 and 1.6.6.2.

The analysis was performed at four spatial scales, using the *con-res maps* numbered 12-15. Therefore, the pixel sizes were 0.5′ to 4.0′ where $|b|$ <20. The extinction values were extracted for the coordinate range of each cloud (see Section 2.5). Histograms of A_V values were produced for each cloud, using varying step sizes. The different step sizes used were 0.125 mag, 0.25 mag, 0.5 mag and 1.0 mag. Analysis shows that providing there are a sufficient number of data items in each bin, the step sizes have little effect on the slope (see Figure 3.10 in the Results chapter). Only pixels with extinction values

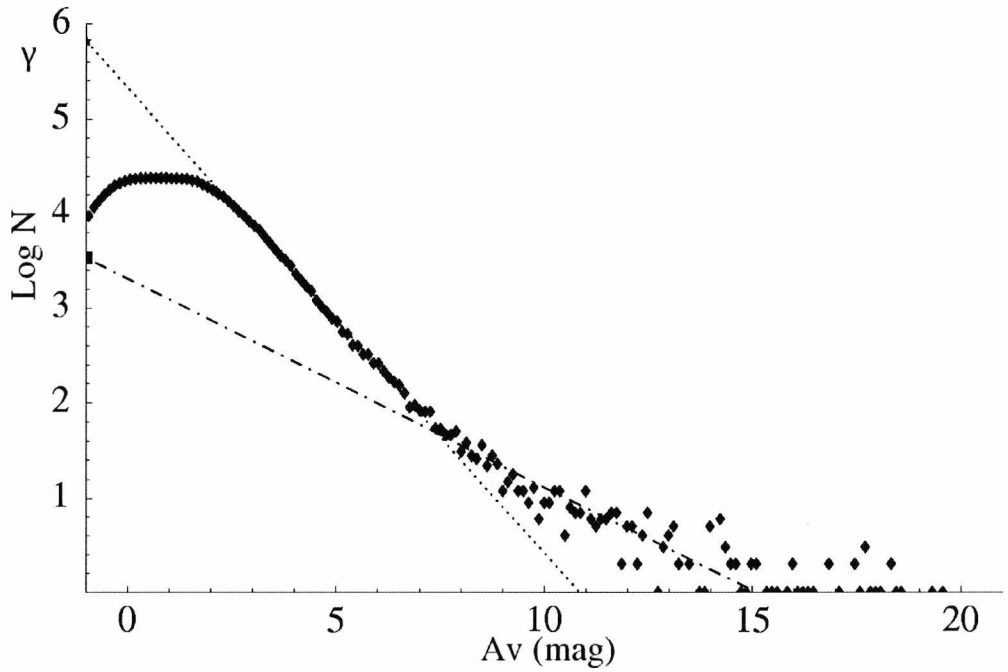

Figure 2.7: Plot of the $\log N$ vs A_V column density distribution for the Auriga 1 cloud (filled diamonds). Overplotted are the two fits obtained for the low and high column density region.

between −1 mag and +20 mag were used. The turbulence dominated bulk of molecular clouds is observed at an A_V range of approximately 1 to 5 mag. whereas the non-turbulent, star forming mass lies at visual extinctions of more than 5 mag. Beyond about 17 mag A_V insufficient data are available for this analysis.

2.7.1 $\log N$ vs A_V Column Density Distribution

Plotting A_V against $\log N$ for molecular clouds revealed that there is a linear relationship over certain magnitude ranges. This is the case since the CDDs arise from turbulent fragmentation, and turbulence is by nature self-similar at differing scales. Therefore, using the gradient from our plots allows characterisation of the CDDs for different clouds. The range of magnitudes over which a linear fit could be made was determined, and then the fitting was performed. The error of the fit was calculated as the RMS deviation of the fit from the data. An example is shown in Figure 2.7, for the cloud Auriga 1.

The example in Figure 2.7 shows that there are two distinct ranges over which a linear

fit can be made. These correspond to the low and high A_V ranges and the slopes are named γ_{low} and γ_{high} respectively. The threshold of the change from low to high varies between clouds but typically occurs between 5 and 10 magnitudes of A_V. The low A_V region is dominated by the turbulent forces in the cloud, whereas in the high A_V region the effect of gravity in the cloud becomes more important.

To compare the data at different spatial scales, the gradient of the slope was plotted against spatial scale. The spatial scale was calculated as the distance that the scale size represents at the distance of the cloud. For example 0.5′ at a distance of 140 pc represents a spatial scale of 0.02 pc, or 4200 AU. Using the relationship between gradient and spatial scale, the gradient at a given spatial scale could be derived for each cloud. This allows us to compare each cloud at the same spatial scale. A scale of 0.1 pc was chosen as this is an approximate size for a core of a molecular cloud (e.g. Larson (2003a)). The results are discussed in Section 3.3.

2.7.2 Log-Normal Fits to the Column Density Distribution

The CDDs were also investigated by fitting the histogram of the data to a relation of the form used by Lombardi et al. (2008a), (Equation 2.14; which is equation 12 from their paper expressed in terms of A_V rather than A_K). This log-normal relation follows from the fact that the probability distribution for the volume density in molecular clouds is log-normal for iso-thermal flows, e.g. Passot & Vázquez-Semadeni (1998). Of course, real observations can only probe the column density of the molecular clouds, which is the volume density integrated along the line of sight. In the event that there are several clouds along the line of sight, the column density distribution should be normal, hence the data should fit to a normal relation not log-normal (Passot & Vázquez-Semadeni, 1998).

Fitting the data to Equation 2.14 was achieved using conventional fit finding techniques, but only after trialling three of the four input parameters to obtain an approximate fit (parameter a can be found by normalisation. See Table 2.7 for a list of the parameter ranges). The 'best' fits were decided by finding the fit with the smallest RMS deviation, in terms of the error bars. Using the 'best' fit, starting values for the parameters were

Table 2.7: Parameter ranges used to create library of trial fit values, for fitting data to Equation 2.14.

Parameter	A_V range	Increment used
A_0	-14.8 mag A_V – -0.9 mag A_V	0.1
A_1	1.1 mag A_V – 13.0 mag A_V	0.1
σ	1.10 mag A_V – 1.70 mag A_V	0.01

fed into the fit finding software. This was only successful in about half of the cases; the 'best/trial' values were used for the remaining fits. The errors for the fits were calculated from the RMS of the fit from the data.

$$N(A_V) = \frac{a}{A_V - A_0} \exp\left[-\frac{(\ln(A_V - A_0) - \ln A_1)^2}{2(\ln\sigma)^2}\right] \tag{2.14}$$

This method of fitting is valid only where there is one cloud along the line of sight. The molecular clouds selected for analysis are sufficiently far away from the Galactic plane for this to be the case. As with the method for fitting $\log N$ against A_V, it is necessary to ascertain the value of the fit parameters at the same spatial scale. This was achieved by working out the relationship between the four parameters (a, A_0, A_1 and σ) in Equation 2.14 and spatial scale. This was done in the same way as in Section 2.7.1. The parameters at a spatial scale of 0.1 pc were then derived to enable like-for-like comparison of clouds.

2.7.3 $\log M$ vs A_V Mass Distribution

Analysis of the distribution of mass against A_V was performed in a similar way to the column density distribution analysis. Firstly, the mass in each pixel was ascertained using Equation 2.15, from Cambrésy (1999) and Dickman (1978). Secondly, the mass of a cloud was calculated by summing up the masses of each pixel from high A_V to low A_V (i.e. integrating the mass of the cloud).

$$M = (\alpha d)^2 \mu \frac{N_H}{A_V} \sum_i A_V(i), \tag{2.15}$$

calculated for the i^{th} pixel in the map, where α is the angular size of the pixel map, d is

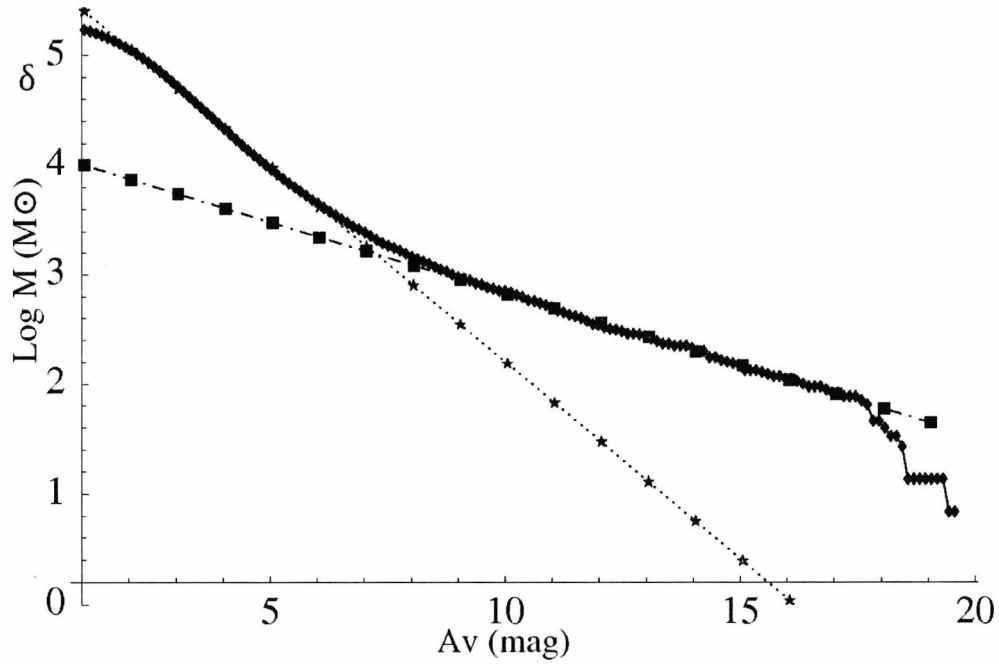

Figure 2.8: Plot of the mass distribution in the cloud Auriga 1, together with the two fits to the low and high column density regime.

the distance of the cloud and μ is the mean molecular weight when corrected for helium abundance. This method can only be applied when the distance to the cloud is known. An example plot for the Auriga 1 cloud is shown in Figure 2.8. This shows the cumulative mass M above the given extinction A_V.

These plots demonstrate the same behaviour as for column density distribution therefore plots of log M vs A_V also show linear relationships in the low A_V and high A_V regions. These two regions can be denoted in a similar way as for the CDDs, by using δ_{low} to represent the slope for the low A_V region and δ_{high} the slope for the high A_V region. As before there is a point where the change in behaviour occurs, which can be understood as the extinction threshold for star formation, $A_{V,SF}$ (e.g. Johnstone et al. (2004) and Kirk et al. (2006)) in each cloud.

Using the mass distribution allows the calculation of several interesting parameters. Firstly, one can calculate M_{1mag}, the mass of the cloud above 1 A_V. This gives a rough estimate of the mass of the cloud in both the turbulence and gravity dominated regimes. Secondly, the extinction at which the two slopes δ_{low} and δ_{high} intercept gives a value for the star formation threshold $A_{V,SF}$ above which material is potentially available for star

formation.

Thirdly, the visual extinction for a core with $M = M_{\odot}$ can be derived. This is found by extrapolating the slope δ_{high} to a mass of 1 $M_{\odot}$. Furthermore, a value for the *maximum* star formation efficiency SFE can be derived by taking the fraction of the mass above the star formation threshold and multiplying by 1/3 (see Alves et al. (2007)). These results are shown in Table 3.7 and discussed in Section 3.3.3.

2.7.3.1 Molecular Cloud Density

The average densities for the region above 1 A_V and for the star formation region (ρ_{A_V} and ρ_{SF} respectively) were calculated, for each of the 30 sample clouds using Equation 2.16. This method projects the cloud (which is only in two dimensions in the data) into the third dimension to find the volume. It assumes that all the material along the line of sight belongs to the cloud.

$$\rho[M_{\odot} \cdot pc^{-3}] = \frac{8.78 \cdot 10^{15} \cdot M[M_{\odot}]}{N^{\frac{3}{2}} \cdot (x[''] d[pc])^3}, \tag{2.16}$$

in units of $M_{\odot} \cdot pc^{-3}$, where N is the number of pixels in the appropriate A_V regime (either the whole cloud or just the part associated with star formation), x is the size of a pixel in arcseconds, d is the distance to the cloud in parsecs. The constant ($8.78 \cdot 10^{15}$) is the number of AU in a parsec to the power of three. The mass M is either M_{1mag} i.e. the mass above one A_V (see Section 2.7.3), or the mass derived from the ratio of mass above the star formation threshold (denoted M_{SF}), depending on which density is being calculated. The results are shown in Table 3.7 and are discussed in Section 3.3.3.1.

2.8 Structure Determination Methods

The methods for analysing the structure of clouds are described in Section 1.8. In this section the application of these methods to the data is discussed.

2.8.1 Structure Function Method

A useful way to quantify the structure of a molecular cloud is to find the structure function. This is defined in the form of Equation 2.17, (following work by e.g. Lombardi et al. (2008a); Padoan et al. (2002) and Padoan et al. (2003)). The equation is expressed here in terms of our observable, A_V.

$$S_p(\Delta r) = \langle |A_V(r') - A_V(r' - \Delta r)|^p \rangle , \tag{2.17}$$

where Δr is the distance between points, r' represents all the map positions, A_V is the extinction at points r' and p is the order. For $p = 2$ the formula is the two-point correlation function of the extinction map. The brackets $\langle\rangle$ denote that the average over all pixel positions is used. For each order p the scaling exponent $\eta(p)$ are found by fitting a power-law to values of $S_p(\Delta r)$ against Δr. It is assumed that the scaling exponents are related to the structure functions by Equation 2.18 (e.g. Padoan et al. Padoan et al. (2003)),

$$S_p(\Delta r) \propto \Delta r^{\eta(p)}. \tag{2.18}$$

The exponents η are determined from Equation 2.18 and the derived structure functions are then normalised to the third order. An example plot of $S_p(r)$ against $S_3(r)$ for the cloud Auriga 1 is shown in Figure 2.9. A universal behaviour should then be exhibited at low Reynolds numbers (predicted by (Benzi et al., 1993)).

To calculate the structure functions, only data in the low A_V regime was used - i.e. data where the A_V values were between the self-shielding threshold and the star formation threshold, $A_{V,SF}$. Also, only the *con-noise maps* were used for this analysis. See the discussion below regarding the possibility of reducing of noise in the *con-res maps* (Section 2.8.1.1). Data at the same spatial scales were used for each cloud - from 0.1 pc to 1.0 pc, to allow comparison of the results.

The results should be modelled to enable comparison of different clouds. Unfortunately, there is no model for incompressible turbulence for the *column density* projection of a molecular cloud. Instead, the work of Padoan et al. (2002) was followed and it was

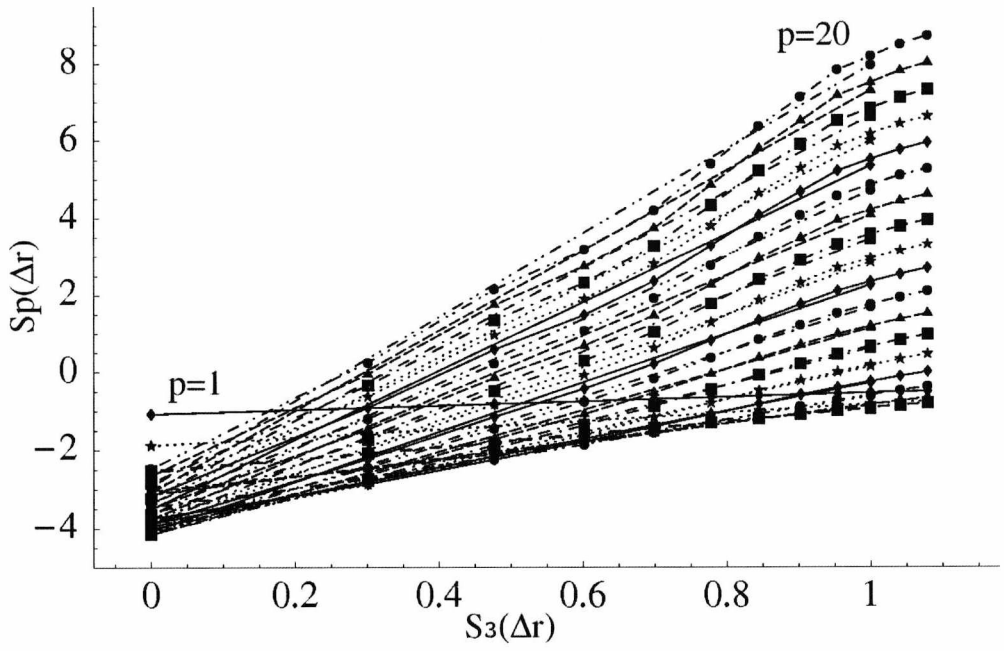

Figure 2.9: An example plot showing the variation of $S_p(r)$ (y-axis) against $S_3(r)$ (x-axis) for values of p ranging from 1 (lowest) to 20 (highest), for the cloud Auriga 1. Data from the *con-noise map* with the nearest 49 neighbouring stars is used. For each power p, a linear fit is also displayed.

instead assumed that the density scaling exponents are equivalent to the velocity scaling exponents, $(\zeta(p)/\zeta(3)$, e.g. Dubrulle (1994)). The relation for the velocity scaling exponents has the form of Equation 2.19,

$$\frac{\zeta(p)}{\zeta(3)} = (1-\Delta)\frac{p}{3} + \frac{\Delta}{1-\beta}(1-\beta^{\frac{p}{3}}), \tag{2.19}$$

where β is the degree of non-intermittency parameter and Δ is related to the codimension C and β as $\Delta = C\cdot(1-\beta)$. The fractal dimension of the cloud, D, is given by $D = 3 - C$. The K41 relation can be expressed by using Equation 2.19 and setting $\Delta = 0$. As discussed earlier, the use of the velocity scaling parameter, ζ, instead of the projected column density scaling parameter, η, is in keeping with Padoan et al. (2002) (they state however that it is not known *a priori* whether this should be the case). The scaling exponents derived from integrated intensity images were found to follow the velocity scaling using the B02 relation (Padoan et al., 2003).

The parameters Δ, C, β and D may then be derived for each cloud and compared with

the velocity field structure functions obtained from the aforementioned theoretical works by K41, SL94, B02 and also by Schmidt et al. (2008) (hereafter S08). This was achieved by creating a library of many possible outputs of Equation 2.19 and selecting the fits with an RMS of less than 0.1 when compared to the derived structure functions. For creating the library of outcomes of Equation 2.19, the parameter Δ was varied from 0.02 to 1.20 with increments of 0.01, and C was varied from 0.02 to 3.00 with increments of 0.01. The values for β and D are not required as they are functions of Δ and C.

Regarding the comparison with previously published models, the simplest model to consider is that of K41 (see Section 1.8.1.1). The energy over a large range of lengths (known as the 'inertial range') in turbulent flows is redistributed from larger scales into ever smaller scales until the effects of viscosity become important. In K41, Kolmogorov considered the velocity structure functions S_2 and S_3, showing that both are power laws of the form of Equation 2.18, with the exponents being 2/3 and 1 respectively. Due to the self-similarity of turbulence at different scales, this law can be extended to all powers of p such that $\eta(p) = p/3$.

Experimental measurements for the velocity scaling exponents show a deviation from the K41 relation for turbulence, for higher orders of p - known as *intermittency*. This is manifested in non-Gaussian tails found in plots of the probability density functions (PDFs) of e.g. the column density, and the anomalous scaling of higher order structure functions (e.g. Anselmet et al. (1984)). Therefore, a relation is needed for the scaling that considers the effects of intermittency.

In SL94, a scaling relation was derived that accounts for intermittency (see Equation 1.45 in Section 1.8.1.2). This relation shows good agreement when compared to simulations of structures that are not influenced by magnetic fields. For incompressible turbulence, SL94 derived that $C = 2$ and $\Delta = \frac{2}{3}$. It then follows that $D = 1$ i.e. that the most intermittent structures are filaments.

The SL94 relation was extended by B02 to model highly supersonic turbulence and also take account of magnetic fields (see Equation 1.46 in Section 1.8.1.3). Using the B02 model, it follows that $C = 1$ with $\Delta = \frac{2}{3}$ as with the SL94 model. Therefore, $D = 2$, i.e.

the structures are sheetlike in form.

The scaling exponents were found to be well described by log-Poisson models in the work by S08. Their models predict $\Delta \simeq 1$, rather than $\frac{2}{3}$. The S08 model applied two different modes of forcing to drive the turbulence, solenoidal (divergence-free) and compressive (rotation-free). The parameters Δ and C differ in value depending on the type of forcing applied. For example, if $\Delta = 1$, then $C \approx 1.1$ for solenoidal forcing (e.g. resulting from the presence of magnetic fields) and $C \approx 1.5$ for compressive forcing (e.g. resulting from large scale flows, shocks etc.). Conversely, if C is fixed so that $C = 1$ (as in the Kolmogorov-Burgers model, see Section 1.8.1.3), then $\Delta \approx 0.79$ for solenoidal forcing and $\Delta \approx 0.94$ for compressive forcing (S08).

2.8.1.1 Reducing the Effects of Noise when Calculating Structure Functions

The uncertainties associated with the A_V maps may have an undesirable effect on the resulting structure functions. This is especially true for the *con-res maps* where the noise varies from pixel to pixel and is generally larger than for the *con-noise maps* (see Figures 3.9 and 3.8 in Sections 3.2.2 and 3.2.1 respectively). One approach is to use only pixels in the extinction maps where the A_V value in the pixel is above the self-shielding threshold (i.e. 1 mag A_V and above). This tends to reduce the number of pixels with a large noise.

Despite discarding pixels below the self-shielding threshold, the effect of noise (originating from photometric errors) may still mean that one is unable to derive a meaningful structure function. One further approach to try and minimise the effect of noise is as follows. An adjustment is made to Equation 2.17 to weight the A_V values in each pixel according to the corresponding uncertainty,

$$S_p(\Delta r) = \left\langle \frac{\Sigma \omega_i^X |A_V(r') - A_V(r' - \Delta r)|^p}{\Sigma \omega_i^X} \right\rangle. \tag{2.20}$$

In Equation 2.20, ω_i is the weight for each pixel i, and X is a power that can be varied experimentally. Values of $\frac{1}{4}$, $\frac{1}{2}$, 1, 2, 3 and 4 were used for X. The weighting factor, ω_i, can be either A_{V_i}/σ_i or just $1/\sigma_i$. Clearly, this approach gives the best results with the

con-res maps, where the noise varies from pixel to pixel. The results of this analysis are discussed in Section 3.4.

2.8.2 The Δ-variance Method

The Δ-variance technique (as described in Section 1.8.2) was applied to the *con-noise maps*, to analyse the structure. One aim was to provide a quantitative measure (e.g. width and length) of the elements of structure such as filaments, sections of filaments (where the filaments are not contiguous) and cores. According to their paper, the method underestimates the peak positions by 10-20%, which should be taken into account with when interpreting the results (Ossenkopf et al., 2008a).

Measurement of the larger elements of structure (that approach the size of the cut for that cloud) may not be possible due to the limitations of the technique - it is not able to identify peaks in σ^2_Δ when the cloud occupies most of the image (Ossenkopf et al., 2008a). However, simply enlarging our cuts for individual clouds might not be beneficial as unwanted sections of other clouds would be introduced, which could affect the measurements. Therefore, our maps were tiled 2×2 so that all peaks were detected.

As well as being applied to the *con-noise maps*, the Δ-variance technique was also applied to the corresponding star-density maps. These show enhanced structure in high A_V regions as the distance to the *nth* nearest star increases logarithmically in high extinction regions. Furthermore, the star density maps do not trace the finer structure at low A_V so any peak in Δ-variance found using these maps will arise from material at higher column densities. As with the A_V maps, they were tiled 2×2 to detect the peaks in Δ-variance; in some cases it was necessary to tile 3×3 to achieve this (for the clouds Lupus 3, Musca and Perseus).

The Δ-variance analysis was also used to calculate the mass index scaling exponent α for each cloud. This is measured by fitting a power-law to the resulting plot of $\sigma\Delta^2$ against scale (see Figure 2.10; right panel). The fit is made over the linear part of the diagram of the Δ-variance σ^2_Δ against lag r. Care must be taken with the fit to avoid any pixels affected by oversampling (at lower values of r). The number of pixels to be discarded

because of oversampling is calculated using the corresponding star density maps.

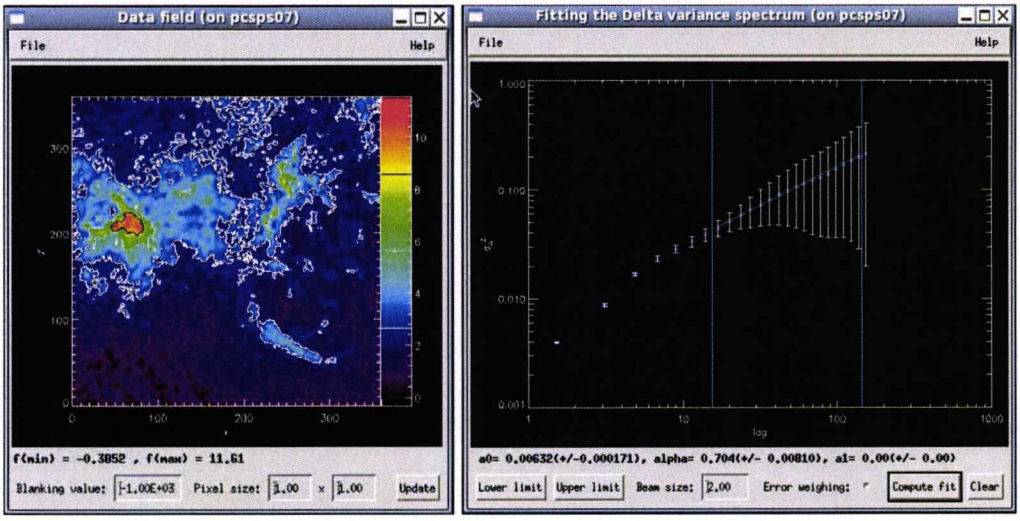

Figure 2.10: Example screenshots obtained while using the IDL DELTAVARWIDGET. The panel on the left shows the input screen with the Circinus cloud as an example (using the *con-noise map* with the nearest 49 stars). The right panel shows the output for the same cloud, with fitting to the appropriate range of values to determine the mass index scaling exponent α.

The Δ-variance results were obtained using the IDL DELTAVARWIDGET[3] provided by Ossenkopf et al. (2008a). Example screenshots obtained while using the widget are shown in Figure 2.10. The panel on the left shows the input screen with the Circinus cloud as an example (using the *con-noise map* with the nearest 49 stars). The right panel shows the output for the same cloud, with fitting to the appropriate range of values to determine the mass index scaling exponent α.

2.9 Correlation Determination Methods

In order to test for correlations in the results, it is necessary to use appropriate methods. This section outlines the methods used for testing for correlations in this thesis.

[3] http://hera.ph1.uni-koeln.de/ ossk/ftpspace/deltavar/

2.9.1 Pearson's Correlation Coefficient

One method of testing for correlations between two groups of data is to find Pearson's correlation coefficient r, using the following formula (Wall & Jenkins, 2003),

$$r = \frac{\Sigma_{i=1}^{N}(X_i - \overline{X})(Y_i - \overline{Y})}{\sqrt{\Sigma_{i=1}^{N}(X_i - \overline{X})^2(Y_i - \overline{Y})^2}}, \tag{2.21}$$

where X and Y are the two groups for which the correlation is being determined. The test returns a value for r between -1 and 1. A positive correlation between groups X and Y will return a positive value and vice versa. A strong correlation will have a value $|r| > 0.9$. Values for r around zero indicate no correlation between the two groups.

2.9.2 The Kolmogorov-Smirnov Test

Another way of testing for correlations is to use the Kolmogorov-Smirnov (two-sample) test (Wall & Jenkins, 2003). This is useful if one wants to be able to reject a *null hypothesis* H_0, i.e. that two distributions do not belong to the same 'parent' group. The following procedure is used (Wall & Jenkins, 2003) to perform the test:

- The observed cumulative frequency distribution under H_0 is calculated for the first group $S_m(x)$, for the number of data items N_m.
- For the number of data items in the second group N_n calculate $S_n(x)$, the cumulative frequency distribution for that group.
- Calculate the test statistic, $D = \max |S_m(x) - S_n(x)|$.
- A table is then consulted (e.g. Table A 2.10. in Wall & Jenkins (2003)) to determine whether D has exceeded a critical value given the number of observations N_m and N_n. If so, then H_0 is rejected at that level of significance.

In practical terms the null hypothesis H_0 may only be used with confidence if the test statistic D has a high degree of certainty (i.e. 99.9% that the distributions are not from the same 'parent' group), otherwise the result is ambiguous.

Chapter 3

The Results

In this chapter the results are presented. The first section deals with the maps created for the project. These are discussed and compared to previously published maps in the following section. The uncertainties arising from the photometric errors are also described. Then, using these maps the CDDs and mass distributions for various clouds/regions are calculated. The results for both CDDs and mass distributions are presented and discussed. In the next section the results from the structure function and Δ-variance analysis of various clouds/regions are reported. The effect of noise on the structure function results, and on the Δ-variance results, is also described.

3.1 All Sky Extinction Maps

The maps created for this thesis are as shown in Table 2.3 (in Section 2.2). The resulting A_V and spatial resolution maps are discussed here, while the maps of uncertainties are discussed in Section 3.2. An example of one of our maps is shown in Figure 3.1. This composite shows the *con-noise map* using the nearest 49 stars (in red), together with the projected FUV radiation field of Galactic B-stars (in green) and the projected EUV radiation field of Galactic O-stars (in blue). Some of the features visible in our map our discussed in the following section.

The maps made for this project are available to download [1].

3.1.1 A_V and Spatial Resolution Maps

Firstly, two examples of the maps created for this thesis are shown in Figure 3.2. In the top panel is the *con-noise map* using the nearest 49 stars. The extinction values are scaled linearly from -1 mag (white) to +7 mag (black). The most obvious feature in this map is the dust distributed along the Galactic plane, with the bulge around the Galactic centre in the middle. The Large and Small Magellanic clouds are also visible to the lower left of the centre. These are visible due to the presence of red giants. Other features shown are nearby GMCs including Ophiuchus (above the centre), Orion (far right) and Taurus

[1] from http://astro.kent.ac.uk/extinction/download.html

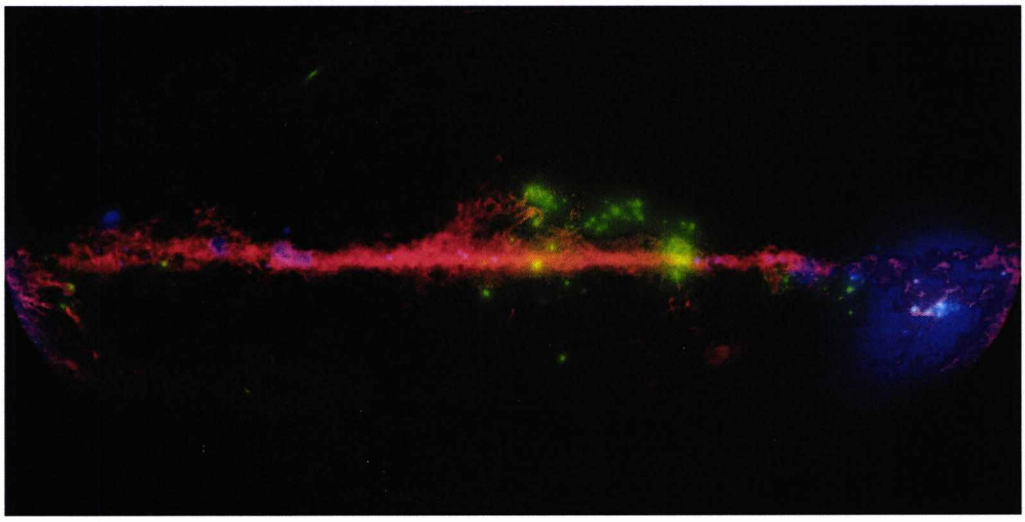

Figure 3.1: A composite of our A_V using the nearest 49 stars (red), with the projected FUV radiation field of Galactic B-stars (green) and the projected EUV radiation field of Galactic O-stars (blue).

(far left). Away from the Galactic plane other features of low A_V are visible, especially in the southern hemisphere at latitudes of $\approx -70°$. A comparison with the $E(B-V)$ maps of Schlegel et al. (1998) also shows material at these positions, so these are real clouds and not artefacts.

In the bottom panel of Figure 3.2, an image illustrating the distance to the 49^{th} nearest neighbour is shown. The distance varies from approximately $1'$ at $b \approx 0°$ to approximately $10'$ at $|b| \approx 90°$. Therefore, the spatial resolution varies by about a factor of 10 from the Galactic plane to the poles in the nearest 49^{th} star maps. The spatial resolution is better than $3'$ to $5'$ in the regions that contain molecular clouds, where $|b| < 30°$.

More detailed prints of the *con-noise maps* using the nearest 49 stars are shown in Appendix A.1.

3.1.2 Theoretical Distance to which Extinction Values may be Calculated

For the maps in this thesis, the theoretical distance to which there are more background stars than foreground stars was calculated using the Besancon Galaxy model [2] (Robin

[2] http://model.obs-besancon.fr/

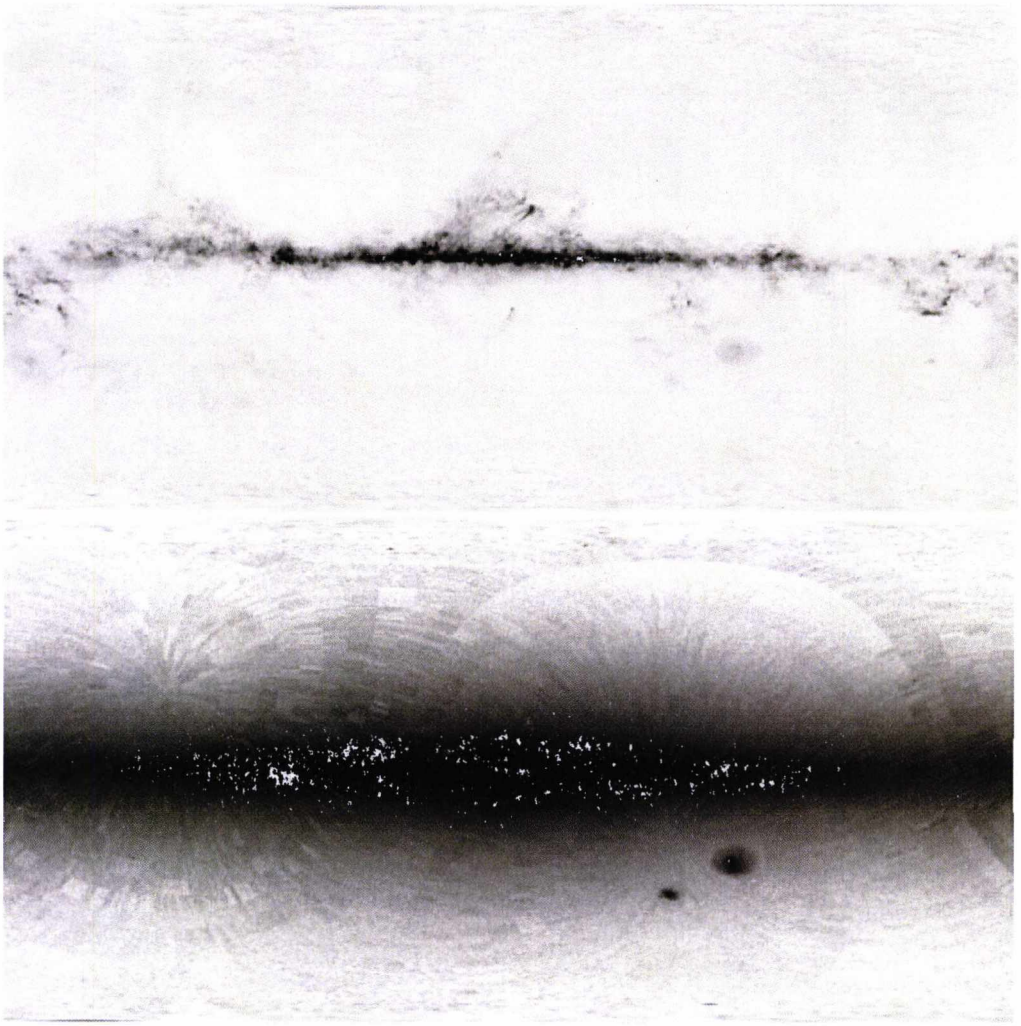

Figure 3.2: **Top Panel:** The all sky extinction map using the nearest 49 stars. The image size is 360° × 180° with the Galactic Centre in the middle. Optical extinction values are scaled linearly from −1 mag (white) to +7 mag (black). **Bottom Panel:** Greyscale map of the distance to the 49^{th} nearest neighbour, i.e. a spatial resolution map of the data. Grey values are scaled from 1′ (black) to 11′ (white). The image scale is the same as in the top panel.

et al., 2003). This represents the theoretical distance to which clouds can be detected. In practice this calculation was restricted to 85 points around the Galactic plane. This area is of interest as it contains a large number of clouds where star formation is occuring. The resulting distances are shown in Table 3.1.

As previously discussed, by using the *median* colour of stars rather than the *mean*, the extinction is either measured correctly for a cloud or the cloud is not observed. Therefore, it is of interest to know the distance to which the ratio of foreground stars to background

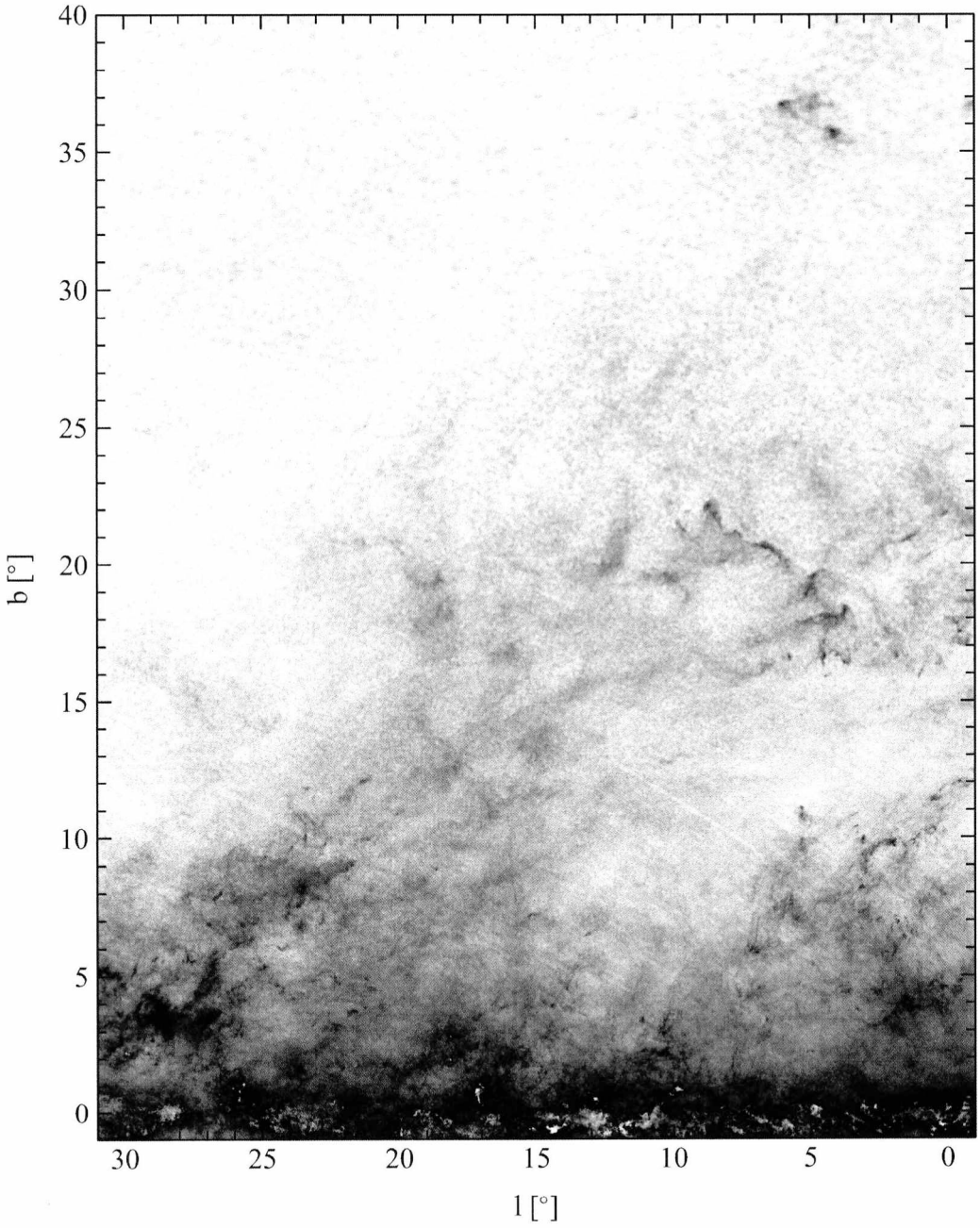

Figure 3.3: Greyscale representation of a detail of the *con-noise* extinction map based on the nearest 49 stars. Extinction values are square root scaled from 0 mag (white) to 15 mag (black) of optical extinction.

stars is unity. To generate the inputs for the Besancon model the completeness limit for the J, H and K bands were calculated. For this the Vizier[3] facility was used to generate a list of 2MASS sources around each point of interest. Then the distance to the median star at each coordinate was taken, to find the approximate distance to which a cloud can be detected at that those coordinates. In practice the actual distance is less than this theoretical maximum, due to the crude estimate of extinction along the Galactic plane used in the model (Robin et al., 2003). It should also be noted that the Besancon Galaxy model assumes a distance of 8.5 kpc to the Galactic centre whereas the current distance is 8.33±0.35 kpc (Gillessen et al. (2009)).

Table 3.1: Table showing distance to which there are an equal number of foreground stars to background stars (i.e. the distance to the *median star*) for various values of l and b. These are obtained using the Besancon Galaxy model (Robin et al., 2003).

l [°]	b [°]	dist (kpc)	b	dist (kpc)	b	dist (kpc)	b	dist (kpc)	b	dist (kpc)	b	dist (kpc)	b	dist (kpc)
0	-5	7.39	-4	7.59	-2	8.07	0	8.57	2	8.39	4	8.00	5	8.04
30	-5	4.07	-4	5.45	-2	6.91	0	7.77	2	7.20	4	5.62	5	4.76
60	-5	2.85	-4	3.27	-2	4.53	0	5.85	2	7.41	4	5.41	5	3.64
90	-5	1.91	-4	2.07	-2	2.45	0	3.01	2	4.32	4	4.51	5	3.97
120	-5	1.63	-4	1.75	-2	1.87	0	2.17	2	2.58	4	2.56	5	2.32
150	-5	1.51	-4	1.59	-2	1.73	0	2.01	2	2.11	4	1.99	5	1.93
180	-5	1.67	-4	1.61	-2	1.87	0	1.97	2	1.85	4	1.69	5	1.57
210	-5	1.85	-4	1.95	-2	2.07	0	1.93	2	1.71	4	1.57	5	1.48
240	-5	2.33	-4	2.53	-2	2.47	0	2.07	2	1.89	4	1.63	5	1.57
270	-5	3.39	-4	4.23	-2	3.75	0	2.89	2	2.43	4	2.08	5	1.93
300	-5	3.95	-4	5.59	-2	7.11	0	5.75	2	4.50	4	3.28	5	2.74
330	-5	4.61	-4	5.73	-2	7.67	0	7.61	2	7.44	4	5.62	5	4.30

3.1.3 Comparison with Previously Published Extinction Maps

In this section the *con-noise maps* are compared with previously published large-scale extinction maps by Dobashi et al. (2005) (D05; see Section 1.6.1) and Schlegel et al. (1998) (S98; see Section 1.6.3). Table 3.2 shows selected properties of eight regions for comparison.

[3] http://vizier.u-strasbg.fr/viz-bin/VizieR

Table 3.2: Summary table of the properties of selected regions in *con-noise map* of the nearest 49 stars. Listed are the region name and the area. The slope and offsets of the extinction when compared between our map, D05 and S98 are also displayed. The (*) indicates slopes and offsets that have been fit by eye, since no satisfactory linear regression fit could be achieved.

Region	Name	l range	b range	Dobashi vs Our map		Schlegel vs Our map		Schlegel vs Dobashi	
				offset	slope	offset	slope	offset	slope
1	Camelopardalis	157.2° - 152.2°	1.4° - 6.4°	0.22	1.21	-0.52	0.52	-0.61	0.36
2	Serpens	31.3° - 26.3°	1.3° - 6.3°	0.17	1.28	-1.70*	1.00*	-1.40*	0.80*
3	Lupus	341.8° - 336.8°	1.9° - 6.9°	0.82	1.06	-0.34	0.73	-0.80*	0.60*
4	Vela	272.0° - 267.0°	1.0° - 6.0°	0.22	1.41	-0.86	0.70	-0.48	0.37
5	Taurus	166.0° - 161.0°	4.9° - 9.9°	0.19	1.13	-0.31	0.62	-0.54	0.56
6	North America Neb.	85.0° - 80.0°	1.0° - 6.0°	0.19	1.34	-0.74	0.73	-0.42	0.46
7	Monoceros	225.5° - 223.5°	1.0° - 6.0°	-0.01	1.23	-0.48	0.58	-0.70*	0.55*
8	Auriga	185.0° - 180.0°	3.0° - 8.0°	0.11	1.23	-0.58	0.65	-0.63	0.46
	Averages:				1.24		0.69		0.52

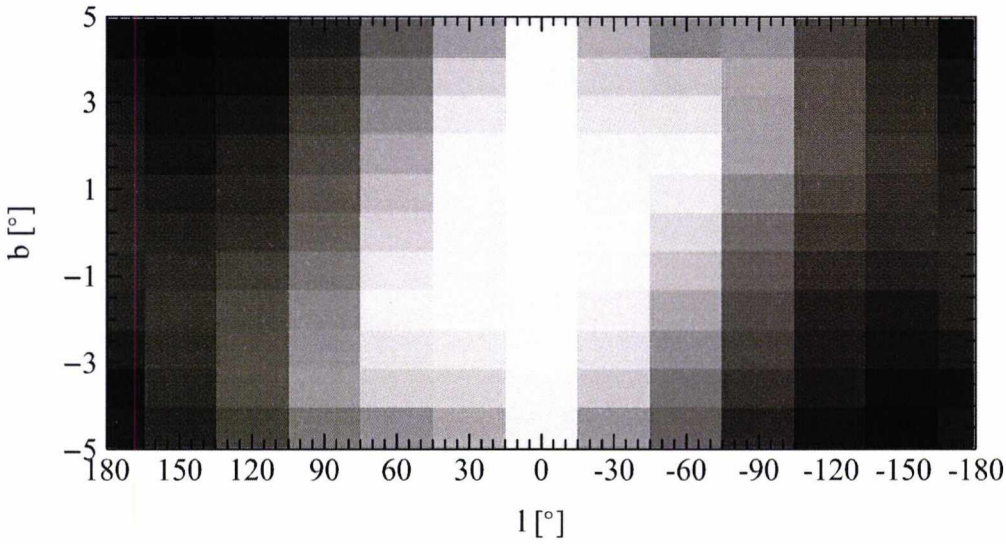

Figure 3.4: A representation of the distance at which there are the same number of foreground stars to background stars, at various points around the Galactic place. The data are scaled linearly from black (1.48 kpc) to white (8.57 kpc). These distances are derived using the Besancon Galaxy model (Robin et al., 2003).

3.1.3.1 A Visual Comparison

A visual comparison of an example region (containing the Serpens molecular cloud) with the maps of D05 and S98 is given in Figure 3.5. The map being compared is the A_V *con-noise map* of the nearest 49 neighbouring stars. The comparison images cover a 100° square region around the Serpens molecular cloud. In the plots the extinction values are scaled linearly from 0.5 mag (white) to 20 mag (black).

The main difference between the plots in Figure 3.5 is the higher spatial resolution of the 49^{th} nearest neighbour map (between 2′ and 4′ for this region) compared to approximately 6′ for the other two maps. Therefore, finer details can be observed in the former - specifically smaller, higher density cores and smaller scale structures.

Comparing the 49^{th} nearest neighbour map with the map of D05, it can be seen that a number of the high density cores are not detected in the D05 map, due to their method of optical star counts not being able to trace high column densities. Also, it is readily apparent that the D05 map does not detect most clouds along the Galactic plane. This is also due to the optical star counting technique not tracing high column densities. The technique used in this thesis is able to trace high column density regions better, with some

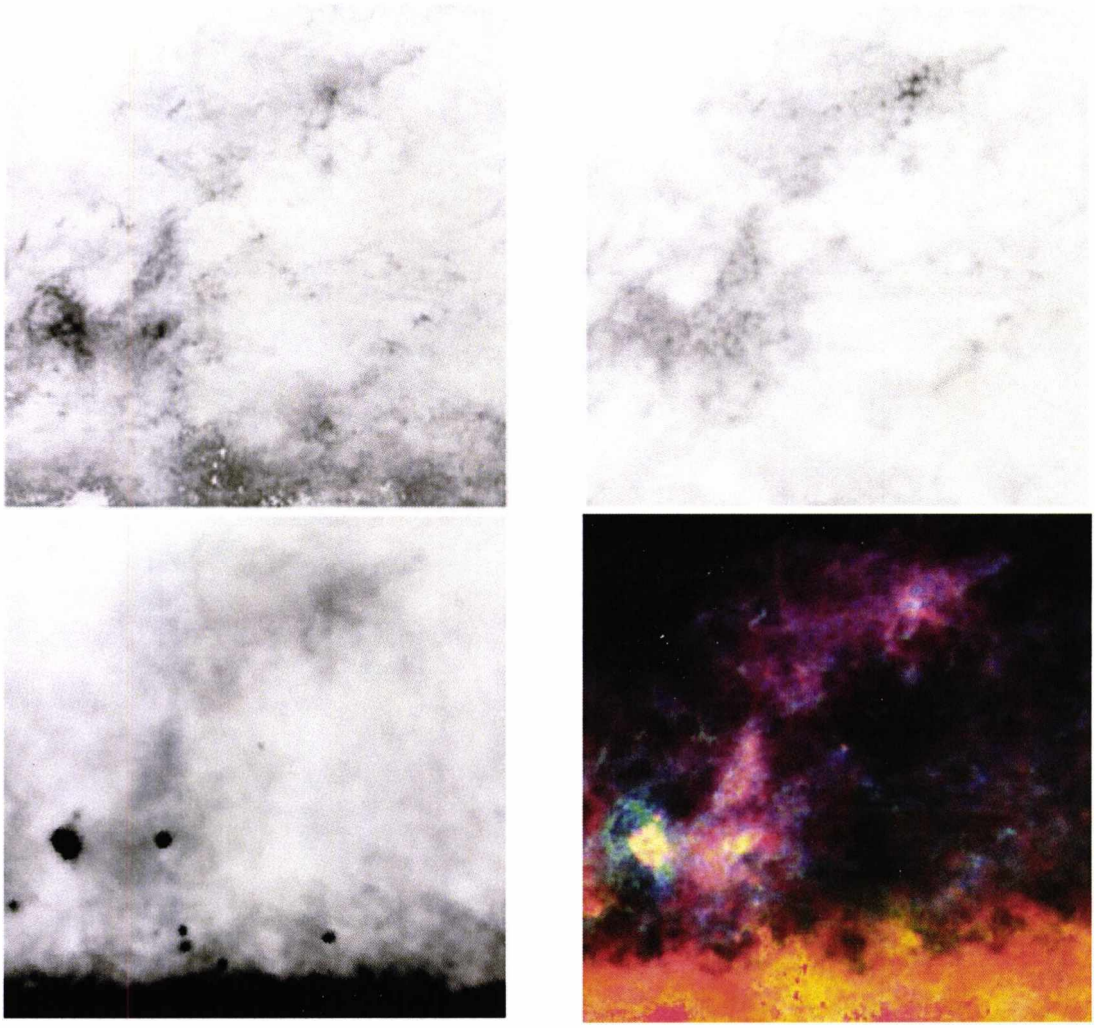

Figure 3.5: Gray scale representation an example region (Serpens) of our A_V map (top left panel), the map of D05 (top right panel), the map of S98 (bottom left panel) and all three images overlaid in colour (bottom right panel). The images are $10° \times 10°$ in size and encompass a coordinate range of $20° < l < 30°$ and $0° < b < 10°$. The extinction values in all maps are scaled linearly. For the black and white images, white represents 0.5 mag optical extinction, while black represents 20 mag A_V. The colour image shows our map (green), S98 (red) and D05 (blue).

exceptions close to the Galactic plane (with $|b| < 1°$). In these cases, foreground stars dominate the stellar population and using the median colour excess results in the cloud not being detected. These small regions are visible as white areas along the bottom of the top left panel of Figure 3.5.

The differences between the three maps are best demonstrated using a colour image (Figure 3.5, bottom right panel). In the figure our map is rendered in green, S98 in red and D05 in blue. For example the core (to the left of the figure, below the middle) is not

well measured in the S98 map due to it's low temperature. The core does not appear in the D05 map due to the star count/optical extinction method used. Thus it appears green in the figure where it is detected by our map. The Galactic plane (with $|b| < 1°$, bottom of the figure) is well detected by the S98 map but not so well by our map (the cloud is not always detected, due to the dominance of foreground stars). The D05 map does not detect this region at all.

There are two main differences when comparing the 49^{th} nearest neighbour map with the map of S98. Firstly, the A_V values calculated from the S98 map are about a factor of 1.5 to 2.0 higher. This was discussed in D05, and the likely cause is systematic uncertainties in the assumed dust temperature and emissivity in the S98 map. Secondly, there are some high extinction regions in the densest cores, and within 1° of the Galactic plane, in the S98 map. The high extinction regions in the densest cores are likely to be superimposed point sources and/or regions where the dust temperature differs significantly. Near the Galactic plane this effect may also occur, but it should be noted that the S98 map traces the emission effectively to infinity. Therefore, the technique used for the S98 map is not limited by distance but detects all material along each line-of-sight.

3.1.3.2 Comparison with Dobashi et al. (2005)

In Figure 3.6, the A_V values obtained from our 49^{th} nearest neighbour map are compared to those obtained using the D05 map. The area compared is a 5° by 5° region in Serpens, the coordinates of which are shown in Table 3.2. In Figure 3.6, only a small selection (≈0.44 %) of random pixels is plotted to improve visibility, due to the high number of pixels in the region. A line of best fit (fitted excluding outliers) is shown in the plot together with the one-to-one line. The plots for the other areas listed in Table 3.2 are shown in Appendix A.2.1.

Figure 3.6 shows that using the D05 map systematically underestimates the extinction being by about 20 %. The systematic offset is only 0.17 mag which is well below the noise level and is therefore negligible. Large differences between the two methods become apparent at higher column densities (greater than 5-6 mag A_V). Two reasons for this are;

i) the optical star count method used in D05 is not able to measure high density cores, and ii) the D05 maps use a lower resolution and are not able to discern the structures seen in our map.

The remaining figures shown in Appendix A.2.1 exhibit the same trend - there is always a systematic underestimation of A_V in the D05 values by about 20 %. There are also systematic offsets which, as before, are below the variance level of our map. This demonstrates that the calibration of the colour excess values is correct at different positions around the map. The only exception to this is the Lupus region (see Appendix A.27). On inspecting the plot, it can be seen that a linear fit is not appropriate for this region. This could be due to the large number of small scale A_V cores (e.g. see Lombardi et al. (2008a)) or perhaps due to the clouds in the Lupus region being at different distances (such as suggested by Knude (2010)).

In the comparison against the D05 map, the slope of the linear fits is around 1.2 (see Table 3.2). One possible explanation is that the incorrect extinction law was used when making the maps for this thesis. However, this is unlikely for the following two reasons. In the first instance, one would expect to find residuals resembling molecular clouds on comparison of the A_H maps determined from $\langle J-H \rangle$ and $\langle H-K \rangle$ colour excess. These residuals were not present. Secondly, the factor of 20 % could be explained by a value for β of 2.2 when converting from colour excess to extinction. Generally the value for β is less than 2.0 so that cannot be the reason.

A likely cause for the 20 % discrepancy is due to the technique used by D05. When using the star counting technique, there is an increasing proportion of foreground stars for more distant clouds. Therefore, the extinction is underestimated for more distant clouds with this technique. With the technique used for this thesis (median colour excess method), either the correct extinction is measured, or the cloud is not detected (see Section 2.3.1 for discussion on this). The paper by Froebrich & del Burgo (2006) gives a comparison of these two techniques and found that the magnitude of the difference is around 20 %.

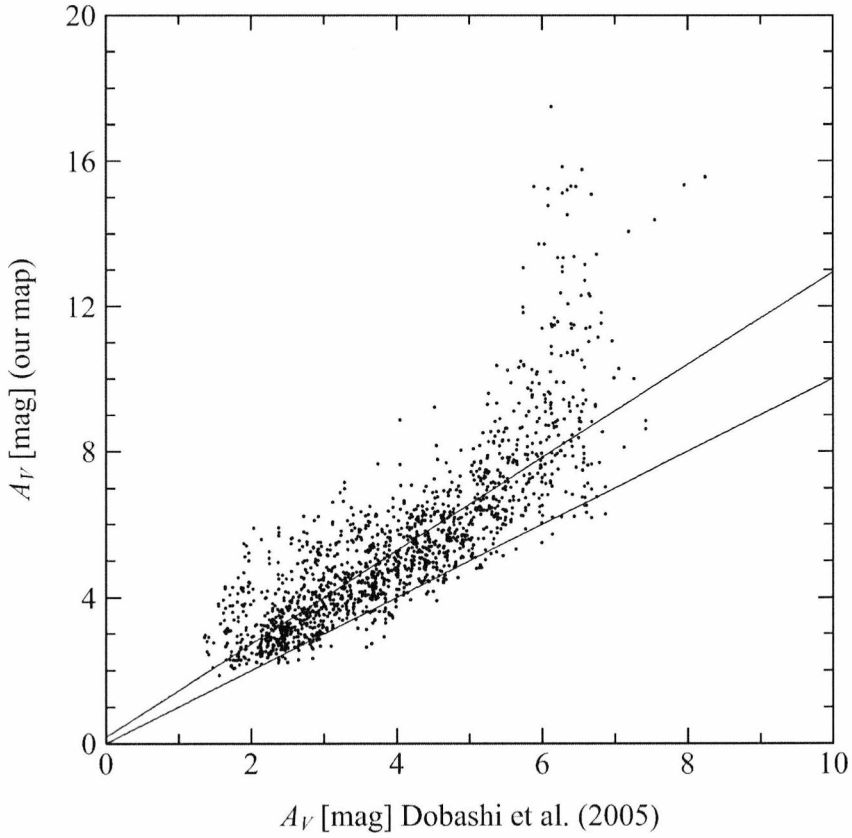

Figure 3.6: Comparison of the optical extinction values for the region Serpens between the nearest 49 stars *con-noise* extinction map and the map from D05. The overplotted solid lines are a one-to-one line, as well as a linear fit. See Table 3.2 for the parameters of the fit.

3.1.3.3 Comparison with Schlegel et al. (1998)

In this section, the *con-noise map* using the nearest 49 stars is compared to extinction values derived from the map by S98. A plot of our A_V values against theirs is shown in Figure 3.7. The region examined is the same as that in the comparison with D05 in Serpens. In this region there is an offset of approximately 1.7 mag A_V, found from the intercept of the line of best fit. This offset is generally higher than the one sigma variance, for reasons detailed in the next paragraph.

The gradient of the fit of our data against S98 is approximately unity. For the cases where our A_V values are higher than those derived from the S98 map, it could be due to the higher spatial resolution of our map at that location. In areas close to the Galactic plane, our technique is limited in areas of high extinction due to the dominance of foreground

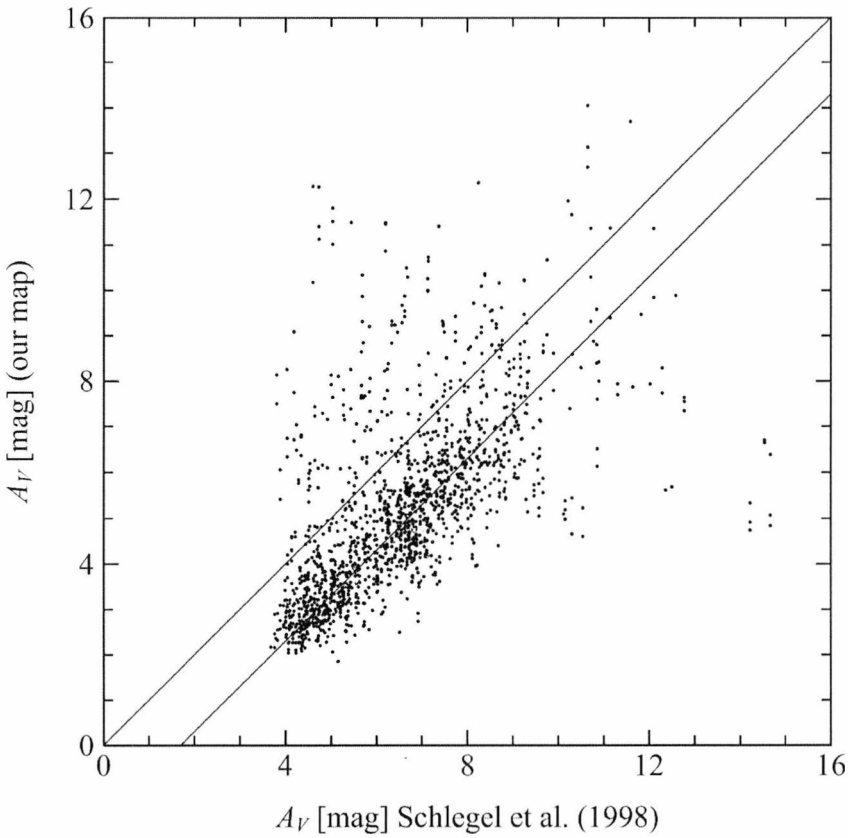

Figure 3.7: Comparison of the optical extinction values for the region Serpens between the nearest 49 stars *con-noise* extinction map and the map from S98. The overplotted solid lines are a one-to-one line, as well as a linear fit. See Table 3.2 for the parameters of the fit.

stars. In these areas, the S98 map leads higher extinction values.

Generally, the extinction values derived from the S98 map are between a factor of 1.5 and 2.0 higher than the 49 nearest stars con-noise map. This result is in agreement with the findings of Dobashi et al. (2005), who found that the values of extinction derived from the S98 map were overestimated by a factor of approximately two. The principle reasons for these differences are uncertainties in the dust temperature and dust emissivity, together with the longer line-of-sight distance (effectively to infinity) in the S98 map.

The plots for the remaining areas shown in Table 3.2 are shown in Appendix A.2.2. As a comparison, plots of the same areas using the Dobashi A_V against those derived from S98 are shown in Appendix A.2.3.

3.2 The Distribution of Uncertainties in the A_V Maps

3.2.1 Con-noise Maps

Maps of the uncertainties were made, corresponding to the maps of A_V and spatial resolution. The *con-noise maps* made for this thesis (shown in Table 2.3) use a fixed number of stars around each pixel. The stars selected have similar photometric errors, and using a fixed number of stars around each pixel results in a near constant noise. When using a fixed pixel size, the number of stars in each pixel varies, hence the noise is more variable.

Using the method outlined in Section 2.4.1, the covariance for each map was calculated. Values for σ_{cov} calculated using this method range from 0.0025 mag^2 to 0.0055 mag^2 (from the *con-noise map* of the nearest 49 stars). The final value used in making the uncertainties map was σ_{cov}=0.004 mag^2. In Table 3.3 example values of σ_{cov} are given for different extinction free regions.

Table 3.3: Examples of the covariance values, σ_{cov}, determined in a number of extinction free regions.

l range	b range	σ_{cov} [mag^2]
163.3° – 158.3°	+32.3° – +37.3°	0.0055
31.3° – 26.3°	+31.3° – +36.3°	0.0031
313.3° – 308.3°	+31.9° – +36.9°	0.0026
272.0° – 267.0°	+31.0° – +36.0°	0.0030
143.0° – 138.0°	−35.7° – −30.7°	0.0039
85.1° – 80.1°	−36.0° – −31.0°	0.0037
225.5° – 220.5°	−36.1° – −31.1°	0.0047
244.2° – 239.2°	−37.5° – −32.5°	0.0052

Some examples of the variance for different regions are shown in Table 3.4. Also shown are the names of the molecular clouds and the coordinates of the areas in which the variance was calculated.

The one sigma variance for the *con-noise maps* 1, 2 and 3 is shown in Figure 3.8. The variance is calculated in a 5°× 5° region near the Galactic plane (2.5° < b < 7.5°; 221.67° < l < 226.67°). In the figure the narrowness of the peaks for these maps is apparent, as the photometric uncertainties do not vary much from star-to-star.

Using Figure 3.8 it can be seen that the peaks in the variance distribution for the

Table 3.4: a table of the variance, σ_{A_V}, in selected regions in the *con-noise* nearest 49 stars map.

Name	l range	b range	σ_{A_V} [mag]
Camelopardalis	157.2° - 152.2°	1.4° - 6.4°	0.286
Serpens	31.3° - 26.3°	1.3° - 6.3°	0.282
Lupus	341.8° - 336.8°	1.9° - 6.9°	0.282
Vela	272.0° - 267.0°	1.0° - 6.0°	0.281
Taurus	166.0° - 161.0°	4.9° - 9.9°	0.282
N. America Neb.	85.0° - 80.0°	1.0° - 6.0°	0.278
Monoceros	225.5° - 223.5°	1.0° - 6.0°	0.281
Auriga	185.0° - 180.0°	3.0° - 8.0°	0.281

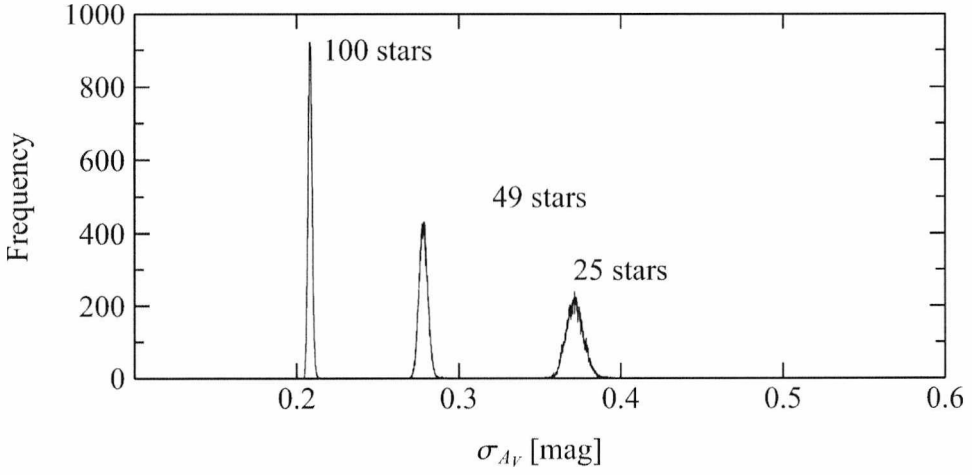

Figure 3.8: Distribution of the individual statistical uncertainties of our A_V values in a 5°× 5° region near the Galactic Plane ($2.5° < b < 7.5°$; $221.67° < l < 226.67°$). The one sigma variance distribution σ_{A_V} is shown for the maps using the nearest 25 (peak at approximately 0.21 mag), 49 (peak at approximately 0.28 mag), and 100 stars (peak at approximately 0.37 mag). Note that the peaks of the distributions will not change with position for the *con-noise* maps (see e.g. Table 3.4) since the same number of stars is included in the A_V calculation.

con-noise maps are at 0.21 mag, 0.28 mag and 0.37 mag for the 25^{th}, 49^{th} and 100^{th} nearest neighbour maps, respectively. For the 49^{th} nearest neighbour map, for example, material at 1 A_V is always detected with a signal-to-noise ratio of greater than three. This is important as 1 A_V is the threshold for self-shielding in molecular clouds (Hartmann et al., 2001).

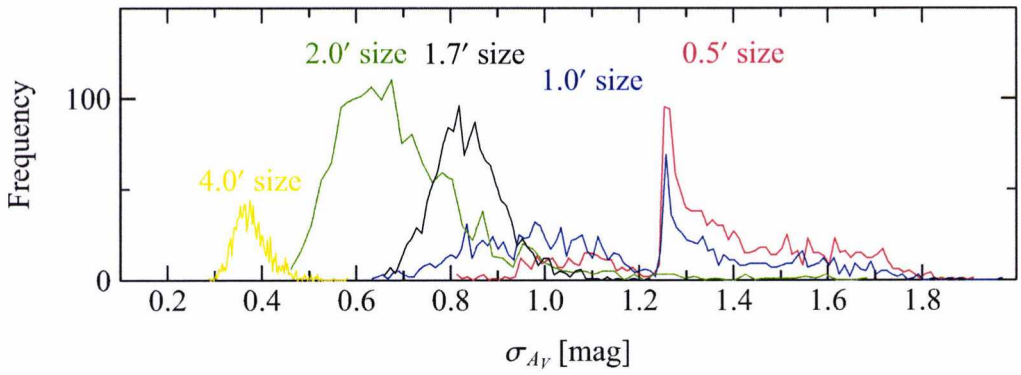

Figure 3.9: Distribution of the individual statistical uncertainties of our A_V values in a 5° × 5° region near the Galactic Plane (2.5° < b < 7.5°; 221.67° < l < 226.67°). The one sigma variance distribution σ_{A_V} is shown for the maps using a constant pixel size (maps 10, 12, 13, 14 and 15 - see Table 2.3). The peaks are at: ~0.85 mag for map 10, ~1.36 mag for map 12, ~1.17 mag for map 13, ~0.72 mag for map 14 and ~0.38 mag for map 15.

3.2.2 Con-res Maps

The one sigma variances for the *con-res maps* 10, 12, 13, 14 and 15 are shown in Figure 3.9. These are calculated in the same 5°× 5° region near the Galactic plane as for the *con-noise maps* (2.5° < b < 7.5°; 221.67° < l < 226.67°). It can be seen from the figure that the noise of the *con-res maps* has a greater width than for the *con-noise maps*, due to the dominance of the covariance term in the calculation of the variance (see Section 2.4.1). Some pixels in the *con-res maps* do not contain any stars, hence no extinction or noise is calculated from them. Multiple peaks in the distribution of uncertainties are seen for maps 12 and 13 in Figure 3.9. These peaks arise as the distribution of uncertainties differs according to the number of stars in the pixel. The majority of pixels only contain 1, 2 or 3 stars in these two maps.

3.3 Column Density and Mass Distributions

This section presents the results of the analysis of the CDDs and mass density distributions. The clouds being compared are those shown in Table 2.6. To allow comparison of the parameters between clouds, a common physical resolution was chosen of 0.1 pc. This is possible since the clouds are all within a kpc, with the exception of the Rosette

Nebula. The physical resolution of 0.1 pc corresponds to the Jeans length of a core with a temperature of 15 K and a density of 5×10^4 cm^{-3}. The analysis of the mass distributions is reported in Section 3.3.3.

In principle there are three ways that the structure parameters of the clouds can be determined at a common scale,

1. Make the extinction maps individually for each cloud at the same spatial resolution (using the known distance of the cloud).

2. Make the extinction maps at a sufficiently high spatial resolution and then rebin the clouds to a common resolution.

3. Calculate the properties of the clouds at several different spatial resolutions and then interpolate the results to derive the parameters at the correct scale.

The first option would be the most ideal solution, but using the method outlined in this thesis, whole sky maps would have to be made for each cloud. This approach would be too laborious. The second option is found to be problematic and the issues are discussed in the following paragraphs. Option 3 was chosen as it allows a comparison at not just one common scale, but the properties at other spatial resolutions can be investigated too.

By using the four *con-res maps*, four spatial resolutions are obtained. In the left panel of Figure 3.10, the variation of the slope of the column density γ_{low} with spatial resolution for the Auriga 1 cloud is shown. At each of the four spatial resolutions the slope is determined four times by using the different sized histogram bins as described in Section 2.7. An example of a histogram for the Auriga 1 cloud is shown in the right panel of Figure 3.10. This shows the log of the number of pixels against A_V.

It can be seen from the left panel in Figure 3.10 that the results using the different sized histogram bins are similar and can be averaged. Similar results were obtained for the other clouds analysed and the plots are shown in Appendix B.1. Most of the clouds do not show any particular dependence of the slope on scale, while about a third (11/30 for the low A_V region, 6/30 for the high A_V region) show a decrease in slope (γ_{low} and γ_{high} respectively) with decreasing resolution.

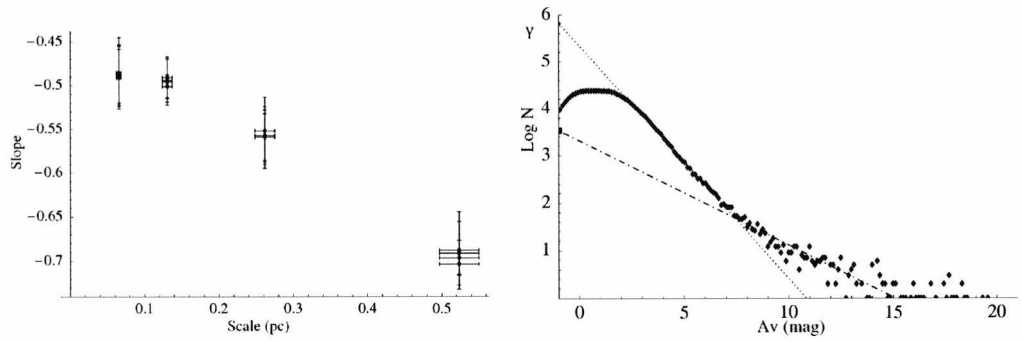

Figure 3.10: Left Panel: A plot showing the measured slopes of the CDD γ_{low} against spatial scale for the Auriga 1 cloud. The four data points at each scale correspond to the four histogram widths used. Right Panel: A histogram showing the log of the number of pixels in each bin against A_V for the Auriga 1 cloud.

Using the cloud Auriga 1 as an example, in both the low A_V and high A_V regions the slope decreases with decreasing resolution. This can interpreted as the cloud having small high extinction cores which are not detected at the larger spatial scales. This is not the case for the majority of clouds. In some cases the slopes either increase with decreasing scale, fluctuate randomly or remain static. These clouds may therefore have a much lower number of small scale high extinction cores.

An appropriate question to ask at this point is whether similar results would be obtained by simply rebinning the highest resolution map to the same resolutions as the other three maps? A comparison of the two methods is shown in Figure 3.11, where the dotted line represents the results by using just the highest resolution map and rebinning it. The general trend of the slopes is preserved, however the individual γ_{low} values differ by up to one sigma from using the four *con-res maps*. The full set of plots for both γ_{low} and γ_{high} values are shown in Appendix B.1. The differences are mostly less than the one sigma uncertainties, but there are some cases where the differences are greater. These are the clouds Chamaeleon II (Figure B.26, left panel), Lupus 2, 6, 7 and 9 (Figures B.33 (left panel), B.37, B.38 (left panel), B.39 (left panel), and B.40), the Rosette Nebula (Figure B.47, left panel) and Scorpius (Figure B.48, left panel).

So the third option was chosen as the method to analyse cloud parameters at the same spatial scale for the reasons discussed in the previous paragraphs. Option two would be unreliable in that the actual results obtained may lie more than one sigma in uncertainty

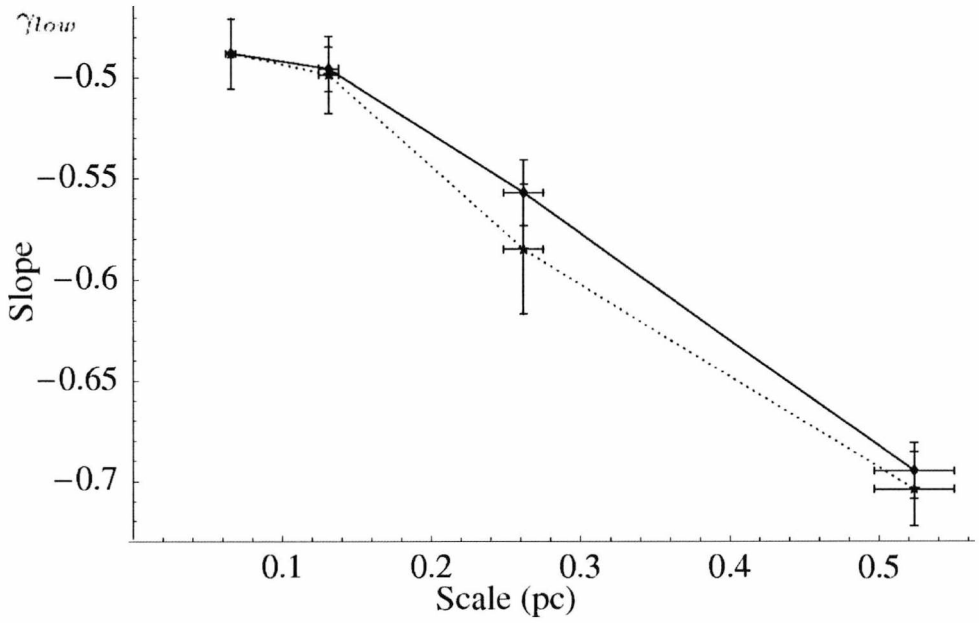

Figure 3.11: Plot showing the variation of slope (γ_{low}) for the Auriga 1 cloud. The solid line connects the points obtained using the *con-res* A_V maps and the dotted line connects the points obtained by rebinning the highest resolution map to obtain the remaining three resolutions.

from the true value. The subsequent analyses are performed using option three.

Analysis was also performed to confirm whether the different slopes measured at different pixel sizes was a real effect or could simply be an effect of rebinning. To do this a sample cloud (Lupus 1 and 2 combined) was compared to a random distribution of the same valued pixels. At the highest resolution (0.5′) no difference was observed, as expected. The randomly distributed image was then rebinned to half resolution (e.g. 1.0′) and compared to the corresponding 'real' cloud at that resolution. It was found that the rebinning process artificially removed higher values resulting in a higher gradient. This is expected as any cores in the 'real cloud' have been lost during the redistribution of pixels. For the next highest resolution of 2.0′ the rebinning process removed all of the pixels in the desired range therefore a gradient could not be measured. Therefore, the slopes measured at the different resolutions are a real effect and not just the result of an artificial rebinning of the data.

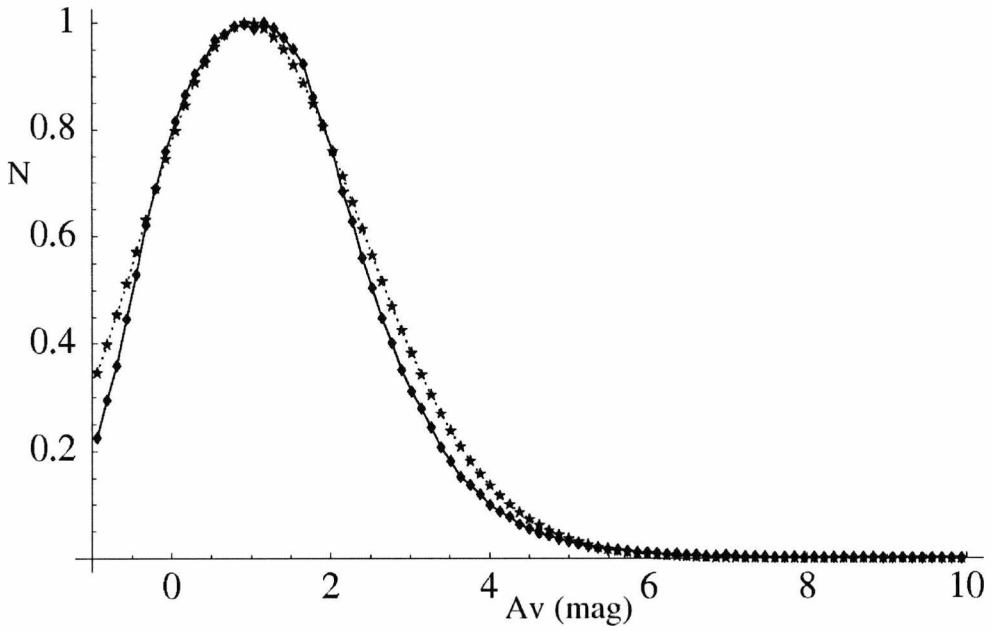

Figure 3.12: Plot of the best log-normal fit (dotted line) to the normalised CDD (solid line) for the Auriga 1 cloud. The fit parameters are interpolated to a spatial scale of 0.1 pc, and the data for the spatial resolution closest to 0.1 pc are shown.

3.3.1 Log-Normal Fits to the Column Density Distribution

The fit parameters for each cloud analysed were obtained using the technique described in Section 2.7.2. The results for an example cloud, Auriga 1, are shown in Table 3.5. These include the spatial resolutions and histogram bin widths used, and also the *rms* values of the fit. It can be seen that there is an apparent trend in the parameters. For example σ, the width of the distribution in Equation 2.14, increases with spatial scale. This can be explained by small scale high extinction cores being undetected at larger spatial scales. Therefore, only the larger scale low extinction cores remain detected which leads to an increase in σ.

The normalised CDD for Auriga 1 is plotted in Figure 3.12. The solid line in the figure shows the data for the spatial resolution closest to 0.1 pc. The dotted line is the fit with parameters interpolated to a spatial scale of 0.1 pc. The plots for all the clouds analysed are shown in Appendix B.1.1. The results for all the clouds, scaled to 0.1 pc, are shown in Table 3.6.

The results from the best (i.e. lowest *rms*) log-normal fits at a spatial scale of 0.1 pc

Table 3.5: Table of fit parameters obtained at various spatial resolutions and histogram bin sizes for the Auriga 1 cloud. Results from the fit of the log-normal distribution (parameters a, A_0, A_1 and σ) are shown together with values for the slopes γ and δ.

Sp. Res. [']	Sp. Res. [pc]	Bin size [mag]	a [mag]	A_0 [mag]	A_1 [mag]	σ [mag]	rms [σ]	γ_{low}	γ_{high}	δ_{low}	δ_{high}
0.5	0.065	0.125	26.2	-24.2	25.0	1.06	6.4	-0.49	-0.22	-0.38	-0.14
0.5	0.065	0.250	26.9	-24.7	25.6	1.06	4.7	-0.49	-0.23	-0.38	-0.14
0.5	0.065	0.500	31.5	-29.2	30.1	1.05	3.4	-0.49	-0.23	-0.38	-0.14
0.5	0.065	1.000	84.6	-80.2	81.0	1.02	2.0	-0.49	-0.22	-0.39	-0.14
1.0	0.131	0.125	11.1	-9.8	10.8	1.12	8.8	-0.50	-0.26	-0.36	-0.13
1.0	0.131	0.250	11.2	-9.8	10.9	1.12	6.5	-0.49	-0.27	-0.36	-0.13
1.0	0.131	0.500	11.5	-10.1	11.5	1.12	4.8	-0.49	-0.26	-0.37	-0.13
1.0	0.131	1.000	13.2	-11.7	12.8	1.11	2.9	-0.49	-0.25	-0.37	-0.13
2.0	0.262	0.125	4.1	-3.2	4.1	1.23	12.2	-0.56	-0.33	-0.36	-0.14
2.0	0.262	0.250	4.1	-3.2	4.2	1.24	9.0	-0.56	-0.32	-0.37	-0.14
2.0	0.262	0.500	4.2	-3.4	4.3	1.23	6.6	-0.56	-0.32	-0.38	-0.14
2.0	0.262	1.000	5.5	-4.1	5.0	1.20	4.2	-0.55	-0.32	-0.39	-0.14
4.0	0.524	0.125	2.2	-1.5	2.3	1.32	16.0	-0.69	-0.45	-0.47	-0.27
4.0	0.524	0.250	2.2	-1.6	2.3	1.32	11.6	-0.69	-0.38	-0.48	-0.27
4.0	0.524	0.500	2.5	-1.8	2.5	1.29	9.3	-0.70	-0.41	-0.48	-0.28
4.0	0.524	1.000	3.4	-2.5	3.3	1.24	4.9	-0.70	-0.39	-0.47	-0.29

Table 3.6: Summary table of the clouds analysed. The parameters a, A_0, A_1 and σ from Equation 2.14 are shown with the *rms* of the fit (in terms of error bars). The parameters γ (CDD) and δ (mass distribution) are also shown.

Name	a [mag]	A_0 [mag]	A_1 [mag]	σ [mag]	*rms* [σ]	γ_{low}	γ_{high}	δ_{low}	δ_{high}
Aquila Rift	5.7	-0.9	6.0	1.35	3.3	-0.23	-0.13	-0.16	-0.12
Auriga 1	15.9	-14.2	15.3	1.10	4.7	-0.48	-0.24	-0.36	-0.13
Auriga 2	5.5	-4.6	5.6	1.14	2.5	-0.71	-0.32	-0.51	-0.21
Cepheus Flare	11.9	-11.1	12.0	1.11	5.4	-0.54	-0.20	-0.42	-0.11
Chamaeleon I	2.1	-1.4	2.3	1.58	1.8	-0.35	-0.17	-0.17	-0.14
Chamaeleon II	2.0	-1.4	2.2	1.52	1.8	-0.34	-0.22	-0.17	-0.15
Chamaeleon III	3.5	-3.0	3.7	1.29	1.4	-0.46	-0.36	-0.30	-0.24
Circinus	9.8	-7.5	9.9	1.17	4.5	-0.36	-0.17	-0.24	-0.16
Corona Australis	2.2	-1.7	2.5	1.46	1.7	-0.40	-0.16	-0.15	-0.16
Cygnus OB7	4.0	-1.3	4.2	1.36	1.1	-0.25	-0.17	-0.24	-0.19
λ Ori	12.8	-12.3	12.9	1.11	4.6	-0.51	-0.34	-0.40	-0.13
Lupus 1	3.8	-3.0	3.9	1.20	2.3	-0.54	-0.21	-0.22	-0.12
Lupus 2	4.4	-3.6	4.4	1.12	1.1	-0.61	-0.24	-0.27	-0.09
Lupus 3	2.0	-0.9	2.1	1.40	1.9	-0.58	-0.23	-0.25	-0.19
Lupus 4	2.8	-1.5	2.8	1.24	2.2	-0.79	-0.18	-0.40	-0.11
Lupus 5	3.3	-1.6	3.4	1.22	2.0	-0.71	-0.54	-0.59	-0.34
Lupus 6	4.6	-2.1	4.6	1.16	0.8	-0.96	-0.70	-0.73	-0.06
Lupus 7	3.5	-1.0	3.6	1.26	1.0	-0.56	-0.35	-0.46	-0.48
Lupus 8	4.9	-1.3	5.0	1.19	1.3	-0.75	-0.58	-0.57	-0.51
Lupus 9	5.4	-3.3	5.4	1.10	1.6	-1.03	-0.45	-0.96	-0.53
Monoceros	5.1	-4.4	5.2	1.18	3.2	-0.42	-0.18	-0.32	-0.12
Musca	8.6	-8.1	8.7	1.14	4.7	-1.04	-0.22	-0.16	-0.24
Ophiuchus	2.1	-1.1	2.3	1.48	5.8	-0.27	-0.11	-0.17	-0.13
Orion A	3.9	-3.0	4.1	1.39	4.2	-0.28	-0.15	-0.18	-0.12
Orion B	6.4	-5.5	6.5	1.23	4.3	-0.39	-0.13	-0.26	-0.11
Perseus	12.9	-12.3	13.0	1.13	3.9	-0.42	-0.22	-0.28	-0.15
Rosette Nebula	5.9	-4.9	6.1	1.34	2.3	-0.20	-0.19	-0.20	-0.15
Scorpius	3.0	-1.8	3.1	1.32	3.0	-0.56	-0.29	-0.31	-0.16
Serpens	12.3	-7.3	12.4	1.13	2.1	-0.32	-0.16	-0.21	-0.14
Taurus	4.5	-3.8	4.6	1.26	3.2	-0.34	-0.15	-0.24	-0.14

give the following statistics. The parameter a, which is associated with the amplitude of the distribution in Equation 2.14, ranges from 2.0 (Chamaeleon II) to 15.9 (Auriga 1) with a mean of 5.8±3.7. Parameter A_0, the offset of the distribution, ranges from −14.2 (Auriga 1) to −0.9 (Aquila Rift and Lupus 3). The mean value is at −4.1±3.4. The parameter A_1 lies between 2.1 (Lupus 3) and 15.3 (Auriga 1) with a mean of 6.0±3.7. The dispersion σ lies between 1.10 (Auriga 1 and Lupus 9) and 1.58 (Chamaeleon I) with a mean of 1.33±0.15.

Table 3.7: Summary table of the clouds analysed. The parameters derived from the mass distribution (M_{1mag}, $A_{V,SF}$, $A_{V,M_\odot}$ and MSF), together with the densities of the low A_V and high A_V regions (ρ_{A_V} and ρ_{SF} respectively).

Name	M_{1mag} [10^3 $M_\odot$]	$A_{V,SF}$ [mag]	$A_{V,M_\odot}$ [mag]	MSF [%]	ρ_{A_V} [$M_\odot \cdot pc^{-3}$]	ρ_{SF} [$M_\odot \cdot pc^{-3}$]
Aquila Rift	154	9.3	41	1.58	24	100
Auriga 1	268	7.4	32	0.19	4.9	99
Auriga 2	12.7	4.9	15	0.33	12	1900
Cepheus Flare	152	6.5	33	0.15	8	550
Chamaeleon I	1.74	1.2	24	31.0	78	12000
Chamaeleon II	1.18	6.7	21	3.81	51	500
Chamaeleon III	1.49	5.7	13	1.31	76	780
Circinus	113	6.8	30	1.36	4.0	42
Corona Australis	1.00	3.7	23	9.60	58	1500
Cygnus OB7	2110	12.0	31	0.07	13	69
λ Ori	122	7.2	28	0.12	6.9	100
Lupus 1	1.27	5.3	23	3.75	26	2100
Lupus 2	0.19	4.2	20	4.71	15	290
Lupus 3	0.93	2.9	16	10.8	18	830
Lupus 4	2.61	3.7	24	2.85	9.2	830
Lupus 5	9.83	5.3	10	0.09	27	220
Lupus 6	40.7	5.6	27	0.01	100	1000
Lupus 7	5.02	11.2	9	0.01	70	10000
Lupus 8	135	5.8	10	0.06	340	590
Lupus 9	32.4	3.3	8	0.22	63	6700
Monoceros	73.9	4.8	35	2.01	1.3	23
Musca	0.31	6.0	13	4.95	4.6	620
Ophiuchus	8.60	8.6	27	0.78	18	3400
Orion A	44.0	5.4	37	5.03	16	330
Orion B	77.9	6.8	38	1.09	7.2	580
Perseus	27.2	5.3	26	2.10	44	2700
Rosette Nebula	248	8.9	34	0.84	1.5	19
Scorpius	4.05	5.6	20	1.28	30	2100
Serpens	46.4	7.7	31	1.28	100	860
Taurus	18.4	4.4	28	4.84	32	6500

The goodness of fit, *rms*, is an indicator of the amount of excess (potentially gravity dominated) material in a cloud. Some of the clouds were well fitted by a function of the form of Equation 2.14. Those fit with an *rms* of less than 3σ were Auriga 2, the Chamaeleon clouds, Corona Australis, Cygnus OB7, the Lupus clouds, the Rosette Nebula and Serpens.

3.3.1.1 Log-Normal Fits to the Column Density Distribution in the Galactic Plane

The CDD results for the central Galactic Plane region for the parameter A_0 (see Equation 2.14) are shown in Figure 3.15. The data are displayed visually for this region by showing the value for each $5^\circ \times 5^\circ$ square as a shade between black and white. The overlaid contours are the 3 mag A_V (outer) and 6 mag A_V (inner) from the nearest 49 star extinction map. This is included to show the position of the central region of the Galaxy. The data for the other parameters is shown in Appendix B.1.2.1.

On inspecting the plots for the parameter a (from Equation 2.14), there are no apparent trends of the value compared with Galactic position (see Appendix B.16) for the 0.5′ map. However, the remaining three maps do show a slight increase in the value of parameter a around the Galactic centre. The values of a range from 3.3 to 12.6 (0.5′) and from ~1.3 (all) to 9.9 (4.0′). The mean values are 6.9 (0.5′), 4.7 (1.0′), 3.9 (2.0′) and 3.9 (4.0′). These values for a compare with a mean of 5.9±3.8 for the 30 selected clouds. The plots for the parameter A_0 (see Figure 3.13 or Appendix B.17) show a trend of higher values in the denser region around the Galactic centre. The values of A_0 range from −8.3 (4.0′) and −12.6 (0.5′) to −1.0 for all pixel sizes. The mean value range from −1.8 (4.0′) to −4.6 (0.5′). These values compare to a mean of −4.4±3.8 for the 30 sample clouds.

For the parameter A_1 the values around the Galactic centre appear generally higher than those away from the centre (see Appendix B.18). The values range from 1.4 (4.0′) and 3.7 (0.5′) to 8.7 (2.0′) and 12.7 (0.5′). The mean values range from 3.9 (4.0′) to 7.2 (0.5′), compared to 6.0±3.7 for the 30 selected clouds. The plots for the dispersion parameter σ (see Appendix B.19) the value are higher around the Galactic centre. Here, the values range from ~1.1 (all) to 1.7 (all). The mean values of σ are ~1.4 (all), compared to 1.25±0.13 for the 30 selected clouds.

The values of the *rms* of the fit range from 1.0 (4.0′) and 3.0 (0.5′) to 9.3 (4.0′) and 40.0 (0.5′). These values show a clear trend with Galactic position (see Appendix B.20) - the value of *rms* are higher in the Galactic centre. This can be understood by the increased likelihood of multiple clouds along the line-of-sight towards the Galactic centre hence the goodness of fit is lower. The mean values of *rms* range from 4.2 (4.0′)

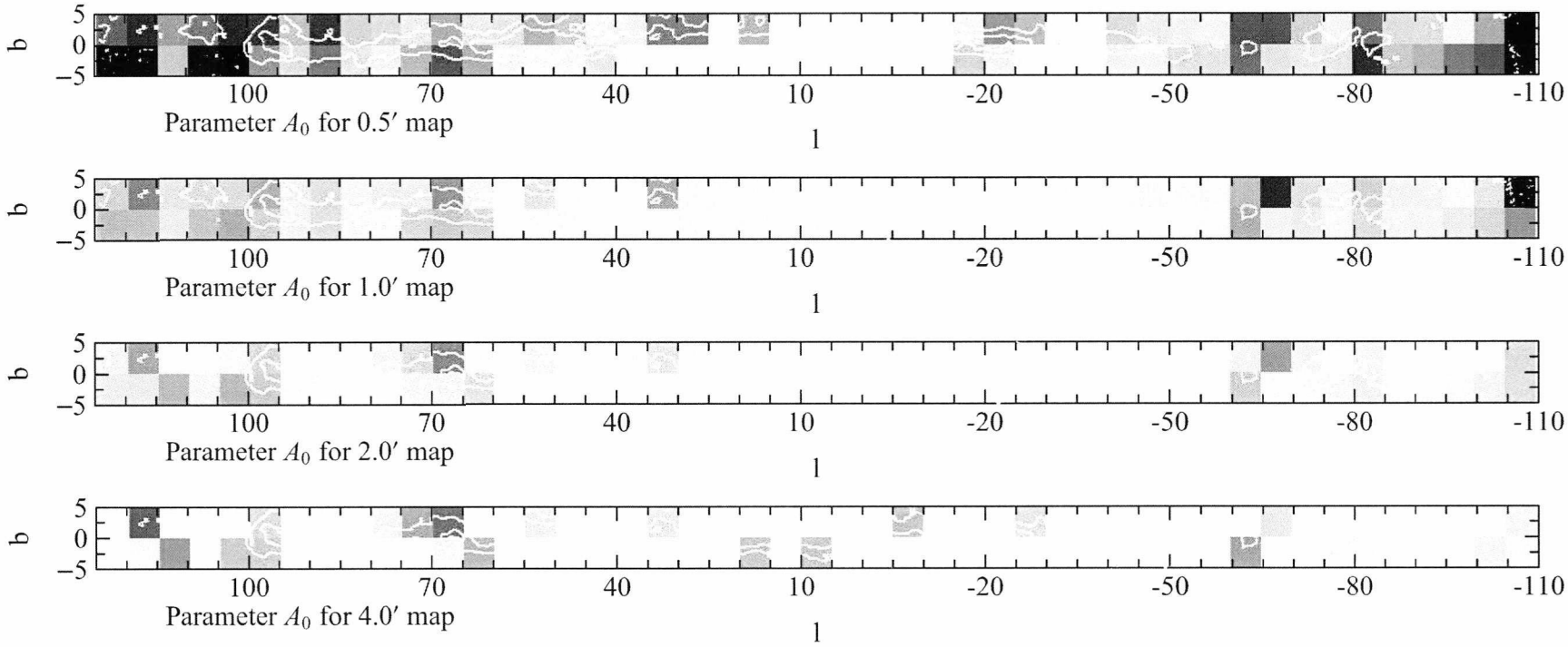

Figure 3.13: Visual representation of the fit parameter A_0 obtained in the central Galactic plane. Results for the *con-res maps* with pixel sizes of 0.5′, 1.0′, 2.0′ and 4.0′ are shown. The data are scaled linearly from -13 (black) to 0 (white). The overlaid contours are the 3 mag A_V (outer) and 6 mag A_V (inner) from the nearest 49 star extinction map.

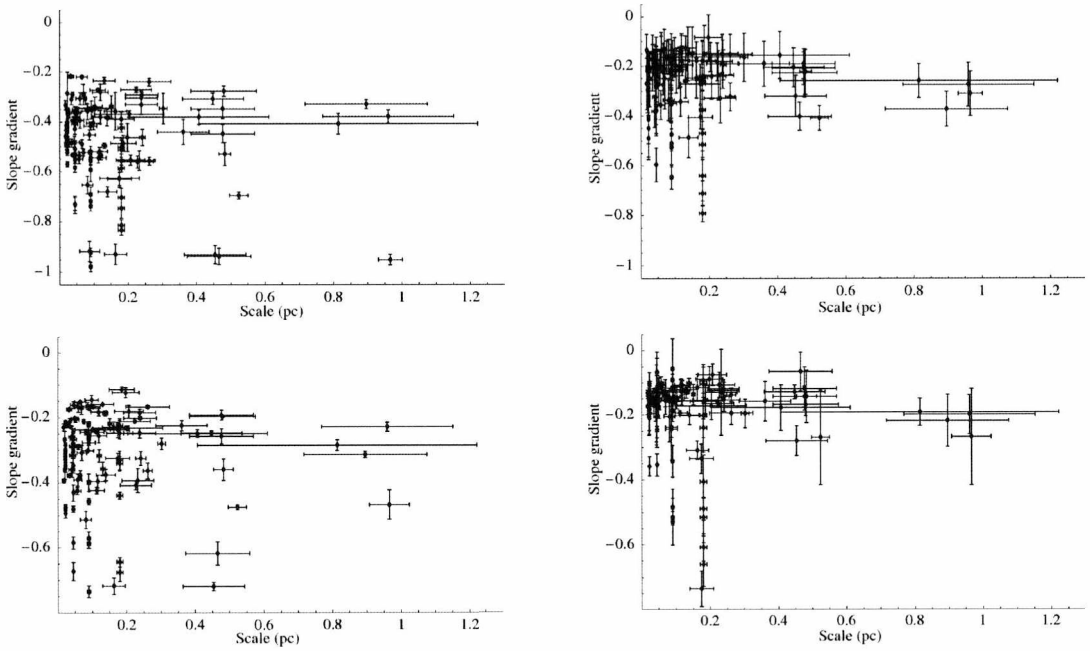

Figure 3.14: **Top Left:** The slope gradients of the column density distribution, γ_{low}, plotted against scale for the sample clouds. **Top Right:** As Top Left but for slope gradients γ_{high}. **Bottom Left:** The slope gradients of the mass distribution, δ_{low}, plotted against scale for the clouds analysed. **Bottom Right:** As Bottom Left but for the slope gradients δ_{high}.

to 14.5 (0.5′), compared to 2.9±1.6 for the 30 sample clouds.

3.3.2 $\log(N)$ vs A_V Column Density Distribution

The CDD gradients γ were calculated as described in Section 2.7.1. As shown in Figure 2.7 (again using the Auriga 1 cloud as an example), there are two distinct regions over which the gradients are obtained, nominally a low A_V range and a high A_V range. The gradients obtained from these ranges are denoted γ_{low} and γ_{high}, respectively. Turbulence in the cloud dominates in the low A_V region and gravity becomes predominant in the high A_V region. The figures for each of the clouds analysed are shown in Appendix B.1.3. In addition to the figures shown in Appendix B.1.3, the data are plotted together in the top panels of Figure 3.14.

The values of the slopes γ_{low} and γ_{high} for each cloud are shown in Table 3.6. The values of γ_{low} range from −1.04 (Musca) to −0.20 (Rosette Nebula) with a mean of −0.51±0.23, while the values of γ_{high} range from −0.70 (Lupus 6) to −0.11 (Ophi-

uchus) with a mean of −0.26±0.14. Generally the values of γ_{low} are double those of γ_{high}. The scatter of values for the high A_V region is much less than the scatter of values for the low A_V region, which is clearly evident in Figure 3.14. This is a strong indication that gravity influences the column density distribution at higher A_V and star formation is commencing. The differences in CDD between the high A_V regions of clouds become lesser as they undergo gravitational collapse. Much larger differences are seen at lower column densities, due to external factors such as the environment of the cloud, or the type of forcing of the turbulence.

It can be seen from Figure 3.14 that there are two distinct groups in the data at low A_V values. These groups may be described as star forming (SF; forming stars in clusters) and non-star forming (non-SF; forming only isolated stars) clouds, as will be described in Section 4.2. The following statistics are found for the two groups. For the SF group, with shallower gradients, the values of γ_{low} range from −0.42 (Perseus) to −0.20 (Rosette Nebula) with a mean of −0.32±0.07. For the non-SF group γ_{low} ranges from −1.04 (Musca) to −0.42 (Monoceros), with a mean of −0.66±0.20. For the SF group the γ_{high} values range from −0.28 (Perseus) to −0.11 (Ophiuchus) with a mean of −0.16±0.03. The non-SF group's values range from −0.70 (Lupus 6) to −0.22 (Musca) with a mean of −0.33±0.15.

3.3.2.1 log(N) vs A_V Column Density Distribution in the Galactic plane

The data are displayed for the Galactic plane region by showing the value for each 5° × 5° square as a shade between black and white. The overlaid contours are the 3 mag A_V (outer) and 6 mag A_V (inner) from the nearest 49 stars A_V map. This is included to show the position of the central region of the Galaxy. The data for the *con-res map* with a pixel size of 0.5′ at the Galactic Plane is shown in Figure 3.15. The data for the other *con-res maps* are shown in Appendix B.1.4.

The plots of γ_{low} for the Galactic Plane show shallower slopes in the higher extinction area around the Galactic centre (see Appendix B.51). The values of γ_{low} range from −0.65 (4.0′) and −0.33 (0.5′) to −0.01 (0.5′) and 7.3 (4.0′ - likely to result from a poor fit). The median values (chosen to eliminate the poor fits) range from −0.14 (2.0′ and 4.0′) to −0.16

Figure 3.15: Visual representation of the slopes γ_{low} and γ_{high} obtained in the central Galactic plane for the 0.5′ *con-res map*. The gradients are scaled linearly from −0.5 (black) to 0.0 (white). The overlaid contours are the 3 mag A_V (outer) and 6 mag A_V (inner) from the nearest 49 star extinction map.

(1.0′ and 0.5′).

These values compare with a mean of −0.51±0.23 for the 30 sample clouds. The same trend is observed for the values of γ_{high} (see Appendix B.52). Here, the values range from −1.5 (4.0′) and −0.26 (0.5′) to −0.07 (2.0′, 1.0′ and 0.5′) to 0.05 (4.0′). The median values (again used to eliminate bad fits) range from −0.27 (4.0′) to −0.17 (0.5′), compared to a mean of −0.26±0.14 for the 30 selected clouds.

3.3.3 $\log(N)$ vs A_V Mass Distribution

The mass distribution gradients were calculated as described in Section 2.7.3. An example is shown for the Auriga 1 cloud in Figure 2.8. The mass distribution slopes δ_{low} and δ_{high}, for the low A_V and high A_V regions respectively, are overplotted. The values of these slopes are shown in Table 3.5.

The mass distribution slopes for our sample clouds are shown in Table 3.6. The data are plotted together in the bottom panels of Figure 3.14. The individual plots for each cloud are shown in Appendix B.2. The data show similar scatter behaviour as for the column density distributions. For the slopes δ_{low} the values range from −0.96 (Lupus 9) to -0.15 (Corona Australis) with a mean of −0.33±0.19. The δ_{high} values range from −0.53 (Lupus 9) to −0.06 (Lupus 6) with a mean of −0.19±0.12. As before, the low A_V regions show a larger scatter than the high A_V regions.

Treating the SF and non-SF groups separately again, the values of δ_{low} for the SF group lie between −0.28 (Perseus) and −0.15 (Corona Australis) with a mean of −0.21±0.04. For the non-SF group the values lie between −0.96 (Lupus 9) and −0.16 (Musca) with a mean of −0.43±0.20. The values of δ_{high} for the SF group range from −0.19 (Cygnus OB7) to −0.06 (Lupus 6) with an average of −0.14±0.02. For the non-SF group the δ_{high} values range from −0.53 (Lupus 9) to −0.06 (Lupus 6) with an average of −0.22±0.15.

The total mass of each cloud (above 1 A_V, denoted M_{1mag}) is calculated by extrapolating the fit of the low A_V regions to 1 mag A_V. For the majority of the clouds 1 mag A_V corresponds to the background extinction (as the clouds are mostly distributed along the

Galactic plane). This means that data from the noisy background (below 1 mag A_V) is excluded from the calculation and that the integration is performed only for material above the threshold for self-shielding from UV radiation (e.g. Hartmann et al. (2001)). The values of M_{1mag} range from $0.31 \cdot 10^3 M_\odot$ (for the Musca cloud) to $2110 \cdot 10^3 M_\odot$ (Cygnus OB7). The median value is $23\pm22 \cdot 10^3 M_\odot$ (using the median absolute deviation for the uncertainty, and thereafter in this section). When considering the two groups (SF and non-SF) separately, the median value for the SF group is $42\pm40 \cdot 10^3 M_\odot$ and for the non-SF group the median value is $9.8\pm9.5 \cdot 10^3 M_\odot$.

The extinction value of a 1 $M_\odot$ core with the Jeans Mass (denoted $A_{V,M_\odot}$ in Table 3.7) can be found by extrapolating the fit of the high A_V region to one solar mass. This value characterises the maximum extinction in the cloud before commencement of the collapse of material to begin star formation. The values of $A_{V,M_\odot}$ range from 8 mag A_V (Lupus 9) to 41 mag A_V (Aquila Rift). The median value for $A_{V,M_\odot}$ is 25±6.5 mag A_V. Considering the SF and non-SF groups separately, the median value for the SF group is 30±4 mag A_V while the median for the non-SF group is 20±7 mag A_V.

A threshold extinction value can be determined for each cloud, which indicates whether material is likely to be involved in star formation (higher A_V), or in the turbulent mass of the cloud (lower A_V). This is found by determining the intercept between the low A_V and high A_V fits of the mass distribution. This can be understood as the star formation threshold $A_{V,SF}$ of the cloud. The values of $A_{V,SF}$ range from 1.2 mag A_V (Chamaeleon I) to 12.0 mag A_V (Cygnus OB7). The median value of $A_{V,SF}$ is 5.6±1.2 mag A_V. For the two groups the median value for the SF group is 6.7±1.8 mag A_V, while the median value for the non-SF group is 5.6±0.8 mag A_V.

The ratio of the mass above $A_{V,SF}$ to the ratio of the mass below the threshold (but above 1 mag A_V) is also determined. If it is assumed that 1/3 of the mass above the threshold is used in the star formation process (Alves et al., 2007), then the mass fraction involved in star formation for the cloud, MSF, can be measured. The values of MSF lie between 0.01% (for Lupus 6 and 7) and 31.0% (Chamaeleon I), with a median of 1.34±1.30%. When considering the SF and non-SF clouds separately, the median

value for the SF group is 2.10±1.71%, while the median value for the non-SF group is 0.33±0.32%.

3.3.3.1 Molecular Cloud Density

The densities of the 30 sample clouds were calculated, both for the whole cloud and for the region associated with star formation, using the method described in Section 2.7.3.1. These are denoted as ρ_{A_V} and ρ_{SF} respectively in Table 3.7. In this section the median and median absolute deviations are quoted to mitigate for the effect of the large outlying values (especially in the high A_V regime). The overall densities for the clouds ρ_{A_V} range from 1.3 $M_\odot \cdot pc^{-3}$ (for Monoceros) to 340 $M_\odot \cdot pc^{-3}$ (in Lupus 8), with a median of 21±15 $M_\odot \cdot pc^{-3}$. For the regions associated with star formation, the values of ρ_{SF} range from 23 $M_\odot \cdot pc^{-3}$ (for Monoceros) to 10000 $M_\odot \cdot pc^{-3}$ (for Lupus 7). The median value for ρ_{SF} is 700±600 $M_\odot \cdot pc^{-3}$.

When treating the SF and non-SF groups separately, the values of ρ_{A_V} for the SF group are found to range from 1.5 $M_\odot \cdot pc^{-3}$ (the Rosette Nebula) to 100 $M_\odot \cdot pc^{-3}$ (for Serpens), with a median value of 24±20 $M_\odot \cdot pc^{-3}$. The values for the non-SF group lie between 1.3 $M_\odot \cdot pc^{-3}$ (for Monoceros) and 340 $M_\odot \cdot pc^{-3}$ (for Lupus 8), with a median value of 18±13 $M_\odot \cdot pc^{-3}$ - slightly higher than for the SF group. For ρ_{SF}, the values of the SF group range from 19 $M_\odot \cdot pc^{-3}$ (for the Rosette Nebula) to 12000 $M_\odot \cdot pc^{-3}$ (for Chamaeleon I). The median value for ρ_{SF} is 580±530 $M_\odot \cdot pc^{-3}$. For the non-SF group the value of ρ_{SF} lie between 23 $M_\odot \cdot pc^{-3}$ (for Monoceros) and 10000 $M_\odot \cdot pc^{-3}$ (for Lupus 7). The median value of ρ_{SF} for the non-SF group is 780±560 $M_\odot \cdot pc^{-3}$, lower than for the SF group.

3.4 Structure Functions

Using the method described in Section 2.8.1, the parameters in Equation 2.19 were derived for the 30 molecular clouds analysed in this thesis. The results are shown in Table 3.8. Note that no fits with an RMS of less than 0.1 were obtained for the Lupus 9 and

Rosette Nebula clouds. The best available data were therefore used for the plots for these clouds. An example plot for the Auriga 1 cloud is shown in Figure 3.16. The red line in the plot shows the best fit and is shown alongside the model data postulated by K41, SL94 and B02. The plot also shows the difference of the fit from the data against the values of the order p. The plots for all of the 30 sample clouds are shown in Appendix C.1.1.

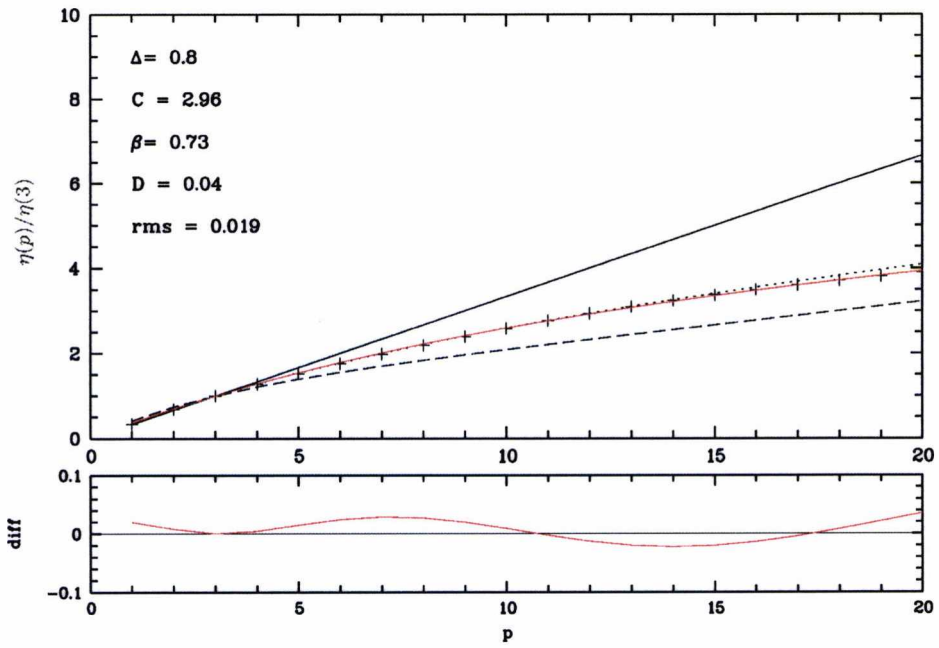

Figure 3.16: The structure function plot for the Auriga 1 cloud. Our data (red line) are compared against the models of K41 (solid line), SL94 (dotted line) and B02 (dashed line). The best fit values of Δ, C, β, D and the RMS value are shown. A plot of the difference of the fit from the data against p is also displayed.

Starting with the parameter Δ, the values lie in the range 0.45 (Auriga 2) to 1.05 (Musca) with a mean of 0.83±0.14. This value lies roughly halfway between the figure of Δ=2/3 quoted in the literature (e.g. (Padoan et al., 2003)), and Δ = 1 (e.g. (Schmidt et al., 2008)). The codimension C lies between 1.18 (Auriga 2) and 2.43 (Scorpius) with a mean of 1.91±0.33. The values of β (the degree of non-intermittency) range from 0.38 (Circinus) to 0.65 (Lupus 2) with a mean of 0.53±0.08. The literature quotes a values for β of either 2/3 (SL94) or 1/3 (B02). The values of the fractal dimension D lie between 0.59 (Scorpius) and 1.82 (Auriga 2), with a mean of 1.08±0.37. A value of D = 1 corresponds to a thin, filamentary structure for the cloud while D = 2 corresponds to a flat, sheetlike

structure.

Now the two groups identified from Figure 3.14 are considered separately. For the SF group, the mean value of Δ is 0.83±0.11, identical to the figure for all 30 selected clouds. The mean of C is 1.81±0.33, slightly lower than the value for the whole group, but easily within 1σ. For the parameter β, the mean is 0.51±0.10, similar to the value for all the clouds. The mean of D is 1.19±0.33, higher than the mean for all clouds but within 1σ.

For the non-SF group, the mean value of Δ is 0.83±0.16, again identical to the value for all 30 sample clouds. For the codimension C the mean is 1.98±0.33, higher then the value for the whole ensemble. For β the mean is 0.56±0.08 and for D the mean is 1.02±0.33, lower than the mean for all clouds together but again within 1σ.

The values quoted in Figure 3.4 were generated using structure functions which only used data in the low A_V ranges (i.e. with A_V values between the self-shielding threshold and the star formation threshold - see Section 2.7.1). These low A_V regions are dominated by turbulence. However, there are many different ways of making the structure functions for each map. These include for example using our *con-res maps* with a variation of Equation 2.17 to include a weighting as discussed in Section 2.8.1.1. For example, the pixels with lower noise were given a higher weighting. In addition the weighting could be varied to favour different *regions* of each map (i.e. different ranges of A_V). One could also take cuts of each map using only pixels with a value greater than the self-shielding threshold of 1 mag A_V.

Using the methods outlined in Section 2.8.1.1 a total of 51 different ways of deriving a structure function for each map were tried. Using 16 different clouds gives a total of 816 different structure function plots. Fitting of the structure functions against the models of K41, SL94 and B02 was attempted. Out of the 816 plots, only 30 fitted to any of the models with an RMS of the fit less than 0.1. Of the fits, 48% fitted to the B02 model, 23% to the K41 model and the remaining 29% to the SL94 model. There was no discernible trend in the fitted models when correlating to the method used to derive the structure functions. Therefore, only the *con-noise maps* were used for the structure function analysis.

Table 3.8: The structure function fitting parameters Δ, C, β and D for the 30 sample clouds, together with the standard deviations and *rms* of the fit. The scaling exponents $\eta(2)$ and $\eta(3)$ are also given.

Name	Δ	σ_Δ	C	σ_C	β	σ_β	D	σ_D	RMS	σ_{RMS}	$\eta(2)$	$\eta(3)$
Aquila Rift	0.96	0.06	2.03	0.40	0.52	0.07	0.97	0.40	0.04	0.01	0.448	0.608
Auriga 1	0.77	0.07	2.05	0.55	0.59	0.13	0.95	0.55	0.05	0.01	1.149	1.664
Auriga 2	0.45	0.20	1.18	0.63	0.57	0.14	1.82	0.63	0.04	0.01	0.701	0.989
Cepheus Flare	0.58	0.25	1.97	0.63	0.69	0.11	1.03	0.63	0.04	0.01	0.991	1.455
Chamaeleon 1	0.74	0.24	2.01	0.52	0.63	0.10	0.99	0.52	0.04	0.01	1.081	1.527
Chamaeleon 2	0.93	0.09	1.88	0.43	0.49	0.09	1.12	0.43	0.05	0.02	0.671	0.927
Chamaeleon 3	0.91	0.06	2.12	0.54	0.54	0.13	0.88	0.54	0.05	0.02	0.456	0.653
Circinus	1.01	0.07	1.67	0.38	0.38	0.10	1.33	0.38	0.06	0.02	0.329	0.436
Corona Australis	0.88	0.07	2.28	0.45	0.60	0.08	0.72	0.45	0.04	0.02	0.658	0.929
Cygnus OB7	0.77	0.14	1.31	0.45	0.37	0.20	1.69	0.45	0.06	0.02	0.596	0.816
λ Ori	0.90	0.11	2.05	0.47	0.54	0.13	0.95	0.47	0.05	0.02	0.651	0.923
Lupus 1	0.69	0.17	1.36	0.57	0.43	0.28	1.64	0.57	0.06	0.02	0.421	0.595
Lupus 2	0.30	2.28	0.41	0.71	0.13	0.72	0.41	0.05	0.03	0.64	0.102	0.161
Lupus 3	0.96	0.07	2.00	0.40	0.51	0.07	1.00	0.40	0.04	0.01	0.735	1.001
Lupus 4	0.84	0.10	2.20	0.44	0.61	0.06	0.80	0.44	0.04	0.01	0.291	0.411
Lupus 5	0.78	0.22	2.16	0.47	0.62	0.15	0.84	0.47	0.05	0.01	0.573	0.816
Lupus 6	0.92	0.07	2.05	0.53	0.53	0.10	0.95	0.53	0.05	0.02	0.315	0.406
Lupus 7	0.88	0.09	1.62	0.35	0.44	0.09	1.38	0.35	0.05	0.02	0.213	0.290
Lupus 8	0.95	0.13	2.05	0.47	0.52	0.11	0.95	0.47	0.05	0.02	0.485	0.679
Lupus 9	-	-	-	-	-	-	-	-	-	-	0.265	0.460
Monoceros	0.93	0.06	1.97	0.45	0.51	0.09	1.03	0.45	0.05	0.01	1.061	1.429
Musca	1.05	0.09	2.23	0.41	0.51	0.11	0.77	0.41	0.06	0.02	0.155	0.212
Ophiuchus	0.74	0.11	1.69	0.54	0.54	0.11	1.31	0.54	0.05	0.02	1.312	1.894
Orion A	0.67	0.28	1.20	0.54	0.40	0.21	1.80	0.54	0.06	0.02	1.128	1.559
Orion B	0.83	0.09	2.05	0.58	0.57	0.11	0.95	0.58	0.05	0.02	1.329	1.911
Perseus	0.74	0.14	1.87	0.62	0.58	0.11	1.13	0.62	0.04	0.01	1.305	1.876
Rosette Nebula	-	-	-	-	-	-	-	-	-	-	-0.15	0.035
Scorpius	0.98	0.10	2.43	0.39	0.59	0.04	0.57	0.39	0.04	0.02	0.866	1.233
Serpens	0.95	0.07	1.63	0.38	0.40	0.10	1.37	0.38	0.06	0.02	0.171	0.216
Taurus	0.75	0.25	2.14	0.55	0.65	0.09	0.86	0.55	0.04	0.01	0.979	1.413

3.4.1 Structure Functions in the Galactic Plane Region

The structure function parameters Δ, C, β and D were derived for the Galactic plane area (described in Section 2.6) using the same method as for our 30 sample clouds. The average *rms* deviation for each fit is also shown (only fits with an *rms* of less than 0.1 were used). The results are shown in Figure 3.17. The data are displayed visually for the region by showing the value for each $5° \times 5°$ square as a shade between black and white. The overlaid contours are the 3 mag A_V (outer) and 6 mag A_V (inner) from the nearest 49

stars extinction map. This is included to show the position of the central bulge of the Galaxy. The full results including the standard deviations are shown in Appendix C.1.2.

The plots for the parameter Δ show higher values around the Galactic centre (see Appendix C.16). The values of Δ range from 0.07 to 1.03 with a mean of 0.66. This compares to 0.83±0.14 for the 30 sample clouds. The values for codimension C range from 0.76 to 2.46 with a mean of 1.51, compared to 1.91±0.33 for the 30 sample clouds. The plots show do not show a clear trend when comparing values to position. The values of β range from 0.09 to 0.97 with a mean of 0.48. These compare to mean value of 0.54±0.09 for the 30 selected clouds. Again, there is no obvious trend in this parameter with Galactic position (see Appendix C.17).

The values of fractal dimension D appear to have higher values around the Galactic centre. The values lie between 0.54 and 2.24 with a mean of 1.49. These values compare to a mean of 1.09±0.33 for the 30 sample clouds. Finally, the *rms* values of the fit do not show any trend compared to the position around the Galactic Plane. The values of *rms* range from 0.03 to 0.10 (only fits with an *rms* of better than 0.1 were selected). The mean value is 0.06 which compares to 0.05±0.01 for the 30 selected clouds. Therefore, the quality of fits is marginally better for the 30 selected clouds.

3.4.2 The effect of Gaussian-Distributed Noise on Structure Functions

An important consideration is to determine the effect of noise in an image when calculating structure functions. With real data the noise is intrinsic and cannot be completely removed from the image. To investigate the effect of noise, a test image was created as a rough analogy of a molecular cloud. The test image consists of a sample grid of 400×400 pixels containing simply a circle of radius 124 pixels, where the values of the pixels in the circle ranged (arbitrarily) from 0.81 (edge) to 10.0 (centre). The remaining pixels in the grid were set to zero. The test image is shown in Figure 3.18.

Performing structure function analysis on this test grid gave a fit to the Kolmogorov model (i.e. with $\Delta = 0$). The test grid was also rebinned three times, each to one half

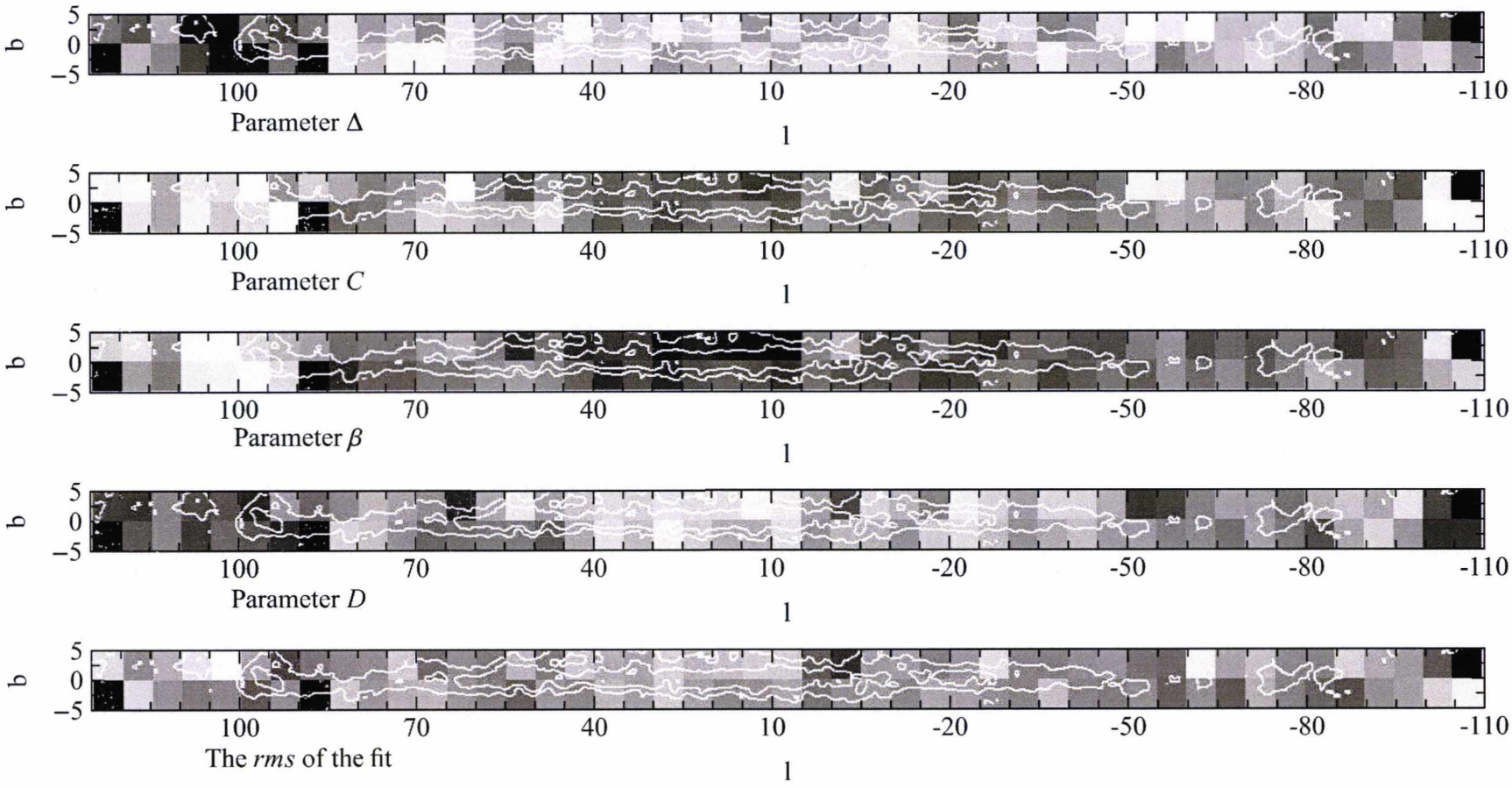

Figure 3.17: Visual representation of the fit parameters for structure functions obtained in the central Galactic plane. The overlaid contours are the 3 mag A_V (outer) and 6 mag A_V (inner) from the nearest 49 star extinction map. The data is scaled linearly from black to white as follow: Δ 0.0 to 1.0, C 0.0 to 2.5, β 0.0 to 1.0, D 0.0 to 2.5, *rms* 0.0 to 0.1.

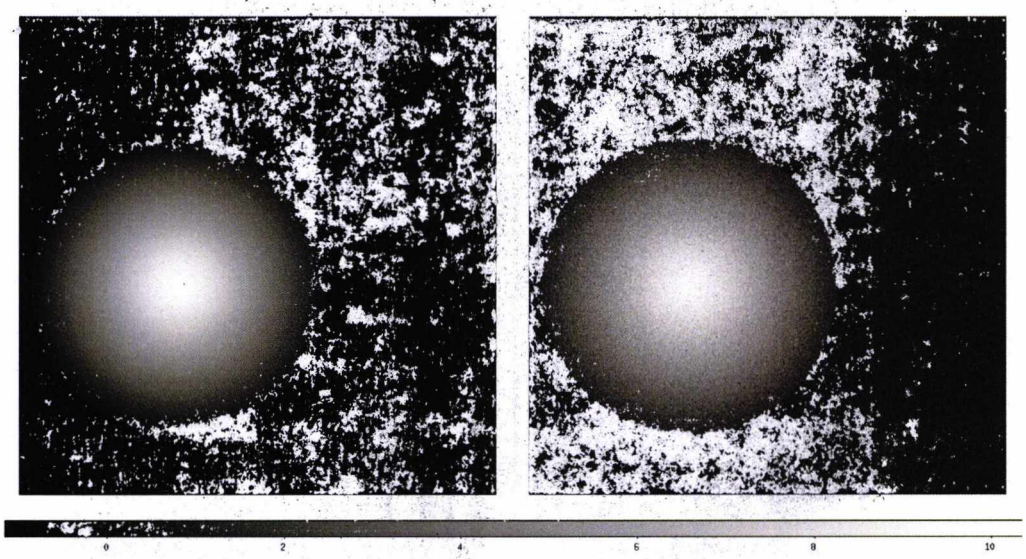

Figure 3.18: The test image used to examine the effect of adding noise on the resulting structure function. Left: the original image without noise, Right: the original image with 1σ Gaussian noise added. Note the lesser quality in the second image.

the resolution of the previous grid, to make grids of 200 × 200, 100 × 100 and 50 × 50 (see Figure 3.19). Structure function analysis on the first two of these grids yielded fits that did not conform to any known model but were approximate to the She-Leveque and Boldyrev models. The final grid of 50 × 50 gave a fit approximate to the Kolmogorov model. Note that even without adding noise, the mere effect of rebinning has caused the second two fits to deviate away from the fit obtained using the original image.

The exercise was repeated using the four test images (original and three rebinned) by adding progressive amounts of Gaussian noise to each image. The results shown in Table 3.9 use the first 100 fits (where available) with an *RMS* of less than 0.1. The table shows the mean value of the parameters Δ, C, β and D for these fits. There is no obvious trend in any of the parameters when the amount of noise is increased, when the uncertainties are taken into account.

In an additional test, 1σ Gaussian noise was added to the original 400 × 400 test image and then further increments of noise were added (in amounts of $1/16\sigma$). In this instance the test image more closely resembles an observed molecular cloud, due to the inherent noise of 1σ. The results are shown in Table 3.10. Adding noise tends to decrease the value of Δ. There are no obvious trends with other parameters when taking the uncertainties into

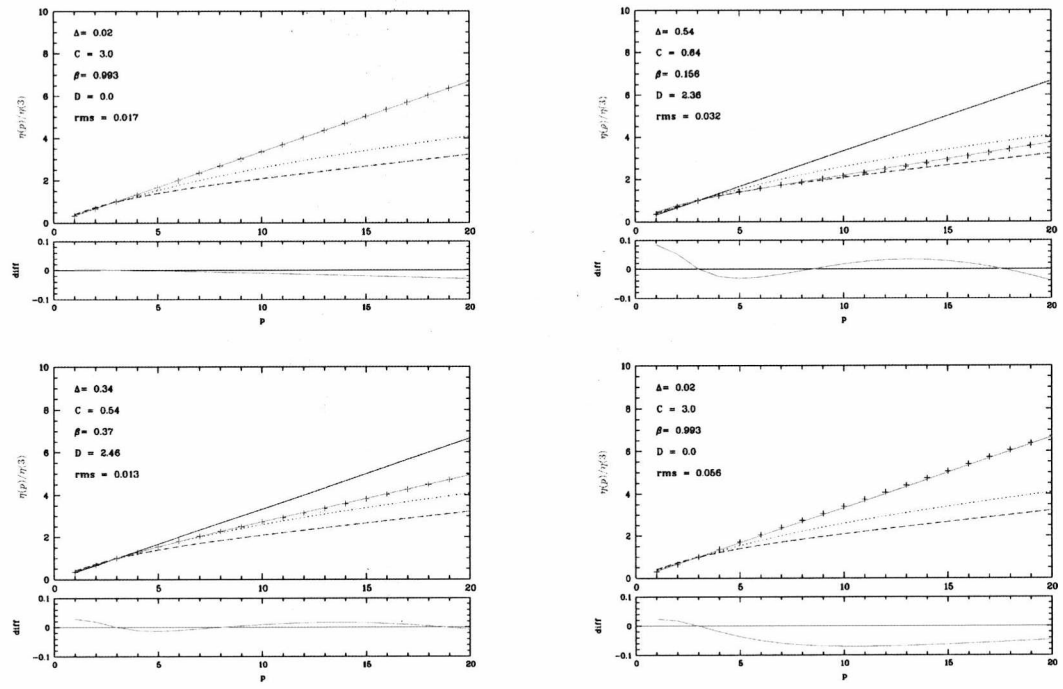

Figure 3.19: **First Panel:** Plot of $\eta(p)/\eta(3)$ against p for a 400 × 400 test grid (solid red line). Also shown are three theoretical models: Kolmogorov (solid black line), She-Leveque (dotted line) and Boldyrev (dashed line). **Second Panel:** As first panel but with a 200 × 200 test grid. **Third Panel:** As first panel but with a 100 × 100 test grid. **Fourth Panel:** As first panel but with a 50 × 50 test grid.

account.

In addition to adding noise to a test cloud, Gaussian noise was also added to a selection of real molecular clouds (as described in Section 3.4.2). The results are shown in Table 3.11. For the parameter Δ there is no obvious trend when the noise increases; the value increases in some cases and decreases in others. The value of the codimension C, however, tends to increase with noise in all cases. This is reflected in a consistent decrease of the fractal dimension D with increasing noise. The degree of non-intermittency parameter β tends to increase with increasing noise, probably due to the dependence of β on Δ and C. However, any apparent trends are within the bounds of the uncertainties so can be disregarded as they are not significant.

Table 3.9: Table of results when adding Gaussian noise to a test image. The size of the test image and amount of noise added is shown in the left column with the grid width/height in pixels. The values of the parameters Δ, C, β and D are shown with the respective uncertainties. The RMS and standard deviation of the RMS are also shown.

Type	Δ	σ_Δ	C	σ_C	β	σ_β	D	σ_D	RMS	σ_{RMS}
No noise, 400	0.02	0.01	2.03	0.58	0.99	0.01	0.97	0.58	0.01	0.01
No noise, 200	0.58	0.04	0.81	0.23	0.23	0.28	2.19	0.23	0.07	0.02
No noise, 100	0.40	0.06	0.86	0.37	0.48	0.15	2.14	0.37	0.05	0.02
No noise, 50	0.22	0.04	1.93	0.72	0.87	0.04	1.07	0.72	0.01	0.01
$1/16\sigma$, 400	0.65	0.07	1.92	0.52	0.65	0.06	1.08	0.52	0.03	0.01
$1/16\sigma$, 200	0.63	0.06	1.32	0.37	0.50	0.09	1.68	0.37	0.05	0.01
$1/16\sigma$, 100	0.42	0.06	0.92	0.40	0.50	0.15	2.08	0.40	0.05	0.01
$1/16\sigma$, 50	0.23	0.04	1.94	0.72	0.87	0.04	1.06	0.72	0.01	0.01
$1/8\sigma$, 400	0.65	0.07	1.92	0.52	0.65	0.06	1.08	0.52	0.03	0.01
$1/8\sigma$, 200	0.67	0.07	1.91	0.52	0.64	0.06	1.09	0.52	0.03	0.01
$1/8\sigma$, 100	0.43	0.06	1.10	0.45	0.57	0.12	1.90	0.45	0.04	0.01
$1/8\sigma$, 50	0.25	0.05	1.77	0.75	0.84	0.06	1.23	0.75	0.01	0.01
$3/16\sigma$, 400	0.32	0.06	1.74	0.71	0.80	0.06	1.26	0.71	0.07	0.01
$3/16\sigma$, 200	0.71	0.06	2.19	0.48	0.67	0.05	0.81	0.48	0.03	0.01
$3/16\sigma$, 100	0.45	0.07	1.26	0.51	0.61	0.10	1.74	0.51	0.03	0.01
$3/16\sigma$, 50	0.25	0.04	2.01	0.69	0.86	0.04	0.99	0.69	0.01	0.01
$1/4\sigma$, 400	-	-	-	-	-	-	-	-	-	-
$1/4\sigma$, 200	0.62	0.07	1.82	0.53	0.64	0.07	1.18	0.53	0.03	0.01
$1/4\sigma$, 100	0.47	0.07	1.39	0.53	0.63	0.09	1.61	0.53	0.03	0.01
$1/4\sigma$, 50	0.23	0.05	1.73	0.75	0.85	0.05	1.27	0.75	0.01	0.01

Table 3.10: Table of results when adding noise to a test image. The amount of noise in the test image is shown in the left column. The values of the parameters Δ, C, β and D are shown with the respective uncertainties. The RMS and it's standard deviation are also shown.

Type	Δ	σ_Δ	C	σ_C	β	σ_β	D	σ_D	RMS	σ_{RMS}
Test Cloud (1 σ)	0.50	0.06	1.18	0.41	0.55	0.11	1.82	0.41	0.04	0.01
With $1/16\sigma$	0.50	0.06	1.21	0.42	0.55	0.10	1.79	0.42	0.04	0.01
With $1/8\sigma$	0.48	0.06	1.09	0.40	0.53	0.12	1.91	0.40	0.05	0.01
With $3/16\sigma$	0.48	0.06	1.17	0.43	0.56	0.11	1.83	0.43	0.04	0.01
With $1/4\sigma$	0.44	0.06	0.96	0.38	0.49	0.14	2.04	0.38	0.05	0.01

3.5 Δ-variance

The Δ-variance results for the 30 sample clouds studied are shown in Table 3.12, using the method described in Section 2.8.2. The table shows the scale (in pc) of any peak in the Δ-variance plot. The peaks reveal the scale at which a change in the structure occurs, i.e. the size of the cloud, the length of filaments etc. Peaks were found for all clouds using both the A_V maps and star-density maps, by tiling the images as described in Section 2.8.2.

Table 3.11: Table of molecular cloud data with noise added. The names of the clouds and the amount of noise added is shown in the left column. The values of the parameters Δ, C, β and D are shown with the respective uncertainties. The RMS and corresponding standard deviation are also shown.

Name	Δ	σ_Δ	C	σ_C	β	σ_β	D	σ_D	RMS	σ_{RMS}
Corona Australis	0.85	0.03	2.64	0.25	0.68	0.02	0.36	0.25	0.09	0.01
with $1/16\sigma$	0.83	0.06	2.35	0.41	0.64	0.04	0.65	0.41	0.03	0.01
with $1/8\sigma$	0.83	0.06	2.39	0.41	0.65	0.04	0.61	0.41	0.03	0.01
with $3/16\sigma$	0.86	0.06	2.42	0.40	0.64	0.04	0.58	0.40	0.03	0.01
with $1/4\sigma$	0.92	0.05	2.57	0.33	0.64	0.03	0.43	0.33	0.04	0.01
Circinus	0.71	0.07	1.68	0.43	0.56	0.07	1.32	0.43	0.04	0.01
with $1/16\sigma$	0.70	0.06	1.51	0.39	0.52	0.08	1.49	0.39	0.04	0.01
with $1/8\sigma$	0.73	0.07	1.75	0.43	0.57	0.07	1.25	0.43	0.04	0.01
with $3/16\sigma$	0.70	0.06	1.50	0.39	0.52	0.08	1.50	0.39	0.04	0.01
with $1/4\sigma$	0.60	0.06	1.33	0.40	0.53	0.09	1.67	0.40	0.04	0.01
Chamaeleon	1.03	0.05	2.50	0.34	0.58	0.04	0.50	0.34	0.04	0.01
with $1/16\sigma$	0.95	0.05	2.54	0.33	0.62	0.03	0.46	0.33	0.04	0.01
with $1/8\sigma$	0.95	0.05	2.54	0.34	0.62	0.03	0.46	0.34	0.04	0.01
with $3/16\sigma$	0.95	0.05	2.56	0.33	0.62	0.03	0.44	0.33	0.05	0.01
with $1/4\sigma$	0.60	0.06	1.33	0.40	0.53	0.09	1.67	0.40	0.04	0.01
Orion A	0.64	0.06	1.21	0.35	0.45	0.11	1.79	0.35	0.05	0.02
with $1/16\sigma$	0.64	0.06	1.24	0.35	0.46	0.11	1.76	0.35	0.05	0.02
with $1/8\sigma$	0.65	0.06	1.25	0.35	0.46	0.10	1.75	0.35	0.05	0.02
with $3/16\sigma$	0.72	0.06	1.53	0.39	0.52	0.08	1.47	0.39	0.04	0.01
with $1/4\sigma$	0.80	0.07	1.90	0.43	0.57	0.06	1.10	0.43	0.04	0.01
Orion B	0.56	0.06	1.18	0.38	0.50	0.11	1.82	0.38	0.05	0.01
with $1/16\sigma$	0.56	0.06	1.18	0.37	0.50	0.11	1.82	0.37	0.05	0.01
with $1/8\sigma$	0.58	0.06	1.25	0.39	0.51	0.10	1.75	0.39	0.05	0.01
with $3/16\sigma$	0.72	0.06	1.53	0.39	0.52	0.08	1.47	0.39	0.04	0.01
with $1/4\sigma$	0.60	0.06	1.33	0.40	0.53	0.09	1.67	0.40	0.04	0.01

The sole exception was for the cloud Lupus 3, which showed no peak in Δ-variance at any scale. Other clouds showed two peaks, such as Monoceros and Musca.

Examples of the plots of Δ-variance for the Aquila Rift cloud are shown in Figure 3.20. These show the results obtained for our *con-noise maps* with the nearest 49 stars. The results obtained when using the nearest 25 and 100 star maps showed peaks at the same scales as for the 49 nearest stars maps. The left panel of the figure shows the plot obtained using the *con-noise map* of A_V. The right panel shows the plot obtained using the corresponding star density map. The data obtained using the A_V maps shows a peak in σ^2_Δ at ~6.0 pc while the data obtained using the corresponding star density maps shows a peak in σ^2_Δ at ~4.5 pc. The plots for all 30 sample clouds are shown in Appendix C.2.

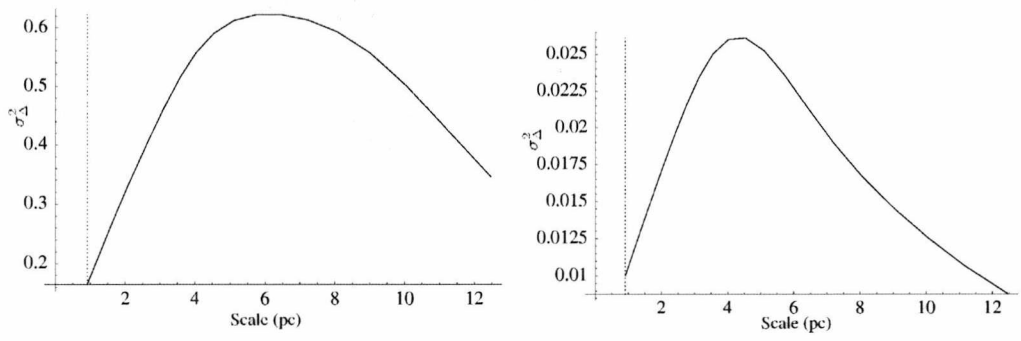

Figure 3.20: Plots showing the output obtained using the Δ-variance analysis using the *con-noise* A_V map (**left panel**) and corresponding star density map (**right panel**) for the Aquila Rift cloud, using the 49 nearest star maps. The dashed vertical line on the left of each plot shows the smallest scale at which data can be reliably used while avoiding oversampling due to the spatial resolution of the it con-noise map.

The mean value of the peaks in Δ-variance ($\widehat{\sigma^2_\Delta, A_V}$) were calculated based on the clusters found in the data. For the A_V map results, a cluster of values ranging from 0.8 pc to 17.0 pc was found, and another cluster was found with values ranging from 30 pc to 50 pc. The mean value of the peaks found in the first cluster is 5.9±5.1 pc, while the mean value of the peaks found in the second cluster is 38.6±7.7 pc.

When considering the SF and non-SF clouds separately, the following results were found. The SF group has two clusters of values for $\widehat{\sigma^2_\Delta, A_V}$. These range from 2.75 pc to 18.0 pc for the first cluster and from 30.0 pc to 50.0 pc for the second. The mean value of the peaks in the first cluster is 8.2±5.8 pc and for the second cluster the mean value is 40.0±10.0 pc. For the non-SF group, there were also two clusters in the values, ranging from 0.8 pc to 16.0 pc and from 33.0 pc to 40.0 pc. The mean value of the first cluster is 4.4±4.1 pc, and for the second cluster is 36.5±4.9 pc.

For the star density maps, the following results for $\widehat{\sigma^2_\Delta, *}$ were found for the 30 sample clouds. There were two clusters of values in the results. These range from 1.0 pc to 25.0 pc and from 32.0 pc to 57.0 pc. The mean value of the peaks in the first cluster is 7.0±6.3 pc and for the second cluster the mean is 44.3±9.2 pc.

Again, considering the SF and non-SF clouds separately, the following results were found for $\widehat{\sigma^2_\Delta, *}$. The SF group has three clusters of values. These range from 1.0 pc to 9.0 pc, from 14.5 pc to 25.0 pc, and from 32.0 pc to 44.0 pc. The mean values

Table 3.12: The Δ-variance results for the sample 30 clouds. The positions of the peaks in σ^2_Δ for both the A_V and star density (*) maps are shown, together with the mass index scaling exponents α for the A_V maps with uncertainties.

Name	$\widehat{\sigma^2_\Delta, A_V}$ [pc]	$\widehat{\sigma^2_\Delta, *}$ [pc]	α_{A_V}	$\sigma_{\alpha_{A_V}}$
Aquila Rift	6.0	4.5	0.85	0.07
Auriga 1	33.0	46.0	0.36	0.07
Auriga 2	8.0	15.0	0.49	0.13
Cepheus Flare	16.0	19.0	0.18	0.10
Chamaeleon I	4.2	1.6, 4.0	0.96	0.10
Chamaeleon II	3.5	4.6	0.83	0.16
Chamaeleon III	2.25	6.0	0.66	0.16
Circinus	18.0	25.0	0.69	0.03
Corona Australis	2.75	1.0	1.08	0.03
Cygnus OB7	40.0	37.0	0.23	0.07
λ Ori	13.0	4.0, 57.0	0.28	0.18
Lupus 1	1.75	7.0	0.69	0.07
Lupus 2	1.25	2.5	0.51	0.06
Lupus 3	2.75	-	0.82	0.05
Lupus 4	2.5	5.0	0.47	0.04
Lupus 5	4.5	7.0	0.58	0.11
Lupus 6	2.5	3.5	0.44	0.16
Lupus 7	2.75	2.2	0.42	0.03
Lupus 8	2.8	3.5	0.48	0.06
Lupus 9	3.0	5.5	0.36	0.02
Monoceros	6.0, 40.0	55.0	0.17	0.04
Musca	0.8, 4.0	6.5	0.05	0.03
Ophiuchus	7.0	1.0, 9.0	0.71	0.06
Orion A	17.0	19.0	0.96	0.18
Orion B	30.0	44.0	0.52	0.05
Perseus	14.0	32.0	0.64	0.12
Rosette Nebula	50.0	39.0	0.77	0.40
Scorpius	1.5, 4.0	5.4	0.61	0.14
Serpens	3.25	1.8, 4.75	0.73	0.03
Taurus	3.5, 11.0	14.5	0.65	0.12

are 3.6±2.6 pc, 19.5±5.3 pc and 38.0±5.0 pc for the first, second and third clusters respectively. For the non-SF group there are two clusters in the data. The range from 2.2 pc to 19.0 pc and from 46.0 pc to 57.0 pc. The mean values are 6.6±4.7 pc for the first cluster and 52.7±5.9 pc for the second cluster.

Also shown in Table 3.12 are values of the mass spectral index scaling exponents (α) for each cloud, using the *con-noise* A_V maps and the corresponding star density maps. However, only the values obtained from using the A_V maps are meaningful in terms of

physics. The values obtained using the three maps were averaged. The values range from 0.05 (Musca) to 1.08 (Corona Australis) with a mean of 0.57±0.25.

3.5.1 The Effect of Noise on the Δ-variance

As with the structure functions it is also necessary to consider the effect of noise on the Δ-variance results. This was investigated in a similar way as for the structure functions (see Section 3.4.2). The same test image of 400 × 400 pixels containing a circle was used. As before the circle contained values scaled linearly from 10.0 (centre) to 0.81 (edge); the rest of the pixels in the image were set to zero. The Δ-variance of this image was calculated. This was repeated for three rebinned images of sizes 200 × 200, 100 × 100 and 50 × 50 as for the structure function analysis. Increments of Gaussian noise were added to each of the images in steps of $1/16\sigma$ (with σ taken as 0.28 mag as for the *con-noise map* using the nearest 49 stars), up to $1/4\sigma$. The results are shown in Table 3.13. It is clear from the table that adding noise has no clear effect on the values for the mass spectral index scaling exponents α, within the uncertainties.

This exercise was repeated using the 400 × 400 test image, first adding 1σ noise (0.28 mag), then steps of $1/16\sigma$ up to $1/4\sigma$. As in Section 3.4.2 this simulates the levels of noise present in the *con-noise maps*. The results are shown in Table 3.14. Again it is clear that adding noise has no effect on the values of α, taking into account the uncertainties.

A further exercise was performed to see if adding Gaussian noise to the test image had any effect on the peak in σ^2_Δ. In this case it was necessary to reduce the size of the circle in the test image so that the Δ-variance analysis measured the peak in σ^2_Δ. The circle was resized to 31 pixels in radius. This analysis was performed for the image firstly without noise, and then with noise added in $1/16\sigma$ increments staring from 1σ. The peak in σ^2_Δ remained constant at a radius of 54 pixels in each case (roughly the diameter of the circle), showing that adding noise does not affect the position of the peak.

As in Section 3.4.2 the analysis was also performed on a selection of real clouds. Gaussian noise was added to the images in increments of $1/16\sigma$ up to $1/4\sigma$, and the Δ-variances were calculated. The results are shown in Table 3.15. Again, the results do not

Table 3.13: Table of results when adding noise to a test image. The size of the test image and amount of noise added is shown in the left column with the grid width/height in pixels. The values of the parameter α are shown with uncertainties.

Type	α	σ_α
No noise, 400	2.81	0.11
No noise, 200	2.97	0.24
No noise, 100	2.89	0.10
No noise, 50	2.79	0.52
$1/16\sigma$, 400	2.91	0.15
$1/16\sigma$, 200	3.02	0.28
$1/16\sigma$, 100	2.95	0.54
$1/16\sigma$, 50	2.79	0.52
$1/8\sigma$, 400	2.81	0.12
$1/8\sigma$, 200	2.95	0.19
$1/8\sigma$, 100	2.98	0.34
$1/8\sigma$, 50	2.79	0.52
$3/16\sigma$, 400	2.91	0.15
$3/16\sigma$, 200	2.96	0.20
$3/16\sigma$, 100	2.98	0.34
$3/16\sigma$, 50	2.79	0.52
$1/4\sigma$, 400	2.81	0.12
$1/4\sigma$, 200	2.95	0.19
$1/4\sigma$, 100	2.98	0.34
$1/4\sigma$, 50	2.79	0.52

Table 3.14: Table of results when adding Gaussian noise to a test image. The amount of noise in the test image is shown in the left column. The values of the parameter α are shown with uncertainties.

Type	α	σ_α
Test Cloud (1 σ)	2.97	0.18
With $1/16\sigma$	2.90	0.16
With $1/8\sigma$	2.96	0.17
With $3/16\sigma$	2.97	0.18
With $1/4\sigma$	2.95	0.17

show any discernible trend.

Table 3.15: Table of molecular cloud data with Gaussian noise added. The names of the clouds and the amount of noise added is shown in the left column. The values of the parameter α and corresponding uncertainties are shown.

Name	α	σ_α
Corona Australis	1.08	0.03
with $1/16\sigma$	0.96	0.01
with $1/8\sigma$	1.00	0.01
with $3/16\sigma$	1.02	0.01
with $1/4\sigma$	0.96	0.01
Circinus	0.69	0.03
with $1/16\sigma$	0.71	0.20
with $1/8\sigma$	0.72	0.16
with $3/16\sigma$	0.72	0.16
with $1/4\sigma$	0.72	0.16
Chamaeleon	0.84	0.16
with $1/16\sigma$	0.69	0.03
with $1/8\sigma$	0.68	0.01
with $3/16\sigma$	0.68	0.01
with $1/4\sigma$	0.68	0.01
Orion A	0.96	0.18
with $1/16\sigma$	0.97	0.18
with $1/8\sigma$	1.02	0.26
with $3/16\sigma$	0.93	0.21
with $1/4\sigma$	0.95	0.20
Orion B	0.52	0.05
with $1/16\sigma$	0.69	0.33
with $1/8\sigma$	0.69	0.01
with $3/16\sigma$	0.67	0.01
with $1/4\sigma$	0.74	0.01

Chapter 4

Interpretation

This chapter contains the interpretation of the data. Firstly, the maps made for the project and their use are discussed. This section reports on the comparison of the maps against previously published maps. The following section features the interpretation of the column density distribution and mass distribution results, including a discussion of the molecular cloud density results. The interpretation is given in the next section of the structure function and Δ-variance analysis. Then a discussion of the individual results for each of the 30 sample clouds is given. Where available, the data are compared to literature values.

4.1 All-Sky Near-infrared Extinction Maps

A number of maps were made for this thesis using data from the 2MASS point source catalogue (Skrutskie et al., 2006). The maps cover all of the sky and were made using the near-infrared colour excess (NICE) method (Lada et al., 1994). Of the extinction maps, two different types were made. The first type are constant noise maps (with a variable spatial resolution) and the second type are constant spatial resolution maps (with a variable noise in each pixel). All the maps were made in a uniform way for the whole sky, so that analysis on different regions can be compared.

The size of the pixels in the maps varies with Galactic latitude b, as detailed in Table 2.4. The smallest pixel sizes are used near the Galactic Plane ($|b| < 20°$) as there are more stars per unit area. The largest pixel sizes are used around the Galactic poles ($|b| > 50°$) where there are not many stars or molecular clouds, and the compression of the latitude coordinates l close to the poles means less pixels are required. Therefore, the maps made for this project are most useful around the Galactic Plane where molecular clouds are abundant.

Using the *con-noise map* with the nearest 49 stars as an example, the following statistics apply. The distance to the 49^{th} nearest star varies from $1'$ near the Galactic Plane to $\sim 10'$ at the poles. The standard measure of the uncertainties, the 1σ variance, is 0.28 mag A_V. This ensures that all regions with an extinction of more than 1 mag A_V

(the self-shielding threshold of molecular clouds, e.g. Hartmann et al. (2001)) are detected with a signal-to-noise ratio of better than 3.6.

There is, however, one area where these maps do not give meaningful results, which are a few small regions of high extinction where $|b| < 1°$. This is due to a large number of foreground stars causing a non-detection of the cloud(s). The maps show patches of lower extinction when compared with the surrounding area (see the lower edge of Figure 3.5 in Section 3.1.3.1). These areas should be mapped using observations at longer wavelengths (see e.g. Schultheis et al. (2009) and Román-Zúñiga et al. (2009)). Longer wavelength observations provide a better resolution in areas of high extinction, as more stars are detected through the denser parts of clouds than with near-infrared observations. Using a combination of near-infrared and mid-infrared wavelength (3-8μm) observations, Román-Zúñiga et al. (2009) measure extinction values in the B 59 cloud of up to nearly 100 mag A_V, for example.

4.1.1 Comparison with Previously Published Maps

In Section 3.1.3 a comparison of the *con-noise maps* was made with the large-scale extinction maps of D05 (Dobashi et al., 2005) and S98 (Schlegel et al., 1998). The major difference between the maps is the spatial resolution, which is about 6′ for both the D05 and S98 maps, but varies between 1-5′ (for $|b| <20°$ where the majority of the clouds analysed in this thesis are found), in our *con-noise map* using the nearest 49 stars. Therefore, our maps are able to show much finer details such as small high-extinction cores and small-scale structures, for $|b| <20°$.

As a result of this comparison, it is shown that the calibration of extinction values in the *con-noise maps* (allowing for systematic differences) is correct to within the 1σ variance on scales of a few degrees. In terms of systematic differences, the extinction values in the *con-noise maps* are ~20% larger than those in D05. This may be due to incorrect values used for the factors (C_{VR} and C_{VB}) to convert their A_R and A_B values into A_V. They used values for these factors of $C_{VR} = 1.21$ and$C_{VB} = 0.76$ (Dickman, 1978) respectively. These factors change depending on the assumption of the reddening law and

therefore could systematically alter the extinction values.

Alternatively, the reason for the higher extinction values in our maps, compared to D05, may be due to differences in the extinction law used (e.g. Equation 1.19), for values of β. A value of β =1.7 was used for this thesis, while values in the literature vary between 1.6-1.8 (e.g. Draine (2003), Froebrich et al. (2007)). For example, a change in β of ±0.2 leads to a difference in visual extinction of 10%. However, the error in β is unlikely to be that large so this is probably not the reason.

Another explanation arises from the star counting technique used in D05 being ineffective in tracing high extinction areas. For example, Kohyama et al. (2010) indicate that the D05 map is of limited use at extinction values above 10 mag A_V due to non-detection of background stars. However, this would lead to differences only in the high extinction areas, which is not the case.

Comparison of our *con-noise maps* against those of S98 found the extinction values in the latter were ~40% larger. This is interpreted as being due to systematic uncertainties in both dust temperature and emissivity in the maps of S98. This result agrees with that reported by Dobashi et al. (2005) and Yasuda et al. (2007), that the reddening in S98 is over-estimated by a factor of 1.4 in regions where $E(B-V) > 0.15$. Furthermore, Cambrésy et al. (2001) found that S98 over-estimated A_V (derived from their $E(B-V)$) by a factor of 2-3 times when compared with the star-count method (for a region in the Polaris cloud). This is also consistent with our result, e.g. when comparing D05 with S98 the differences in A_V are close to a factor of two. In addition to the over-estimation of extinction, an under-estimation is also found in some areas by Gorbikov & Brosch (2010).

The variation in dust emissivity between dense and diffuse regions is examined in Lehtinen et al. (2007), which potentially explains the differences found in our comparisons with the S98 map. Lehtinen et al. (2007) found that the dust emissivity increases with decreasing temperature by a factor of two in the temperature range from 19 K to 14 K. As a consequence of this temperature dependent effect, the apparent optical depth τ_{app} (at infrared wavelengths) is always lower than the true optical depth. Therefore, the apparent emissivity of the dust is lower than the true value. The change in τ_{app} is greatest at low

temperatures, such as those found in dense molecular cores.

A map using far-infrared data (at 100μm) with improved resolution compared to S98 was made by Miville-Deschênes & Lagache (2005). They achieved a better resolution at 100μm by keeping the full resolution from the ISSA data. Their map also improves on S98 by taking into account variations in responsivity with brightness at scales smaller than 1°. A recent paper giving corrections to the S98 map, by using passively evolving galaxies to determine corrections to the reddening, was published by Peek & Graves (2010). Maximum deviations of 45 mmag in $E(B-V)$ are quoted in this paper, caused by underestimation of reddening in areas of low dust temperature. However, this paper aims to constrain the errors in S98 over large areas of the sky at high precision, whereas the differences noted earlier relate to high extinction regions (hence of interest for star formation).

4.2 Analysis of Column Density Distribution

This section presents the results obtained from the analysis of the column density distribution data, as described in Section 2.7. One result of this analysis is that the slope of the column density distribution γ decreases with increasing spatial scale for about half of the clouds studied. This can be interpreted as the smaller scale high extinction cores no longer being detected at the larger spatial scales. Therefore, the slope γ for these cases is steeper (more negative).

The remaining clouds do not show any overall trend in the values of γ against spatial scale. In these cases there may be fewer or no small scale high extinction cores - which is implausible since all of the clouds involved in star formation are known to have small scale cores. An alternative explanation could be a lack of small scale (about 8 pixels in the highest resolution map, i.e. 4′) structure in these clouds, which would otherwise be 'lost' when the map is rebinned.

Fitting the column density distributions to a log-normal function (see Equation 2.14 in Section 2.7.2) gave mixed results. Some clouds could be fitted well by this type of relation

(with an *rms* of less than ~1 mag A_V). Examples of these include Auriga 2, Chamaeleon, Corona Australis, Lupus, the Rosette Nebula and Serpens. Most of the remaining clouds however, could not be fit well by this type of function. Some examples of these include Auriga 1, Cepheus Flare, Circinus, λ-Ori, Musca, Ophiuchus, Orion A and Orion B. This result agrees with earlier works, such as on the Lupus and Ophiuchus clouds by Lombardi et al. (2008a) and that on the clouds analysed by Kainulainen et al. (2009).

Using the results from Table 3.6 to compare the SF (clustered SF mode) and non-SF (isolated SF mode) clouds, it is found that the non-SF clouds are fit better by Equation 2.14 than the SF clouds. The mean value of the *rms* is 2.6±1.5 for the non-SF group compared to 3.4±1.8 for the SF group (also note the slightly larger standard deviation for the latter). The lower quality of fits for the SF group is due to the presence of excess material at higher A_V values, which is hence available for current and future star formation.

All of the clouds analysed showed an excess of material, at higher extinction values, than what might be expected when compared to a simple log-normal distribution. The goodness of fit to the log-normal relation might therefore be anticipated to correlate to the amount of high A_V excess material of a particular cloud. The excess of column density could relate to material that has decoupled from the turbulent field in the cloud and is now dominated by gravity. With this in mind, any correlations between the goodness of fit *rms* and other cloud properties were searched for, but none could be found.

One might expect that the *rms* shows a correlation with γ_{low}, if the lower quality fits are due to excess material at higher values of A_V. However, the value of the correlation coefficient was only $r = 0.26$ (see Section 2.9.1 for the correlation coefficient method). This may be due to the disparity between the fits and the data *not* occuring in the high A_V regime. On inspecting the plots of the log-normal fits against A_V (see Appendix B.1.1) it is evident that the majority of deviations occur in the low A_V regime between 1 mag A_V and 4 mag A_V, i.e. not in the high A_V regime.

Furthermore, one might expect a correlation between *rms* and MSF (the mass fraction involved in star formation). However, the correlation coefficient for this is $r = -0.07$. This is likely to be for the same reason as with the γ_{low} values; since the fits with worse (higher)

rms values tend to deviate from the data in the lower A_V regime. The fact that the *rms* values were better for the non-SF group may be a chance effect. The large standard deviations in the *rms* values also obscure the meaning of these values.

When comparing the values of γ at low column densities against high column densities, a difference in the scatter of values was found. This amounts to a factor of 2.5 larger scatter for γ_{low} values compared to γ_{high}. The values of γ_{high} differ less from cloud to cloud. This can be interpreted as the high A_V regions of the cloud being dominated by gravity and therefore decoupled from the turbulence in the remainder of the cloud. Whereas, in the low A_V turbulence dominated regions, the values of γ_{low} vary from cloud to cloud depending on the environment of the cloud and the feedback from star formation within.

There are several factors which influence the turbulence in molecular clouds. One likely source of turbulence is the large-scale gas flows that form the clouds (e.g. Ballesteros-Paredes et al. (2007)). Hence, one expects the nature of the turbulence to vary according to the parameters of the flows (e.g. amount of material available, velocity of the flows, angles at which flows collide etc.). There may also be nearby supernovae giving rise to compressive shocks in the cloud. Additionally, the nature and amount of feedback caused by young stars within molecular clouds will vary according to the number and size of YSOs in the cloud. (e.g. Clark et al. (2005)). Therefore, one may expect the column density distribution in the turbulence dominated regime (i.e. low A_V) to vary from cloud to cloud.

Returning to the search for correlations, the two groups identified in the left panels of Figure 3.14 of Section 3.3.2 (i.e. the SF and non-SF groups) are now compared with data published in the literature. A correlation exists between our two groups and the number of Young Stellar Objects (YSOs, as listed in Table 1 of Kainulainen et al. (2009) - using results collated from the Handbook of Star Formation Volumes I (Reipurth, 2008a) and II (Reipurth, 2008b)). The relevant data are displayed here in Table 4.1, with pertinent data repeated from Tables 3.6 and 3.7.

The data in Table 4.1 show that most of the clouds listed by Kainulainen et al. (2009)

Table 4.1: Table of star formation status for the 30 selected clouds, arranged by the two distributions identified from Figure 3.14. The column density distributions slopes γ_{low} and γ_{high}, mass distributions δ_{low} and δ_{high}, and the star formation extinction threshold $A_{V,SF}$ are repeated here for comparison. The fourth column shows whether the clouds are star forming or not according to Kainulainen et al. (2009) (where available). The fifth column gives an approximate number of YSOs in the cloud, the data collated from the Handbook of Star Formation Volumes I (Reipurth, 2008a) and II (Reipurth, 2008b).

Name	γ_{low}	γ_{high}	δ_{low}	δ_{high}	$A_{V,SF}$	Star forming? (Y/N)	N_{YSOs}
Aquila Rift	-0.23	-0.13	-0.16	-0.12	9.3	-	-
Chamaeleon I	-0.35	-0.17	-0.17	-0.14	1.2	Y	200
Chamaeleon II	-0.34	-0.22	-0.17	-0.15	6.7	Y	50
Circinus	-0.36	-0.17	-0.24	-0.16	6.8	-	-
Corona Australis	-0.40	-0.16	-0.15	-0.16	3.7	Y	tens
Cygnus OB7	-0.25	-0.17	-0.24	-0.19	12.0	-	-
Ophiuchus	-0.27	-0.11	-0.17	-0.13	4.9	Y	300
Orion A	-0.28	-0.15	-0.18	-0.12	5.3	Y	> 2000
Orion B	-0.39	-0.13	-0.26	-0.11	6.8	Y	> 100
Perseus	-0.42	-0.22	-0.28	-0.15	5.3	Y	> 100
Rosette Nebula	-0.20	-0.19	-0.20	-0.15	8.9	-	-
Serpens	-0.16	-0.21	-0.21	-0.14	7.7	Y	300
Taurus	-0.15	-0.24	-0.24	-0.14	4.4	Y	300
Auriga 1	-0.48	-0.24	-0.36	-0.13	7.4	Y	tens
Auriga 2	-0.71	-0.32	-0.51	-0.21	4.9	-	-
Cepheus Flare	-0.54	-0.20	-0.42	-0.11	6.5	-	-
Chamaeleon III	-0.46	-0.36	-0.30	-0.24	5.7	N	-
λ Ori	-0.51	-0.34	-0.40	-0.13	7.2	-	-
Lupus 1	-0.54	-0.21	-0.22	-0.12	5.3	Y	tens
Lupus 2	-0.61	-0.24	-0.27	-0.09	4.2	-	-
Lupus 3	-0.58	-0.23	-0.25	-0.19	2.9	Y	50
Lupus 4	-0.79	-0.18	-0.40	-0.11	3.7	-	-
Lupus 5	-0.71	-0.54	-0.59	-0.34	5.3	N	-
Lupus 6	-0.96	-0.70	-0.73	-0.06	5.6	-	-
Lupus 7	-0.56	-0.35	-0.46	-0.48	11.2	-	-
Lupus 8	-0.75	-0.58	-0.57	-0.51	5.8	-	-
Lupus 9	-1.03	-0.45	-0.96	-0.53	3.3	-	-
Monoceros	-0.42	-0.18	-0.32	-0.12	4.8	-	-
Musca	-1.04	-0.22	-0.16	-0.24	6.0	N	-
Scorpius	-0.56	-0.29	-0.31	-0.16	5.6	-	-

as star forming appear in group one of the two distributions. This may be understood from the fact that these clouds have generally less negative values of γ (i.e. shallower slopes) hence more material at higher A_V available for star formation. However, two clouds listed as star forming appear in group two, but have only tens of YSOs (Lupus 1) and ~50 YSOs (Lupus 3) contained in them. The clouds listed in Kainulainen et al. (2009) as non-star forming all appear in group two of the two distributions. A strong correlation is implied here between the two groups (SF and non-SF) and the star formation activity taking place in the clouds.

4.2.1 Galactic Plane Column Density Distribution

The results for the Galactic plane analysis, using the log-normal fits to the column density distribution, were presented in Section 3.3.1.1. The parameters a, A_0, A_1 and σ differ with position around the Galactic centre (denoted by the contours of A_V). There is a trend in that the values of the parameters close to the centre are systematically higher/lower than those outside of the centre. This is likely due to the higher extinction around the Galactic centre. Furthermore, this trend is repeated with the values of the goodness of fit *rms* which show that the fits are of poorer quality around the centre. This is probably due to multiple clouds along the line of sight in this region, hence the CDDs cannot be well fit by the log-normal function.

The following results were found, for the log(N) fits to the CDDs presented in Section 3.3.2.1. One expects the values of the slopes γ to decrease around the Galactic centre, where the column densities are higher, hence there is more material at higher extinctions. This is indeed the case. The effect is more pronounced with increasing pixel size, which may be understood as less high extinction features (e.g. cores and filaments) are detected at lower resolutions. The mean standard deviation for the γ_{low} data is nearly four times that as for the γ_{high} data. This is likely due to the different factors that influence the low A_V region (such as turbulence) when compared with the high A_V regions, which are dominated by gravity.

4.3 Analysis of Mass Distribution

Using the method described in Section 2.7.3, the slopes of the mass distribution δ were obtained for our sample clouds. As with the column density distributions, about half of the clouds showed a decrease in the slope δ with increasing spatial scale, while the remainder showed no overall trend. The reasons are likely the same as those discussed in Section 4.2. As the spatial scale increases, smaller structures are no longer detected, which leads to a decrease in δ.

However, the change in the slope δ is more prominent than for the column density slopes γ. Therefore, it is somewhat easier to ascertain the threshold in A_V (i.e. $A_{V,SF}$ in Table 4.1) at which the dominant force in the cloud switches from turbulence to gravity.

Values for $A_{V,SF}$ range from 1.2 mag A_V (Chamaeleon I) to 12.0 mag A_V (Cygnus OB7) (see Table 3.7). This threshold can be associated with the extinction threshold for star formation, originally quoted as 7 mag A_V in Ophiuchus (Johnstone et al., 2004). This is in good agreement with the mean value calculated for this thesis of 5.9 mag A_V (with a standard deviation of 2.3 mag A_V). One might expect clouds with a lower star formation threshold to be undergoing star formation as this implies there is more material available at higher A_V values. This is the case - the clouds Chamaeleon I and Corona Australis have reasonably low star formation thresholds and are undergoing star formation (Kainulainen et al., 2009).

An indicator of whether a cloud has the potential to form stars in the next 10^6yrs is the mass fraction involved in star formation (denoted MSF). In this study, values for the MSF were found to vary from 0.07% to 31.0% (though the second highest figure is 10.8%). Even so, this represents a range of more than two orders of magnitude. This large spread of values may be due to the clouds being observed at different stages of their evolution. Some of the clouds undergoing star formation (listed in Kainulainen et al. (2009) and listed here in Table 4.1) have a higher value of MSF than those with only low star formation. Examples of these include Chamaeleon I, Corona Australis, Orion A and Taurus. This implies that they have material dominated by gravity which is expected to form more new stars with in the future.

However, other examples such as Ophiuchus and Orion B have low values of MSF (around 1 % each). In this case, the interpretation is that these clouds are nearing the end of their star formation phase. Only a small proportion of the mass in these clouds is found in the regime dominated by gravity. Another explanation is that more material will accumulate into higher density regions in these clouds and become available for star formation at a later date. Whether this will happen depends on the interplay of turbulence, gravity and magnetism at work in the clouds and as such can only be speculated on. Molecular clouds are also surrounded by macro-turbulent HI regions which exchange mass, energy and momentum both with other clouds and the molecular components within (Ballesteros-Paredes et al., 1999).

The cloud properties listed in Tables 3.6 and 3.7 were tested to find correlations. It might be expected that a link could be found to the predominant mode of star formation (i.e. clustered or isolated). However, no correlation could be found. When comparing clouds which form stars in clusters (SF clouds such as Orion A), with clouds that form few, isolated stars (non-SF clouds such as Auriga 1), the differences between the column density parameters are too ambiguous to discern any trend. For example, while the average values of parameters δ_{low}, $A_{V,SF}$ and MSF differ between the SF and non-SF groups, the statistical uncertainties mean that the differences are not significant for the latter two parameters.

A correlation against the properties of the turbulent (i.e. low A_V) parts of the cloud was also searched for. Such a correlation might be expected as the turbulent regions of the cloud may drive the star formation mode, or perhaps the different turbulent properties originate from feedback from young star clusters or YSOs. Once again no correlation was found in the data. It is plausible that a correlation might exist with some environmental attributes of the clouds, such as position above/below the Galactic plane (which can be inferred from the latitude b), or the distance of the cloud from the Galactic centre, or the direction of the cloud with respect to the solar system. However, the clouds analysed here are all relatively nearby (~1 kpc or less except for the Rosette Nebula); this may explain the lack of correlations. When testing for correlations the SF and non-SF groups were

also considered separately but no correlations were found.

One might expect a correlation between the values of δ_{low} and parameters such as $A_{V,SF}$ and MSF. These parameters can potentially all be linked to the level of star formation of the clouds. Again, no correlations were found between any of the mass parameters derived for this thesis. This can be explained by the following. Firstly, the values of δ_{low} relate to the distribution of material in the clouds rather than the explicit amount available for star formation. Secondly, the threshold values $A_{V,SF}$ appear to be independent of the mass of the molecular cloud so again may not relate to the amount of material available for star formation. This testing was repeating with the SF and non-SF groups treated separately, and the same result was found.

Overall, the behaviour of the mass distribution δ values resembled that of the column density distribution γ. The values of δ_{low} have a much larger scatter than the values of δ_{high} (4.5 times larger). This behaviour is hardly surprising since the mass distributions are derived from the column density measurements. The reason for the larger scatter in δ_{low} values is that the lower A_V regions of the clouds are dominated by turbulence, which may be caused by large-scale flows acting on the clouds, supernovae and possible feedback from stars within. This was discussed further in Section 4.2.

4.3.1 Molecular Cloud Density

The molecular cloud densities for the each of our sample clouds (ρ_{A_V}) were calculated, as well as for the region in each cloud associated with star formation (ρ_{SF}). These were presented in Section 3.3.3.1. For both ρ_{A_V} and ρ_{SF} the results cover a couple of orders of magnitude (see Table 3.7). For the entire clouds - i.e. the low *and* high extinction regions - the following results were found. The values of ρ_{A_V} range from 52 cm^{-3} to $1.4 \cdot 10^4$ cm^{-3} ($1.3\ M_\odot \cdot pc^{-3}$ to $340\ M_\odot \cdot pc^{-3}$). For ρ_{SF} the values range from 920 cm^{-3} to $4 \cdot 10^5$ cm^{-3} ($23\ M_\odot \cdot pc^{-3}$ to $1 \cdot 10^4\ M_\odot \cdot pc^{-3}$). As expected the densities are higher for the star forming regions of the clouds.

When considering the two groups identified from Figure 3.14, one would expect the median density of the SF group to be higher than that of the non-SF group.

This is not the case (compare ρ_{SFI} = 2.3±2.1 10^4 cm^{-3} (580±530 $M_\odot \cdot pc^{-3}$) with ρ_{SFII} = 3.1±2.2 · 10^4 cm^{-3} (780±560 $M_\odot \cdot pc^{-3}$)). However, the size of the uncertainties removes the significance of these value. This ambiguity may result from the highest density material not being detected, due to lack of resolution of the smallest structures in the clouds.

4.4 Analysis of the Structure of Molecular Clouds

A selection of nearby GMCs were investigated by calculating structure functions, as described in Section 2.8. For this analysis only the low A_V parts of the clouds were selected (i.e. pixels between 1 mag A_V and the star formation threshold for each cloud (see Section 2.7.1)) as turbulence is expected to dominate in these regions. The structure functions were calculated for each cloud using the *con-noise* A_V maps and $\eta(p)/\eta(3)$ was plotted against p. The structure functions were derived at a common range of scales for the clouds, from 0.1 pc to 1.0 pc (where the data were available). The Δ-variance technique was also used to investigate structure, using the *con-noise maps*, and this is discussed in Section 4.4.3.

4.4.1 Structure Functions

Structure function analysis was performed on our sample of clouds, and the results are shown in Table 3.8. The method used was described in Section 3.4. Correlations were searched for between the structure function parameter Δ and codimension C obtained from the structure function analysis, and the parameters shown in Tables 3.6 and 3.7 (Section 3.3.1). The correlations were tested for by finding Pearson's correlation coefficient r (see Section 2.9.1) for all combinations of the parameters. No correlations were found with a value for r of better than 0.7 (generally only values of r = 0.9 and above are convincing).

The structure function analysis was repeated by considering the SF and non-SF groups separately (i.e. based on the two distinct distributions seen in the left panels of Figure 3.14

of Section 3.3.2). Once again no correlations were found, for either group. This result implies there is no link between the structure function parameters and the results obtained from the column density and mass distribution analysis. Alternatively, any correlation may have been obscured by the uncertainties in the results. This is unlikely as one would still expect some correlations, but with less convincing coefficients, which is not the case.

When comparing the mean values of the parameters obtained from the structure function analysis for the SF and non-SF groups, slight differences are found. For example, the mean value of the codimension C is 1.81 ± 0.33 for the SF group and 1.98 ± 0.33 for the non-SF group. The Kolmogorov-Smirnov test (K-S test, see Section 2.9.2) was performed to investigate the significance of any differences between the two groups for the parameters Δ, C (also β and D). Only for the parameter Δ was the result convincing that the distributions are *not* the same (0.0019% from the same group). For the parameter C (and therefore fractal dimension D) the result was a 1.62% probability of being from the same distribution. It should be noted that when using the K-S test, even this low probability of 1.62% does not ensure that the data are not from the same distribution. For the intermittency parameter β there was a 55.7% likelihood that the distributions are the same, which is again inconclusive.

The results of the K-S test lead to a couple of possible conclusions. Perhaps the two groups are only distinct with respect to the parameter Δ and the other parameters are common to both groups. In this case, only Δ may be used to distinguish which group (SF or non-SF) a cloud belongs to when using structure functions. Alternatively, both parameters Δ and C may be used to distinguish the groups, but uncertainties in the values have lead to the K-S test giving an unconvincing result. The parameter β is highly likely to be common to both groups, as both SF and non-SF clouds exhibit intermittency.

One correlation that was searched for was an increase in values of codimension C with distance, i.e. for the value of the fractal dimension D to *decrease* with distance. This may be expected to occur as clouds are less well resolved at larger distances. Structural details are less well determined resulting in a more simplistic appearance. However, in the analysis no such correlation was found. This may be due to the way each cloud was 'cut'

from the larger A_V map (i.e. the region selected for each cloud was chosen to encompass each cloud in a similar way). Additionally, the structure functions are determined on the same scale - 0.1 pc to 1 pc; this scale is resolved for all the clouds analysed. Alternatively, the structure in each cloud may therefore be similar, on a macroscopic scale of the order of the cloud size.

The variation of codimension C with distance for modelled clouds will be discussed in a future paper (Froebrich et al. (in preparation)). Analysis will be performed to ascertain whether varying the distance has an effect on the calculated structure function parameters for a synthetic cloud. This analysis will be performed to closely match what is observed with real molecular clouds, i.e. the synthetic cloud should have a realistic *column* density distribution.

Two other questions will be addressed in this future paper. Firstly, it is likely that the parameters Δ and C change when the same cloud is viewed from a different orientation. The extent of differences in these values can be ascertained by theoretical modelling of clouds, whereas this cannot be determined from observations. Theoretical modelling will aim to elucidate what effect changing the viewing angle has on the parameters Δ and C. If the calculated structure functions change significantly with viewing angle, this implies that the structure functions parameters for different clouds cannot be compared like-for-like. If the structure function parameters do not change significantly with viewing angle then this effect can be discounted.

Secondly, a similar question applies for the positioning of background/foreground stars - how do the values of the structure function parameters change if the positions of background/foreground stars are altered? This will have a larger effect on *con-res maps*, compared with *con-noise maps*, where most pixels only contain a few stars. So, changing the position of stars may have a large effect on the observed structure function parameters (hence justifying our use of the *con-noise maps* for this purpose). Again this is something that can be investigated by theoretical modelling.

For each of our sample clouds it was possible to fit the parameters Δ and C (and hence β and D) with RMS values of less than 0.1. However, fitting our data to the models of

K41, SL94 and B02 proved problematic. Several different ways of generating structure functions - including the use of weightings to accentuate different A_V regions - were discussed in Section 2.8.1.1. Only in a tiny minority of cases (~4%) was it possible to fit to the models with an RMS of less than 0.1, and these cases were likely to be serendipitous fits (since there was no pattern or trend in the few cases which did fit).

Therefore, fitting our calculated structure functions to the models of K41, SL94 and B02 did not yield meaningful results. Although the *con-noise maps* were also used for this analysis, using a weighting in the equation for deriving the structure functions (Equation 2.20) did not give acceptable results. It is thus concluded that the models of K41, SL94 and B02 are insufficient to explain the observed structure in molecular clouds as they are too simplistic. Furthermore, had this analysis produced a positive result the interpretation would have to take account of the effect that the weightings had on the maps, which is not a straightforward assessment. For example, different weightings accentuate different regions in an extinction map, but not necessarily in a linear way. Therefore, this type of analysis (the use of weightings) was discarded.

Using the method outlined in Section 2.8.1, the following structure function results were obtained. The mean value for Δ of 0.83 ± 0.14 is higher than $\Delta = 0$ expected by K41 and $\Delta = 2/3$ predicted by SL94 and B02. But it is lower than the value of $\Delta = 1$ predicted by S08. However, the 1σ uncertainty in our result means the value could be as low as $\Delta = 0.69$ or as high as $\Delta = 0.97$. The results for Δ quoted in this thesis imply that the models by SL94 and B02 are too simplistic and that in reality a mixture of structures (e.g. filamentary and sheetlike structures) are present in clouds. Note that the mean values of Δ for the SF and non-SF groups are identical at $\Delta = 0.83$. This implies that both groups contain a mixture of filamentary and sheetlike structures. High extinction features such as small, high-density cores do not contribute to this analysis since only material at low column densities was used to calculate the structures.

The mixture of solenoidal and compressive forcing in both SF and non-SF clouds is not unexpected since transfer between the two forcing modes is possible. The vorticity ($\omega = \nabla \times u$) and dilation ($\nabla \cdot u$) equations have an asymmetry that favours transfer

from solenoidal to compressive components (Vazquez-Semadeni et al., 1996; Kornreich & Scalo, 2000). Furthermore, compressive components may be transferred to solenoidal when the pressure and density gradients are not aligned, such as in the case of oblique shocks (Elmegreen & Scalo, 2004). Therefore, one expects a mixture of forcings in molecular clouds.

The mean value of codimension parameter C is 1.91 ± 0.33, which is close to the SL94 predicted value of $C = 2$, where the most dissipative structures are filamentary. B02 theorised a value of $C = 1$, i.e. that the most dissipative structures are sheetlike, arising from e.g. shocks. Different theoretical values for C were postulated in S08 depending on the type of forcing; they found $C \approx 1.1$ for compressive forcing and $C \approx 1.5$ for solenoidal forcing. Neither of these two results are close to the average value determined here.

Most of the results for C are closer to the expected value for solenoidal forcing, apart from the results for the clouds Auriga 2 ($C = 1.18$), Cygnus OB7 ($C = 1.31$) and Orion A ($C = 1.20$) (a mixture of SF and non-SF clouds). The mean value for the SF group is $C = 1.81$ and for the non-SF group $C = 1.98$. This may imply that the SF group includes a greater element of compressive forcing than for the non-SF group, which hence lowers the mean value for both groups. This in turn implies that shearing forces play a greater part in determining the structure of the low A_V, turbulence dominated regions of molecular clouds.

4.4.1.1 The Effect of Noise on Structure Functions

The effect of noise on the structure function results was investigated by adding Gaussian-distributed noise to a test image, and also to a selection of real clouds as described in Section 3.4.2. Generally, the structure functions calculated did not conform to the published models of K41, SL94 and B02. Instead, the data were fitted to Equation 2.19 and the parameters Δ and C were derived. The parameters β and D are simply functions of Δ and C, hence dependent on them.

For the test image (see Figure 3.18), a structure function corresponding to Kolmogorov-type turbulence was calculated (i.e. $\Delta = 0$). However, once noise was

added to the image, the derived structure function parameters changed to $\Delta \simeq 0.50$ and $C \simeq 1.2$. Adding increasing quantities of noise only had a slight effect (a small decrease) on the structure function parameter Δ. However, when adding artificial Gaussian noise to the real clouds the opposite was found (a slight increase in the parameter Δ). The size of the uncertainties means that these small trends are insignificant. Only the 'jump' from Kolmogorov-type turbulence once noise is added is meaningful.

In conclusion, the effect of noise is to cause a deviation from the true structure function, with no obvious trend in real clouds, due to the random nature of the noise. In further tests, when Gaussian noise above $1/4\sigma$ (i.e. 0.07 mag A_V) was added (above the inherent 1σ noise of 0.28 mag A_V), the resulting structure function could no longer be fit by a relation of the form of Equation 2.19 with an rms of less than 0.1 σ.

An implication of this result is that the complete removal of noise would be necessary to derive the true structure function. In practice, the noise may only be reduced and cannot be totally removed. As discussed earlier (Sections 3.4 and 4.4.1), the *con-noise maps* were used for the structure analysis for this reason. Even having used the *con-noise maps* the noise may still have obscured any trend(s) present in the data, given the size of the deviations in the results.

4.4.2 The Structure Functions Values in the Galactic Plane

The results of the structure function analysis for the Galactic plane region were presented in Section 3.4.1. The plots showing how the values of the parameters vary with Galactic coordinates are shown in Appendix C.1.2. Starting with the structure function parameter Δ, the values are generally around $\Delta \simeq 0.6 - 1.0$, except for longitudes $l > 85°$ to the left of the centre and $l < -100°$ to the right. For these areas at the two ends of the region analysed the values are lower ($\Delta \simeq 0.1 - 0.5$). These lower values may be indicative of Kolmogorov type turbulence, or relate to a lack of material in these positions. However, the region chosen for the analysis of the Galactic plane has clouds throughout, so the latter explanation is unlikely. Therefore, there may be genuine change in the nature of the turbulence in these areas.

For the codimension C, there is a trend in that the values are lower in the high-extinction region around the Galactic centre. The values are about $C \simeq 0.8 - 1.7$; the lower values are close to those expected for compressive forcing ($C \approx 1.1$ assuming $\Delta = 1$ (Schmidt et al., 2008)), whereas the higher values are closer to that expected for solenoidal forcing ($C \approx 1.5$ (Schmidt et al., 2008)). Therefore, the Galactic centre region contains a mixture of these two types of driver. The areas to the left and right of the Galactic centre have values $C \simeq 1.6-2.2$, which are generally higher than for the Galactic centre, but closer to a value expected for solenoidal forcing.

The intermittency parameter β is related to Δ and C by the relation $\beta = 1-\Delta/C$. There is a trend of lower β values around the Galactic centre ($\beta \simeq 0.1 - 0.6$). The values to the left and right of the Galactic centre are higher ($\beta \simeq 0.6 - 1.0$). The values of the fractal dimension D are related to C by $C = 3-D$. Therefore, they show the opposite trend as for C, with the values being higher around the Galactic centre ($D \simeq 2$, implying a sheetlike structure). To the left and right of the Galactic centre the values are $D \simeq 1$, implying a filamentary-type structure.

4.4.3 Δ-variance

The Δ-variance technique was applied to the *con-noise maps* (both A_V maps and star density maps), as described in Section 2.8.2. The results are shown in Table 3.12 in Section 3.5. Peaks identified in plots of σ_Δ^2 against Δr were used to quantify the scale of structure in our sample clouds. It should be noted that this method underestimates peak positions by ~10-20% (Ossenkopf et al., 2008a). The peak positions quoted here do not reflect the exact scale of the structure, due to the uncertainty in the quoted error.

Using the Δ-variance technique, peaks in σ_Δ^2 were generally found (where the data were available) at scales of around ~0.8 pc to ~57.0 pc in both types of map (i.e. A_V maps and star density maps). The star density maps tended to find peaks on a larger scale than those found using the A_V maps, with a few exceptions (Aquila Rift, Chamaeleon I, Corona Australis, λ-Ori, Lupus 7, Ophiuchus and Serpens). In the case of the exceptions, this is due to the star density maps allowing the detection of structure on smaller

scales (the small-scale structure is enhanced). On the whole, such small-scale structure is not detected, probably due to not being resolved or lost when the oversampled data is discarded.

Both our A_V and star density maps yield peaks in Δ-variance which fall into two clusters; 'smaller' scale peaks and 'larger' scale peaks. The peaks in σ^2_Δ typically correspond to the width of filaments or sheets in a cloud rather than the length of filaments which are much longer (e.g. of the order of 40-50 pc for the Cepheus Flare cloud, where a peak was found at 16 pc - see Figure C.21 in Appendix C.2). However, in e.g. Lupus 9 the peaks correspond to the length of *sections* of the filaments rather than the width of the filaments (see Figure C.37 in Appendix C.2).

Correlations were searched for in the results for the SF clouds and the non-SF clouds, but none could be found. The results are within error bars, therefore any differences are not statistically significant. A Kolmogorov-Smirnov test was performed, to see whether the peaks in σ^2_Δ belonged to the same distribution for the two groups. For the 'smaller' scale peaks (of the order 0.8-17.0 pc), the result was a 1.598% probability that the distributions belong to the same group, therefore it is possible (but not conclusive) that there is a fundamental difference in the peak scales for the SF clouds when compared to the non-SF clouds. For the 'larger' scale peaks (of the order 30.0-50.0 pc), the probability of belonging to the same distribution was 53.4%, i.e. inconclusive.

Regarding the scaling exponent α for the density field, Federrath et al. (2010) found different values depending on the type of forcing present in the cloud. They found that $\alpha = 0.55$ for solenoidal forcing and $\alpha = 1.34$ for compressive forcing. The results obtained for this thesis (see Section 3.5) show a considerable variation in measured values for α, with the bulk of the values around the predicted amount for solenoidal forcing (the mean value for α is 0.57 ± 0.25).

Some of the calculated values of α are close to the predicted value for solenoidal forcing, e.g. Auriga 2 ($\alpha = 0.49\pm0.13$), Lupus 2 ($\alpha = 0.51\pm0.06$), Lupus 4 ($\alpha = 0.47\pm0.04$), Lupus 5 ($\alpha = 0.58\pm0.11$) and Orion B ($\alpha = 0.52\pm0.05$). The clouds which have a value of α expected from the theoretical value for solenoidal forcing do not have any other

parameters in common, therefore further theoretical work is required to understand the significance of these values. Future modelling work should include a mixture of both solenoidal and compressive forcing to match the observations.

Other values for α are closer to the predicted value for compressive forcing. Examples of these are Corona Australis (α = 1.08±0.03) and Orion A (α = 0.96±0.18). However, other than both being SF clouds these two clouds do not have any other common parameters, so that no other parameter can be directly linked to the presence of compressive forcing in the cloud. The remainder of the clouds, on the whole, are subject to solenoidal forcing. Furthermore, there are no correlations between the values of α and other cloud parameters for the remaining clouds. In practice, it is likely that the forcing in individual clouds with $0.55 \leq \alpha \leq 1.34$ is a combination of both solenoidal and compressive forcing.

When considering the SF and non-SF groups separately, it was found that the mean value of α was 60% larger for the SF group. This can be interpreted as due to the presence of structure at higher A_V in the SF clouds. The mean value for the SF group is $\langle\alpha\rangle$ = 0.74 which implies a mixture of predominantly solenoidal forcing with some compressive forcing. For the non-SF group the mean value is $\langle\alpha\rangle$ = 0.45 which implies that the forcing is likely to be exclusively solenoidal.

The values of α should be taken in the context of the uncertainties in the Δ-variance results. As shown in Figure 2.10 (see Section 2.8.2), the error bars for the Δ-variance can be quite large (especially at large lags - i.e. scales). This leads to large uncertainties in the values of α. Work needs to be done to revise the Δ-variance technique to reduce the large uncertainties in the results.

4.4.3.1 The Effect of Noise on the Δ-variance

Analysis was performed to see what effect adding Gaussian noise had on the Δ-variance results. The results of this analysis are shown in Section 3.5.1. When adding noise to the test images there was no trend in the values of the mass index scaling exponent α when compared with the amount of noise added. This shows that the Δ-variance technique is robust against noise in the pixels in this respect. Further analysis using the test image

showed that the position of a peak in σ^2_Δ did not change with increasing noise.

Using a selection of our sample of real clouds, further analysis was performed to see what effect (if any) adding Gaussian noise to the image had. There was no discernible trend in the values of α, when compared to the amount of noise added. However, noise was an important factor when performing Δ-variance analysis using the *con-res* maps. The results were inconsistent when comparing the four spatial resolution maps for each cloud. This was due to the larger variation in noise between pixels caused by the low number of stars in each pixel. Therefore, the Δ-variance analysis was performed using the *con-noise maps*.

4.5 Individual Clouds

In this section the interpretation is given for individual clouds. The results obtained for this thesis (from Sections 3.3, 3.4 and 3.5) are discussed and compared with the literature. The distance and mass estimates are discussed, and the area of the selection for each cloud is quoted. The star forming status of each cloud is given and compared to the literature (where available). The type of forcing (solenoidal or compressive, see e.g. Federrath et al. (2010)) suggested by the data for each cloud is postulated. This discussion also quotes the value of the mass index scaling exponent α (see e.g. Stutzki et al. (1998)) which gives an indication of the type of turbulent forcing in each cloud.

4.5.1 Aquila Rift

The Aquila Rift is a ~430 pc^2 area at a distance of about 200-250 pc (Straižys et al., 2003). It includes the star forming region W 40 (Rodney & Reipurth, 2008). A mass for the cloud calculated here of 154 $\cdot 10^3 M_\odot$ compares well with the literature value of 150-270 $\cdot 10^3 M_\odot$ (Straižys et al., 2003). The mass fraction involved in star formation MSF is calculated at 1.58% and the star formation threshold is found to be 9.3 mag A_V above which the material in the cloud is dominated by gravity. From the shallow gradient of the column density distribution γ_{low}, the cloud is in the distribution of clouds likely to be star

forming.

One puzzle concerning this region is that not many new stars are found (Prato et al., 2008), yet the nearby Serpens region (discussed separately in Section 4.5.19) has many new stars forming within it. The possible reasons behind this are either disruption to the star formation by environmental factors (colliding super-bubbles converging on the cloud, nearby supernovae etc., (Frisch, 1998)) or by the star formation being only sporadic within the cloud. The few stars found in the region appear to be related (sharing similar radial velocities (Prato et al., 2008)) but are spread out, implying an isolated mode of star formation for this cloud.

In terms of structure, the cloud has a value of $\Delta = 0.96$ and codimension $C \simeq 2$, which leads to a value for $D = 1$ i.e. a thin, filamentary type structure. This also implies that this cloud is subject to solenoidal forcing since Federrath et al. (2010) find that filamentary structures are likely to arise from that type of forcing. The mass index scaling exponent has a value $\alpha = 0.85$ which is in between the values expected for solenoidal and compressive forcing.

4.5.2 Auriga 1

The Auriga 1 cloud (also known as the California Molecular Cloud) is located at a distance of ~450 pc (Lada et al., 2009) (though Knude (2010) suggests a closer distance of 330 pc) and covers an area of 9400 pc^2. The mass of the cloud is calculated at 268 $\cdot 10^3 M_\odot$ which of the same order of magnitude as that calculated by Lombardi et al. (2010b) of 132 $\cdot 10^3 M_\odot$ and Lada et al. (2009) of ~110 $\cdot 10^3 M_\odot$. The MSF is calculated as 0.19% and the cloud is categorised as non-star forming. This is at odds with some literature, e.g. Kainulainen et al. (2009), who state that the cloud *is* forming stars albeit at a low rate (tens of stars - an order of magnitude less than the Orion Molecular Cloud (Lada et al., 2009)). Furthermore, Auriga 1 contains only one significant embedded cluster of stars (Lada et al., 2009).

The structure analysis for this cloud gave a value for $\Delta = 0.77$ and a value for $C \simeq 2$. These indicate that the cloud has a thin, filamentary type structure. A visual inspection

of the structure function plot (see Figure C.1, right panel, in Appendix C.1.1) with the lowest RMS shows a close fit to the SL94 model, for values of p up to 15. This implies vortex/filament type dissipative structures in the cloud rather than sheetlike dissipative structures. Hence, the cloud is more likely to be subject to solenoidal forcing. The value of α derived from the Δ-variance analysis is $\alpha = 0.36$, which is lower than the values predicted by Federrath et al. (2010), but more likely associated with solenoidal forcing.

4.5.3 Auriga 2

The cloud Auriga 2 covers an area of 590 pc^2 and lies at a distance of ~140 pc (Kenyon et al., 2008). The mass of the cloud is calculated as 12.7 $\cdot 10^3 M_{\odot}$, and a star formation threshold of 4.9 mag A_V. The cloud has a MSF of 0.33%, and is categorised as non-star forming due to the value of γ_{low} (-0.71). According to the literature, most of the new stars in this region are in small groups (Luhman, 2006). Furthermore, many of the pre-main sequence stars are in binary or multiple systems (see Table 5 in Kenyon et al. (2008)). Therefore, the mode of star formation is more likely clustered than isolated for this cloud.

The structure of the cloud is likely to be sheetlike in nature as the structure parameter $D \simeq 2$. This value suggests that the cloud is subject to compressive forcing. The value of the structure parameter Δ is 0.45. The mass index scaling exponent $\alpha = 0.49$ which is slightly lower than the value expected by Federrath et al. (2010) for solenoidal forcing. This suggests the cloud is subject to solenoidal forcing which contradicts the results found from the structure function analysis.

4.5.4 Cepheus Flare

The Cepheus Flare cloud lies at a distance of 390 pc (Kun et al., 2008, 2009), and covers an area of 7900 pc^2. The region is forming stars and contains about 130 YSOs (Kirk et al., 2009b). However, the MSF calculated here is only 0.15%, hence the region may be nearing the end of its star producing phase. The region is classified here as non-star forming due to the γ_{low} value of -0.54. Nevertheless, star formation is known to be

occuring in the Cepheus Flare, with YSOs found in small isolated groups (Kirk et al., 2009b).

The structure function analysis yielded mean values of $\Delta = 0.58$ and $C = 1.97$, implying a filamentary-type structure in the cloud. The value of the parameter C also implies that the cloud is subject to solenoidal forcing. The parameter $\alpha = 0.18$ is rather low but is suggestive of solenoidal forcing than compressive forcing.

4.5.5 Chamaeleon

The Chamaeleon cloud is usually split into three components which each have a slightly different distance. Knude (2010) also gives three individual distances for these clouds, but since the uncertainties in distance mean these overlap, a 'common' distance of 194 pc is also quoted.

4.5.5.1 Chamaeleon I

The cloud Chamaeleon I covers an area of 68 pc^2 and lies at a distance of 160 pc (Whittet et al., 1997) (however, Knude (2010) gives a distance of 196 pc). The value for the cloud mass calculated here is $1.74 \cdot 10^3 M_\odot$ which compares closely to $1.8 \cdot 10^3 M_\odot$ (Cambrésy, 1999) and $2.3 \cdot 10^3 M_\odot$ (Kainulainen et al., 2009). This cloud has a high MSF of 31%, the highest among the selection of analysed clouds. Thus it has a high potential to form stars in the future. The cloud is classified here as a star forming cloud on the basis of it's value of $\gamma_{low} = -0.35$. The star forming status agrees with the literature (e.g. Kainulainen et al. (2009)) which shows the presence of about 200 YSOs in the cloud. The star formation mode is found to be clustered in this cloud (e.g. Luhman (2007)).

The values of the structure parameters are $\Delta = 0.74$ and $C = 2.01$, the latter of which suggests a filamentary structure ($D \simeq 1$). This also suggests that the cloud is subject to solenoidal forcing, but the mass index scaling exponent has a value of $\alpha = 0.96$ which implies a mix of solenoidal and compressive forcing.

4.5.5.2 Chamaeleon II

The Chamaeleon II cloud covers an area of 60 pc^2 and lies at a distance of 178 pc (Whittet et al., 1997) (Knude (2010) gives a distance of 209 pc). The cloud mass calculated here is $1.18 \cdot 10^3 M_\odot$ which compares to $0.8 \cdot 10^3 M_\odot$ (Cambrésy, 1999) and $1.5 \cdot 10^3 M_\odot$ (Kainulainen et al., 2009). This cloud is also classified here as star forming and has a potential MSF of 3.8%. The mode of star formation is found to be clustered for this cloud (Spezzi et al., 2009).

The structure parameter values of the cloud are $\Delta = 0.93$ and $C = 1.88$ which imply a filamentary structure for the cloud. The value of C also suggests the cloud is subject to solenoidal forcing. However, the value $\alpha = 0.83$ suggests a mixture of solenoidal and compressive forcing.

4.5.5.3 Chamaeleon III

The cloud Chamaeleon III covers an area of 84 pc^2 and lies at a distance of 150 pc (Whittet et al., 1997) (Knude (2010) quotes a distance of 217 pc). The mass of the cloud is calculated here as $1.49 \cdot 10^3 M_\odot$ compared to literature values of $1.3 \cdot 10^3 M_\odot$ (Cambrésy, 1999) and $1.8 \cdot 10^3 M_\odot$ (Kainulainen et al., 2009). This cloud is classified as non-star forming and has a MSF of 1.3%. The non-star forming status is confirmed by the literature (e.g. Gahm et al. (2002)).

The values of the structure parameters for this cloud are $\Delta = 0.91$ and $C = 2.12$. The latter implies a filamentary type structure and that the turbulence is driven by solenoidal forcing. The value of $\alpha = 0.66$ is in keeping with this result as it is much closer to the value expected for solenoidal forcing.

4.5.6 Circinus

The Circinus cloud is a 1300 pc^2 region at a distance of about 700 pc (Bally et al., 1999) (Knude (2010) quotes a distance of 436 pc for this cloud). The mass for the cloud calculated here of $113 \cdot 10^3 M_\odot$ compares to the literature value of $50 \cdot 10^3 M_\odot$. A value for MSF

of 1.36% is calculated and the star formation threshold is found to be 6.8 mag A_V above which the material in the cloud is dominated by gravity. From the shallow gradient of the column density distribution γ_{low} the cloud is in the distribution of clouds likely to be star forming. In the literature, the star formation in this cloud is stated as likely to be caused by the shock from a supernova (Reipurth et al., 2008).

In terms of structure, the cloud has a value of $\Delta = 1.01$ and codimension $C = 1.67$, which leads to a value for $D = 1.33$ i.e. likely to have a thin, filamentary type structure. This result is in agreement with the value of $\alpha = 0.69$ for the mass index scaling exponent, and with the literature (e.g. Reipurth et al. (2008)).

4.5.7 Corona Australis

The Corona Australis cloud is located at a distance of ~170 pc (Knude & Høg, 1998) (Knude (2010) quote a distance of 148 pc and Neuhäuser & Forbrich (2008) quote a distance of 130 pc) and covers an area of 53 pc^2. The mass of the cloud is calculated here at $1.0 \cdot 10^3 M_\odot$ which of the same order of magnitude as that calculated of $1.6 \cdot 10^3 M_\odot$ by Cambrésy (1999) and also by Kainulainen et al. (2009). The MSF is calculated as 9.6% and the cloud is found to be in the second group of clouds that are likely to be star forming. The star formation mode is likely to clustered, since the cloud has a cluster at it's core (Neuhäuser & Forbrich, 2008).

The values of the structure function parameters are $\Delta = 0.88$ and $C = 2.28$. The latter points to a filamentary structure for the cloud and solenoidal forcing as the driver for the turbulence. The value of the mass index scaling exponent $\alpha = 1.08$ suggests mainly compressive forcing, however.

4.5.8 Cygnus OB7

The Cygnus OB7 cloud lies at a distance of 770 pc (Uyanıker et al., 2001), and covers an area of 5700 pc^2. A detailed overview of this region is presented in Reipurth & Schneider (2008), and in Aspin et al. (2009). The region is forming stars and is likely to contain a significant number of YSOs. However, the value of MSF calculated here is only 0.07%,

hence the region may be nearing the end of its star producing phase. The region is classified here as star forming due to the γ_{low} value of -0.25.

The structure function analysis yielded mean values of $\Delta = 0.77$ and $C = 1.31$. The latter leads to a value for the fractal dimension $D \simeq 1.7$, i.e. the cloud is likely to have a sheetlike structure and is subject to compressive forcing. However, the value of $\alpha = 0.23$ is much lower than that expected for either solenoidal or compressive forcing.

4.5.9 λ-Ori

Located at a distance of 400 pc (the same distance as the nearby Orion Nebula Muench et al. (2008), see also Dolan & Mathieu (2001)), the λ-Ori cloud covers an area of 7600 pc^2. This makes the cloud the third largest area studied (after the Rosette Nebula and Monoceros). A low value of MSF is found for this cloud (0.12%) and it is also classified as non-star forming due to the γ_{low} value of -0.51. This is at odds with the literature, which confirms that star formation *is* ongoing in this cloud (Mathieu, 2008). Star formation in the centre of the cloud has ceased, however, most likely due to a nearby supernova.

The structure parameter values are $\Delta = 0.90$ and $C = 2.05$, indicating a filamentary structure for the cloud and that the cloud is subject to solenoidal forcing. The value of $\alpha = 0.28$ is rather low but is closer to the expected value for solenoidal forcing rather than compressive forcing.

4.5.10 Lupus

The Lupus region may be split into 9 individual clouds (e.g. Lombardi et al. (2008a)). The same distance is used for all of the clouds (155 pc, Lombardi et al. (2008b)). However, Knude (2010) gives different distances for the first six clouds, between 144 pc for Lupus 1 to 230 pc for Lupus 3. All 9 of the Lupus clouds had values of γ_{low} that led to them being classified as non-star forming. Some of the clouds here are relatively small in terms of the numbers of pixels available hence the values should be used with caution (e.g. the masses of clouds Lupus 6 and Lupus 8). A mass estimate is quoted in Froebrich & Rowles (2010),

giving a total mass of 28.6 $\cdot 10^3 M_\odot$ for clouds Lupus 1 through 6. This compares with the literature value for the total cloud mass in Lupus of 18.2 $\cdot 10^3 M_\odot$ (Lombardi et al., 2008a).

Three of the Lupus clouds (1, 3 and 4) are analysed in Spezzi et al. (2009). They found that the YSOs in Lupus 1 and Lupus 3 tend to be clustered around the high density peaks. In Lupus 4 the YSOs do not follow this pattern, but are randomly distributed away from the high extinction regions.

4.5.10.1 Lupus 1

The cloud Lupus 1 has a mass of 1.27 $\cdot 10^3 M_\odot$, which is lower than the literature values of 10 $\cdot 10^3 M_\odot$ (Cambrésy, 1999) and 2.9 $\cdot 10^3 M_\odot$ (Kainulainen et al., 2009). The area of the cloud is 88 pc^2. The cloud is classified as non-star forming as the value of γ_{low} is -0.51; however the MSF is 3.75%. Perhaps this cloud is undergoing a transition and will exhibit increased star formation in the future. Presently, the cloud has only tens of YSOs within (Kainulainen et al., 2009).

The structure parameter values for the cloud are $\Delta = 0.69$ and $C = 1.36$. The latter indicates the structure of the cloud is more likely sheetlike than filamentary. It also indicates that the cloud may be subject to a mixture of compressive forcing and solenoidal forcing with a prevalence to the former. The value of $\alpha = 0.69$ is closer to that expected for solenoidal forcing, but perhaps suggests a mixture of the two types.

4.5.10.2 Lupus 2

The Lupus 2 cloud has a mass of 0.19 $\cdot 10^3 M_\odot$, compared to the literature value of 0.08 $\cdot 10^3 M_\odot$ (Cambrésy, 1999). It covers an area of 22 pc^2. This cloud has a similar MSF to Lupus 1 of 4.71%; so this cloud has the potential to produce stars in the future. The values of the structure parameters for this cloud are $\Delta = 0.64$ and $C = 2.28$, which indicates a filamentary structure for the cloud and that solenoidal forcing is most likely driving the turbulence in the cloud. The value of $\alpha = 0.51$ is close to that expected for solenoidal forcing.

4.5.10.3 Lupus 3

The Lupus 3 cloud has a mass of 0.93 $\cdot 10^3 M_\odot$, which is slightly lower than the literature values of 1.15 $\cdot 10^3 M_\odot$ (Cambrésy, 1999) and 1.1 $\cdot 10^3 M_\odot$ (Kainulainen et al., 2009). It covers an area of 37 pc^2. Although the cloud is classified here as non-star forming it has a MSF of 10.8%. The literature confirms the presence of tens of YSOs (Kainulainen et al., 2009). The structure parameter values for the cloud are $\Delta = 0.96$ and $C = 2.00$. The latter indicates a filamentary structure for the cloud and that the turbulence is driven by solenoidal forcing. This is not in agreement with the value of $\alpha = 0.82$, which implies a mixture of solenoidal and compressive forcing.

4.5.10.4 Lupus 4

The mass of the Lupus 4 cloud of 2.61 $\cdot 10^3 M_\odot$ is significantly higher than the literature value of 0.63 $\cdot 10^3 M_\odot$ (Cambrésy, 1999). The area of this cloud is 88 pc^2. The MSF of this cloud is 2.85%. The values of the structure parameters for this cloud are $\Delta = 0.84$ and $C = 2.20$, indicating a filamentary structure for the cloud, and that the cloud is subject to solenoidal forcing. The value of $\alpha = 0.47$ also suggests solenoidal forcing.

4.5.10.5 Lupus 5

The Lupus 5 cloud has a mass of 9.83 $\cdot 10^3 M_\odot$ which is significantly higher than the literature values of 2.5 $\cdot 10^3 M_\odot$ (Cambrésy, 1999) and 3.6 $\cdot 10^3 M_\odot$ (Kainulainen et al., 2009). It covers an area of 100 pc^2. The MSF is just 0.09% and the non-star forming status determined here agrees with Kainulainen et al. (2009). The structure parameter values for the cloud are $\Delta = 0.78$ and $C = 2.16$. The latter indicates a filamentary structure for the cloud, and that the cloud is subject to solenoidal forcing. This is also suggested from the value of $\alpha = 0.58$.

4.5.10.6 Lupus 6

The mass of the Lupus 6 cloud of 40.7 $\cdot 10^3 M_\odot$ is higher than the literature value of 10 $\cdot 10^3 M_\odot$ (Cambrésy, 1999), but in the same order of magnitude. This cloud covers

an area of 73 pc^2. The MSF for the cloud is just 0.01% which is in keeping with the non-star forming status. The values of the structure parameters for this cloud are $\Delta = 0.92$ and $C = 2.05$, indicating a filamentary structure for the cloud, and that solenoidal forcing is the driver of the turbulence. The value of $\alpha = 0.44$ is closer to that expected for solenoidal forcing.

4.5.10.7 Lupus 7

The cloud Lupus 7 has a mass of $5.02 \cdot 10^3 M_\odot$ and a MSF of just 0.01%. The area of this cloud is 22 pc^2. It is listed among the clouds of non-star forming status. The structure parameter values are $\Delta = 0.88$ and $C = 1.62$. The latter indicates the structure is perhaps a transition between filamentary and sheetlike. Therefore, the turbulence in this cloud may be driven by a mixture of solenoidal and compressive forcing. However, the value of $\alpha = 0.42$ is indicative of solenoidal forcing.

4.5.10.8 Lupus 8

The Lupus 8 cloud lies closest to the Galactic plane of any of the individual Lupus cloud and has a mass of $135 \cdot 10^3 M_\odot$, which seems rather too high. This is likely to arise from when the slopes δ_{low} and δ_{high} are fit; due to the low number of pixels for this cloud the slope fitting was problematic. The area of this cloud is 58 pc^2. The high value for the mass may be due to the low number of pixels used in the calculation for this small cloud generating a large uncertainty in the value. The MSF for this cloud is 0.06%. The values of the structure parameters are $\Delta = 0.95$ and $C = 2.05$, indicating a filamentary structure. Therefore, the driver of turbulence in this cloud is most likely to be solenoidal forcing. The value of $\alpha = 0.48$ strongly suggests solenoidal forcing.

4.5.10.9 Lupus 9

The cloud Lupus 9 has a mass of $32.4 \cdot 10^3 M_\odot$ and a value for MSF of 0.22%. The cloud has an area of 88 pc^2. The structure parameter values could not be calculated for this clouds as there were no values with an RMS of less than 0.1 (chosen as this represented

a good visual fit to the data). A value was obtained for the mass index scaling exponent of $\alpha = 0.36$. This is somewhat lower than the expected values for both solenoidal forcing and compressive forcing, but is much closer to the solenoidal figure.

4.5.11 Monoceros

The Monoceros cloud (sometimes referred to as the Mon R2 cloud) lies at a distance of 830 pc (Carpenter & Hodapp, 2008), and covers an area of 13000 pc^2. The mass calculated here is 73.9 $\cdot 10^3 M_\odot$, which is similar to literature values of 90 $\cdot 10^3 M_\odot$ (Maddalena et al., 1986) and 40 $\cdot 10^3 M_\odot$ (Xie, 1992). The MSF is 2.01% but the cloud is classified as non-star forming due to the γ_{low} value of -0.42; this value is on the threshold between star forming and non-star forming. The literature, however, confirms that Monoceros is forming new stars (Carpenter & Hodapp, 2008). The mode of star formation is clustered.

The structure function analysis yielded mean value of $\Delta = 0.93$ and $C = 1.97$. The latter leads to a value for the fractal dimension $D \simeq 1$, i.e. the cloud is likely to have a filamentary structure. This also indicates that the cloud is subject to solenoidal forcing. The value for $\alpha = 0.17$ is rather lower than those predicted by (Federrath et al., 2010), but is closer to the figure for solenoidal forcing.

4.5.12 Musca

Located at a distance of 150 pc (Knude & Høg, 1998) (Knude (2010) quotes a distance of 171 pc), the Musca cloud covers an area of 82 pc^2. The mass is calculated here as 0.31 $\cdot 10^3 M_\odot$, which is close to the literature value of 0.55 $\cdot 10^3 M_\odot$ Cambrésy (1999). This cloud has the lowest mass of any of the selected clouds analysed in this thesis. A value for MSF is calculated at 4.95% but Musca is also classified as non-star forming due to the γ_{low} value of -1.04. However, the cloud has the potential to form stars in the future.

The structure parameter values are $\Delta = 1.05$ and $C = 2.23$, indicating a filamentary structure for the cloud. Inspection of the image for this cloud (see Figure A.23 in Appendix A.1) appears to show either a filament or a sheet viewed edge-on. The value of $D = 0.77$ implies that the cloud is subject to solenoidal forcing. The value of $\alpha = 0.05$

calculated from the Δ-variance analysis is the lowest value for any of the selected clouds. This may be due to the 'edge-on' appearance of the cloud in the image. This could be tested by using the Δ-variance technique with models of clouds to evaluate how the values of both Δ_σ^2 and α vary with viewing angle (this is discussed in Section 5.2.1).

4.5.13 Ophiuchus

The Ophiuchus cloud (also referred to as the ρ-Ophiuchus cloud or L1688 - see Figure 4.1) lies at a distance of 119 pc (Lombardi et al., 2008b). This distance compares to 133 pc quoted by Knude (2010), or a value of between 120-140 pc quoted by Wilking et al. (2008). It is 300 pc^2 in size. A value for the mass is calculated here as $8.6 \cdot 10^3 M_\odot$ as compared to literature values of $6.6 \cdot 10^3 M_\odot$ (Cambrésy, 1999) and $8.3 \cdot 10^3 M_\odot$ (Lombardi et al., 2008a). The Ophiuchus cloud is a well known star forming cloud (e.g. Wilking et al. (2008); the value of γ_{low} calculated here puts the cloud in this classification) and it has a value for MSF of 7.18%. The star formation mode for this cloud is clustered (Friesen et al., 2009).

The values of the structure parameters are calculated as $\Delta = 0.74$ and $C = 1.69$. The latter figure suggests a transition between filamentary and sheetlike structure. Therefore, the turbulence is probably driven by a combination of solenoidal and compressive forcing with a predominance of the latter. The value of $\alpha = 0.71$ is closer to that expected for solenoidal forcing but perhaps with some compressive forcing included.

4.5.14 Orion A

The Orion A cloud (also known as the Orion Molecular Cloud; this area contains the famous nebula M 42 and the Orion Nebula Cluster) is situated at a distance of 410 pc (Muench et al., 2008). Both the clouds Orion A and Orion B are surrounded by a large bubble of material known as Barnard's Loop. The region covers 2300 pc^2 in size. The mass calculated here is $42 \cdot 10^3 M_\odot$. This area is forming stars prolifically (the number of YSOs is in excess of 2000 (Kainulainen et al., 2009)), and has a MSF of 5.33%. This

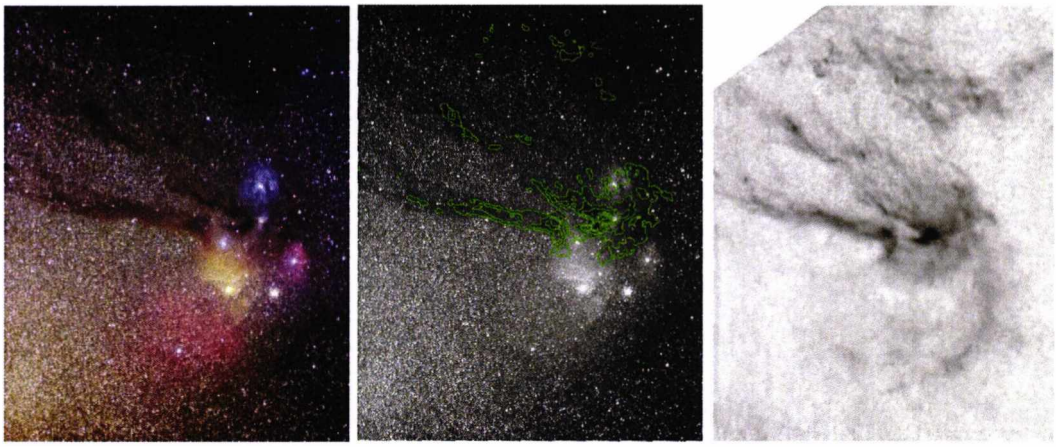

Figure 4.1: The ρ Ophiuchus region in the optical (© Chris Cook) (**left** in colour and **middle** greyscale with overlaid contours of A_V from 3 mag A_V to 21 mag A_V) and **right** detail of the *con-noise* extinction map based on the nearest 49 stars. Extinction values are square root scaled from 0 mag (white) to 15 mag (black) of optical extinction.

indicates that the cloud will continue to form stars in the future. The star formation mode for the Orion A and Orion B clouds is clustered (Lada, 1992).

The structure function parameters have the values $\Delta = 0.67$ and $C = 1.20$. The latter figure suggests a sheetlike structure. It also implies the predominant driver of turbulence is compressive forcing rather than solenoidal. This factor is the probable cause of the high star formation rate. The value of $\alpha = 0.96$ is in-between the expected values also suggesting a mixture of the two forcings.

4.5.15 Orion B

The Orion B cloud extends roughly north from the Orion A cloud and covers 4600 pc^2. It has a mass of $77.9 \cdot 10^3 M_\odot$. Incidentally, the mass for the wider Orion area is quoted as $300 \cdot 10^3 M_\odot$ in Cambrésy (1999); the total mass here for Orion A and B plus λ-Ori is $241.9 \cdot 10^3 M_\odot$. The Orion B cloud is forming stars (but less prolifically than Orion A; here the number of YSOs is around 100 (Kainulainen et al., 2009)) and has a MSF of 1.09%. This is relatively low and may indicate the cloud is nearing the end of its production of stars. As with Orion A the star formation mode is clustered.

The values of the structure function parameters are $\Delta = 0.83$ and $C = 2.05$, which indicates a filamentary structure for the cloud. Hence, solenoidal forcing is implied as the

driver of the turbulence in this cloud. The value of $\alpha = 0.52$ is much closer to the value expected for solenoidal forcing rather than compressive.

4.5.16 Perseus

The Perseus cloud covers an area of 1000 pc^2 and the cloud lies at a distance of 310 pc (Motte & André, 2001). However, the dark cloud LDN 1459 and reflection nebula NGC 1333 associated with this cloud are located at a distance of 213 pc according to Knude (2010)). The mass of the cloud calculated here is 27.2 $\cdot 10^3 M_\odot$ (compared to the literature values of 27 $\cdot 10^3 M_\odot$ (Lombardi et al., 2010b), ~19 $\cdot 10^3 M_\odot$ (Kirk et al., 2006) and 20 $\cdot 10^3 M_\odot$ (Kainulainen et al., 2009)). The cloud is classed as star forming and has a value for MSF of 2.1%. Therefore it has potential to form new stars in the future. The star formation mode in Perseus is clustered.

The structure function parameters are $\Delta = 0.74$ and $C = 1.87$. The latter points to a filamentary structure for this cloud. The driver of the turbulence is more likely to be solenoidal forcing rather than compressive. This is also implied from the value of $\alpha = 0.64$ which is closer to the value expected by solenoidal forcing.

4.5.17 Rosette Nebula

The Rosette Nebula in Monoceros (also known as NGC 2237-9/NGC 2244 or Caldwell 49 - see Figure 4.2) lies at a distance of 1650 pc (Román-Zúñiga & Lada, 2008) and covers 14000 pc^2. The mass is calculated here as 248 $\cdot 10^3 M_\odot$ (compared to the literature value of 500 $\cdot 10^3 M_\odot$ (Cambrésy, 1999)). The cloud is classed here as star forming and has a value for MSF of 0.84%. Therefore, the potential to form stars in the future is fairly low. The star formation mode is clustered.

The structure parameter values could not be calculated for this cloud as there were no values with an RMS of less than 0.1. However, a value was obtained for the mass index scaling exponent ($\alpha = 0.77$) which suggests solenoidal forcing as the driver of turbulence for this cloud, with a lesser component of compressive forcing.

Figure 4.2: An optical image of the nebula associated with the molecular cloud - The Rosette Nebula (optical image © Chris Cook).

4.5.18 Scorpius

Lying at a distance of 120 pc (Cambrésy, 1999) is the Scorpius molecular cloud located in the constellations Scorpius and Ophiuchus. The cloud has an area of 160 pc^2. The mass calculated here is $4.05 \cdot 10^3 M_\odot$, close to the literature value of $6 \cdot 10^3 M_\odot$ (Cambrésy (1999), though the cloud analysed in that paper is only the material on the right-hand side of our cut. The left-hand side of our cut includes *Cloud name 57* as identified by D05, which contains 15 associated clouds including LDN 162 and LDN 141. The material is classified here as non-star forming, and has a MSF of 1.28%. The structure function parameters are $\Delta = 0.98$ and $C = 2.43$, indicating a filamentary/point-like structure. This also suggests that solenoidal forcing is the principal driver of turbulence in the cloud, the value of $\alpha = 0.61$ agrees with this.

4.5.19 Serpens

The Serpens (sometimes referred to as Serpens Cauda) cloud is at a distance of 260 pc (Straižys et al., 1996). However, a value of 193 pc is quoted by Knude (2010) and a value of 230 pc is quoted by Eiroa et al. (2008). The region examined here is contained within the Aquila Rift cloud. It is an active area of star formation and contains new,

young clusters of stars hence the mode of star formation is clustered. The cloud has an area of 82 pc^2. It has a mass of 46.4 $\cdot 10^3 M_\odot$, close to the literature value of 36 $\cdot 10^3 M_\odot$ (Kainulainen et al., 2009).

The cloud is classed as star forming and the MSF is 1.28%. The values of the structure function parameters are $\Delta = 0.95$ and $C = 1.63$, indicating a mixture between a predominantly filamentary, but partly sheetlike structure. This implies that the turbulence is driven by a combination of mostly solenoidal and also compressive forcing. The value of $\alpha = 0.73$ also confirms this interpretation.

4.5.20 Taurus

The Taurus cloud is located at a distance of 140 pc (Kenyon et al., 2008) (this is close to the value of 147 pc quoted by Knude (2010)). This cloud includes an elliptical feature known as the Taurus Molecular Ring (see Figure A.18 in Appendix A.1). It covers an area of 750 pc^2. The mass calculated here is 18.4 $\cdot 10^3 M_\odot$ which compares to literature values of 20.3 $\cdot 10^3 M_\odot$ (Lombardi et al., 2010b), 15 $\cdot 10^3 M_\odot$ (Pineda et al., 2010), 11 $\cdot 10^3 M_\odot$ (Cambrésy, 1999) and 8.1 $\cdot 10^3 M_\odot$ (Kainulainen et al., 2009).

The Taurus cloud is forming stars and has a MSF of 4.84%. Therefore, it has the potential to keep forming stars in the future. In a recent paper, Schmalzl et al. (2010) find 39 star forming cores in a filament devoid of YSOs (named B 211). They postulate that fragmentation is still taking place in this filament and that star formation is yet to occur. In this cloud, stars tend to form in isolation rather than in clusters (Mizuno et al., 1995), hence the mode of star formation is isolated. The Taurus molecular cloud is unusual due to the number of YSOs observed in the cloud, given the isolated mode of star formation. This could be due to the proximity of the cloud allowing observation of the YSOs, which would not all be detected if the cloud were more distant.

The structure function parameters are $\Delta = 0.75$ and $C = 2.14$. The latter figure indicates a filamentary structure for this cloud, and that solenoidal forcing is the predominant driver of turbulence in this cloud. The value of $\alpha = 0.62$ concurs with this, perhaps with a lesser component of compressive forcing.

Chapter 5

Conclusions and Future Prospects

This chapter outlines the conclusions of the thesis. These are dealt with in three sections; the extinction maps, the column density and mass distributions, and the structure function and Δ-variance analysis. Finally, a description of future work is presented, specifically of techniques that would improve resolution, and allow higher extinction regions to be probed. This includes a list of surveys that are collecting data that could be used for such analysis.

5.1 Conclusions

5.1.1 All-Sky Maps

The first part of this thesis involved determining the all-sky median near-infrared extinction maps. Two types of map were created (*con-noise maps* and *con-res maps*). The extinction maps were compared to existing maps published by D05 and S98. The map using the nearest 49 stars to the centre of each pixel, as an example, has a resolution of 1′ near the Galactic plane and up to 5′ where $|b| = 30°$, and in dense cloud regions. This is a superior resolution than those attained by D05 and S98 (both approximately 6′). Hence, the maps made for this thesis offer a significant advantage in resolution for objects along the Galactic plane (for $|b| < 30°$). All nearby GMCs are found within this region. When compared with D05 and S98, our maps show enhanced details such as the finer structure and cores etc..

When comparing the *con-noise maps* to those made by D05, it was found that the latter systematically underestimate the visual extinction by about 20%. The most likely cause is that the star-count method used by D05 has the drawback of a limiting extinction which can be measured, determined by the fraction of foreground to background stars (e.g. Cambrésy et al. (2002)). For example, the maps of D05 only measure values of A_V up to approximately 10 mag, whilst ours measure up to about 20 mag A_V, thus doubling the traceable A_V range.

However, when comparing the *con-noise maps* to those by S98, it was found that the latter systematically overestimate the visual extinction by around 40%. This is likely due

to the assumptions of dust temperature and emissivity in the technique of S98. The line of sight dust temperature distribution is impossible to ascertain. Deviations in dust emissivity in molecular clouds lead to large changes in the measured colour excess, especially at longer wavelengths (i.e. 100μm used by S98), as previously pointed out by Dobashi et al. (2005) and Yasuda et al. (2007). These factors may explain the differences in values between the maps.

In conclusion, the maps presented in this thesis offer a significantly improved resolution than S98 and D05. The A_V range that is traced is double that of D05, at higher extinctions. Our maps are independent of dust temperature and use the best tracer of the true column density.

5.1.2 Column Density and Mass Distributions

The *con-res maps* were used to investigate the CDDs of a selection of 30 nearby giant molecular clouds. By calculating the slopes of the CDDs at four different spatial scales, it was possible to determine the dependence of the slope with spatial scale. Thus, the slopes were interpolated to a common spatial scale of 0.1 pc (the approximate size of a molecular cloud core e.g. Larson (2003a)). The CDDs showed two distinct regions which could be fitted with a log-normal relationship - in the low A_V (turbulence dominated) regime and the high A_V (gravity dominated) regime.

Plotting the slopes of the low A_V CDDs and mass distributions showed two distinct groups, which corresponded to those clouds identified as 'star forming' and 'non-star forming' (by Kainulainen et al. (2009)). A threshold extinction value dividing the low A_V and high A_V regimes was found (using the mass distributions) to have a median value of $A_{V,SF} = 5.6 \pm 1.2$ mag. The low A_V, turbulence dominated regions showed different behaviour between the clouds, which may be expected if the clouds are being acted on by external influences dependent on their environment (e.g. large-scale flows, nearby supernovae etc.).

However, plotting the slopes of the high A_V CDDs and mass distributions did not reveal any separate groups. This was interpreted as the high A_V material being dominated

by gravity and hence showing similar behaviour for all clouds. No external influence affects the CDDs of the high A_V regions of the clouds. This indicates that the feedback from stars within the clouds has only a small effect on the CDDs and mass distributions. The sample of clouds contains some which are forming many stars and some which have very low star formation. Yet the CDDs and mass distributions of the high extinction regions are similar for all of the clouds irrespective of star formation activity.

The mass fraction of material involved in star formation MSF covers several orders of magnitude, from just 0.01% to 31.0%, with a median value of $MSF = 1.34\%$. This shows that some clouds in the selection have the potential to form stars in the next 10^6 years (e.g. Chamaeleon I, Corona Australis, Orion A and Taurus), whilst other clouds may have ended their star forming epoch (such as Ophiuchus and Orion B). Therefore, the clouds are observed at different stages in their evolution.

Correlations were searched for as to whether any of the parameters determined from the CDDs and mass distributions correlated to the mode of star formation, but none were found. No correlation was found, for example, with any of the CDD or mass distribution properties and the predominant mode of star formation (i.e. clustered or isolated). This may be due to the extinction maps only showing the material with the potential to be involved in star formation, rather than the conditions that lead to the star formation mode that is now observed.

It might be expected that the low A_V, turbulence dominated, regions of the clouds show some dependence on the mode of star formation, but no dependence was found. This indicates that the feedback from young clusters and isolated YSOs in the cloud plays an insignificant role in determining the mode of star formation.

5.1.3 Structure Function and Δ-variance

Structure function analysis was performed on our sample of clouds. The analysis used the *con-noise maps* and only pixels with extinction values between the 1 mag A_V self-shielding threshold and the star formation threshold $A_{V,SF}$ - i.e. the turbulence dominated part of the clouds. The calculated structure function parameters indicate a diver-

sity between the clouds. These differences may arise from a mixture of turbulent fields (solenoidal and compressive forcing) in the clouds or from the effects of projection and viewing angle.

The average value of the structure parameter $\Delta = 0.83 \pm 0.14$ does not agree with that expected by published models. For example, SL94 and S08 assume that the most intense dissipative structures in the turbulence are vortex filaments, hence $\Delta = 1$ is predicted. Vortical structures arise when the forcing is solenoidal. However, the model by B02 assumes that the most dissipative structures are shocks (appearing as sheetlike structures), and that $\Delta = 2/3$. In this case the forcing is compressive.

Our result indicates that for the average cloud, the forcing is a mixture of solenoidal and compressive forcing, in order to account for our value of Δ. This is expected as compressible turbulence interacts strongly with the solenoidal mode, even at moderate Mach numbers (Elmegreen & Scalo, 2004). The similar value of Δ for both the 'star forming' and 'non-star forming' groups, also implies the same mixture of forcings.

For the codimension parameter C, the average value was found to be $C = 1.9 \pm 0.3$, leading to a value for the fractal dimension of $D \simeq 1$, i.e. that the clouds are largely filamentary in form. This is close to the theoretical value predicted by SL94 of $C = 2$ (i.e. $D = 1$, a filamentary structure), while B02 predicted $C = 1$ ($D = 2$; a 2D sheetlike structure). The work by S08 predicts a value of $C \approx 1.5$ for solenoidal forcing and $C \approx 1.1$ for compressive forcing (both of these results assume $\Delta = 1$). Therefore, the result for C appears to favour solenoidal forcing. For the 'star forming' group, the lower value of the codimension C (1.81, implying $D = 1.19$) suggests that while solenoidal forcing is dominant, compressive forcing has a greater influence than when compared to the 'non-star forming' group.

On the whole, the individual clouds are governed by a mixture of solenoidal and compressive forcing. It was therefore not possible to obtain a perfect fits for any particular cloud to any existing theoretical model, as they each use only one forcing mechanism. The physical reason for this is likely due to the 'ideal' conditions assumed by the models, which do not exist in practice. The precise mixture of turbulent driving mechanisms is

likely to depend on the local conditions of the cloud.

Regarding the Δ-variance results, the following conclusions were reached. Peaks in σ^2_Δ were found for almost all of the clouds, the only exception being for the cloud Lupus 3 when using the star-density map. The values of the peaks in σ^2_Δ generally fall into two clusters; 'smaller' peaks with sizes 0.8 17.0 pc (when using the A_V maps), and 'larger' peaks with sizes 30.0-50.0 pc (again, for the A_V maps). The 'smaller' scale structures correspond to the width of filaments/sheets. The 'larger' scale structures correspond to, the length of individual sections of filaments, rather than the length of whole filaments.

No correlations were found between the peaks in σ^2_Δ and the star forming status of the clouds. However, a Kolmogorov-Smirnov test showed the possibility that the 'smaller' peaks in σ^2_Δ for the SF clouds may belong to a different distribution to those of the non-SF clouds. This possibility was much less likely for the 'larger' peak values. This may indicate a physical difference in the width of sheets or filaments between the SF and non-SF clouds.

The results for the mass index scaling exponent α show an average value of $\alpha = 0.57 \pm 0.25$. This average value is almost exactly the value predicted by Federrath et al. (2010) for solenoidal forcing ($\alpha = 0.55$) rather than the value expected for compressive forcing ($\alpha = 1.34$). However, the large spread in our values means that about half are in-between those expected for solenoidal and compressive forcing, and the remainder are lower than the value expected for solenoidal forcing.

This can be interpreted as all of the clouds being subject to solenoidal forcing, either by transfer from compressive forcing (Elmegreen & Scalo, 2004) or by mechanisms within the clouds such as stellar feedback. For those clouds which do show evidence of compressive forcing, this may indicate that the compression originates from external; influence such as supernova shocks or large-scale flows, or even a transfer from solenoidal forcing (Vazquez-Semadeni et al., 1996; Kornreich & Scalo, 2000).

When considering the SF (i.e. forming clusters) and non-SF (i.e. isolated star formation) groups separately, it is found that the higher mean value for the SF group implies a mixture of solenoidal and compressive forcing, while for the non-SF group the forcing

is exclusively solenoidal. This result links the presence of compressive forcing to clustered star formation. Compressive forcing is likely to be the trigger for the onset of star formation in a cloud. For example, Federrath et al. (2010) find evidence of compressive forcing happening predominantly in swept-up shells, in the Perseus and Rosette Nebula molecular clouds. This indicates that, in these instances, compressive forcing originates from an external source.

5.2 Future Prospects

This section outlines future prospects. Firstly, a discussion is given of the implications of biases introduced by simulations. Then, alternative techniques for determining extinction are presented. This is followed by a section outlining a selection of future missions and surveys that could provide data useful for analysing the structure of molecular clouds.

5.2.1 Comparison to Models

It is not clear how much of the differences in structure function parameters between the clouds can be attributed to the turbulence, or from other biases. These biases relate to effects such as the viewing angle of the cloud or the distance to the cloud. Additionally, the random distribution of background stars also has an influence on the A_V map, which in turn affects the structure function results. For example, if the background stars happened to be distributed in a different way, this may affect the calculated structure function parameters. The extent of this influence can only be ascertained by modelling different distributions of background stars and analysing the results.

The conversion of the true column density into the extinction map also has an affect on the calculated structure functions results. Certainly, simulations must model clouds correctly in order to represent what is observed, otherwise the results may be invalid. A comparison is being undertaken of how the derived structure function parameters are affected by these biases (Froebrich et al. (in prep.)). This will also determine to what extent the differences observed between clouds are real or result from the biases.

5.2.2 Other Techniques for Determining Extinction

5.2.2.1 NICEST

The maps presented in this thesis were prepared using the median near-infrared colour excess (NICE) technique. This allowed the maps to be prepared in sufficient time to perform the column density and structure function analysis. However, the use of more refined techniques (e.g. NICEST, see Section 1.6.6.3) would allow higher resolutions to be attained (1′ or better - Lombardi (2009)), at the cost of increased computation and preparation time. The NICEST technique also allows high extinction filaments/cores to be probed, resulting in higher extinction values being measured of up to $A_V \simeq 25$ mag (3.8 mag A_V higher than the largest value measured in B 59 using the NICER method, for example (Lombardi, 2009)). NICEST reduces noise as foreground stars - which contribute to the noise of the estimators - are identified and removed.

5.2.2.2 Multi-wavelength Techniques

In addition to applying an enhanced technique (such as NICEST), data at other wavelengths could be combined with near-infrared wavelength data. For example, mid-infrared wavelength data can be used to probe high extinction filaments and cores. This technique was used by Román-Zúñiga et al. (2009), to combine Spitzer mid-infrared data with near-infrared data to obtain A_V values of up to 100 mag in the core of B 59. Therefore, combining data from different wavelengths reveals more about the structure of regions of high extinction. As with using the refined techniques such as NICEST, the time taken to determine extinction maps with multi-wavelength data is greater, due to the increased observational requirements and complexity in combining the data.

5.2.3 Future Missions and Surveys

There are several surveys ongoing at near-infrared wavelengths. The results of these surveys *could* be used for analysing the structure of molecular clouds. The benefits of this would be:

- Improved completeness limits. Fainter background stars could be detected which would allow detection of clouds at greater distances.
- Improved resolution. Finer details such as filaments and cores could be resolved.
- Higher extinction structures could be probed (i.e. A_V values from 25-100 mag.)

This section outlines some of the currently planned or proposed missions and surveys.

5.2.3.1 The GAIA mission

The GAIA mission aims to provide more accurate information on the positions and proper motions of an unprecedented number of stars (approximately one billion stars - Perryman et al. (2001); Mignard (2005)). The survey will gather photometric data on stars using 14 wavebands at wavelengths between 300 nm and 1000 nm (i.e. mainly optical wavelengths). This data can be used in a similar way to Knude & Høg (1998, 1999), who used HIPPARCOS data to measure interstellar reddening. They also used the data to estimate more accurate distances to molecular clouds (such as Corona Australis and ρ Ophiuchus) than had been possible before. Alternatively, GAIA data may be combined with other data (e.g. infrared and near-infrared data such as 2MASS) to provide independent determinations of extinction. Furthermore, GAIA parallax data may be combined with photometric data to make 3D extinction maps (Knude, 2002). This technique will allow individual clouds along the same line-of-sight to be separated (this is a problem along the Galactic plane where there are perhaps several clouds along the line-of-sight).

5.2.3.2 UKIDSS

One major survey that began in 2005 is the UKIRT Infrared Deep Sky Survey (UKIDSS, Lawrence et al. (2007)). Envisaged as a near-infrared counterpart to the Sloan Digital Sky Survey, UKIDSS will cover about 7500 square degrees of the northern hemisphere sky. The survey has a sensitivity of approximately three times greater than 2MASS.

5.2.3.3 VISTA

The near-infrared wavelength will be covered by the Visible and Infrared Survey Telescope for Astronomy (VISTA, see Emerson et al. (2004)), which has recently undergone commissioning (Emerson & Sutherland, 2010). This telescope has a 4m main mirror that will cover a wide field (a 1.65° diameter field of view), with observations detecting objects 3 mag fainter than 2MASS. A major survey covering the Galactic plane area is the VISTA Variables in the Via Lactea (VVV) survey (Minniti et al., 2010). The aim of the survey is to produce a 520 square degree atlas in the near-infrared, in the mid-plane of the Galaxy which is rich in star formation. Using objects with reliably known distances the atlas will provide a 3-D map of the area surveyed.

5.2.3.4 NIRSS

Another proposed survey is called the Near Infrared Sky Surveyor (NIRSS, see Stern et al. (2010)). The proposal is for a space-based telescope with a 1.5m mirror situated at Lagrangian point L2. The survey would be able to detect sources up to 3000 times fainter than 2MASS. This survey could be used to improve on e.g. 2MASS by obtaining better resolution data with the detection of fainter stars. This could be used for analysing the structure of molecular clouds with higher sensitivity and better resolution.

5.2.3.5 James Webb Space Telescope

Due to launch in 2014/5, the James Webb Space Telescope (JWST, see Lightsey et al. (2004)), will use a ~6.5m segmented mirror to observe in infrared wavelengths from 0.6-28μm. It will be able to resolve objects with a separation of ~0.5″ (Krist et al., 2007). The telescope will be situated at Lagrange point L2 which means that the earth will shield the telescope from most of the Sun's radiation. Remaining radiation from the Sun (and that reflected by the Moon) will be removed by a shield on the spacecraft. It will carry a near-infrared camera known as NIRCam. This instrument will operate at wavelengths from 0.7-5.0μm, hence the data obtained would be useful for analysing the structure of molecular clouds.

5.2.3.6 Herschel

The Herschel space telescope, launched in May 2009, has the largest mirror on a telescope in space. It detects radiation in the far-infrared (55-671μm (Pilbratt et al., 2010)). Of particular interest is the work of André et al. (2010), who have used the SPIRE (Spectral and Photometric Imaging Receiver) and PACS (Photodetecting Array Camera and Spectrometer) cameras to observe the filamentary structure within the Aquila Rift and Polaris Flare regions. These filaments contain embedded cores. Miville-Deschênes et al. (2010) also used Herschel SPIRE data to show the this structure (filaments with embedded cores) is found even on sub-parsec scales in the diffuse clouds of the Polaris Flare. Hence, this instrument can be used to probe the structure of molecular clouds on sub-parsec scales even in diffuse clouds.

5.2.3.7 Akari

The Akari (meaning: *Light*) spacecraft surveyed up to 94% of the sky in the mid-infrared (9 and 18 μm) and far-infrared (65, 90, 140, 160 μm) from May 2006 to August 2007 (Onaka & Salama, 2009; Bertout, 2010). The mission surveyed many star forming regions (Nakajima & The Atlas Team, 2009), an example being the Taurus-Auriga region (Zahorecz et al., 2010). The mid-infrared and far-infrared wavelength observations could be used to probe regions of high extinction.

5.2.3.8 WISE

Wide-field Infrared Survey Explorer (WISE, Wright et al. (2010)) was launched in October 2009 and functioned for one year before it's hydrogen coolant ran out. The sensitivity of the detections is more than 1000 times greater than that of previous missions, including Akari. WISE can detect fainter sources than e.g. the 2MASS survey by at least one magnitude in the K_s band (used by 2MASS). Maps of interstellar dust distribution can be made with WISE data (Wright et al., 2010). The 3.4μm and 12μm bands can be used to detect PAH emission, while the 4.6μm filter detects continuum emission from dust grains. The 22μm waveband detects emission from small grains and thermal emission from large

grains.

In conclusion, these surveys will provide more sensitive measurements than 2MASS. However, the distance to which clouds may be detected (using a median near infrared colour excess (NICE) technique) may actually reduce due to the increased number of foreground objects that will be detected. Hence, techniques such as NICEST are required to remove the foreground stars that are detected and this will lead to longer computation time to determine the extinction. If these surveys are used to examine the structure of molecular clouds, the main improvements will be that finer structure can be observed due to improved resolution and the high extinction zones around the cores will be available for analysis.

Bibliography

Ali-Haïmoud, Y., Hirata, C. M., & Dickinson, C. 2009, MNRAS, 395, 1055

Alves, J., Lombardi, M., & Lada, C. J. 2007, A&A, 462, L17

André, P., Men'shchikov, A., Bontemps, S., et al. 2010, A&A, 518, L102+

André, P., Motte, F., & Neri, R. 2000, in Astronomical Society of the Pacific Conference Series, Vol. 217, Imaging at Radio through Submillimeter Wavelengths, ed. J. G. Mangum & S. J. E. Radford, 152–+

Anselmet, F., Gagne, Y., Hopfinger, E. J., & Antonia, R. A. 1984, Journal of Fluid Mechanics, 140, 63

Arce, H. G. & Goodman, A. A. 1999, ApJ, 512, L135

Aspin, C., Beck, T. L., Pyo, T., et al. 2009, AJ, 137, 431

Audit, E. & Hennebelle, P. 2010, A&A, 511, A76+

Ballesteros-Paredes, J., Klessen, R. S., Mac Low, M., & Vazquez-Semadeni, E. 2007, Protostars and Planets V, 63

Ballesteros-Paredes, J. & Mac Low, M. 2002, ApJ, 570, 734

Ballesteros-Paredes, J., Vázquez-Semadeni, E., & Scalo, J. 1999, ApJ, 515, 286

Bally, J., Reipurth, B., Lada, C. J., & Billawala, Y. 1999, AJ, 117, 410

Bate, M. R. 2009, MNRAS, 397, 232

Baumgardt, H. & Kroupa, P. 2007, MNRAS, 380, 1589

Bensch, F., Stutzki, J., & Ossenkopf, V. 2001, A&A, 366, 636

Benzi, R., Ciliberto, S., Tripiccione, R., et al. 1993, Phys. Rev. E, 48, 29

Bernstein, R. A., Freedman, W. L., & Madore, B. F. 2002, ApJ, 571, 107

Bertout, C. 2010, A&A, 514

Blaauw, A., Gum, C. S., Pawsey, J. L., & Westerhout, G. 1960, MNRAS, 121, 123

Bok, B. J. 1956, AJ, 61, 309

Boldyrev, S. 2002, ApJ, 569, 841

Boldyrev, S., Nordlund, ., & Padoan, P. 2002, ApJ, 573, 678

Brandenburg, A. & Nordlund, A. 2009, ArXiv e-prints

Brunt, C. M., Federrath, C., & Price, D. J. 2010, MNRAS, 405, L56

Brunt, C. M., Heyer, M. H., & Mac Low, M.-M. 2009, A&A, 504, 883

Cambrésy, L. 1999, A&A, 345, 965

Cambrésy, L., Beichman, C. A., Jarrett, T. H., & Cutri, R. M. 2002, AJ, 123, 2559

Cambrésy, L., Boulanger, F., Lagache, G., & Stepnik, B. 2001, A&A, 375, 999

Carpenter, J. M. & Hodapp, K. W. 2008, The Monoceros R2 Molecular Cloud, ed. B. Reipurth, 899–+

Carroll, J. J., Frank, A., Blackman, E. G., Cunningham, A. J., & Quillen, A. C. 2009, ApJ, 695, 1376

Chen, H. & Ko, C. 2009, ApJ, 698, 1659

Cho, W. & Kim, J. 2010, ArXiv e-prints

Clark, P. C. & Bonnell, I. A. 2004, MNRAS, 347, L36

Clark, P. C., Bonnell, I. A., Zinnecker, H., & Bate, M. R. 2005, MNRAS, 359, 809

Cohen, M. & Barlow, M. J. 2005, MNRAS, 362, 1199

Dickman, R. L. 1978, AJ, 83, 363

Dobashi, K., Uehara, H., Kandori, R., et al. 2005, PASJ, 57, 1

Dolan, C. J. & Mathieu, R. D. 2001, AJ, 121, 2124

Draine, B. T. 2003, ARA&A, 41, 241

—. 2008, Space Science Reviews, 123

Draine, B. T. 2009, in Astronomical Society of the Pacific Conference Series, Vol. 414, Astronomical Society of the Pacific Conference Series, ed. T. Henning, E. Grün, & J. Steinacker, 453–+

Dubrulle, B. 1994, Physical Review Letters, 73, 959

Eiroa, C., Djupvik, A. A., & Casali, M. M. 2008, The Serpens Molecular Cloud, ed. Reipurth, B., 693–+

Elmegreen, B. G. 2000, ApJ, 530, 277

Elmegreen, B. G., Efremov, Y., Pudritz, R. E., & Zinnecker, H. 2000, Protostars and Planets IV, 179

Elmegreen, B. G. & Scalo, J. 2004, ARA&A, 42, 211

Emerson, J. & Sutherland, W. 2010, The Messenger, 139, 2

Emerson, J. P., Sutherland, W. J., McPherson, A. M., et al. 2004, The Messenger, 117, 27

Engargiola, G., Plambeck, R. L., Rosolowsky, E., & Blitz, L. 2003, ApJS, 149, 343

Evans, II, N. J. 1999, ARA&A, 37, 311

Falgarone, E., Phillips, T. G., & Walker, C. K. 1991, ApJ, 378, 186

Federrath, C., Klessen, R. S., & Schmidt, W. 2009, ApJ, 692, 364

Federrath, C., Roman-Duval, J., Klessen, R. S., Schmidt, W., & Mac Low, M. 2010, A&A, 512, A81+

Feldmann, R. & Gnedin, N. Y. 2010, ArXiv e-prints

Foster, J. B. & Goodman, A. A. 2006, ApJ, 636, L105

Friesen, R., Di Francesco, J., Shirley, Y. L., & Myers, P. C. 2009, in Bulletin of the American Astronomical Society, Vol. 41, Bulletin of the American Astronomical Society, 383–+

Frisch, P. C. 1998, in Lecture Notes in Physics, Berlin Springer Verlag, Vol. 506, IAU Colloq. 166: The Local Bubble and Beyond, ed. D. Breitschwerdt, M. J. Freyberg, & J. Truemper, 269–278

Froebrich, D. & del Burgo, C. 2006, MNRAS, 369, 1901

Froebrich, D., Murphy, G. C., Smith, M. D., Walsh, J., & Del Burgo, C. 2007, MNRAS, 378, 1447

Froebrich, D., Ray, T. P., Murphy, G. C., & Scholz, A. 2005, A&A, 432, L67

Froebrich, D. & Rowles, J. 2010, MNRAS, 406, 1350

Gahm, G. F., Lehtinen, K., Carlqvist, P., et al. 2002, A&A, 389, 577

Gillessen, S., Eisenhauer, F., Trippe, S., et al. 2009, ApJ, 692, 1075

Girichidis, P., Federrath, C., Banerjee, R., & Klessen, R. S. 2010, ArXiv e-prints

Glover, S. C. O., Federrath, C., Mac Low, M., & Klessen, R. S. 2010, MNRAS, 404, 2

Glover, S. C. O. & Mac Low, M. 2010, ArXiv e-prints

Goldreich, P. & Kwan, J. 1974, ApJ, 189, 441

Goodman, A. A., Pineda, J. E., & Schnee, S. L. 2009, ApJ, 692, 91

Gorbikov, E. & Brosch, N. 2010, MNRAS, 401, 231

Hartmann, L. 2003, ApJ, 585, 398

Hartmann, L., Ballesteros-Paredes, J., & Bergin, E. A. 2001, ApJ, 562, 852

Hennebelle, P. & Chabrier, G. 2008, ApJ, 684, 395

Hildebrand, R. H. 1983, QJRAS, 24, 267

Hunter, C. 1977, ApJ, 218, 834

Indebetouw, R., Mathis, J. S., Babler, B. L., et al. 2005, ApJ, 619, 931

Jeans, J. H. 1928, Astronomy and cosmogony, ed. Jeans, J. H.

Jenniskens, P. & Desert, F. 1994, A&AS, 106, 39

Johnston, K. G., Shepherd, D. S., Aguirre, J. E., et al. 2009, ApJ, 707, 283

Johnstone, D., Di Francesco, J., & Kirk, H. 2004, ApJ, 611, L45

Joung, M. K. R. & Mac Low, M. 2007, in IAU Symposium, Vol. 237, IAU Symposium, ed. B. G. Elmegreen & J. Palous, 358–362

Kainulainen, J., Beuther, H., Henning, T., & Plume, R. 2009, A&A, 508, L35

Kauffmann, J. & Pillai, T. 2010, ApJ, 723, L7

Kauffmann, J., Pillai, T., Shetty, R., Myers, P. C., & Goodman, A. A. 2010a, ApJ, 712, 1137

—. 2010b, ApJ, 716, 433

Kawamura, A., Mizuno, Y., Minamidani, T., et al. 2009, ApJS, 184, 1

Kenyon, S. J., Gómez, M., & Whitney, B. A. 2008, Low Mass Star Formation in the Taurus-Auriga Clouds, ed. B. Reipurth, 405–+

Kirk, H., Johnstone, D., & Basu, S. 2009a, ApJ, 699, 1433

Kirk, H., Johnstone, D., & Di Francesco, J. 2006, ApJ, 646, 1009

Kirk, J. M., Ward-Thompson, D., Di Francesco, J., et al. 2009b, ApJS, 185, 198

Klessen, R. S., Heitsch, F., & Mac Low, M.-M. 2000, ApJ, 535, 887

Klessen, R. S. & Hennebelle, P. 2010, A&A, 520, A17+

Klessen, R. S., Krumholz, M. R., & Heitsch, F. 2009, ArXiv e-prints

Knude, J. 2002, Ap&SS, 280, 97

—. 2010, ArXiv e-prints

Knude, J. & Høg, E. 1998, A&A, 338, 897

—. 1999, A&A, 341, 451

Kohyama, T., Shibai, H., Fukagawa, M., & Hibi, Y. 2010, ApJ, 719, 873

Kolmogorov, A. 1941, Akademiia Nauk SSSR Doklady, 30, 301

Koornneef, J. 1983, A&A, 128, 84

Kornreich, P. & Scalo, J. 2000, ApJ, 531, 366

Krist, J. E., Beichman, C. A., Trauger, J. T., et al. 2007, in Society of Photo-Optical Instrumentation Engineers (SPIE) Conference Series, Vol. 6693, Society of Photo-Optical Instrumentation Engineers (SPIE) Conference Series

Kroupa, P. 2002, Science, 295, 82

Kun, M., Balog, Z., Kenyon, S. J., Mamajek, E. E., & Gutermuth, R. A. 2009, ApJS, 185, 451

Kun, M., Kiss, Z. T., & Balog, Z. 2008, Star Forming Regions in Cepheus, ed. B. Reipurth, 136–+

Lada, C. J. 1987, in IAU Symposium, Vol. 115, Star Forming Regions, ed. M. Peimbert & J. Jugaku, 1–17

Lada, C. J. & Lada, E. A. 2003, ARA&A, 41, 57

Lada, C. J., Lada, E. A., Clemens, D. P., & Bally, J. 1994, ApJ, 429, 694

Lada, C. J., Lombardi, M., & Alves, J. F. 2009, ApJ, 703, 52

—. 2010, ApJ, 724, 687

Lada, E. A. 1992, ApJ, 393, L25

Larson, K. A. & Whittet, D. C. B. 2005, ApJ, 623, 897

Larson, R. B. 1972, MNRAS, 156, 437

—. 1981, MNRAS, 194, 809

—. 1985, MNRAS, 214, 379

—. 2002, MNRAS, 332, 155

—. 2003a, Reports of Progress in Physics, 66, 1651

Larson, R. B. 2003b, in Astronomical Society of the Pacific Conference Series, Vol. 287, Galactic Star Formation Across the Stellar Mass Spectrum, ed. J. M. De Buizer & N. S. van der Bliek, 65–80

Lawrence, A., Warren, S. J., Almaini, O., et al. 2007, MNRAS, 379, 1599

Lazarian, A. 2009, in Astronomical Society of the Pacific Conference Series, Vol. 414, Astronomical Society of the Pacific Conference Series, ed. T. Henning, E. Grün, & J. Steinacker, 482–+

Lazarian, A. & Hoang, T. 2009, ArXiv e-prints

Lehtinen, K., Juvela, M., Mattila, K., Lemke, D., & Russeil, D. 2007, A&A, 466, 969

Li, A. 2008, ArXiv e-prints, 808

Lightsey, P. A., Barto, A. A., & Contreras, J. 2004, in Society of Photo-Optical Instrumentation Engineers (SPIE) Conference Series, Vol. 5487, Society of Photo-Optical Instrumentation Engineers (SPIE) Conference Series, ed. J. C. Mather, 825–832

Liszt, H. S., Pety, J., & Lucas, R. 2010, A&A, 518, A45+

Lombardi, M. 2009, A&A, 493, 735

Lombardi, M. & Alves, J. 2001, A&A, 377, 1023

Lombardi, M., Alves, J., & Lada, C. J. 2006, A&A, 454, 781

—. 2010a, A&A, 519, L7+

Lombardi, M., Lada, C. J., & Alves, J. 2008a, A&A, 489, 143

—. 2008b, A&A, 480, 785

—. 2010b, A&A, 512, A67+

Luhman, K. L. 2006, ApJ, 645, 676

—. 2007, ApJS, 173, 104

Mac Low, M., Klessen, R. S., Burkert, A., & Smith, M. D. 1998, Physical Review Letters, 80, 2754

Mac Low, M.-M. & Klessen, R. S. 2004, Reviews of Modern Physics, 76, 125

Maddalena, R. J., Morris, M., Moscowitz, J., & Thaddeus, P. 1986, ApJ, 303, 375

Marshall, D. J., Robin, A. C., Reylé, C., Schultheis, M., & Picaud, S. 2006, A&A, 453, 635

Masunaga, H. & Inutsuka, S. 2000, ApJ, 531, 350

Mathieu, R. D. 2008, The λ Orionis Star Forming Region, ed. Reipurth, B., 757–+

Mathis, J. S. 1990, ARA&A, 28, 37

Matzner, C. D. 2007, ApJ, 659, 1394

Mazzei, P. & Barbaro, G. 2010, ArXiv e-prints

McCall, M. L. 2004, AJ, 128, 2144

McKee, C. F. & Ostriker, E. C. 2007, ARA&A, 45, 565

Mignard, F. 2005, in ESA Special Publication, Vol. 576, The Three-Dimensional Universe with Gaia, ed. C. Turon, K. S. O'Flaherty, & M. A. C. Perryman, 5–+

Minniti, D., Lucas, P. W., Emerson, J. P., et al. 2010, NA, 15, 433

Miville-Deschênes, M. & Lagache, G. 2005, ApJS, 157, 302

Miville-Deschênes, M., Martin, P. G., Abergel, A., et al. 2010, A&A, 518, L104+

Mizuno, A., Onishi, T., Yonekura, Y., et al. 1995, ApJ, 445, L161

Mokrane, H., Chaabouni, H., Accolla, M., et al. 2009, ApJ, 705, L195

Molinari, S., Pezzuto, S., Cesaroni, R., et al. 2008, A&A, 481, 345

Motte, F. & André, P. 2001, A&A, 365, 440

Mouschovias, T. C. 1991, in NATO ASIC Proc. 342: The Physics of Star Formation and Early Stellar Evolution, ed. C. J. Lada & N. D. Kylafis, 61–+

Muench, A., Getman, K., Hillenbrand, L., & Preibisch, T. 2008, Star Formation in the Orion Nebula I: Stellar Content, ed. B. Reipurth, 483–+

Murray, N. 2010, ArXiv e-prints

Murray, N. & Rahman, M. 2010, ApJ, 709, 424

Myers, P. C. 1983, ApJ, 270, 105

Nakajima, Y., Nagata, T., Sato, S., et al. 2003, AJ, 125, 1407

Nakajima, Y. & The Atlas Team. 2009, in Astronomical Society of the Pacific Conference Series, Vol. 418, Astronomical Society of the Pacific Conference Series, ed. T. Onaka, G. J. White, T. Nakagawa, & I. Yamamura, 61–+

Nakano, T. 1998, ApJ, 494, 587

Neugebauer, G. & Leighton, R. B. 1969, Two-micron sky survey. A preliminary catalogue (NASA SP, Washington: NASA, 1969)

Neuhäuser, R. & Forbrich, J. 2008, The Corona Australis Star Forming Region, ed. Reipurth, B., 735–+

Onaka, T. & Salama, A. 2009, Experimental Astronomy, 27, 9

Ossenkopf, V. 1993, A&A, 280, 617

Ossenkopf, V., Krips, M., & Stutzki, J. 2008a, A&A, 485, 917

—. 2008b, A&A, 485, 719

Ossenkopf, V. & Mac Low, M. 2002, A&A, 390, 307

Ostriker, E. C., Stone, J. M., & Gammie, C. F. 2001, ApJ, 546, 980

Padoan, P., Boldyrev, S., Langer, W., & Nordlund, . 2003, ApJ, 583, 308

Padoan, P., Cambrésy, L., & Langer, W. 2002, ApJ, 580, L57

Padoan, P., Juvela, M., & Pelkonen, V. 2006, ApJ, 636, L101

Padoan, P., Nordlund, A., & Jones, B. J. T. 1997, MNRAS, 288, 145

Passot, T., Pouquet, A., & Woodward, P. 1988, A&A, 197, 228

Passot, T. & Vázquez-Semadeni, E. 1998, Phys. Rev. E, 58, 4501

Pathak, A. & Sarre, P. J. 2008, MNRAS, 391, L10

Peek, J. E. G. & Graves, G. J. 2010, ApJ, 719, 415

Perryman, M. A. C., de Boer, K. S., Gilmore, G., et al. 2001, A&A, 369, 339

Pilbratt, G. L., Riedinger, J. R., Passvogel, T., et al. 2010, A&A, 518, L1+

Pineda, J. E., Caselli, P., & Goodman, A. A. 2008, ApJ, 679, 481

Pineda, J. L., Goldsmith, P. F., Chapman, N., et al. 2010, ApJ, 721, 686

Prato, L., Rice, E. L., & Dame, T. M. 2008, Where are all the Young Stars in Aquila?, ed. Reipurth, B., 18–+

Preibisch, T., Ossenkopf, V., Yorke, H. W., & Henning, T. 1993, A&A, 279, 577

Reipurth, B. 2000, AJ, 120, 3177

Reipurth, B. 2001, in IAU Symposium, Vol. 200, The Formation of Binary Stars, ed. H. Zinnecker & R. Mathieu, 249–+

—. 2008a, Handbook of Star Forming Regions, Volume I: The Northern Sky, ed. Reipurth, B.

—. 2008b, Handbook of Star Forming Regions, Volume II: The Southern Sky, ed. Reipurth, B.

Reipurth, B., Bally, J., & Walawender, J. 2008, The Circinus Star Forming Complex, ed. B. Reipurth, 285–+

Reipurth, B. & Schneider, N. 2008, Star Formation and Young Clusters in Cygnus, ed. Reipurth, B., 36–+

Rho, J., Reach, W. T., Tappe, A., et al. 2009, in Astronomical Society of the Pacific Conference Series, Vol. 414, Astronomical Society of the Pacific Conference Series, ed. T. Henning, E. Grün, & J. Steinacker, 22–+

Ridge, N. A., Di Francesco, J., Kirk, H., et al. 2006, AJ, 131, 2921

Rieke, G. H. & Lebofsky, M. J. 1985, ApJ, 288, 618

Robin, A. C., Reylé, C., Derrière, S., & Picaud, S. 2003, A&A, 409, 523

Rodney, S. A. & Reipurth, B. 2008, The W40 Cloud Complex, ed. Reipurth, B., 683–+

Román-Zúñiga, C. G., Lada, C. J., & Alves, J. F. 2009, High Resolution Near-Infrared Survey of the Pipe Nebula. I. A Deep Infrared Extinction Map of Barnard 59

Román-Zúñiga, C. G. & Lada, E. A. 2008, Star Formation in the Rosette Complex, ed. Reipurth, B., 928–+

Rosolowsky, E. W., Pineda, J. E., Kauffmann, J., & Goodman, A. A. 2008, ApJ, 679, 1338

Salpeter, E. E. 1955, ApJ, 121, 161

Scalo, J. 1990, in Astrophysics and Space Science Library, Vol. 162, Physical Processes in Fragmentation and Star Formation, ed. R. Capuzzo-Dolcetta, C. Chiosi, & A. di Fazio, 151–176

Scalo, J. & Elmegreen, B. G. 2004, ARA&A, 42, 275

Schlegel, D. J., Finkbeiner, D. P., & Davis, M. 1998, ApJ, 500, 525

Schmalzl, M., Kainulainen, J., Quanz, S. P., et al. 2010, ArXiv e-prints

Schmidt, W., Federrath, C., & Klessen, R. 2008, Physical Review Letters, 101, 194505

Schnee, S., Bethell, T., & Goodman, A. 2006, ApJ, 640, L47

Schultheis, M., Sellgren, K., Ramírez, S., et al. 2009, A&A, 495, 157

Schulz, N. S., Cui, W., Canizares, C. R., et al. 2002, ApJ, 565, 1141

She, Z.-S. & Leveque, E. 1994, Physical Review Letters, 72, 336

Shu, F. H. 1977, ApJ, 214, 488

Shull, J. M. & Beckwith, S. 1982, ARA&A, 20, 163

Skrutskie, M. F., Cutri, R. M., Stiening, R., et al. 2006, AJ, 131, 1163

Smith, R. J., Clark, P. C., & Bonnell, I. A. 2009, MNRAS, 396, 830

Solomon, P. M., Rivolo, A. R., Barrett, J., & Yahil, A. 1987, ApJ, 319, 730

Spezzi, L., Alcalá, J. M., Chapman, N., et al. 2009, Mem. Soc. Astron. Italiana, 80, 67

Spitzer, L. 1978, Physical processes in the interstellar medium, ed. Spitzer, L.

Spitzer, Jr., L. 1968, Dynamics of Interstellar Matter and the Formation of Stars, ed. Middlehurst, B. M. & Aller, L. H. (the University of Chicago Press), 1–+

Stahler, S. W. & Palla, F. 2005, The Formation of Stars (The Formation of Stars, by Steven W. Stahler, Francesco Palla, pp. 865. ISBN 3-527-40559-3. Wiley-VCH , January 2005.)

Stead, J. J. & Hoare, M. G. 2009, MNRAS, 400, 731

Stern, D., Bartlett, J. G., Brodwin, M., et al. 2010, ArXiv e-prints

Straižys, V., Černis, K., & Bartašiūtė, S. 1996, Baltic Astronomy, 5, 125

—. 2003, A&A, 405, 585

Stutz, A., Launhardt, R., Linz, H., et al. 2010, A&A, 518, L87+

Stutzki, J., Bensch, F., Heithausen, A., Ossenkopf, V., & Zielinsky, M. 1998, A&A, 336, 697

Tassis, K., Christie, D. A., Urban, A., et al. 2010, MNRAS, 408, 1089

Trumpler, R. J. 1931, Leaflet of the Astronomical Society of the Pacific, 1, 145

Uyanıker, B., Fürst, E., Reich, W., Aschenbach, B., & Wielebinski, R. 2001, A&A, 371, 675

Vázquez-Semadeni, E. 1994, ApJ, 423, 681

—. 2010, ArXiv e-prints

Vázquez-Semadeni, E., Gómez, G. C., Jappsen, A., Ballesteros-Paredes, J., & Klessen, R. S. 2009, ApJ, 707, 1023

Vázquez-Semadeni, E., Gómez, G. C., Jappsen, A. K., et al. 2007, ApJ, 657, 870

Vázquez-Semadeni, E., Kim, J., Shadmehri, M., & Ballesteros-Paredes, J. 2005, ApJ, 618, 344

Vazquez-Semadeni, E., Passot, T., & Pouquet, A. 1996, ApJ, 473, 881

Vázquez-Semadeni, E., Ryu, D., Passot, T., González, R. F., & Gazol, A. 2006, ApJ, 643, 245

Visser, A. E., Richer, J. S., & Chandler, C. J. 2002, AJ, 124, 2756

Wada, S., Mizutani, Y., Narisawa, T., & Tokunaga, A. T. 2008, in IAU Symposium, Vol. 251, IAU Symposium, ed. S. Kwok & S. Sandford, 417–424

Wall, J. V. & Jenkins, C. R. 2003, Practical Statistics for Astronomers, ed. Wall, J. V. & Jenkins, C. R.

Weingartner, J. C. & Draine, B. T. 2001, ApJ, 548, 296

Whittet, D. C. B., Prusti, T., Franco, G. A. P., et al. 1997, A&A, 327, 1194

Whitworth, A. P. 2001, in IAU Symposium, Vol. 200, The Formation of Binary Stars, ed. H. Zinnecker & R. Mathieu, 33–+

Wilking, B. A., Gagné, M., & Allen, L. E. 2008, Star Formation in the ρ Ophiuchi Molecular Cloud, ed. Reipurth, B., 351–+

Wolf, M. 1923, Astronomische Nachrichten, 219, 109

Wright, E. L., Eisenhardt, P. R. M., Mainzer, A. K., et al. 2010, AJ, 140, 1868

Xie, T. 1992, PhD thesis, Massachusetts Univ., Boston.

Yasuda, N., Fukugita, M., & Schneider, D. P. 2007, AJ, 134, 698

Yun, J. L., Elia, D., Palmeirim, P. M., Gomes, J. I., & Martins, A. M. 2009, A&A, 500, 833

Zahorecz, S., Toth, L. V., Munetaka, U., et al. 2010, Journal of Physics Conference Series, 218, 012022

Zuckerman, B. & Evans, II, N. J. 1974, ApJ, 192, L149

Appendix A

All-Sky Extinction Maps

A.1 High Resolution A_V Maps

In this section cut-outs from the *con-noise maps* using the nearest 49 stars are presented. These cut-outs covers the Galactic plane region around the whole plane where $|b| < 40°$. The extinction values are square root scaled from 0 mag (white) to 15 mag (black) of optical extinction. The cloud regions investigated for this thesis are shown on the appropriate plots.

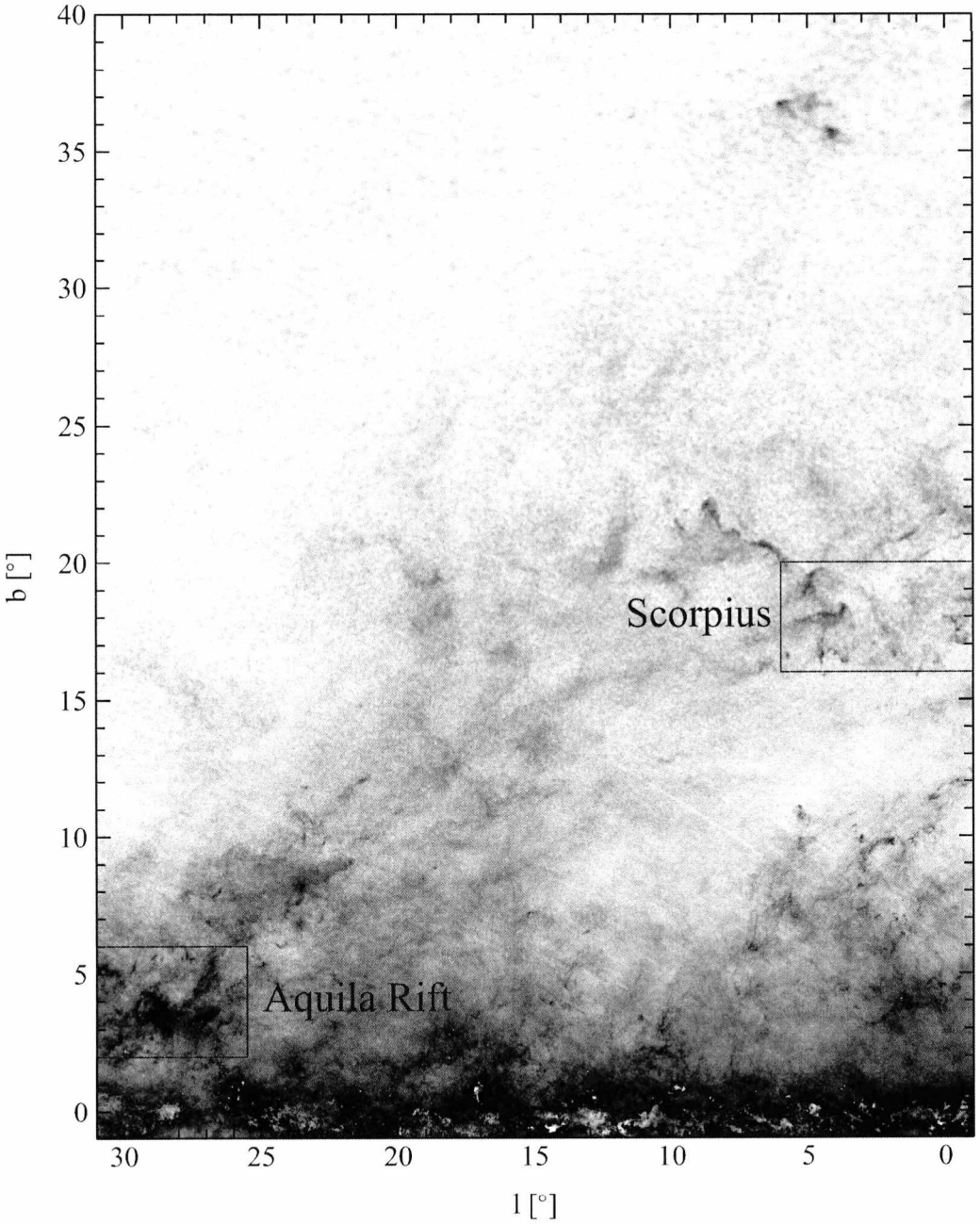

Figure A.1: Grey scale representation of a detail of the *con-noise* extinction map based on the nearest 49 stars. Extinction values are square root scaled from 0 mag (white) to 15 mag (black) of optical extinction.

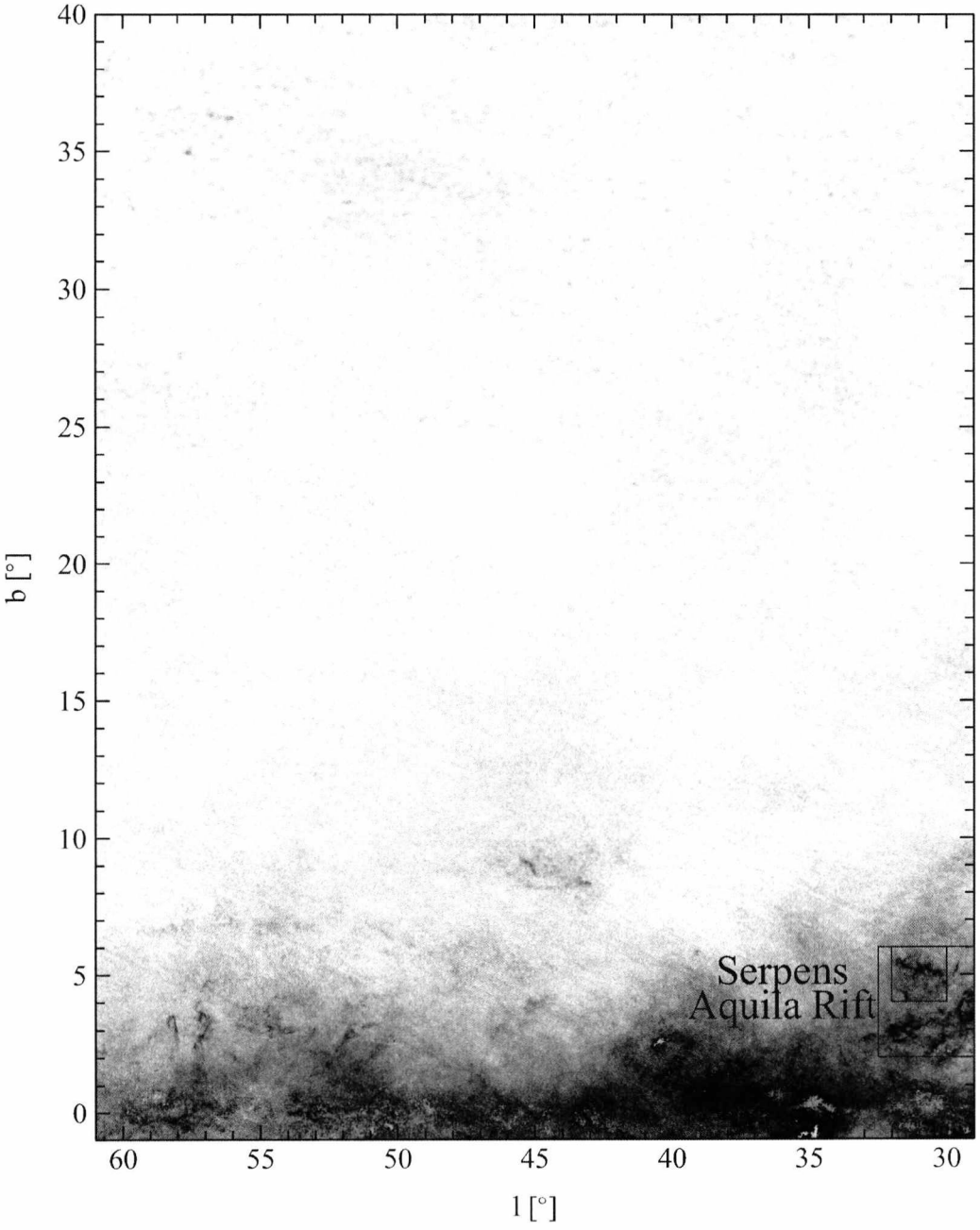

Figure A.2: Grey scale representation of a detail of the *con-noise* extinction map based on the nearest 49 stars. Extinction values are square root scaled from 0 mag (white) to 15 mag (black) of optical extinction.

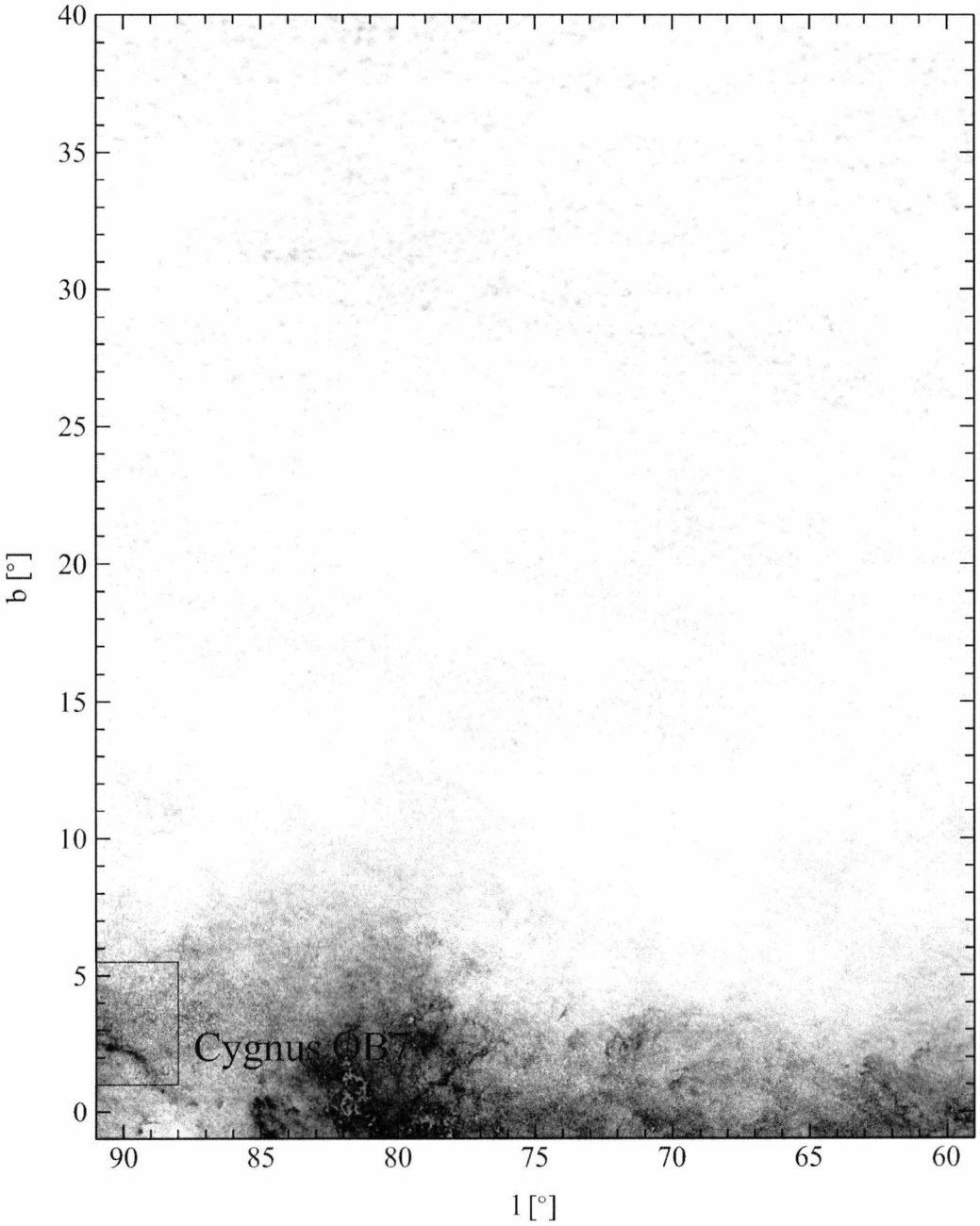

Figure A.3: Grey scale representation of a detail of the *con-noise* extinction map based on the nearest 49 stars. Extinction values are square root scaled from 0 mag (white) to 15 mag (black) of optical extinction.

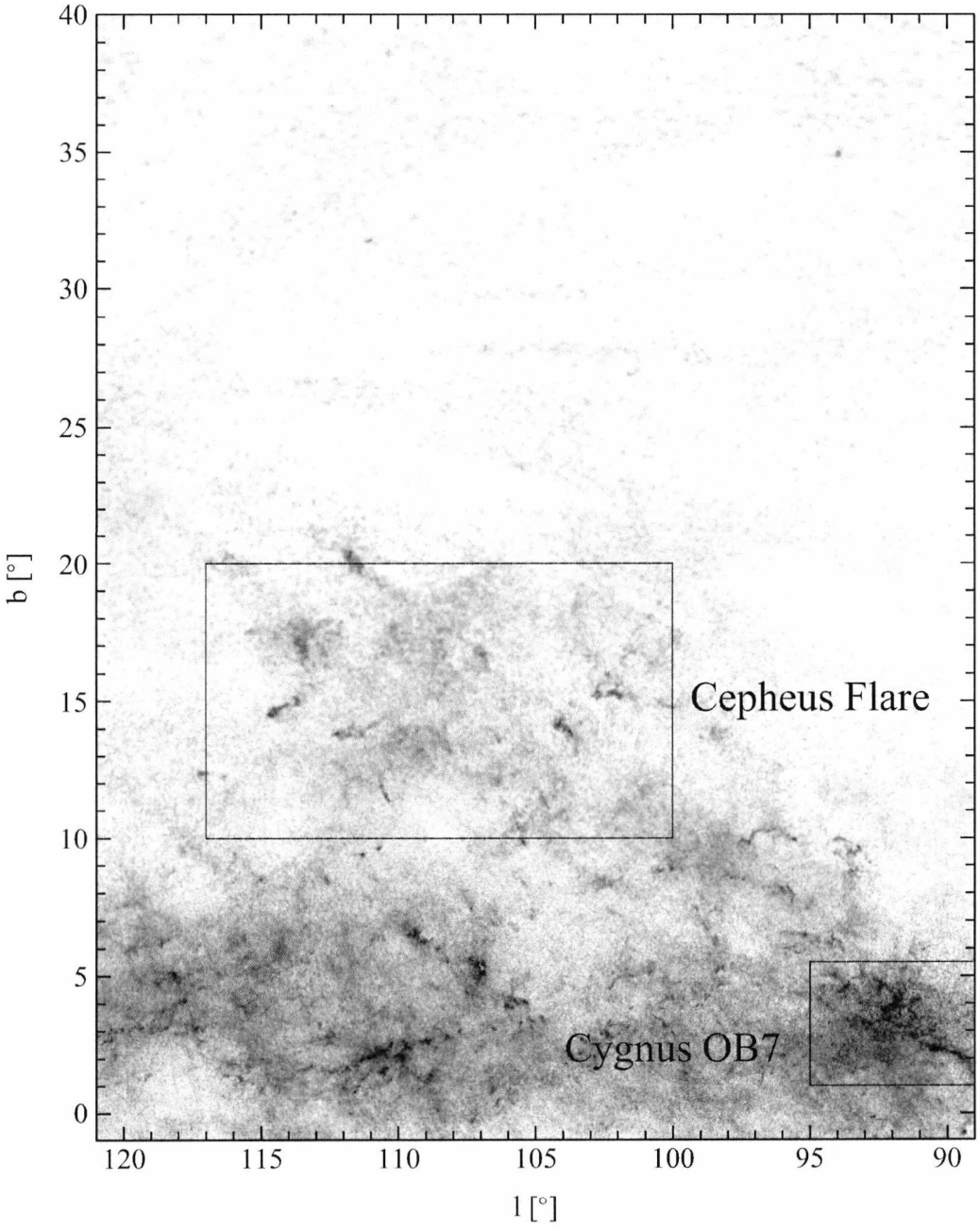

Figure A.4: Grey scale representation of a detail of the *con-noise* extinction map based on the nearest 49 stars. Extinction values are square root scaled from 0 mag (white) to 15 mag (black) of optical extinction.

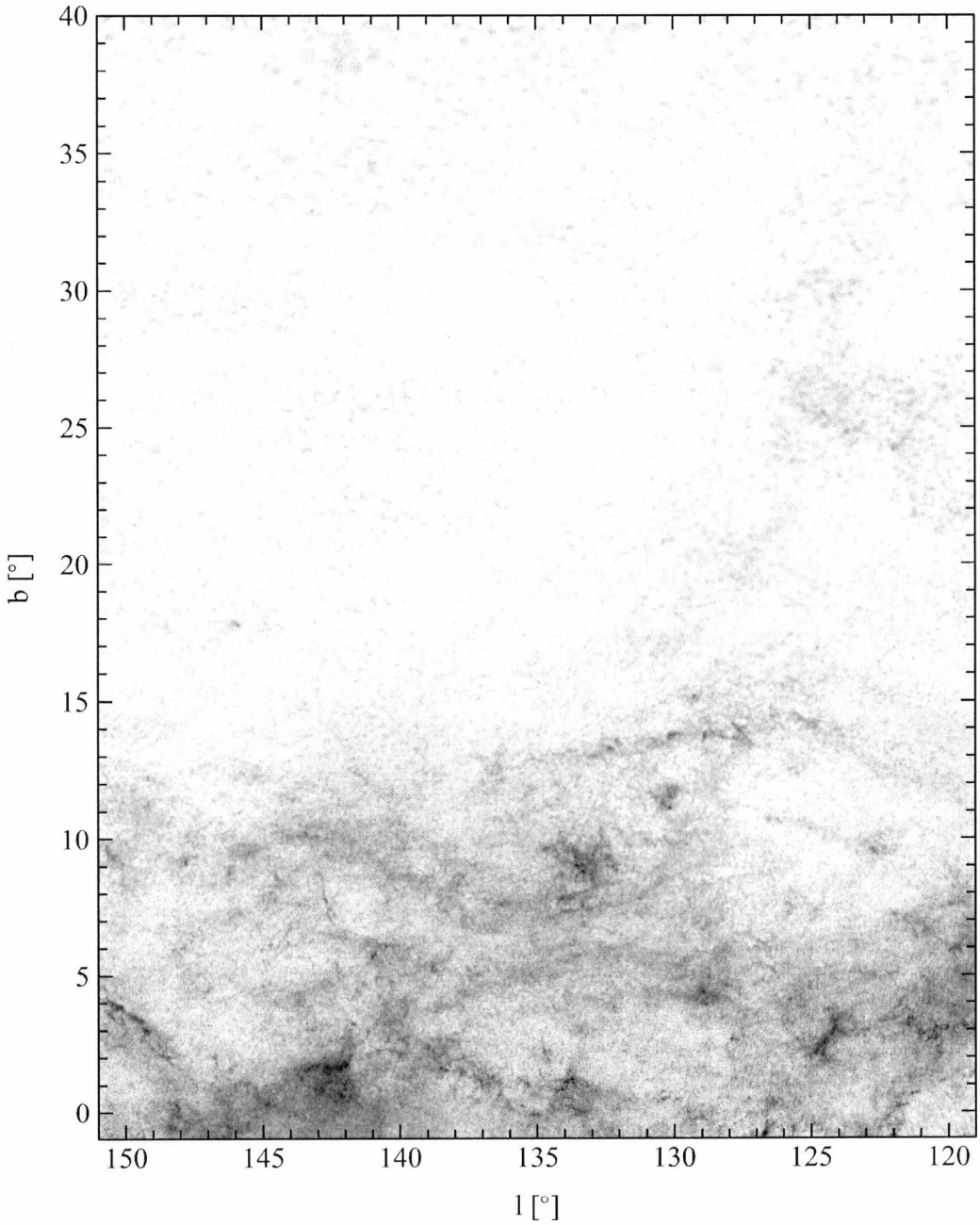

Figure A.5: Grey scale representation of a detail of the *con-noise* extinction map based on the nearest 49 stars. Extinction values are square root scaled from 0 mag (white) to 15 mag (black) of optical extinction.

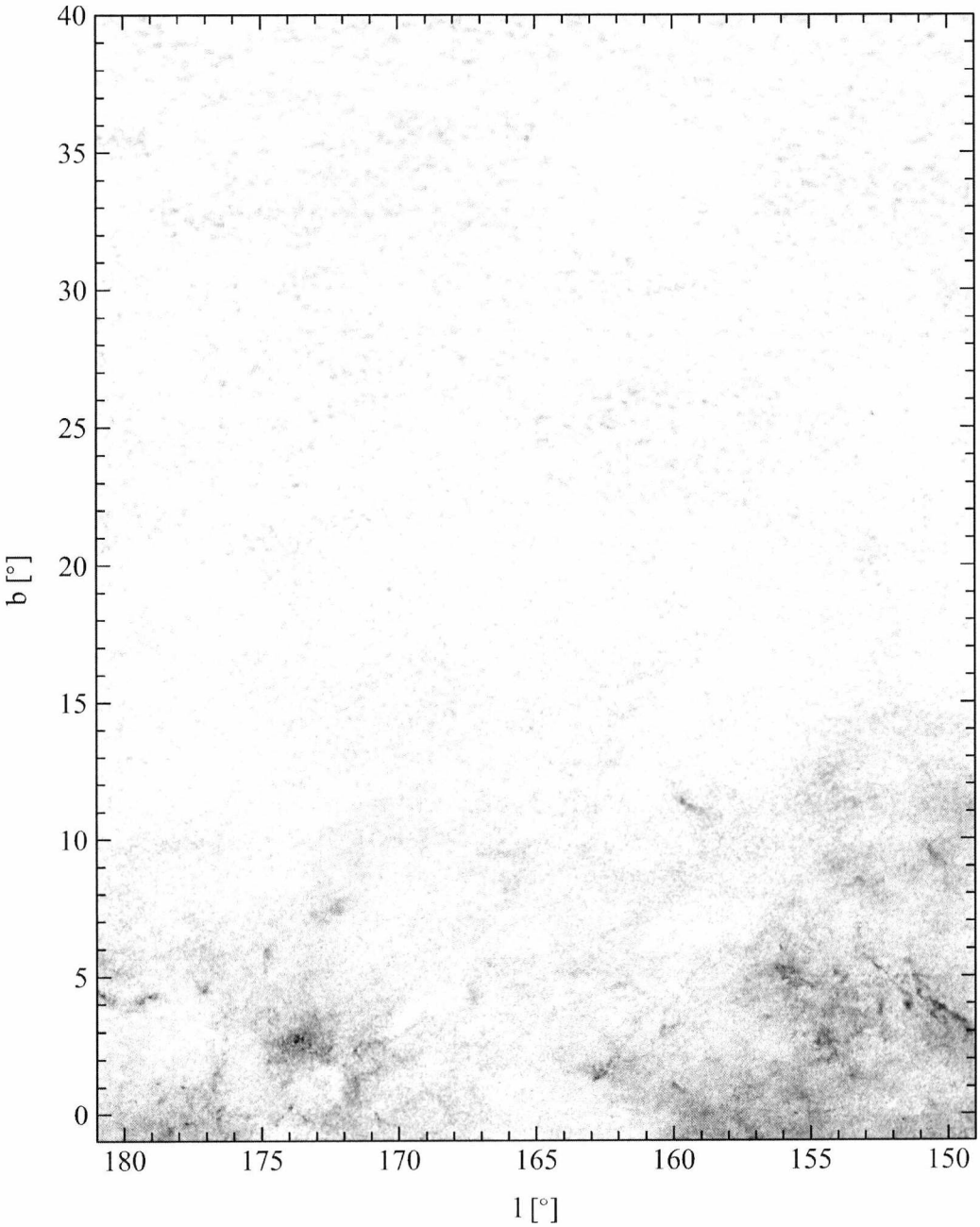

Figure A.6: Grey scale representation of a detail of the *con-noise* extinction map based on the nearest 49 stars. Extinction values are square root scaled from 0 mag (white) to 15 mag (black) of optical extinction.

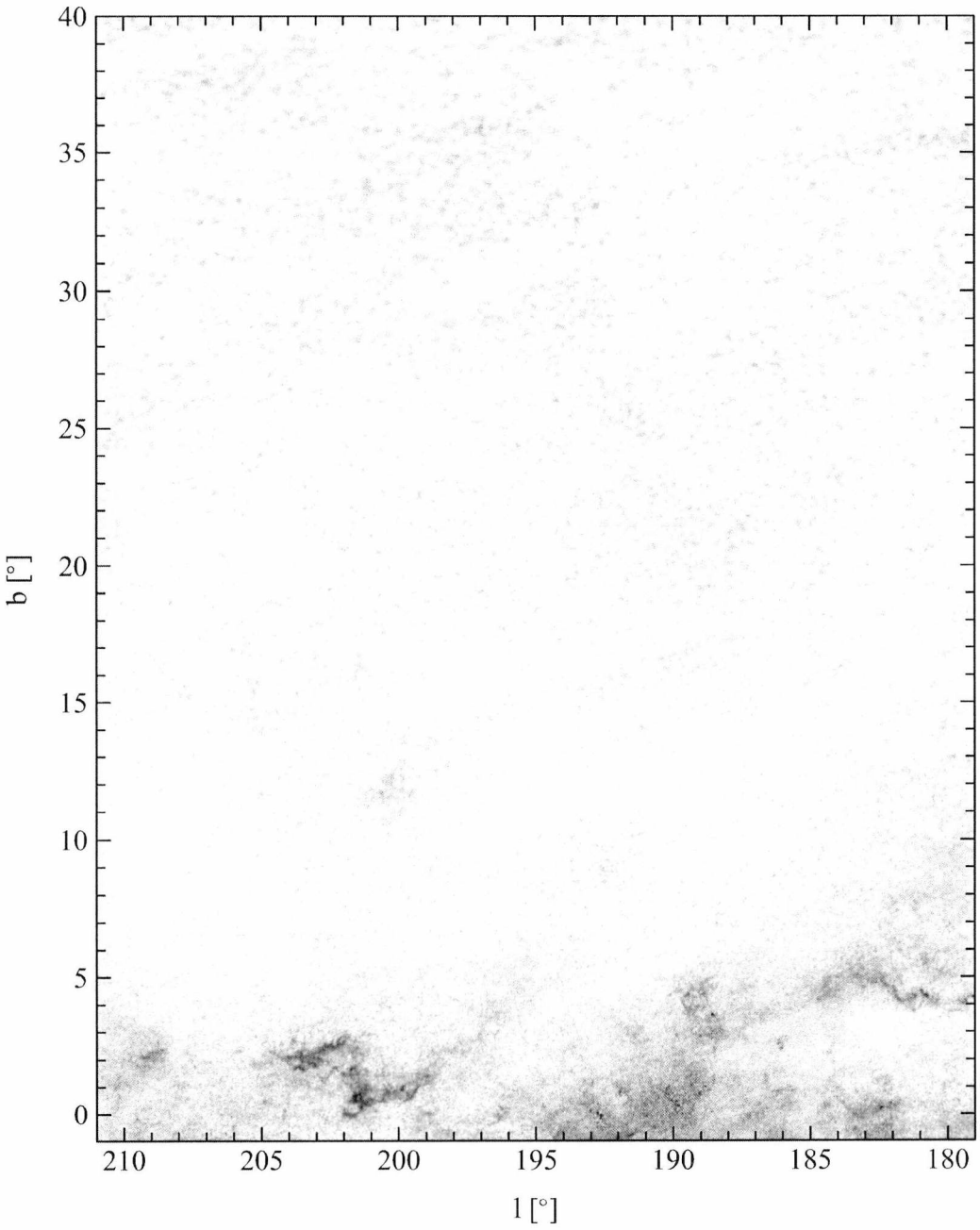

Figure A.7: Grey scale representation of a detail of the *con-noise* extinction map based on the nearest 49 stars. Extinction values are square root scaled from 0 mag (white) to 15 mag (black) of optical extinction.

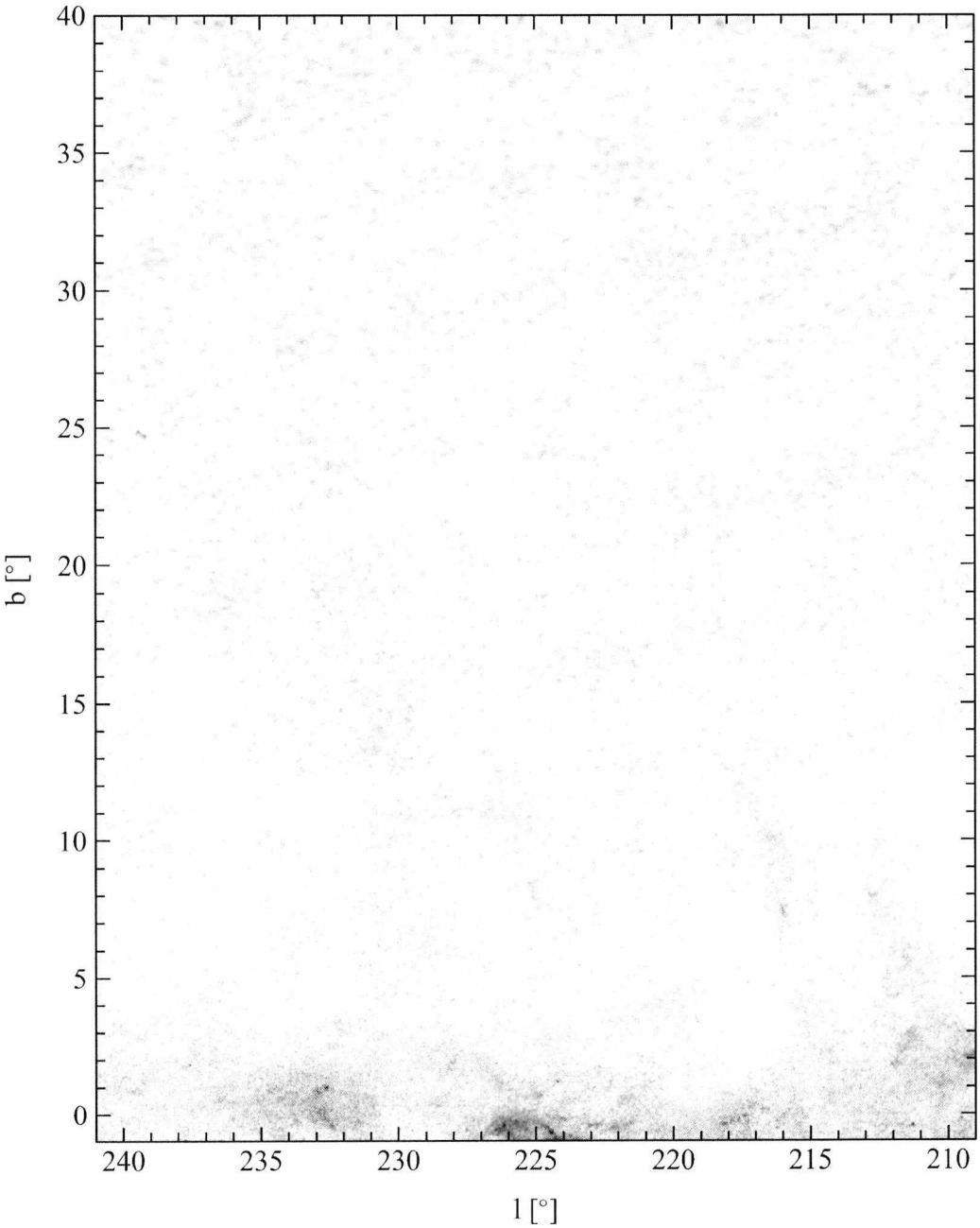

Figure A.8: Grey scale representation of a detail of the *con-noise* extinction map based on the nearest 49 stars. Extinction values are square root scaled from 0 mag (white) to 15 mag (black) of optical extinction.

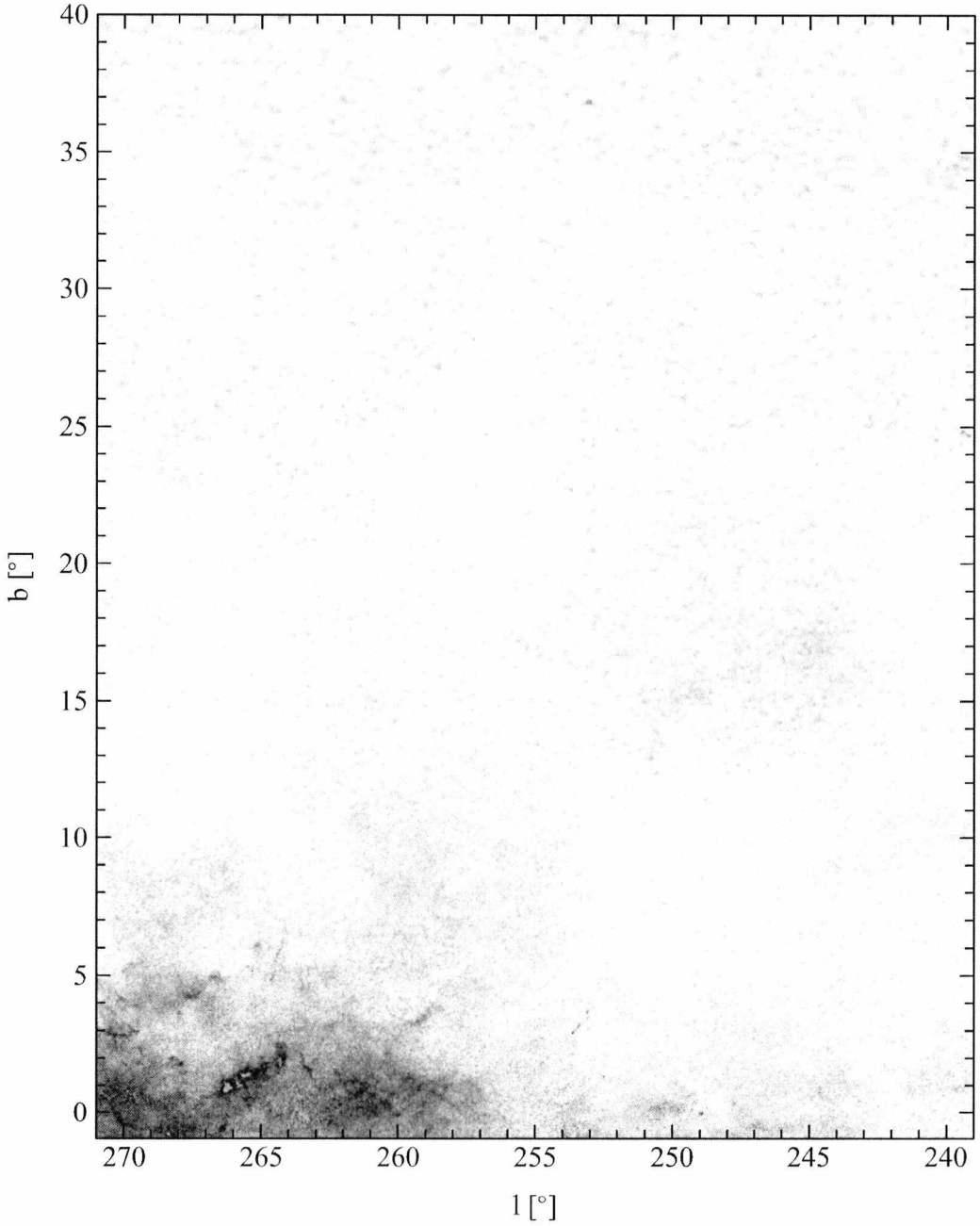

Figure A.9: Grey scale representation of a detail of the *con-noise* extinction map based on the nearest 49 stars. Extinction values are square root scaled from 0 mag (white) to 15 mag (black) of optical extinction.

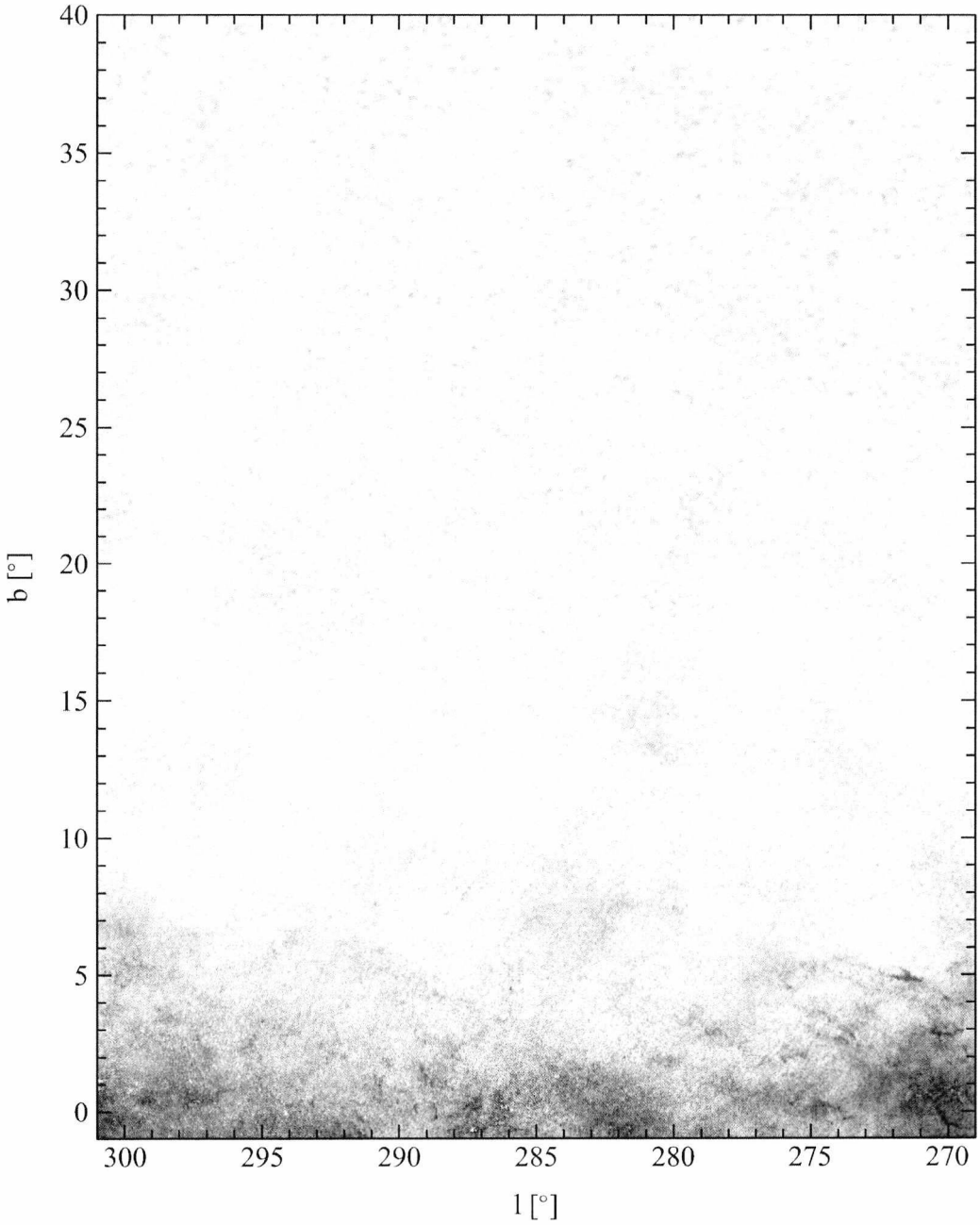

Figure A.10: Grey scale representation of a detail of the *con-noise* extinction map based on the nearest 49 stars. Extinction values are square root scaled from 0 mag (white) to 15 mag (black) of optical extinction.

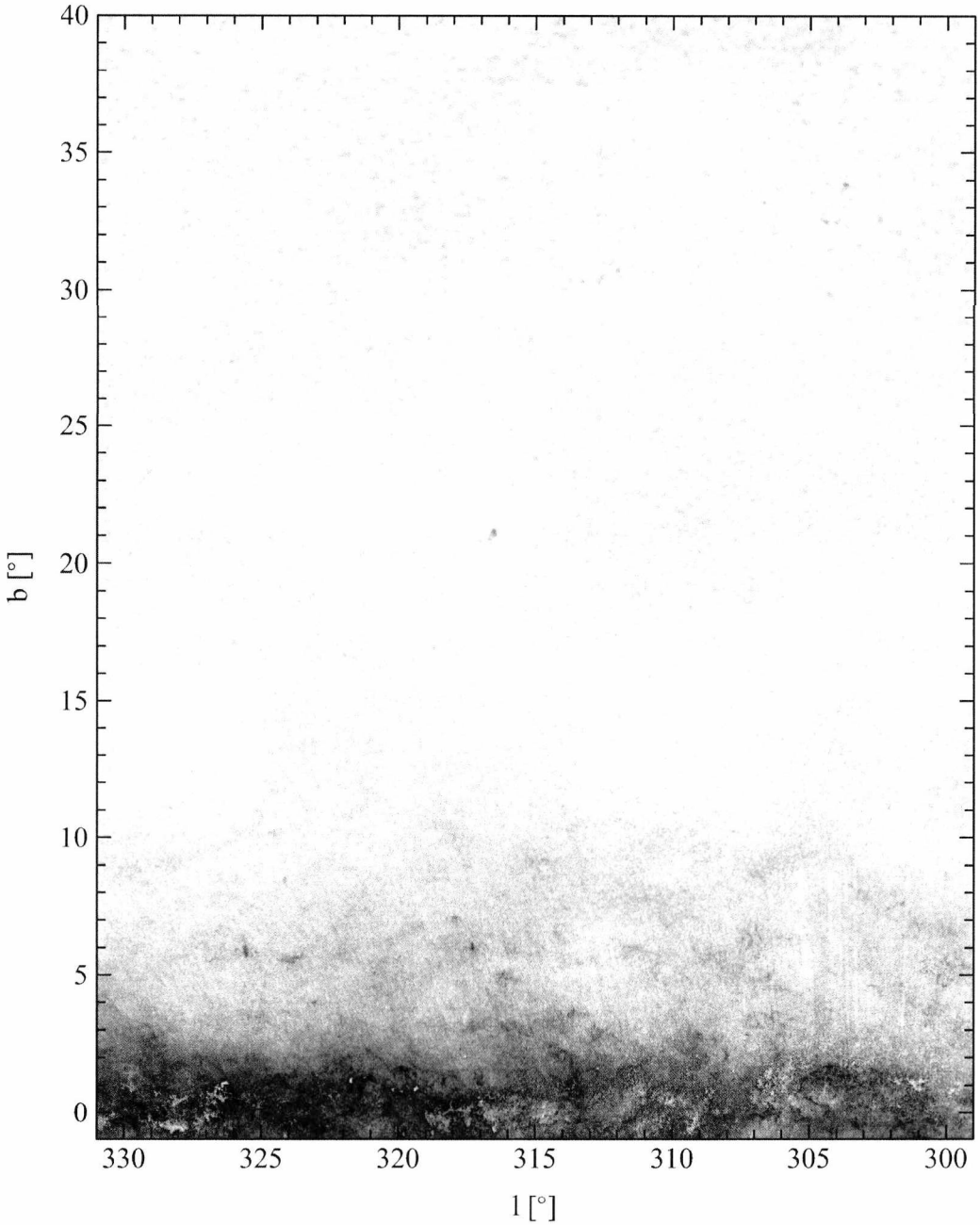

Figure A.11: Grey scale representation of a detail of the *con-noise* extinction map based on the nearest 49 stars. Extinction values are square root scaled from 0 mag (white) to 15 mag (black) of optical extinction.

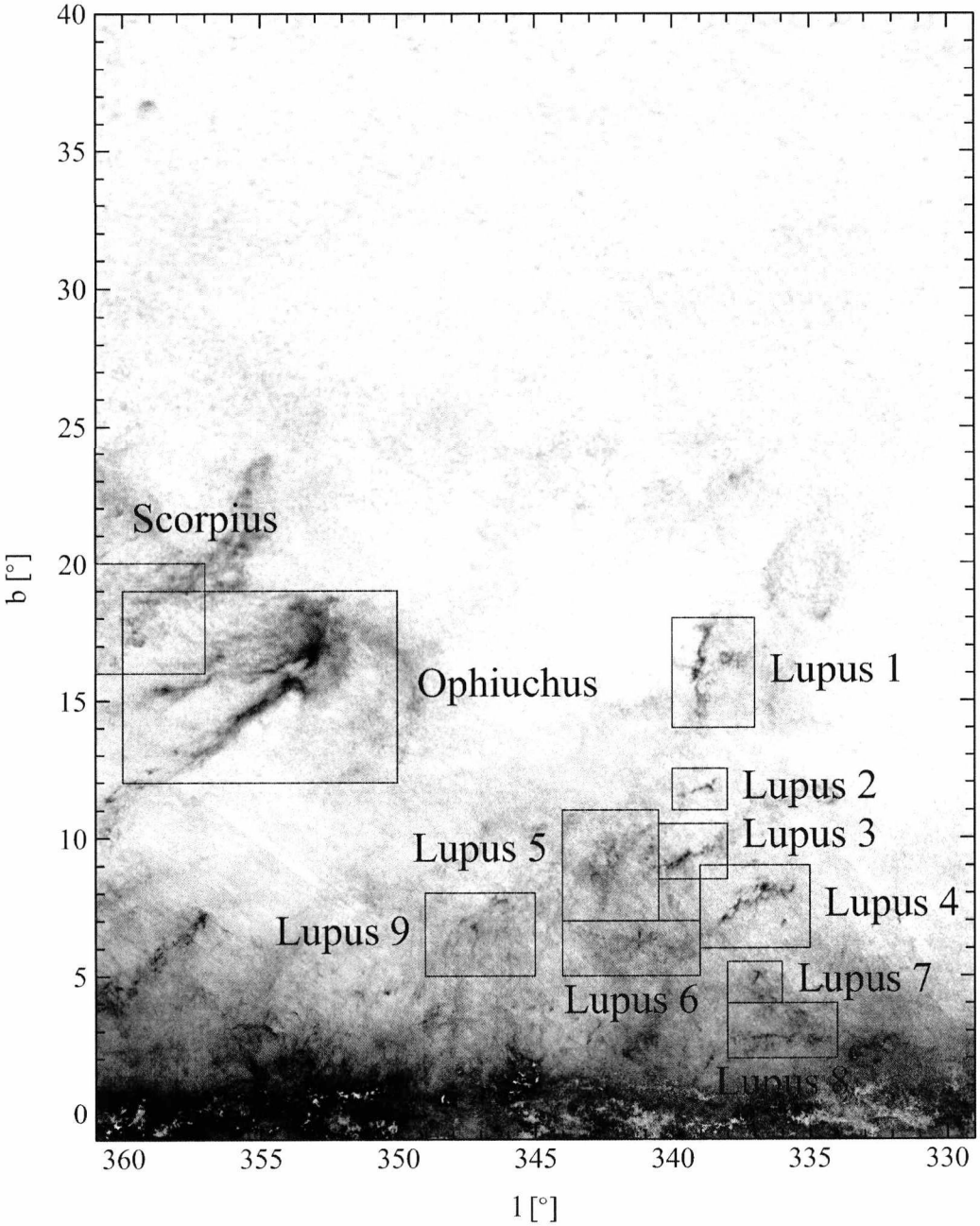

Figure A.12: Grey scale representation of a detail of the *con-noise* extinction map based on the nearest 49 stars. Extinction values are square root scaled from 0 mag (white) to 15 mag (black) of optical extinction.

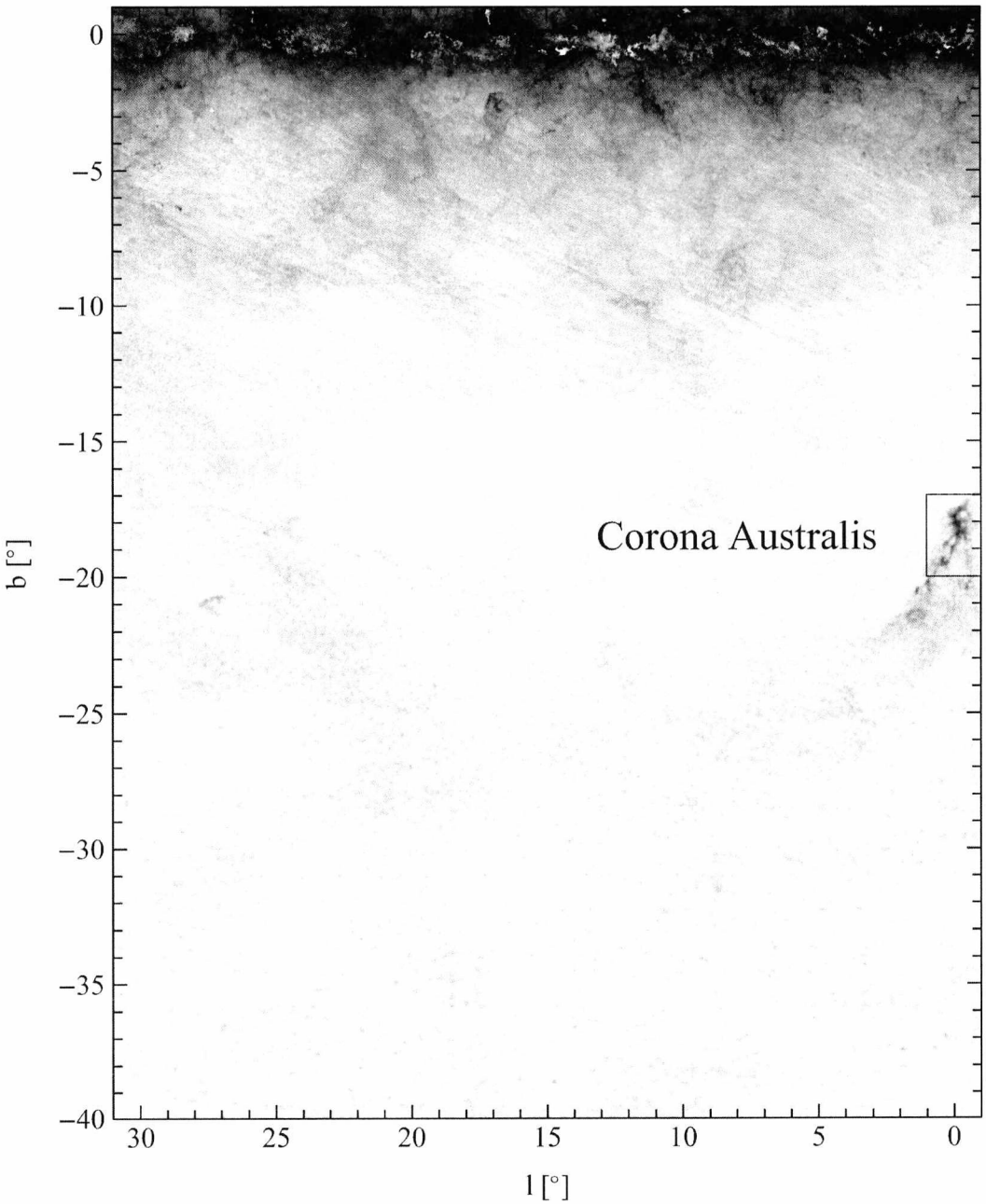

Figure A.13: Grey scale representation of a detail of the *con-noise* extinction map based on the nearest 49 stars. Extinction values are square root scaled from 0 mag (white) to 15 mag (black) of optical extinction.

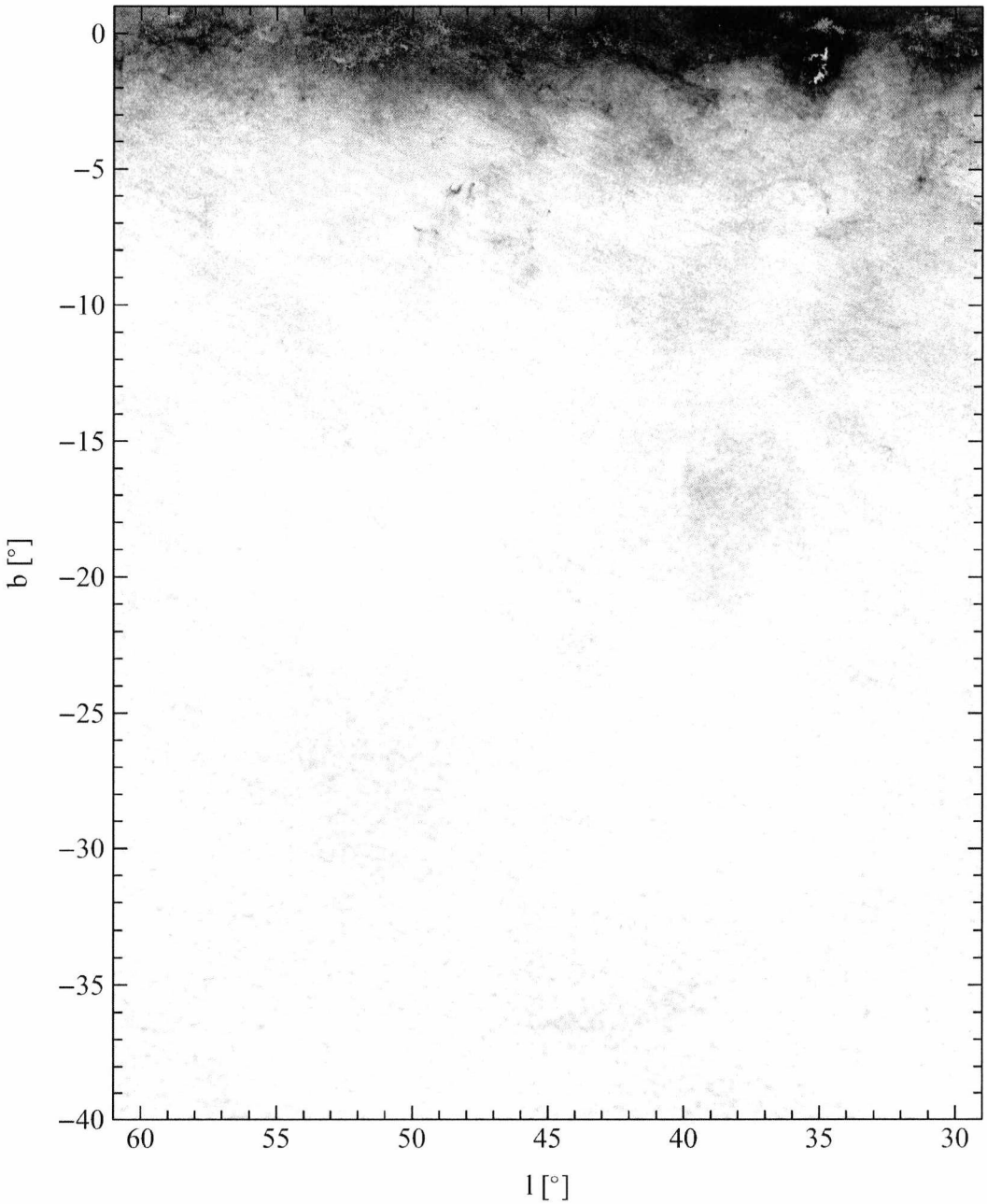

Figure A.14: Grey scale representation of a detail of the *con-noise* extinction map based on the nearest 49 stars. Extinction values are square root scaled from 0 mag (white) to 15 mag (black) of optical extinction.

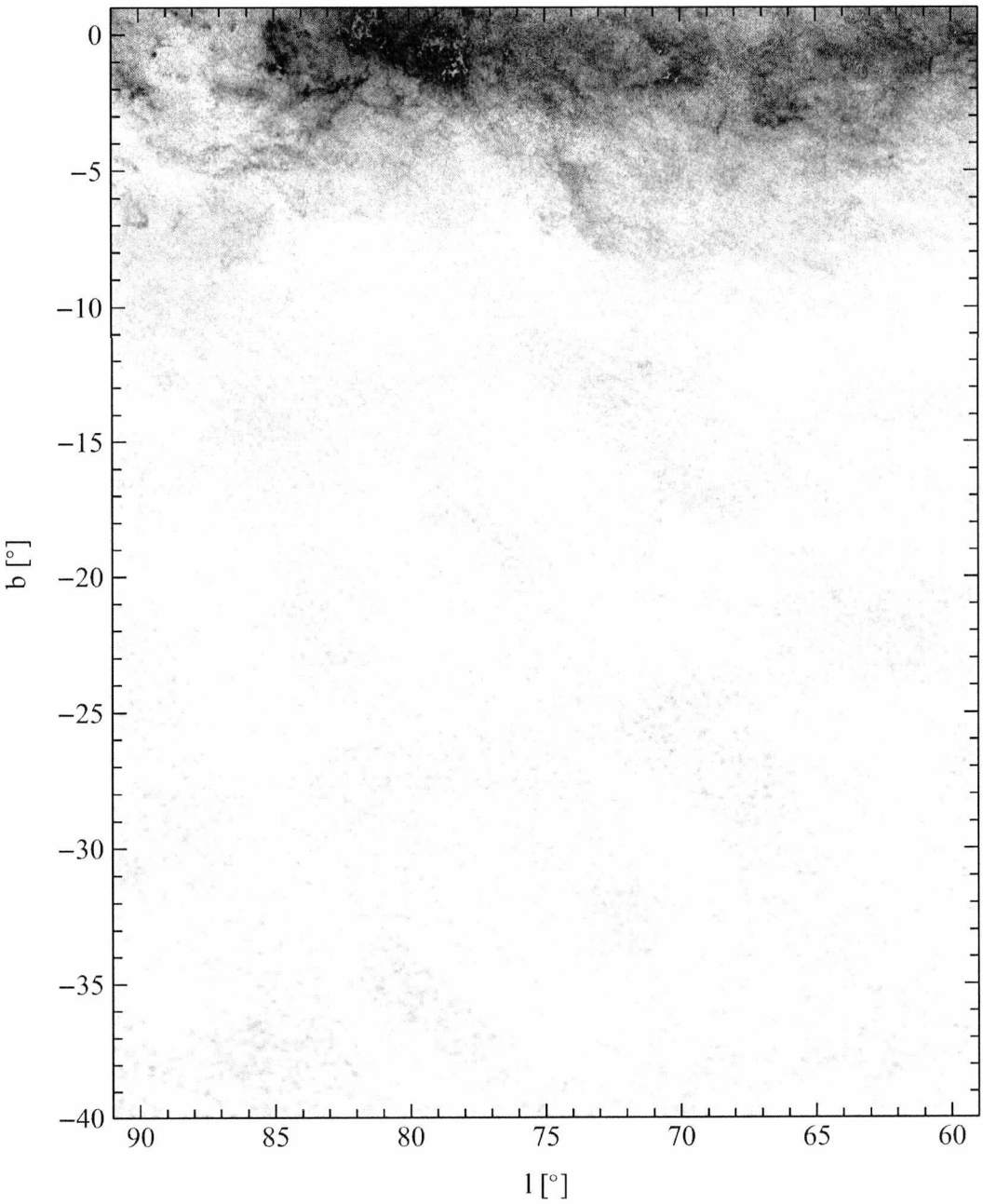

Figure A.15: Grey scale representation of a detail of the *con-noise* extinction map based on the nearest 49 stars. Extinction values are square root scaled from 0 mag (white) to 15 mag (black) of optical extinction.

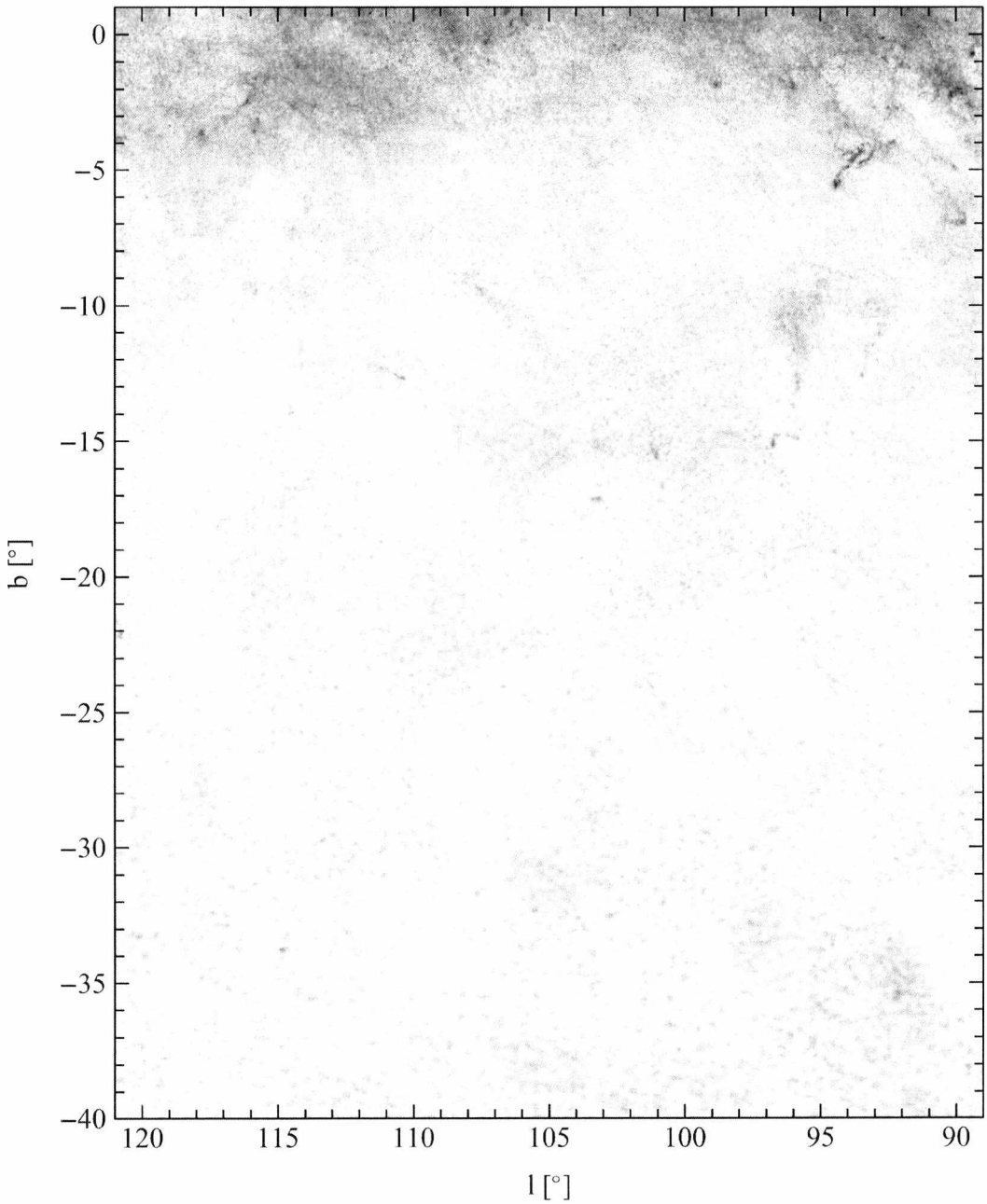

Figure A.16: Grey scale representation of a detail of the *con-noise* extinction map based on the nearest 49 stars. Extinction values are square root scaled from 0 mag (white) to 15 mag (black) of optical extinction.

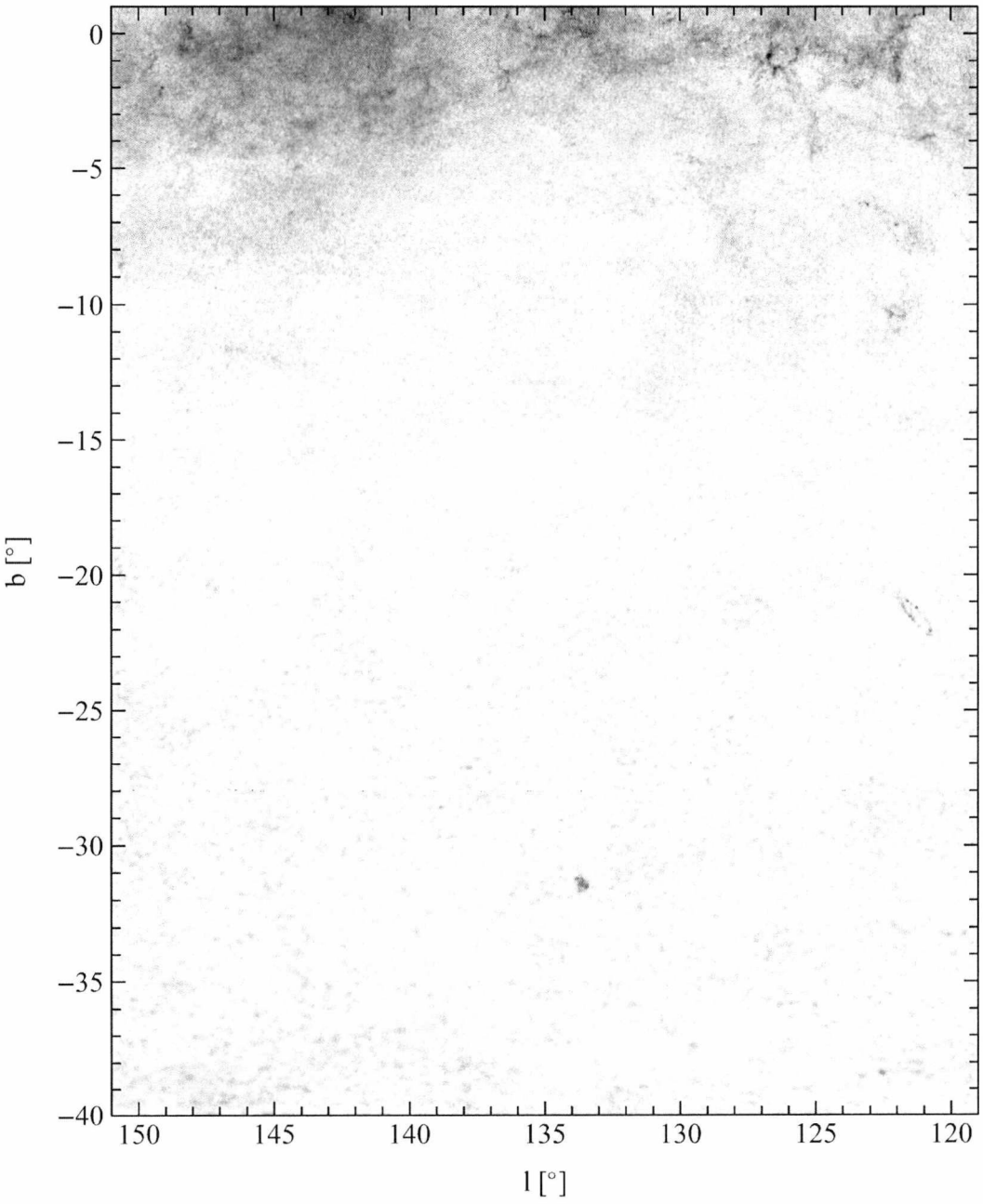

Figure A.17: Grey scale representation of a detail of the *con-noise* extinction map based on the nearest 49 stars. Extinction values are square root scaled from 0 mag (white) to 15 mag (black) of optical extinction.

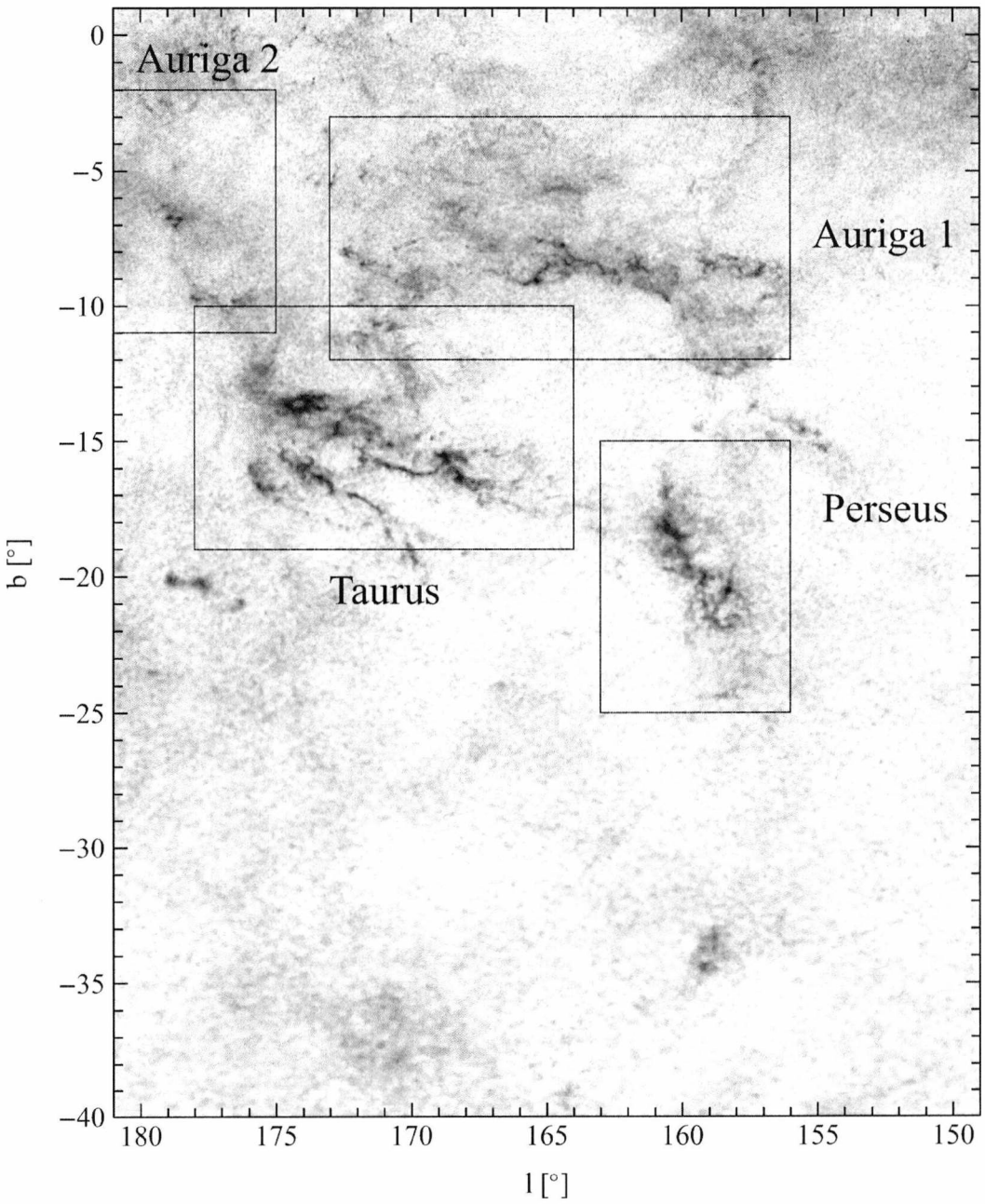

Figure A.18: Grey scale representation of a detail of the *con-noise* extinction map based on the nearest 49 stars. Extinction values are square root scaled from 0 mag (white) to 15 mag (black) of optical extinction.

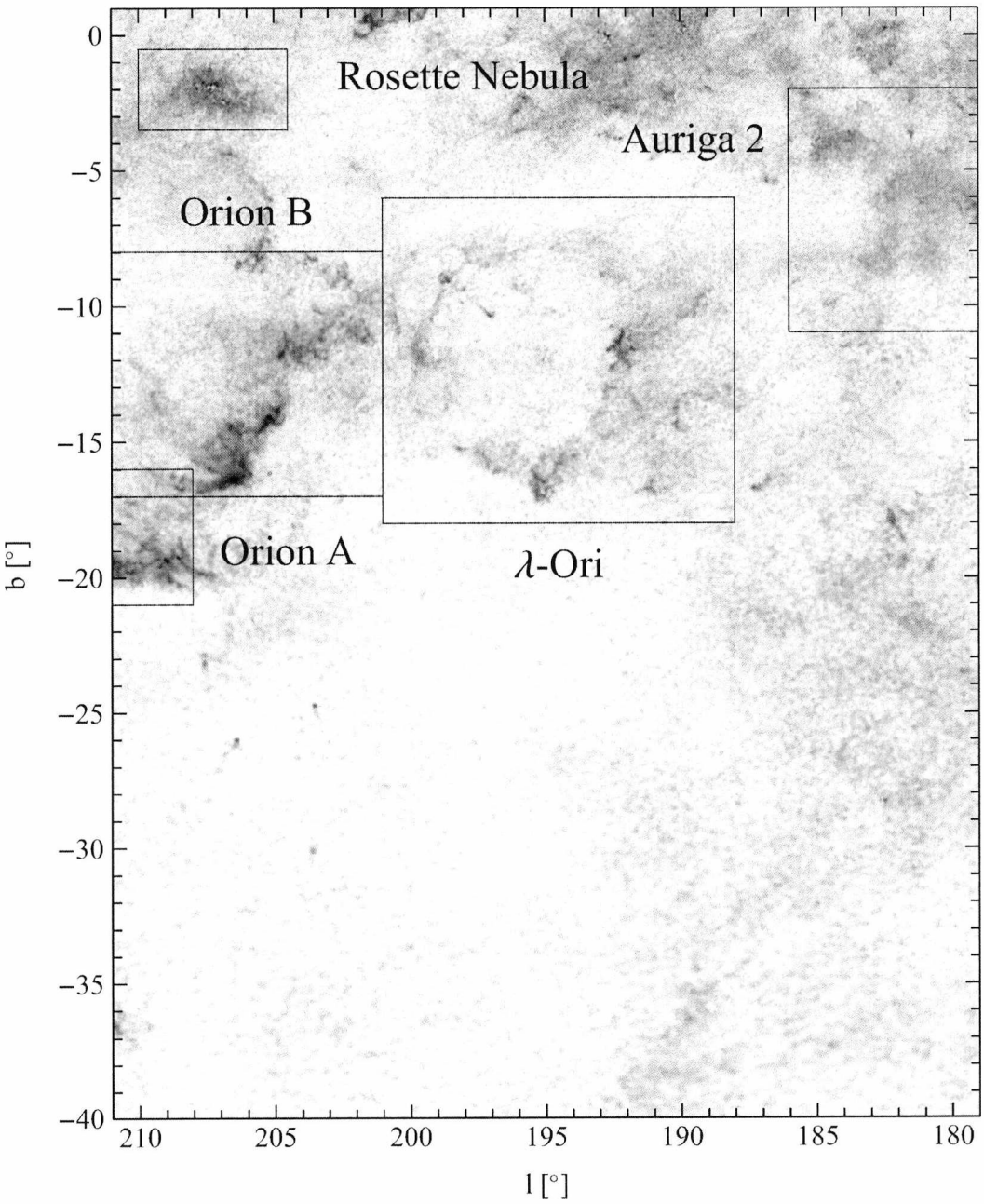

Figure A.19: Grey scale representation of a detail of the *con-noise* extinction map based on the nearest 49 stars. Extinction values are square root scaled from 0 mag (white) to 15 mag (black) of optical extinction.

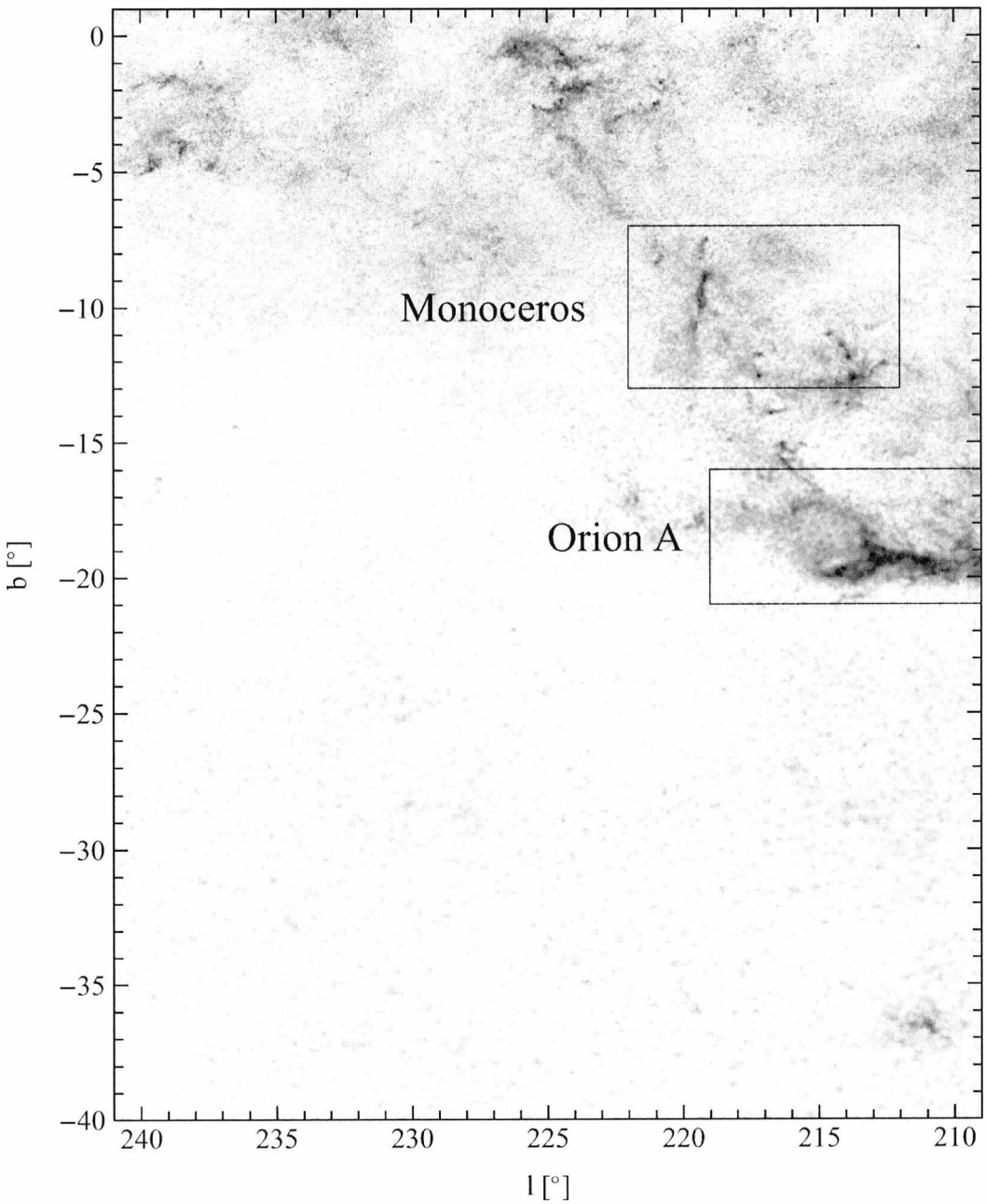

Figure A.20: Grey scale representation of a detail of the *con-noise* extinction map based on the nearest 49 stars. Extinction values are square root scaled from 0 mag (white) to 15 mag (black) of optical extinction.

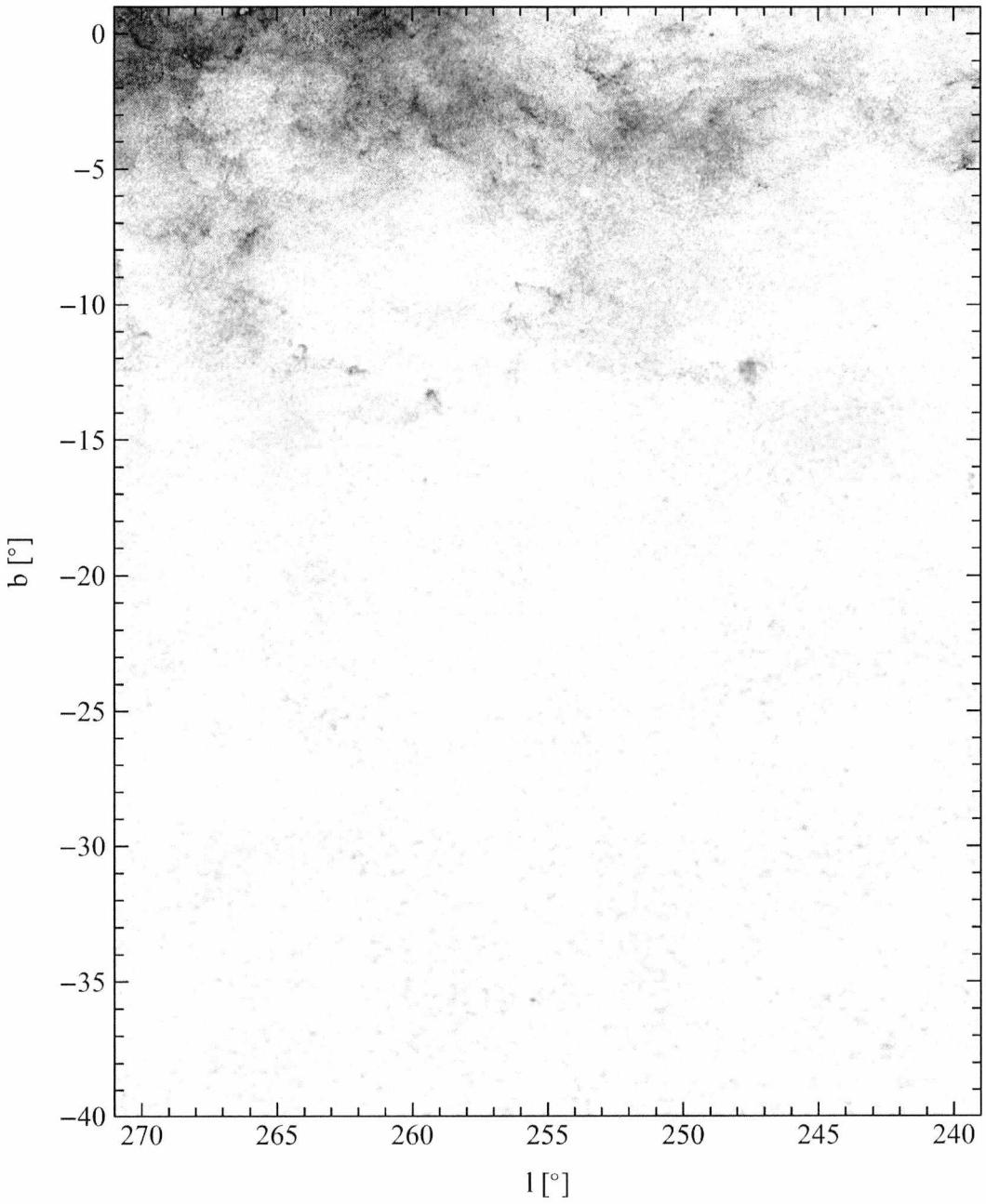

Figure A.21: Grey scale representation of a detail of the *con-noise* extinction map based on the nearest 49 stars. Extinction values are square root scaled from 0 mag (white) to 15 mag (black) of optical extinction.

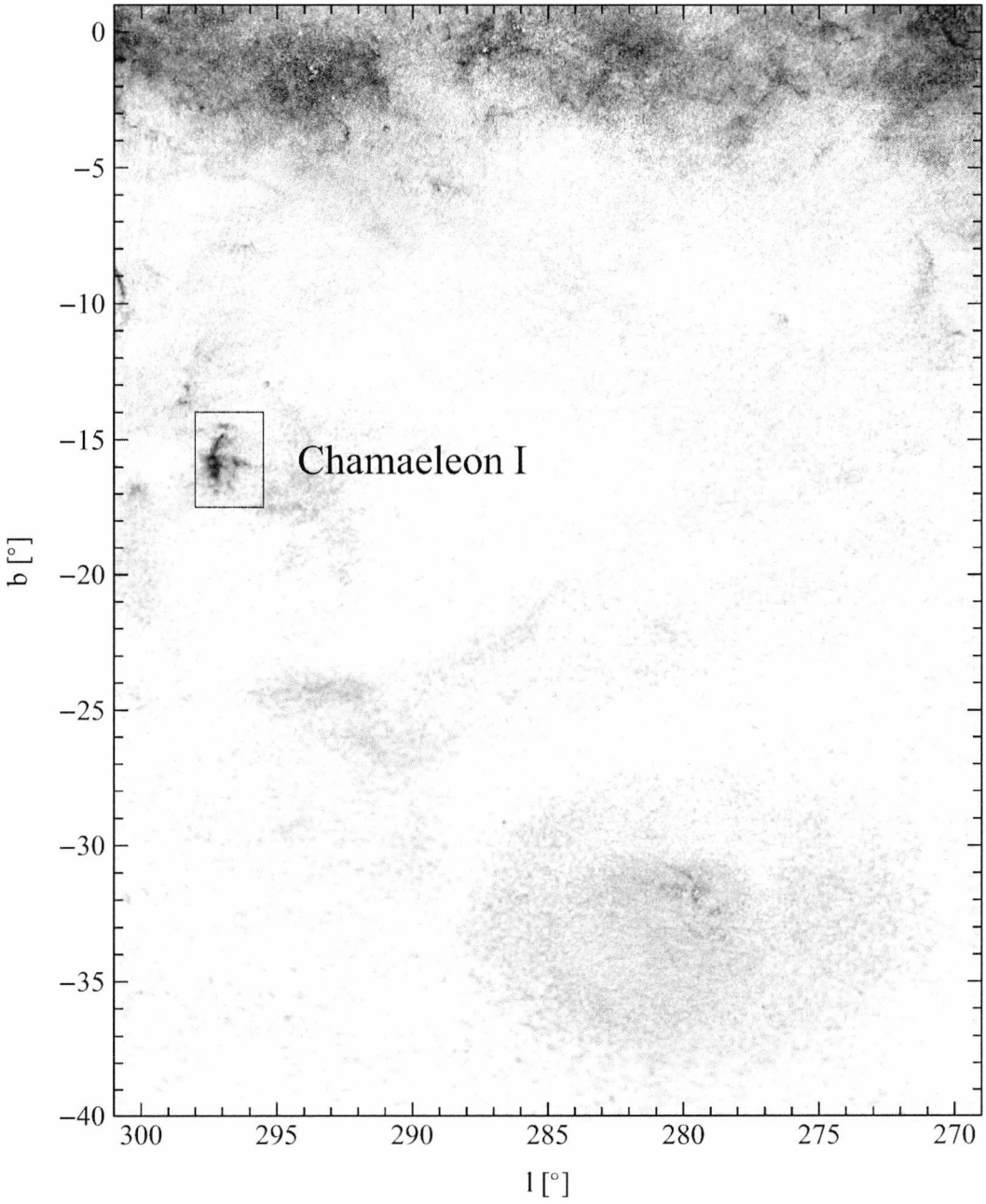

Figure A.22: Grey scale representation of a detail of the *con-noise* extinction map based on the nearest 49 stars. Extinction values are square root scaled from 0 mag (white) to 15 mag (black) of optical extinction.

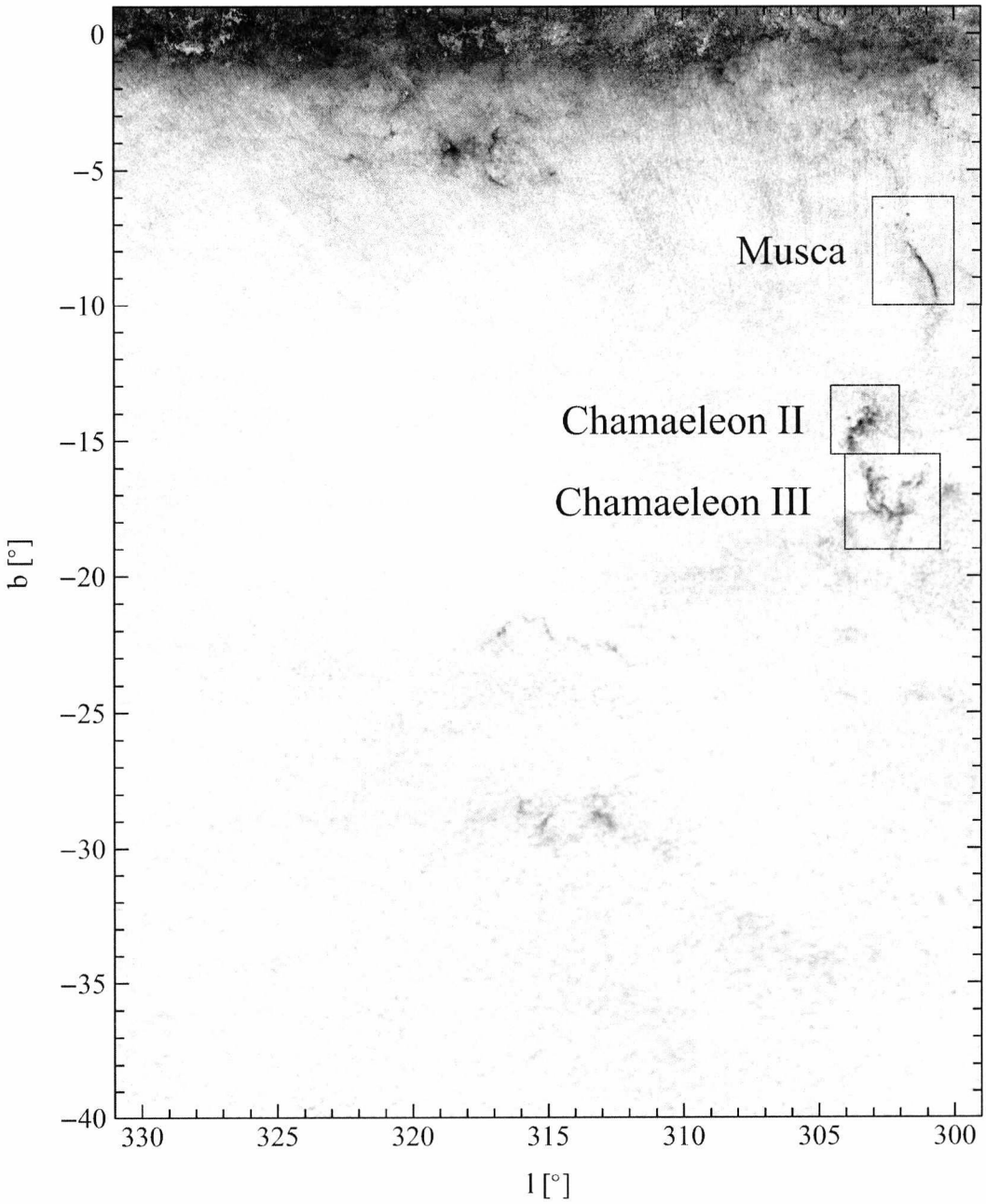

Figure A.23: Grey scale representation of a detail of the *con-noise* extinction map based on the nearest 49 stars. Extinction values are square root scaled from 0 mag (white) to 15 mag (black) of optical extinction.

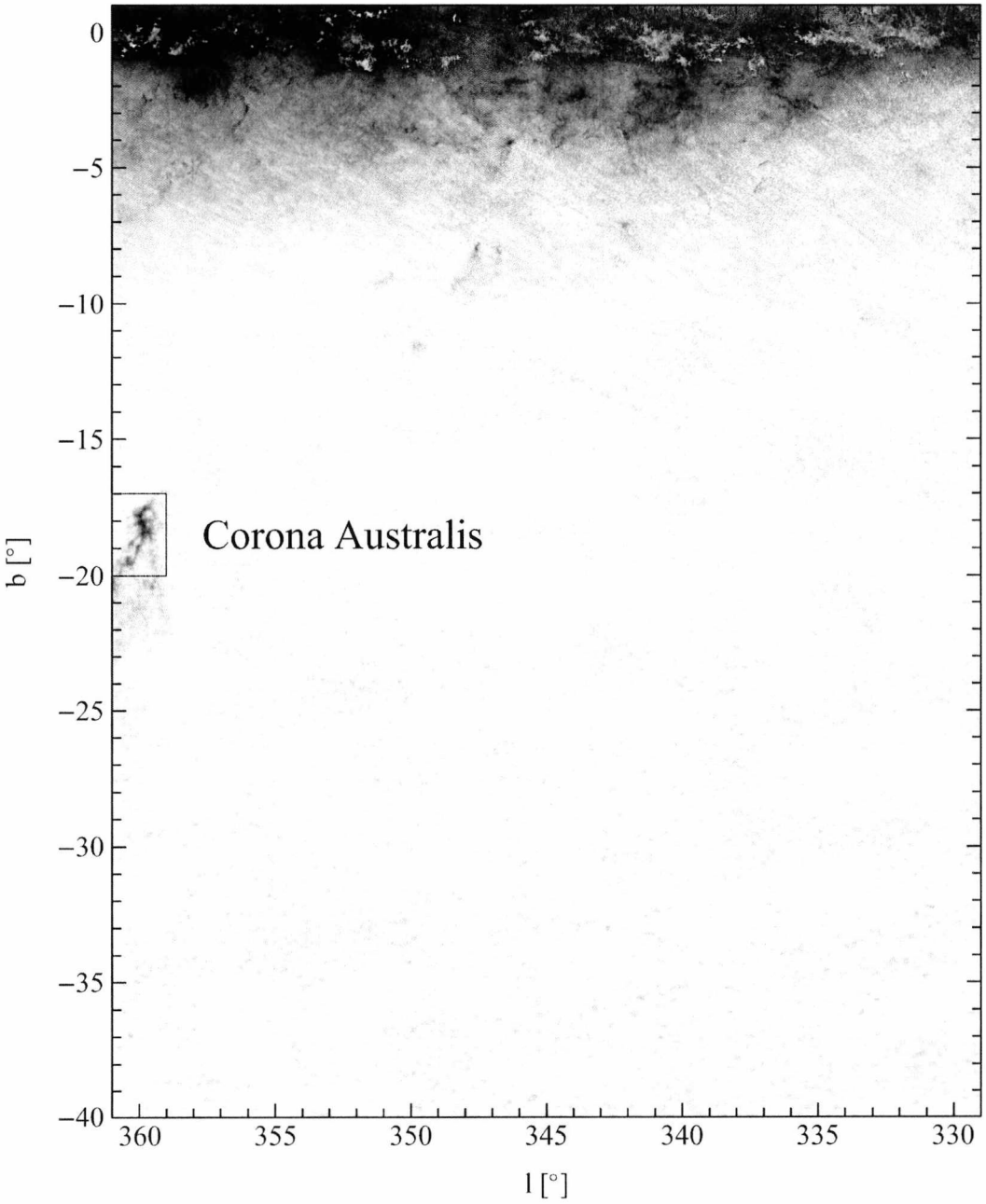

Figure A.24: Grey scale representation of a detail of the *con-noise* extinction map based on the nearest 49 stars. Extinction values are square root scaled from 0 mag (white) to 15 mag (black) of optical extinction.

A.2 Comparison of Maps for Selected Regions

A.2.1 Our Map vs. Dobashi et al. (2005)

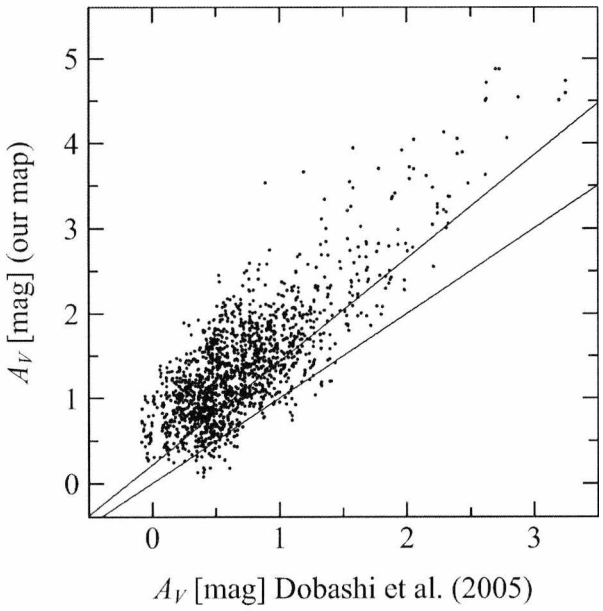

Figure A.25: Comparison of the optical extinction values for region1 (Camelopardalis) in Table 3.4 between our extinction map and the map from Dobashi et al.. As solid line we overplot a one-to-one line, as well as a linear fit. See Table 3.4 for the parameters of the fit.

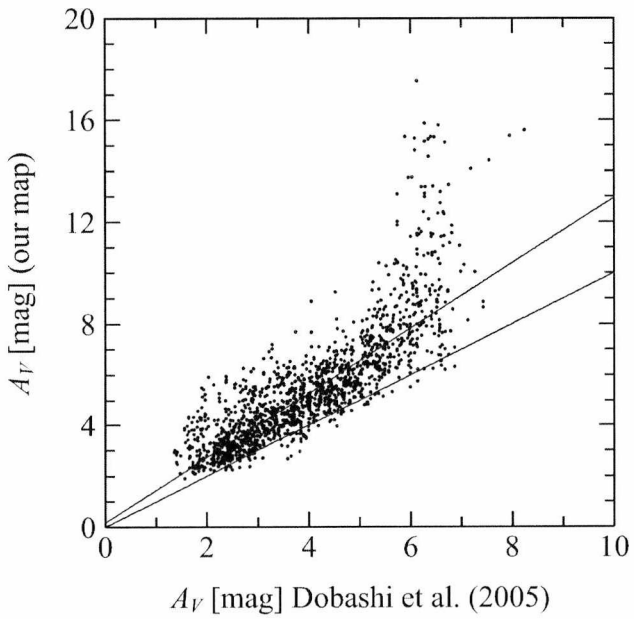

Figure A.26: Comparison of the optical extinction values for region2 (Serpens) in Table 3.4 between our extinction map and the map from Dobashi et al. As solid line we overplot a one-to-one line, as well as a linear fit. See Table 3.4 for the parameters of the fit.

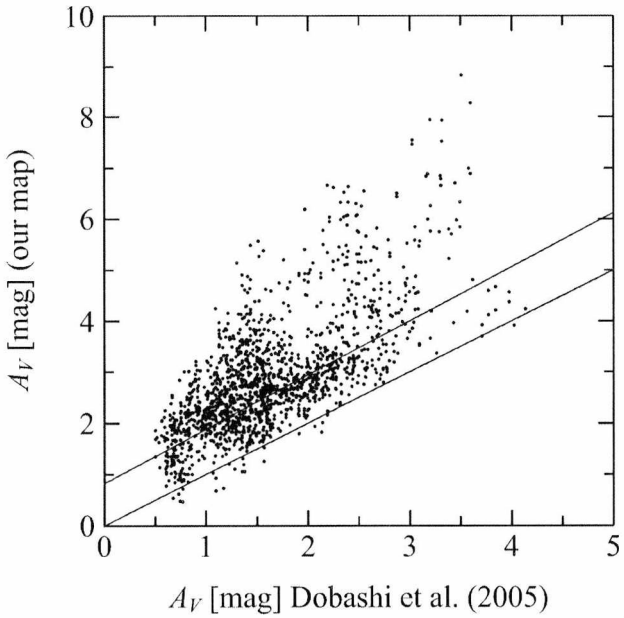

Figure A.27: Comparison of the optical extinction values for region3 (Lupus) in Table 3.2 between our extinction map and the map from Dobashi et al. As solid line we overplot a one-to-one line, as well as a linear fit. See Table 3.2 for the parameters of the fit.

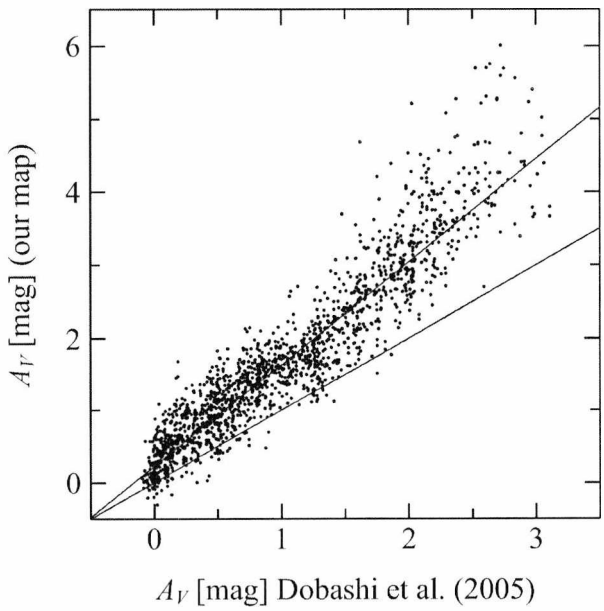

Figure A.28: Comparison of the optical extinction values for region4 (Vela) in Table 3.2 between our extinction map and the map from Dobashi et al. As solid line we overplot a one-to-one line, as well as a linear fit. See Table 3.2 for the parameters of the fit.

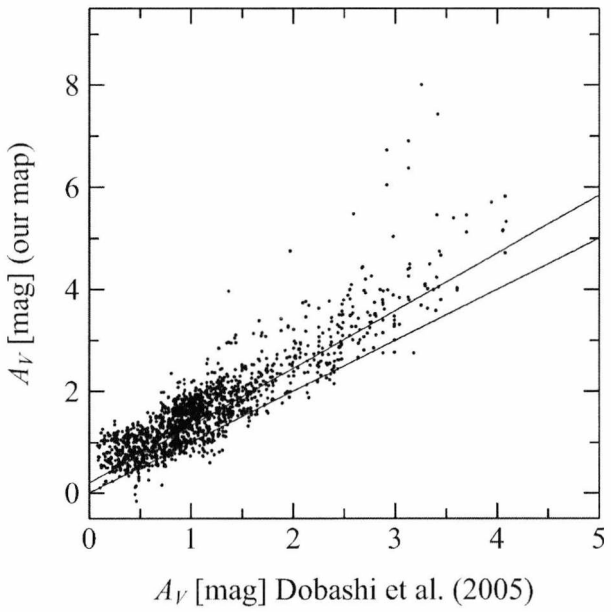

Figure A.29: Comparison of the optical extinction values for region5 (Taurus) in Table 3.2 between our extinction map and the map from Dobashi et al. As solid line we overplot a one-to-one line, as well as a linear fit. See Table 3.2 for the parameters of the fit.

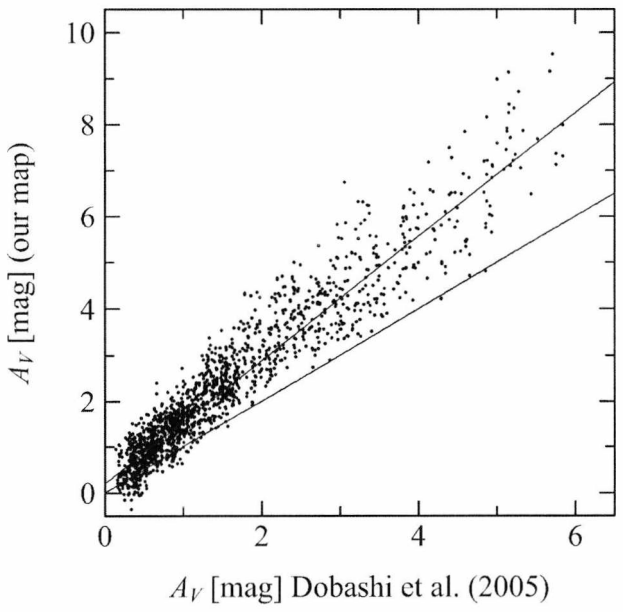

Figure A.30: Comparison of the optical extinction values for region6 (North America Nebula) in Table 3.2 between our extinction map and the map from Dobashi et al. As solid line we overplot a one-to-one line, as well as a linear fit. See Table 3.2 for the parameters of the fit.

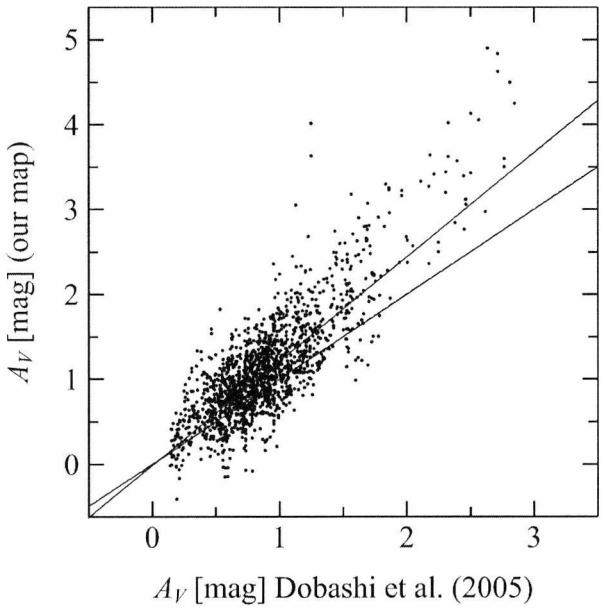

Figure A.31: Comparison of the optical extinction values for region7 (Monoceros) in Table 3.2 between our extinction map and the map from Dobashi et al. As solid line we overplot a one-to-one line, as well as a linear fit. See Table 3.2 for the parameters of the fit.

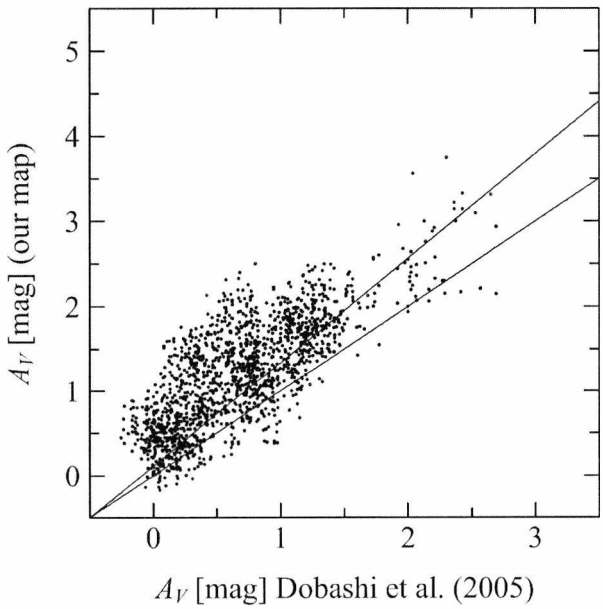

Figure A.32: Comparison of the optical extinction values for region8 (Auriga) in Table 3.2 between our extinction map and the map from Dobashi et al. As solid line we overplot a one-to-one line, as well as a linear fit. See Table 3.2 for the parameters of the fit.

A.2.2 Our Map vs. Schlegel et al. (1998)

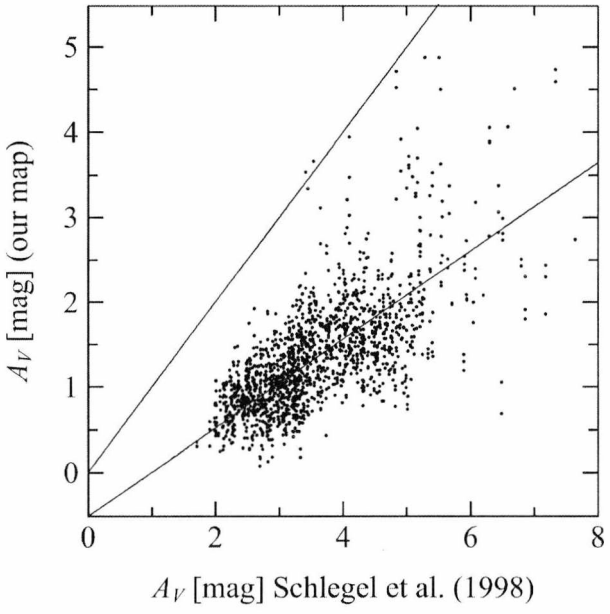

Figure A.33: Comparison of the optical extinction values for region1 (Camelopardalis) in Table 3.2 between our extinction map and the map from Schlegel et al. As solid line we overplot a one-to-one line, as well as a linear fit. See Table 3.2 for the parameters of the fit.

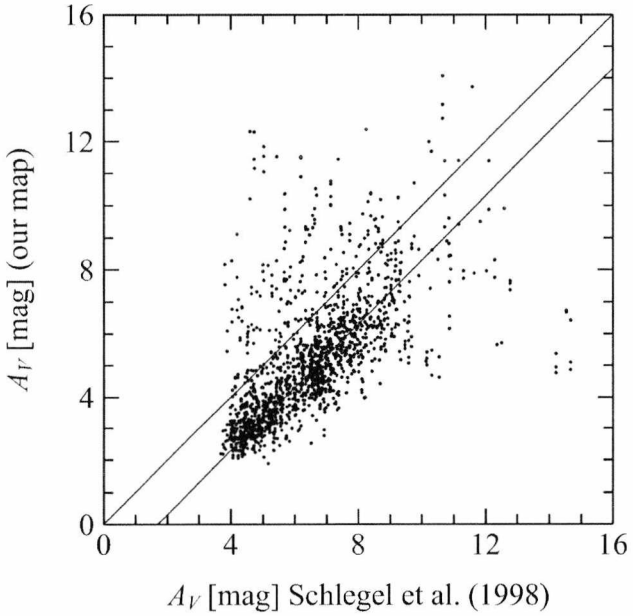

Figure A.34: Comparison of the optical extinction values for region2 (Serpens) in Table 3.2 between our extinction map and the map from Schlegel et al. As solid line we overplot a one-to-one line, as well as a linear fit. See Table 3.2 for the parameters of the fit.

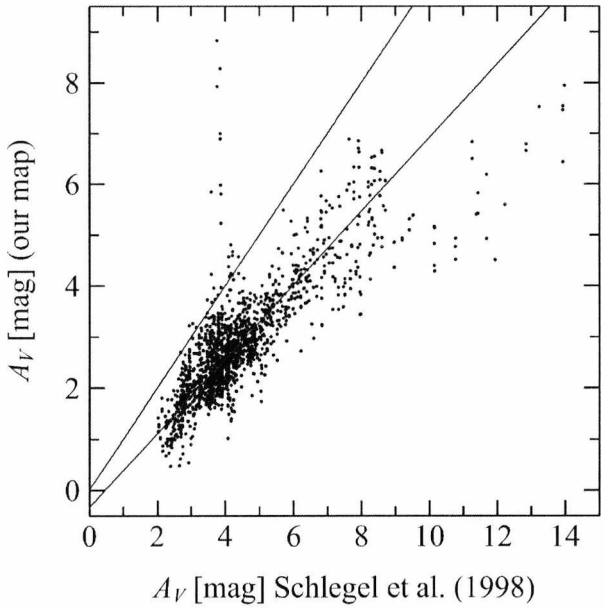

Figure A.35: Comparison of the optical extinction values for region3 (Lupus) in Table 3.2 between our extinction map and the map from Schlegel et al. As solid line we overplot a one-to-one line, as well as a linear fit. See Table 3.2 for the parameters of the fit.

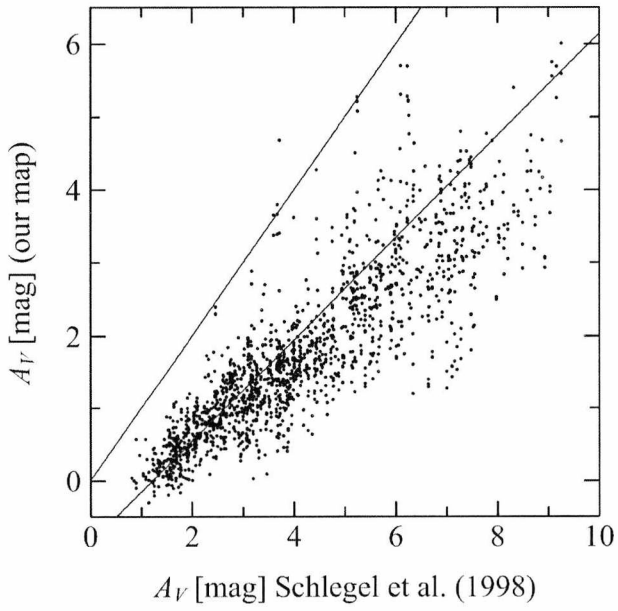

Figure A.36: Comparison of the optical extinction values for region4 (Vela) in Table 3.2 between our extinction map and the map from Schlegel et al. As solid line we overplot a one-to-one line, as well as a linear fit. See Table 3.2 for the parameters of the fit.

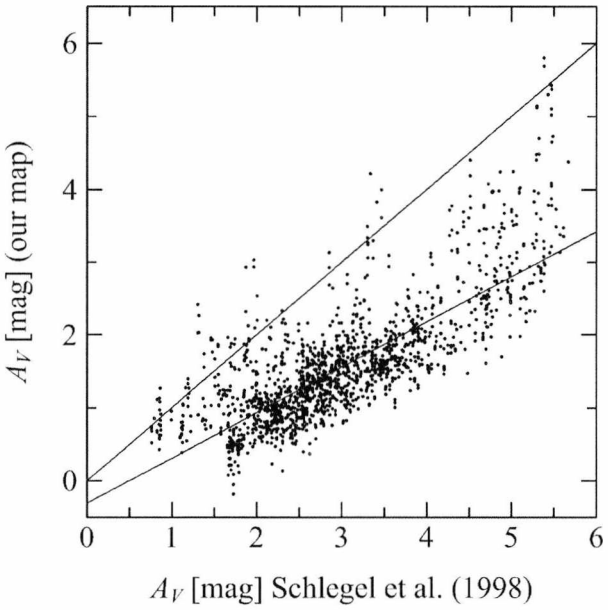

Figure A.37: Comparison of the optical extinction values for region5 (Taurus) in Table 3.2 between our extinction map and the map from Schlegel et al. As solid line we overplot a one-to-one line, as well as a linear fit. See Table 3.2 for the parameters of the fit.

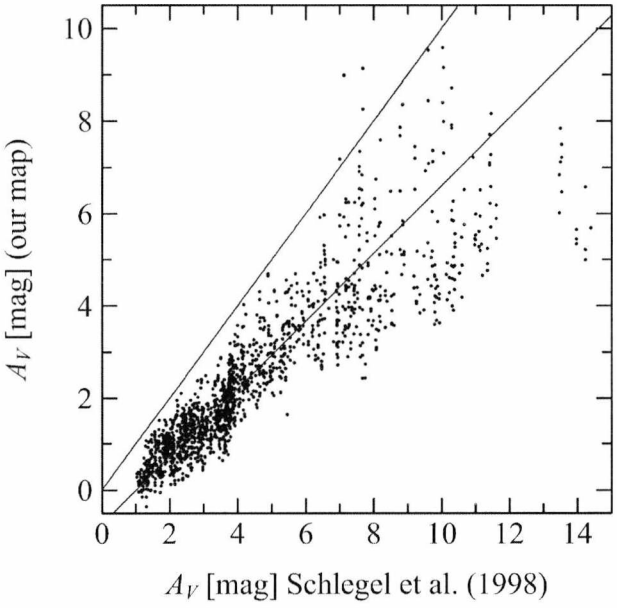

Figure A.38: Comparison of the optical extinction values for region6 (North America Nebula) in Table 3.2 between our extinction map and the map from Schlegel et al. As solid line we overplot a one-to-one line, as well as a linear fit. See Table 3.2 for the parameters of the fit.

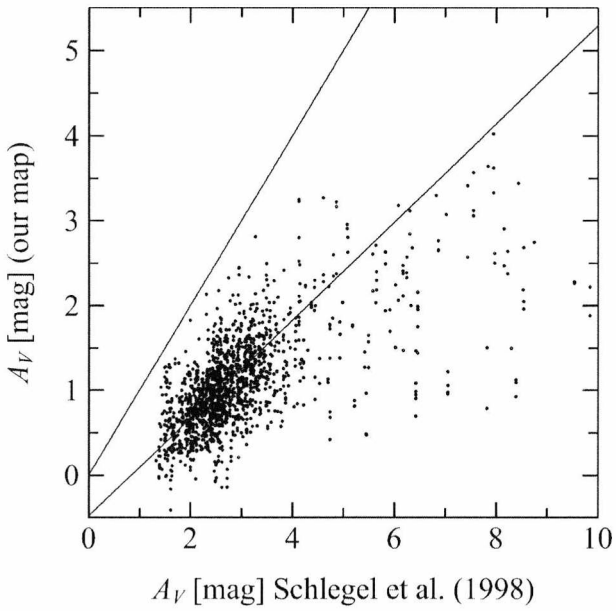

Figure A.39: Comparison of the optical extinction values for region7 (Monoceros) in Table 3.2 between our extinction map and the map from Schlegel et al. As solid line we overplot a one-to-one line, as well as a linear fit. See Table 3.2 for the parameters of the fit.

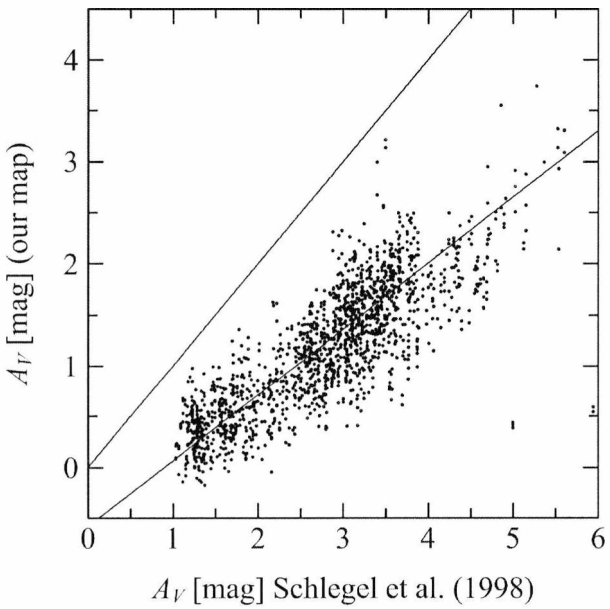

Figure A.40: Comparison of the optical extinction values for region8 (Auriga) in Table 3.2 between our extinction map and the map from Schlegel et al. As solid line we overplot a one-to-one line, as well as a linear fit. See Table 3.2 for the parameters of the fit.

A.2.3 Dobashi et al. (2005) vs. Schlegel et al. (1998)

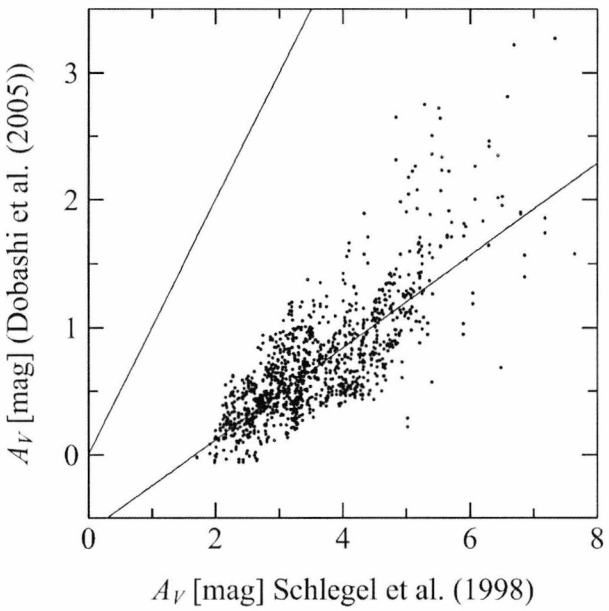

Figure A.41: Comparison of the optical extinction values for region1 (Camelopardalis) in Table 3.2 between the map of Dobashi et al. and the map from Schlegel et al. As solid line we overplot a one-to-one line, as well as a linear fit. See Table 3.2 for the parameters of the fit.

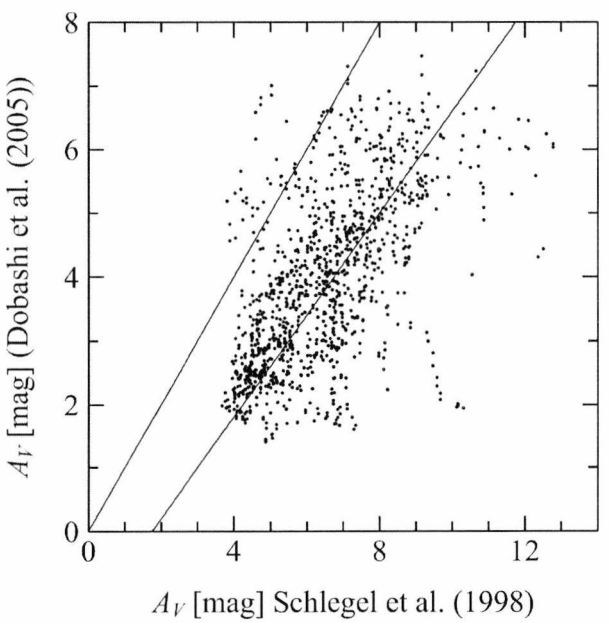

Figure A.42: Comparison of the optical extinction values for region2 (Serpens) in Table 3.2 between the map of Dobashi et al. and the map from Schlegel et al. As solid line we overplot a one-to-one line, as well as a linear fit. See Table 3.2 for the parameters of the fit.

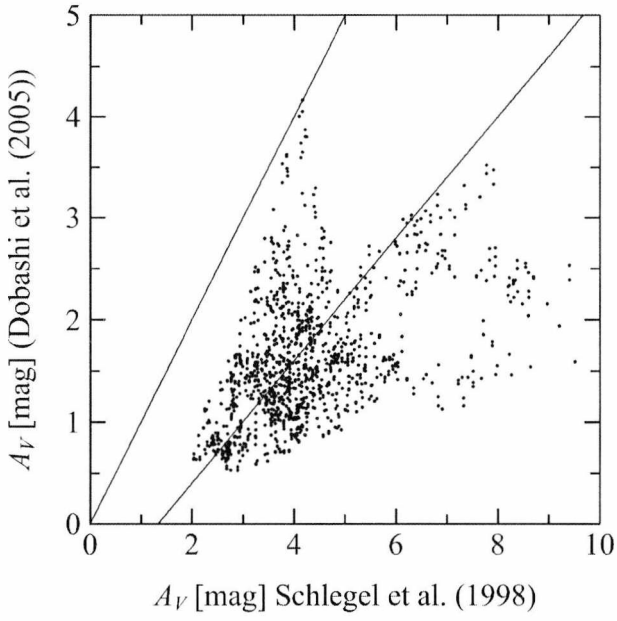

Figure A.43: Comparison of the optical extinction values for region3 (Lupus) in Table 3.2 between the map of Dobashi et al. and the map from Schlegel et al. As solid line we overplot a one-to-one line, as well as a linear fit. See Table 3.2 for the parameters of the fit.

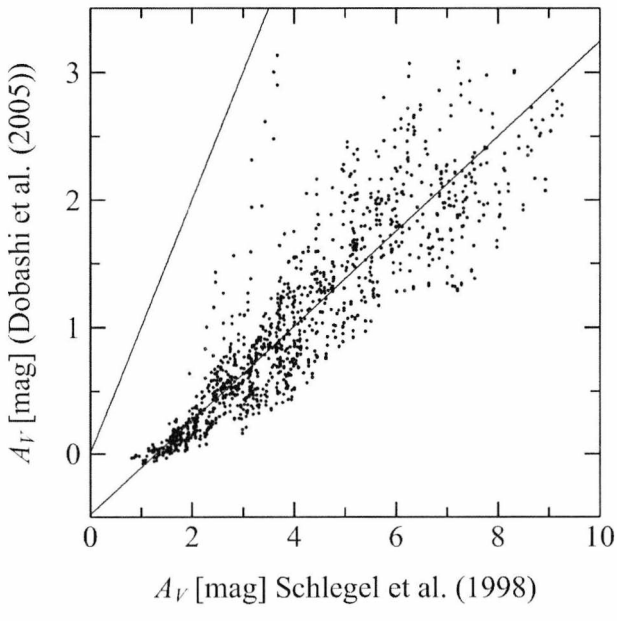

Figure A.44: Comparison of the optical extinction values for region4 (Vela) in Table 3.2 between the map of Dobashi et al. and the map from Schlegel et al. As solid line we overplot a one-to-one line, as well as a linear fit. See Table 3.2 for the parameters of the fit.

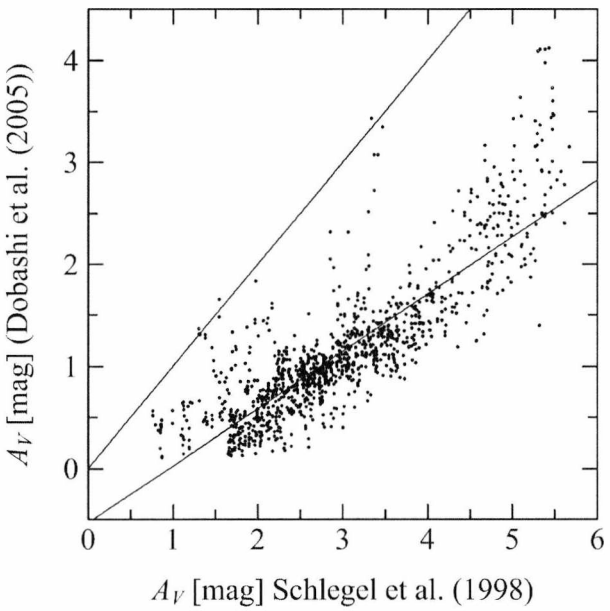

Figure A.45: Comparison of the optical extinction values for region5 (Taurus) in Table 3.2 between the map of Dobashi et al. and the map from Schlegel et al. As solid line we overplot a one-to-one line, as well as a linear fit. See Table 3.2 for the parameters of the fit.

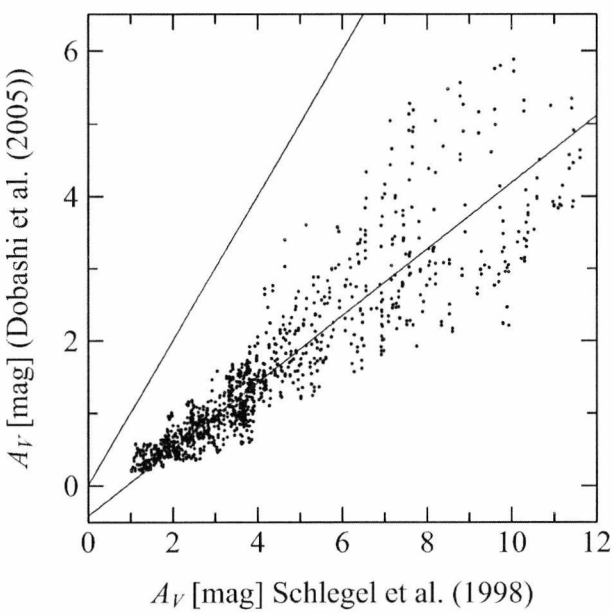

Figure A.46: Comparison of the optical extinction values for region6 (North America Nebula) in Table 3.2 between our extinction map and the map from Schlegel et al. As solid line we overplot a one-to-one line, as well as a linear fit. See Table 3.2 for the parameters of the fit.

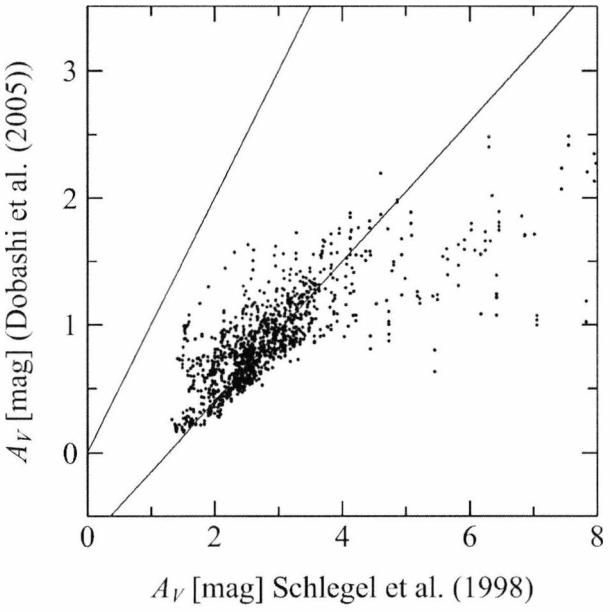

Figure A.47: Comparison of the optical extinction values for region7 (Monoceros) in Table 3.2 between the map of Dobashi et al. and the map from Schlegel et al. As solid line we overplot a one-to-one line, as well as a linear fit. See Table 3.2 for the parameters of the fit.

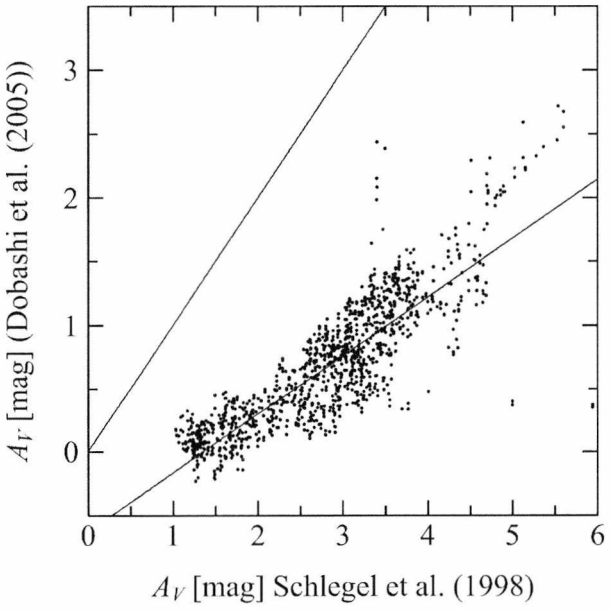

Figure A.48: Comparison of the optical extinction values for region8 (Auriga) in Table 3.2 between the map of Dobashi et al. and the map from Schlegel et al. As solid line we overplot a one-to-one line, as well as a linear fit. See Table 3.2 for the parameters of the fit.

Appendix B

Figures of Cloud Data

B.1 Column Density Distribution

B.1.1 Log-Normal Fits to the Column Density Distribution

The normalised CDD for the 30 selected clouds are plotted in this section. The solid line in the figure shows the data for the spatial resolution closest to 0.1 pc. The dotted line is the fit with parameters interpolated to a spatial scale of 0.1 pc. These were obtained using the method in Section 2.7.2.

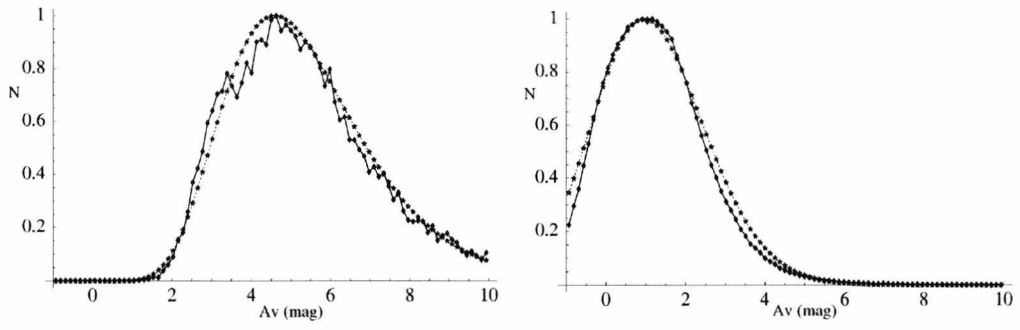

Figure B.1: The normalised CDD for the Aquila Rift (left panel) and Auriga 1 clouds (right panel). The solid line in the figure shows the data for the spatial resolution closest to 0.1 pc. The dotted line is the fit with parameters interpolated to a spatial scale of 0.1 pc.

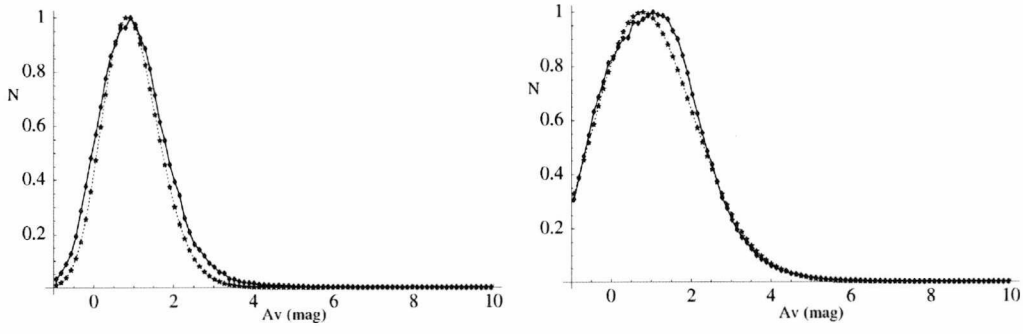

Figure B.2: The normalised CDD for the Auriga 2 (left panel) and Cepheus Flare clouds (right panel). The solid line in the figure shows the data for the spatial resolution closest to 0.1 pc. The dotted line is the fit with parameters interpolated to a spatial scale of 0.1 pc.

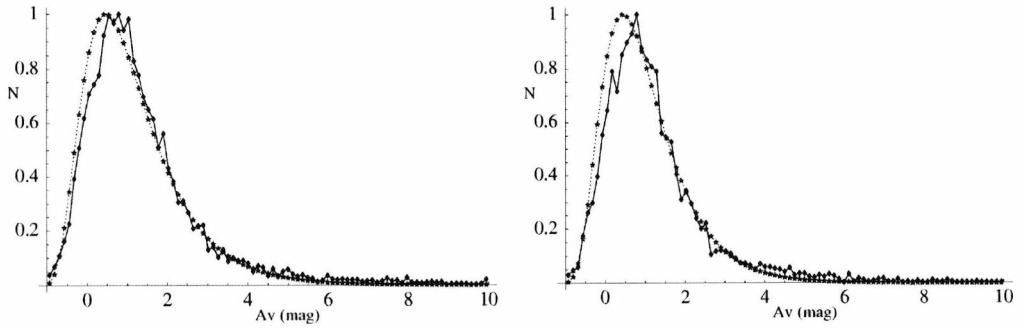

Figure B.3: The normalised CDD for the Chamaeleon I (left panel) and Chamaeleon II clouds (right panel). The solid line in the figure shows the data for the spatial resolution closest to 0.1 pc. The dotted line is the fit with parameters interpolated to a spatial scale of 0.1 pc.

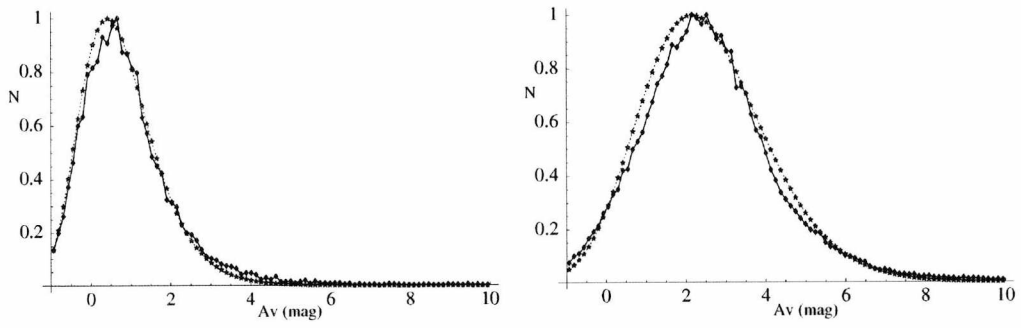

Figure B.4: The normalised CDD for the Chamaeleon III (left panel) and Circinus clouds (right panel). The solid line in the figure shows the data for the spatial resolution closest to 0.1 pc. The dotted line is the fit with parameters interpolated to a spatial scale of 0.1 pc.

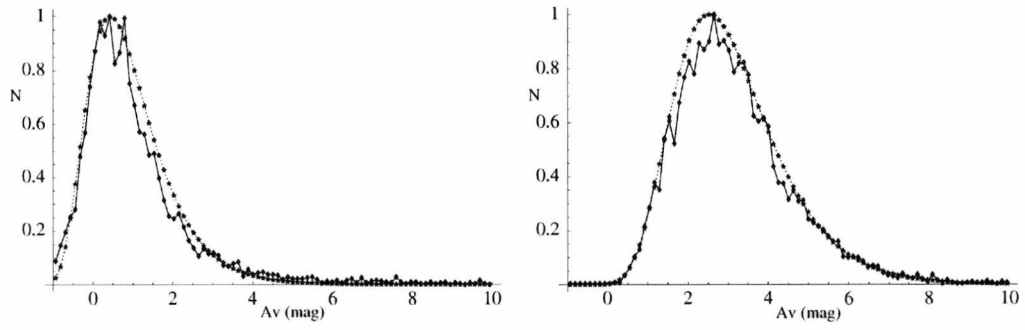

Figure B.5: The normalised CDD for the Corona Australis (left panel) and Cygnus OB7 clouds (right panel). The solid line in the figure shows the data for the spatial resolution closest to 0.1 pc. The dotted line is the fit with parameters interpolated to a spatial scale of 0.1 pc.

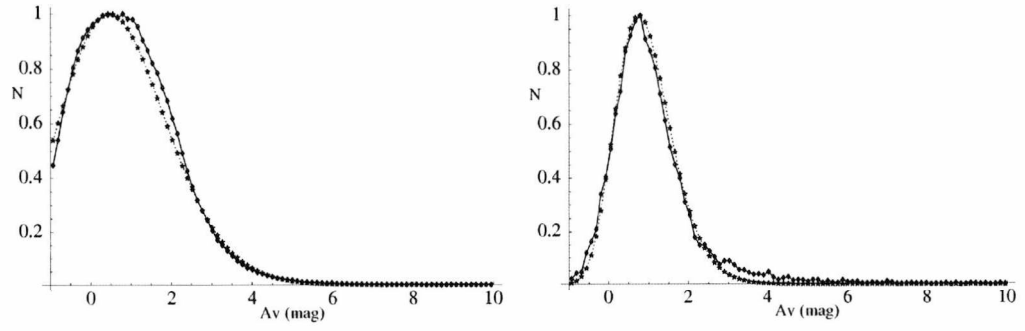

Figure B.6: The normalised CDD for the λ-Ori (left panel) and Lupus 1 clouds (right panel). The solid line in the figure shows the data for the spatial resolution closest to 0.1 pc. The dotted line is the fit with parameters interpolated to a spatial scale of 0.1 pc.

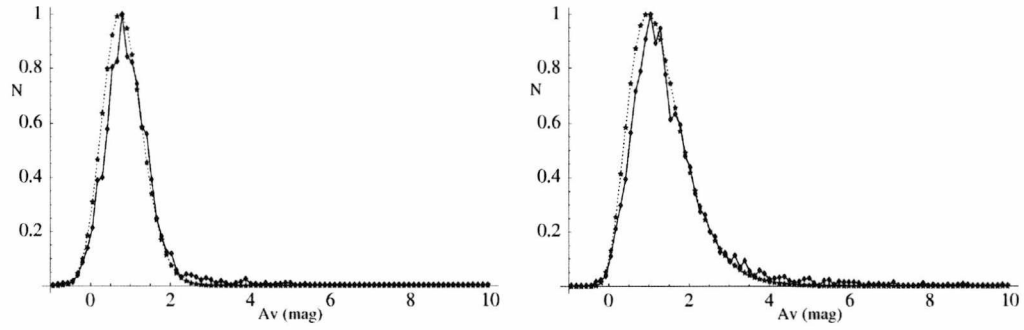

Figure B.7: The normalised CDD for the Lupus 2 (left panel) and Lupus 3 clouds (right panel). The solid line in the figure shows the data for the spatial resolution closest to 0.1 pc. The dotted line is the fit with parameters interpolated to a spatial scale of 0.1 pc.

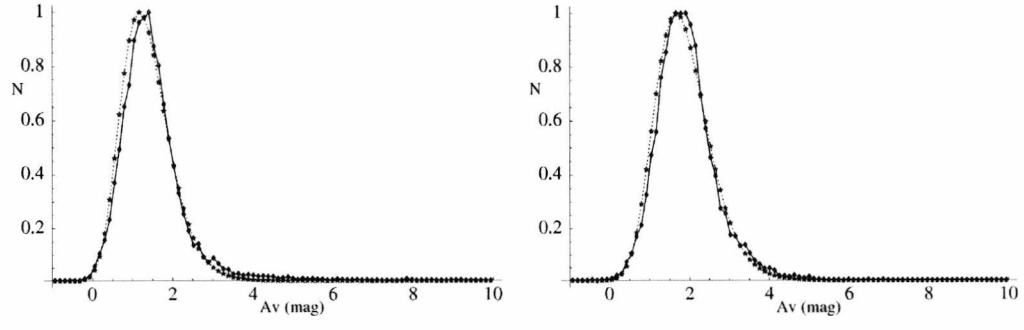

Figure B.8: The normalised CDD for the Lupus 4 (left panel) and Lupus 5 clouds (right panel). The solid line in the figure shows the data for the spatial resolution closest to 0.1 pc. The dotted line is the fit with parameters interpolated to a spatial scale of 0.1 pc.

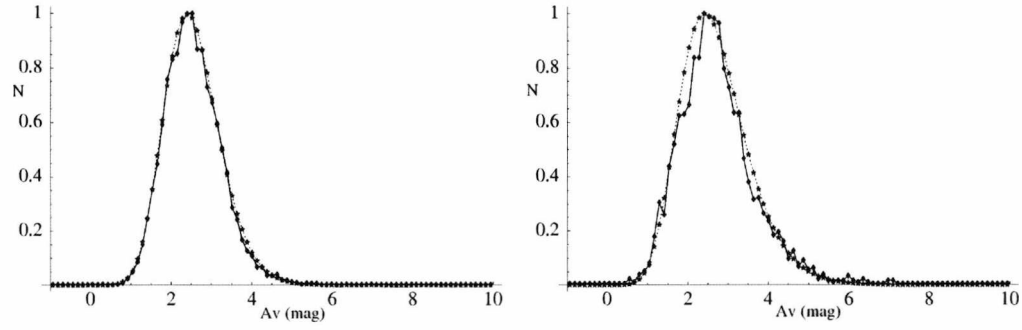

Figure B.9: The normalised CDD for the Lupus 6 (left panel) and Lupus 7 clouds (right panel). The solid line in the figure shows the data for the spatial resolution closest to 0.1 pc. The dotted line is the fit with parameters interpolated to a spatial scale of 0.1 pc.

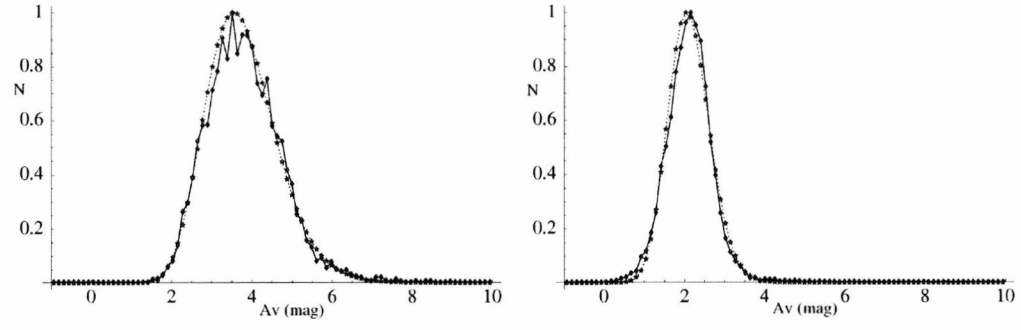

Figure B.10: The normalised CDD for the Lupus 8 (left panel) and Lupus 9 clouds (right panel). The solid line in the figure shows the data for the spatial resolution closest to 0.1 pc. The dotted line is the fit with parameters interpolated to a spatial scale of 0.1 pc.

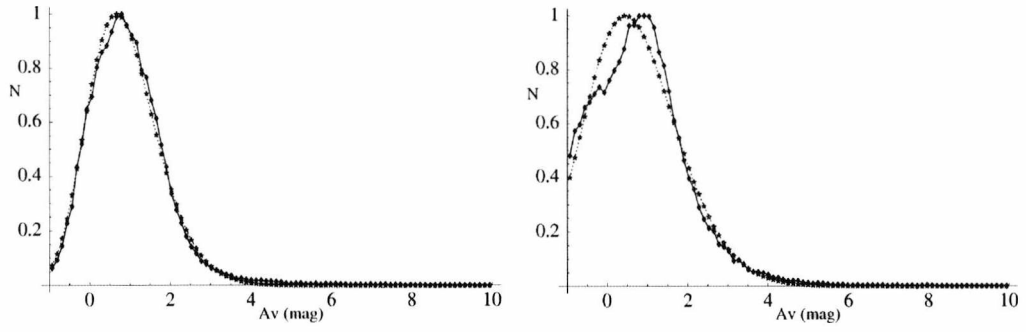

Figure B.11: The normalised CDD for the Monoceros (left panel) and Musca clouds (right panel). The solid line in the figure shows the data for the spatial resolution closest to 0.1 pc. The dotted line is the fit with parameters interpolated to a spatial scale of 0.1 pc.

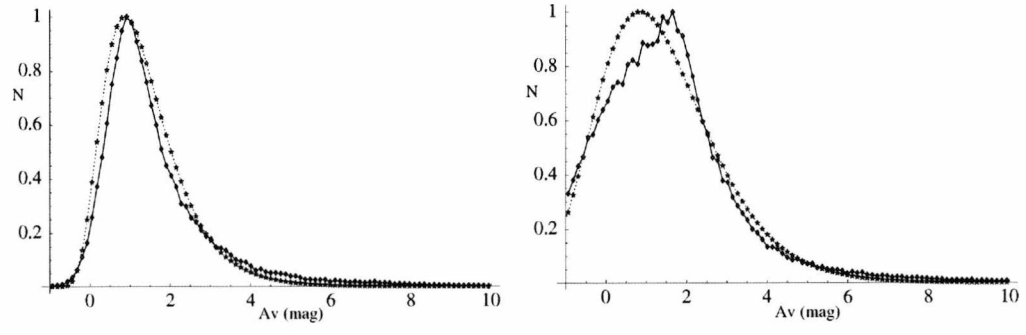

Figure B.12: The normalised CDD for the Ophiuchus (left panel) and Orion A clouds (right panel). The solid line in the figure shows the data for the spatial resolution closest to 0.1 pc. The dotted line is the fit with parameters interpolated to a spatial scale of 0.1 pc.

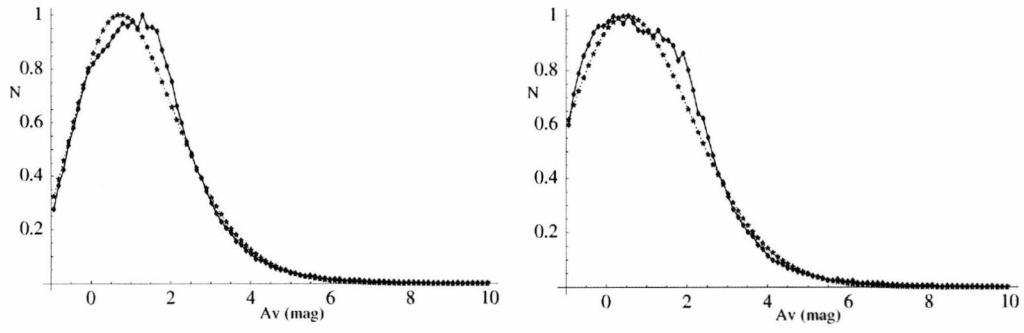

Figure B.13: The normalised CDD for the Orion B (left panel) and Perseus clouds (right panel). The solid line in the figure shows the data for the spatial resolution closest to 0.1 pc. The dotted line is the fit with parameters interpolated to a spatial scale of 0.1 pc.

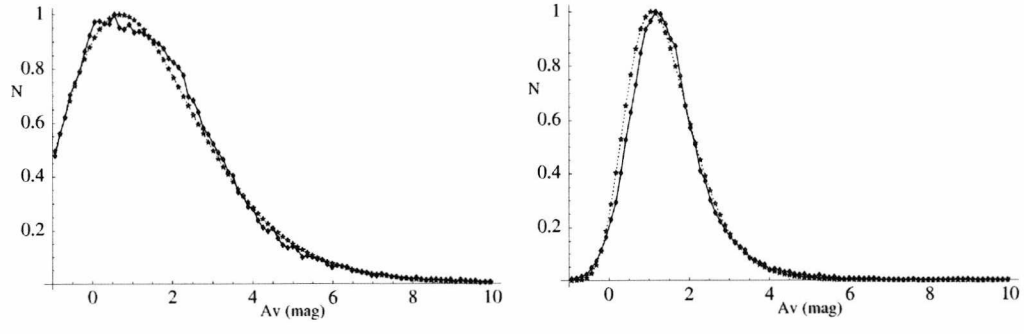

Figure B.14: The normalised CDD for the Rosette Nebula (left panel) and Scorpius clouds (right panel). The solid line in the figure shows the data for the spatial resolution closest to 0.1 pc. The dotted line is the fit with parameters interpolated to a spatial scale of 0.1 pc.

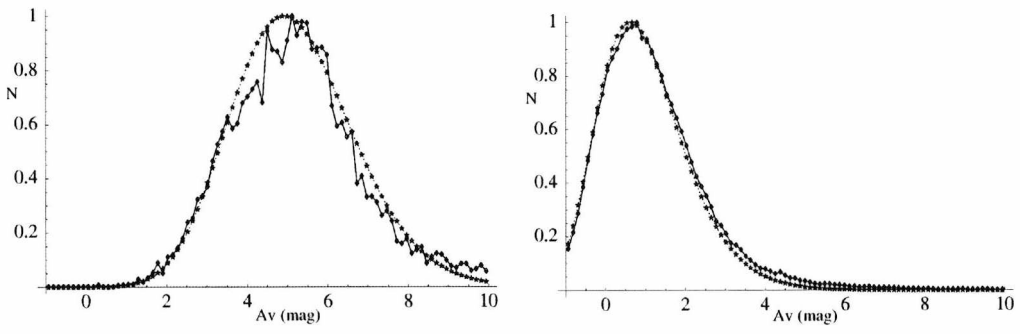

Figure B.15: The normalised CDD for the Serpens (left panel) and Taurus clouds (right panel). The solid line in the figure shows the data for the spatial resolution closest to 0.1 pc. The dotted line is the fit with parameters interpolated to a spatial scale of 0.1 pc.

B.1.2 Galactic Plane results

The results for the Galactic Plane region are shown in this section.

B.1.2.1 Log-Normal fits to the Column Density Distribution

Figure B.16: Visual representation of the fit parameter a obtained in the central Galactic plane. Results for the *con-res maps* with pixel sizes of 0.5′, 1.0′, 2.0′ and 4.0′ are shown. The data are scaled linearly from 0 (black) to 13 (white). The overlaid contours are the 3 mag A_V (outer) and 6 mag A_V (inner) from the nearest 49 star extinction map.

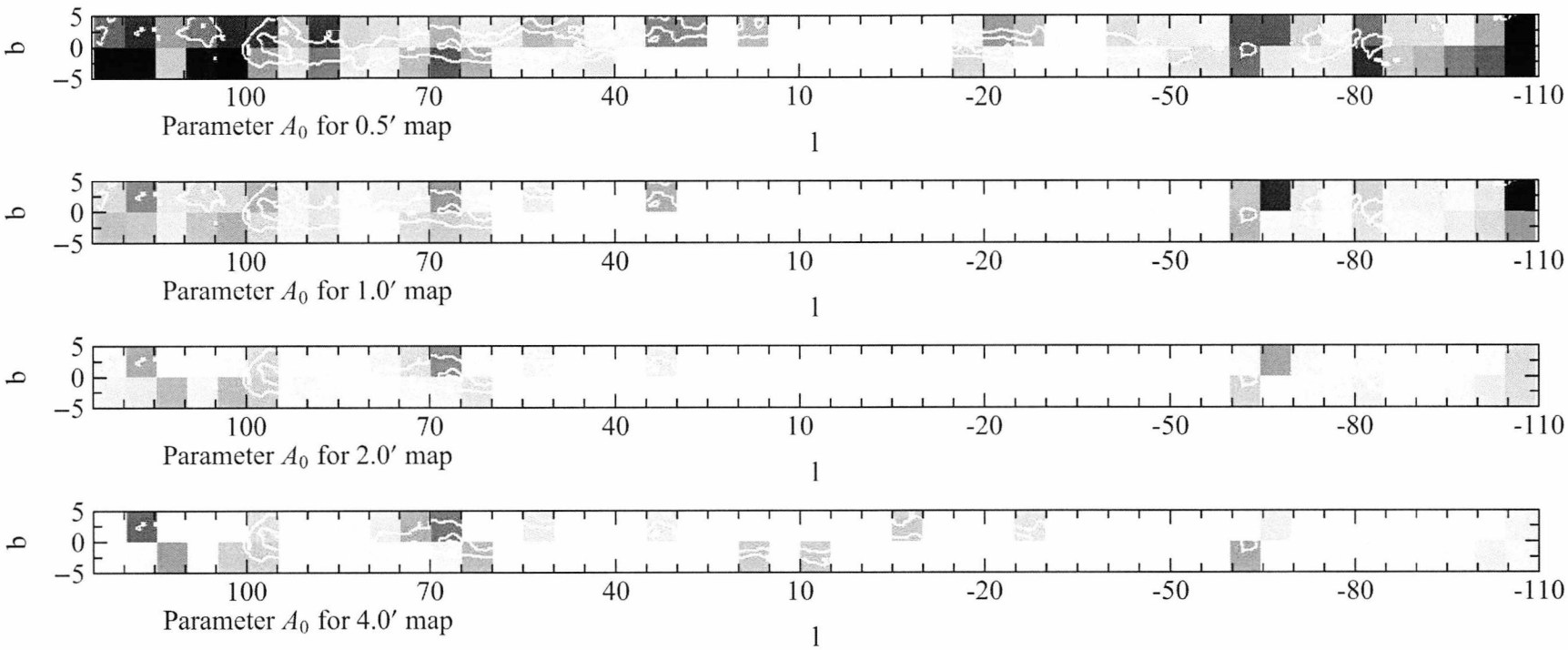

Figure B.17: Visual representation of the fit parameter A_0 obtained in the central Galactic plane. Results for the *con-res maps* with pixel sizes of 0.5′, 1.0′, 2.0′ and 4.0′ are shown. The data are scaled linearly from -13 (black) to 0 (white). The overlaid contours are the 3 mag A_V (outer) and 6 mag A_V (inner) from the nearest 49 star extinction map.

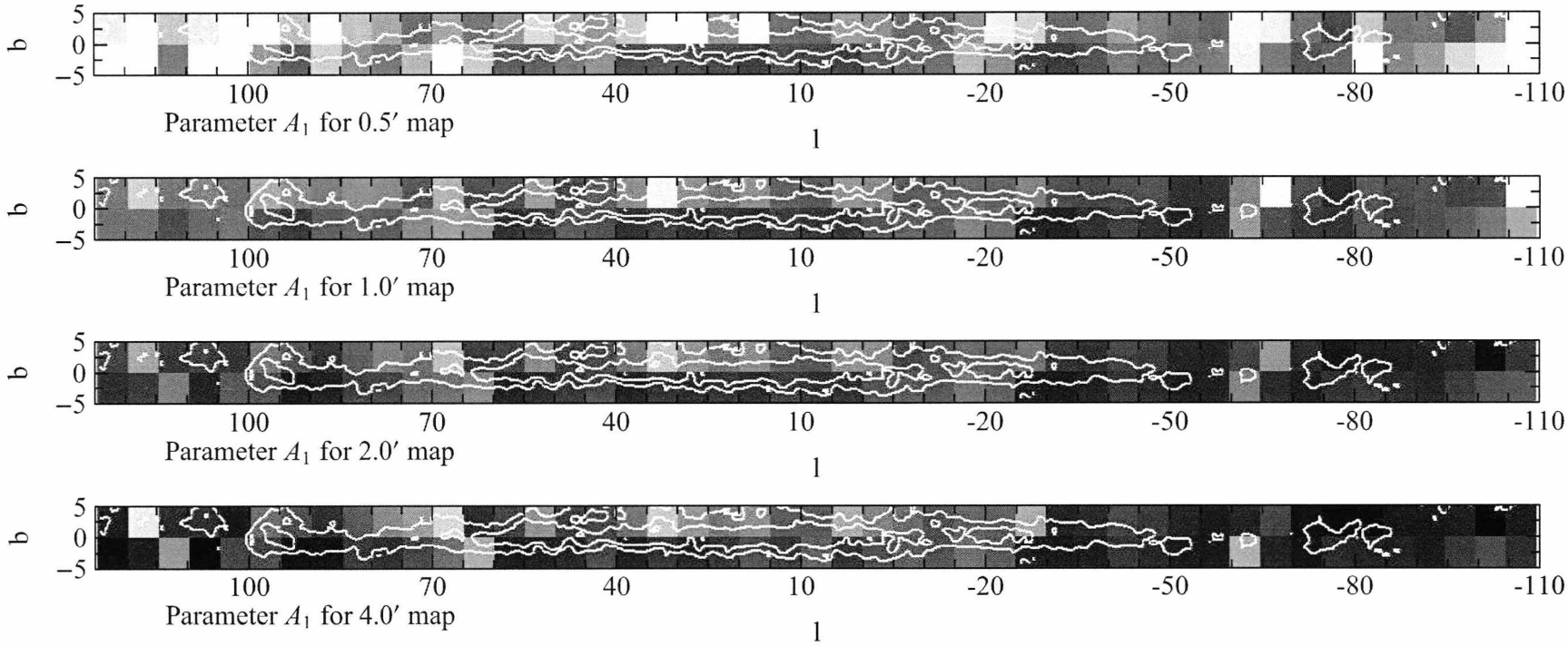

Figure B.18: Visual representation of the fit parameter A_1 obtained in the central Galactic plane. Results for the *con-res maps* with pixel sizes of 0.5′, 1.0′, 2.0′ and 4.0′ are shown. The data are scaled linearly from 0 (black) to 13 (white). The overlaid contours are the 3 mag A_V (outer) and 6 mag A_V (inner) from the nearest 49 star extinction map.

Figure B.19: Visual representation of the fit parameter σ obtained in the central Galactic plane. Results for the *con-res maps* with pixel sizes of 0.5′, 1.0′, 2.0′ and 4.0′ are shown. The data are scaled linearly from 1.1 (black) to 1.7 (white). The overlaid contours are the 3 mag A_V (outer) and 6 mag A_V (inner) from the nearest 49 star extinction map.

Figure B.20: Visual representation of the fit parameter *rms* obtained in the central Galactic plane. Results for the *con-res maps* with pixel sizes of 0.5′, 1.0′, 2.0′ and 4.0′ are shown. The data are scaled linearly from 0 (black) to 40 (white). The overlaid contours are the 3 mag A_V (outer) and 6 mag A_V (inner) from the nearest 49 star extinction map.

B.1.3 $\log(N)$ vs A_V Column Density Distribution

The plots of the CDDs γ_{low} and γ_{high} against scale for the 30 sample clouds are shown here. These were obtained using the method in Section 2.7.1.

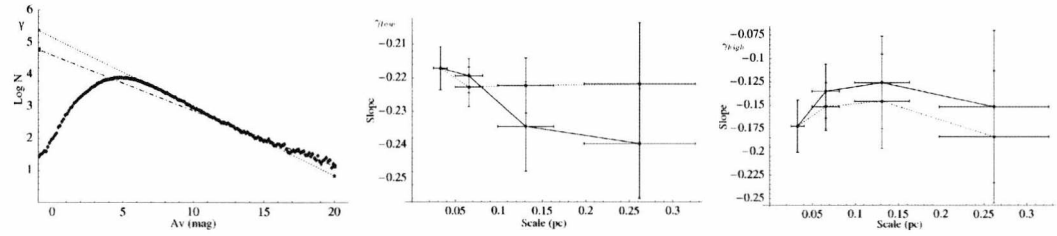

Figure B.21: A histogram showing the log of the number of pixels in each bin against A_V for the Aquila Rift cloud (left panel). Plot showing the variation of slopes γ_{low} (middle panel) and γ_{high} (right panel) for the Aquila Rift cloud. The solid line connects the points obtained using the *con-res* A_V maps and the dotted line connects the points obtained by rebinning the highest resolution map to obtain the remaining three resolutions.

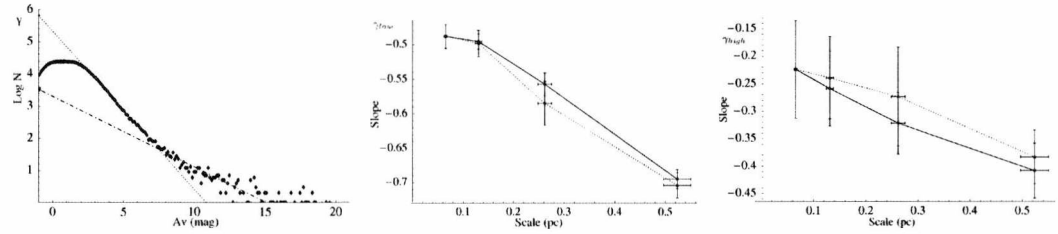

Figure B.22: A histogram showing the log of the number of pixels in each bin against A_V for the Auriga 1 cloud (left panel). Plot showing the variation of slopes γ_{low} (middle panel) and γ_{high} (right panel) for the Auriga 1 cloud. The solid line connects the points obtained using the *con-res* A_V maps and the dotted line connects the points obtained by rebinning the highest resolution map to obtain the remaining three resolutions.

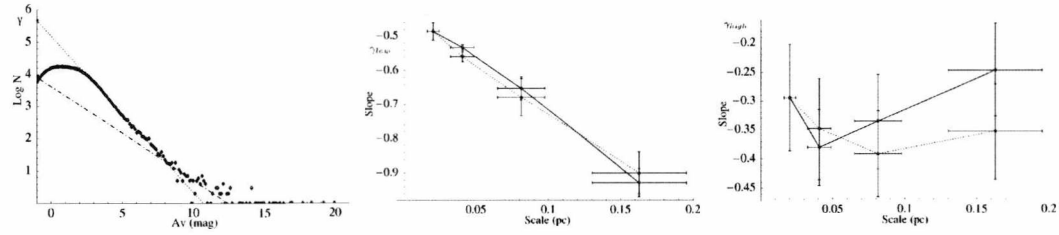

Figure B.23: A histogram showing the log of the number of pixels in each bin against A_V for the Auriga 2 cloud (left panel). Plot showing the variation of slopes γ_{low} (middle panel) and γ_{high} (right panel) for the Auriga 2 cloud. The solid line connects the points obtained using the *con-res* A_V maps and the dotted line connects the points obtained by rebinning the highest resolution map to obtain the remaining three resolutions.

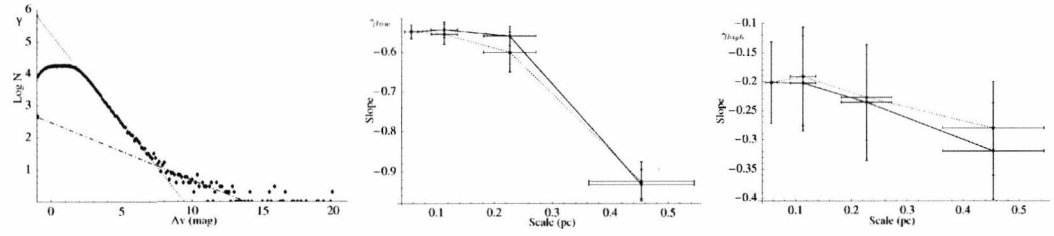

Figure B.24: A histogram showing the log of the number of pixels in each bin against A_V for the Cepheus Flare cloud (left panel). Plot showing the variation of slopes γ_{low} (middle panel) and γ_{high} (right panel) for the Cepheus Flare cloud. The solid line connects the points obtained using the *con-res* A_V maps and the dotted line connects the points obtained by rebinning the highest resolution map to obtain the remaining three resolutions.

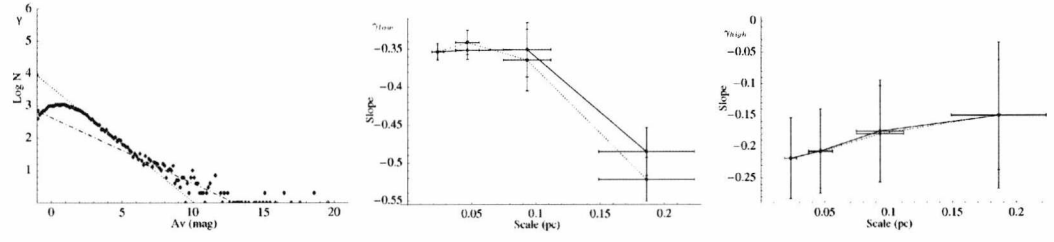

Figure B.25: A histogram showing the log of the number of pixels in each bin against A_V for the Chamaeleon I cloud (left panel). Plot showing the variation of slopes γ_{low} (middle panel) and γ_{high} (right panel) for the Chamaeleon I cloud. The solid line connects the points obtained using the *con-res* A_V maps and the dotted line connects the points obtained by rebinning the highest resolution map to obtain the remaining three resolutions.

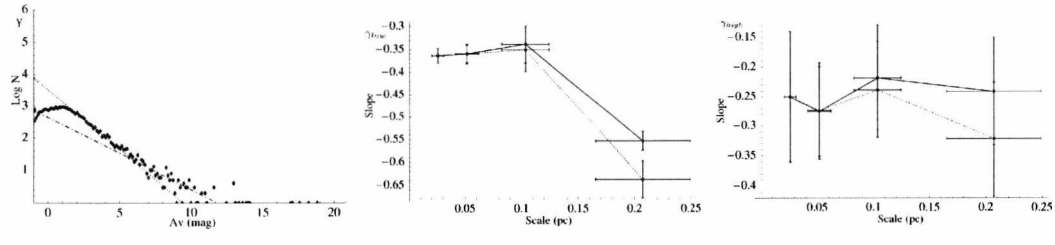

Figure B.26: A histogram showing the log of the number of pixels in each bin against A_V for the Chamaeleon II cloud (left panel). Plot showing the variation of slopes γ_{low} (middle panel) and γ_{high} (right panel) for the Chamaeleon II cloud. The solid line connects the points obtained using the *con-res* A_V maps and the dotted line connects the points obtained by rebinning the highest resolution map to obtain the remaining three resolutions.

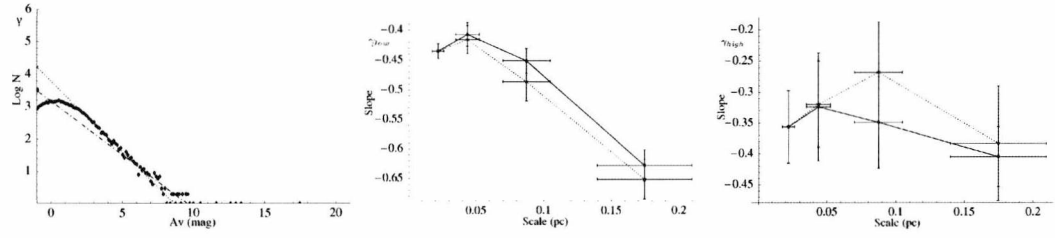

Figure B.27: A histogram showing the log of the number of pixels in each bin against A_V for the Chamaeleon III cloud (left panel). Plot showing the variation of slopes γ_{low} (middle panel) and γ_{high} (right panel) for the Chamaeleon III cloud. The solid line connects the points obtained using the *con-res* A_V maps and the dotted line connects the points obtained by rebinning the highest resolution map to obtain the remaining three resolutions.

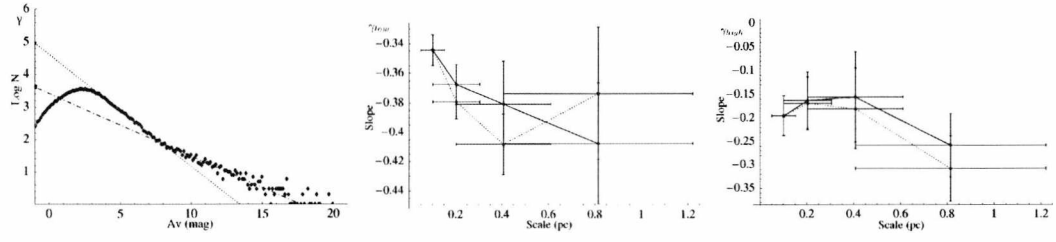

Figure B.28: A histogram showing the log of the number of pixels in each bin against A_V for the Circinus cloud (left panel). Plot showing the variation of slopes γ_{low} (middle panel) and γ_{high} (right panel) for the Circinus cloud. The solid line connects the points obtained using the *con-res* A_V maps and the dotted line connects the points obtained by rebinning the highest resolution map to obtain the remaining three resolutions.

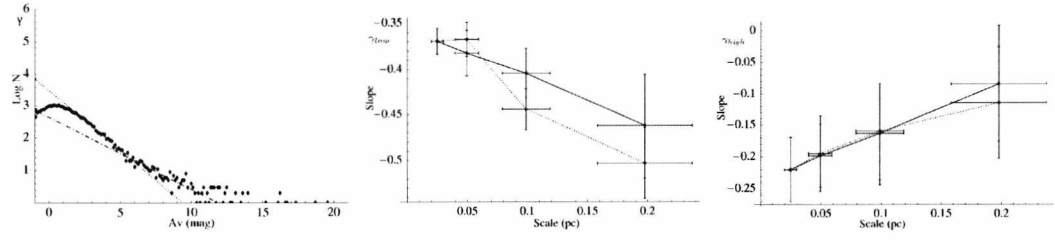

Figure B.29: A histogram showing the log of the number of pixels in each bin against A_V for the Corona Australis cloud (left panel). Plot showing the variation of slopes γ_{low} (middle panel) and γ_{high} (right panel) for the Corona Australis cloud. The solid line connects the points obtained using the *con-res* A_V maps and the dotted line connects the points obtained by rebinning the highest resolution map to obtain the remaining three resolutions.

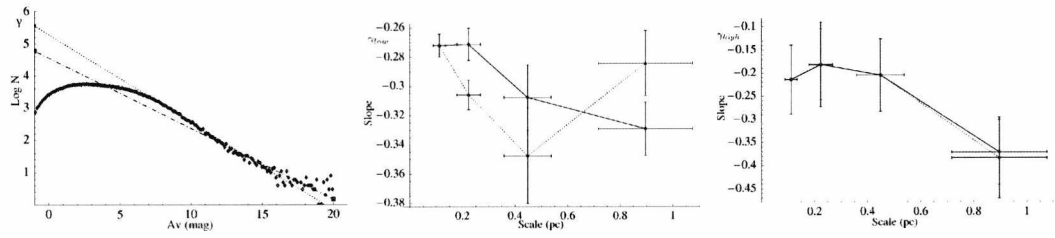

Figure B.30: A histogram showing the log of the number of pixels in each bin against A_V for the Cygnus OB7 cloud (left panel). Plot showing the variation of slopes γ_{low} (middle panel) and γ_{high} (right panel) for the Cygnus OB7 cloud. The solid line connects the points obtained using the *con-res* A_V maps and the dotted line connects the points obtained by rebinning the highest resolution map to obtain the remaining three resolutions.

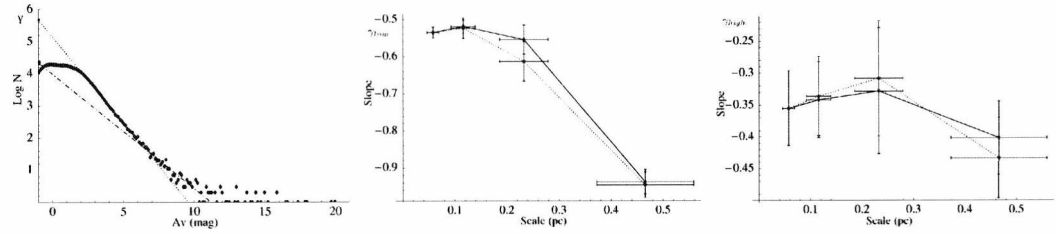

Figure B.31: A histogram showing the log of the number of pixels in each bin against A_V for the λ-Ori cloud (left panel). Plot showing the variation of slopes γ_{low} (middle panel) and γ_{high} (right panel) for the λ Ori cloud. The solid line connects the points obtained using the *con-res* A_V maps and the dotted line connects the points obtained by rebinning the highest resolution map to obtain the remaining three resolutions.

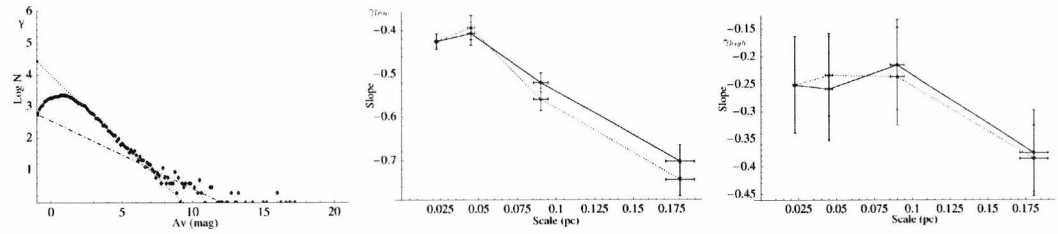

Figure B.32: A histogram showing the log of the number of pixels in each bin against A_V for the Lupus 1 cloud (left panel). Plot showing the variation of slopes γ_{low} (middle panel) and γ_{high} (right panel) for the Lupus 1 cloud. The solid line connects the points obtained using the *con-res* A_V maps and the dotted line connects the points obtained by rebinning the highest resolution map to obtain the remaining three resolutions.

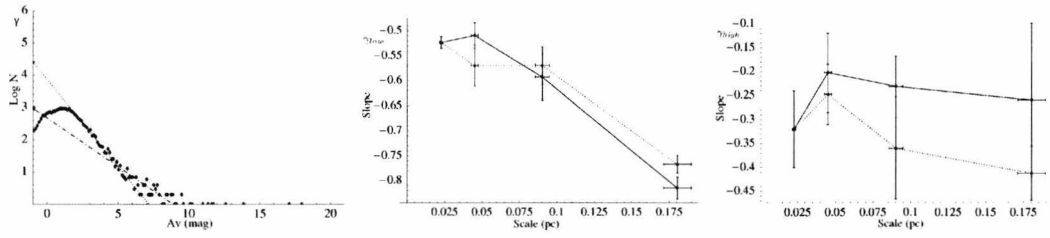

Figure B.33: A histogram showing the log of the number of pixels in each bin against A_V for the Lupus 2 cloud (left panel). Plot showing the variation of slopes γ_{low} (middle panel) and γ_{high} (right panel) for the Lupus 2 cloud. The solid line connects the points obtained using the *con-res* A_V maps and the dotted line connects the points obtained by rebinning the highest resolution map to obtain the remaining three resolutions.

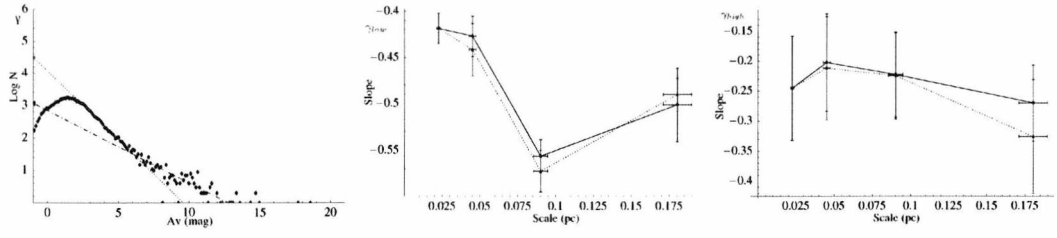

Figure B.34: A histogram showing the log of the number of pixels in each bin against A_V for the Lupus 3 cloud (left panel). Plot showing the variation of slopes γ_{low} (middle panel) and γ_{high} (right panel) for the Lupus 3 cloud. The solid line connects the points obtained using the *con-res* A_V maps and the dotted line connects the points obtained by rebinning the highest resolution map to obtain the remaining three resolutions.

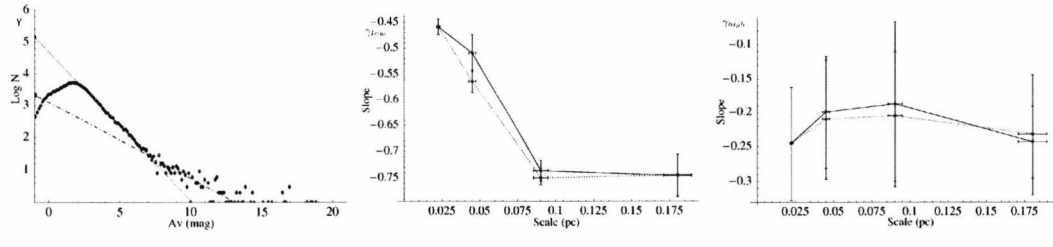

Figure B.35: A histogram showing the log of the number of pixels in each bin against A_V for the Lupus 4 cloud (left panel). Plot showing the variation of slopes γ_{low} (middle panel) and γ_{high} (right panel) for the Lupus 4 cloud. The solid line connects the points obtained using the *con-res* A_V maps and the dotted line connects the points obtained by rebinning the highest resolution map to obtain the remaining three resolutions.

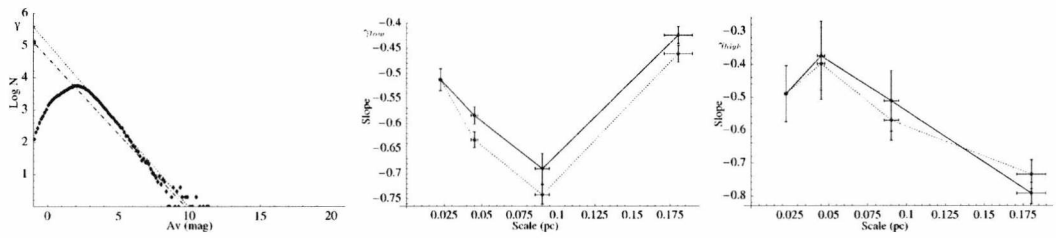

Figure B.36: A histogram showing the log of the number of pixels in each bin against A_V for the Lupus 5 cloud (left panel). Plot showing the variation of slopes γ_{low} (middle panel) and γ_{high} (right panel) for the Lupus 5 cloud. The solid line connects the points obtained using the *con-res* A_V maps and the dotted line connects the points obtained by rebinning the highest resolution map to obtain the remaining three resolutions.

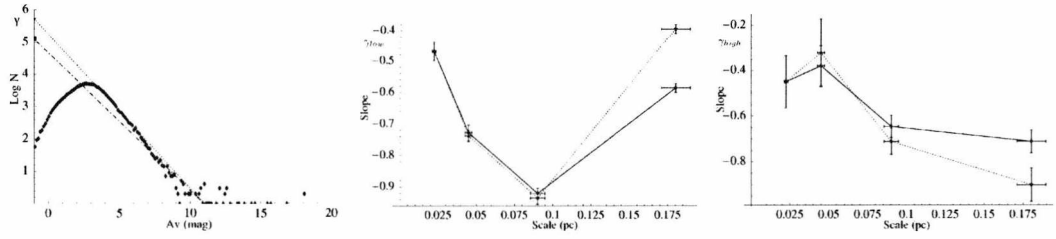

Figure B.37: A histogram showing the log of the number of pixels in each bin against A_V for the Lupus 6 cloud (left panel). Plot showing the variation of slopes γ_{low} (middle panel) and γ_{high} (right panel) for the Lupus 6 cloud. The solid line connects the points obtained using the *con-res* A_V maps and the dotted line connects the points obtained by rebinning the highest resolution map to obtain the remaining three resolutions.

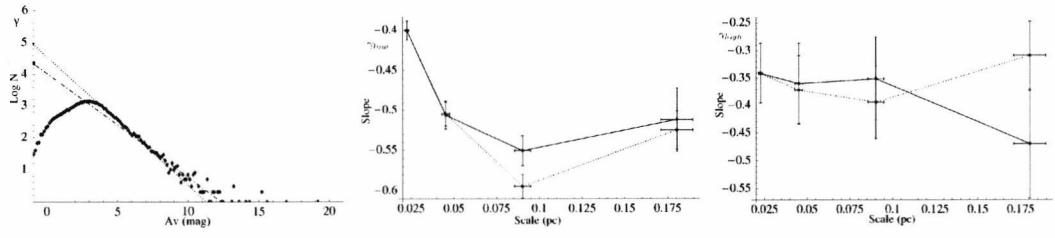

Figure B.38: A histogram showing the log of the number of pixels in each bin against A_V for the Lupus 7 cloud (left panel). Plot showing the variation of slopes γ_{low} (middle panel) and γ_{high} (right panel) for the Lupus 7 cloud. The solid line connects the points obtained using the *con-res* A_V maps and the dotted line connects the points obtained by rebinning the highest resolution map to obtain the remaining three resolutions.

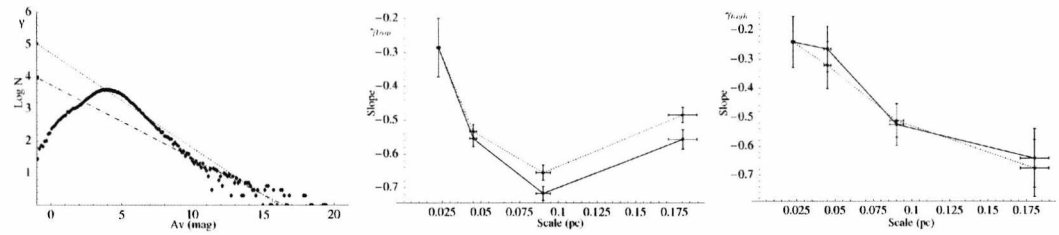

Figure B.39: A histogram showing the log of the number of pixels in each bin against A_V for the Lupus 8 cloud (left panel). Plot showing the variation of slopes γ_{low} (middle panel) and γ_{high} (right panel) for the Lupus 8 cloud. The solid line connects the points obtained using the *con-res* A_V maps and the dotted line connects the points obtained by rebinning the highest resolution map to obtain the remaining three resolutions.

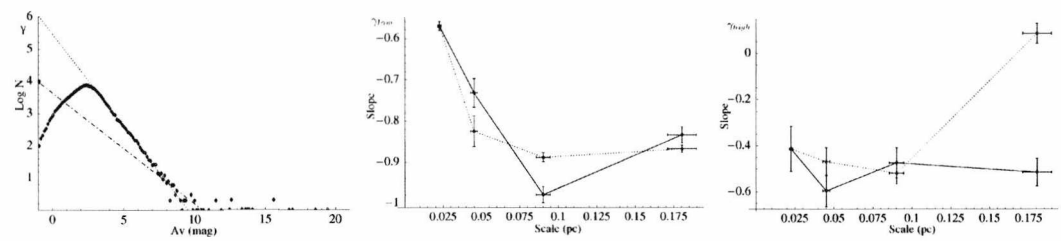

Figure B.40: A histogram showing the log of the number of pixels in each bin against A_V for the Lupus 9 cloud (left panel). Plot showing the variation of slopes γ_{low} (middle panel) and γ_{high} (right panel) for the Lupus 9 cloud. The solid line connects the points obtained using the *con-res* A_V maps and the dotted line connects the points obtained by rebinning the highest resolution map to obtain the remaining three resolutions.

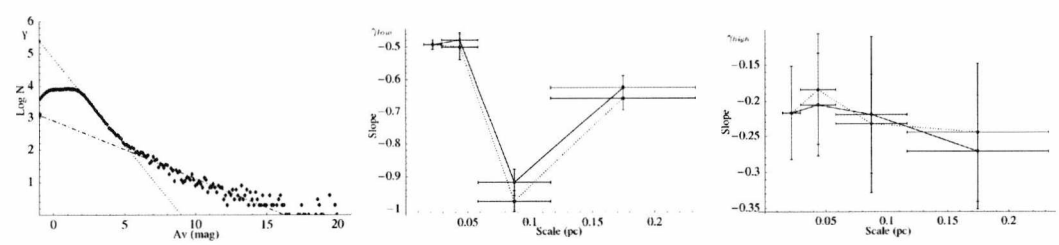

Figure B.41: A histogram showing the log of the number of pixels in each bin against A_V for the Monoceros cloud (left panel). Plot showing the variation of slopes γ_{low} (middle panel) and γ_{high} (right panel) for the Monoceros cloud. The solid line connects the points obtained using the *con-res* A_V maps and the dotted line connects the points obtained by rebinning the highest resolution map to obtain the remaining three resolutions.

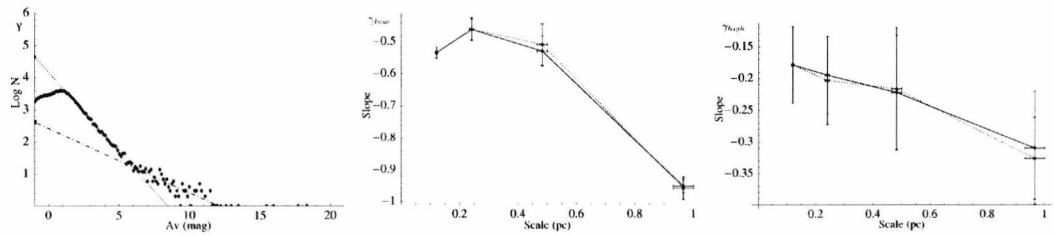

Figure B.42: A histogram showing the log of the number of pixels in each bin against A_V for the Musca cloud (left panel). Plot showing the variation of slopes γ_{low} (middle panel) and γ_{high} (right panel) for the Musca cloud. The solid line connects the points obtained using the *con-res* A_V maps and the dotted line connects the points obtained by rebinning the highest resolution map to obtain the remaining three resolutions.

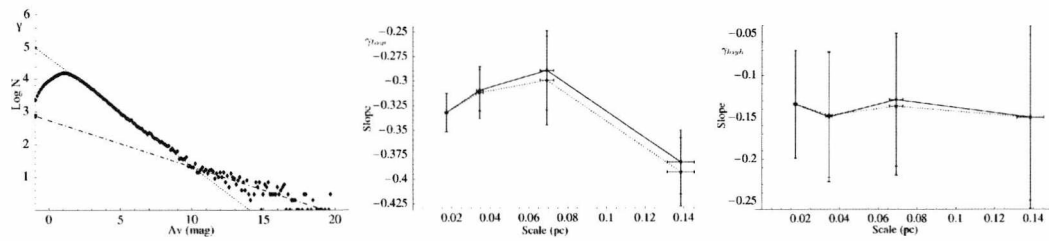

Figure B.43: A histogram showing the log of the number of pixels in each bin against A_V for the Ophiuchus cloud (left panel). Plot showing the variation of slopes γ_{low} (middle panel) and γ_{high} (right panel) for the Ophiuchus cloud. The solid line connects the points obtained using the *con-res* A_V maps and the dotted line connects the points obtained by rebinning the highest resolution map to obtain the remaining three resolutions.

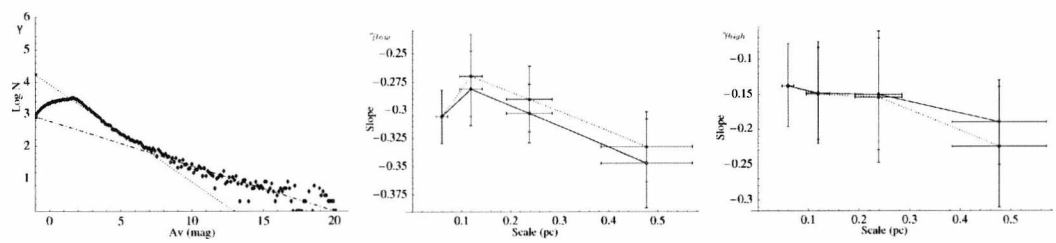

Figure B.44: A histogram showing the log of the number of pixels in each bin against A_V for the Orion A cloud (left panel). Plot showing the variation of slopes γ_{low} (middle panel) and γ_{high} (right panel) for the Orion A cloud. The solid line connects the points obtained using the *con-res* A_V maps and the dotted line connects the points obtained by rebinning the highest resolution map to obtain the remaining three resolutions.

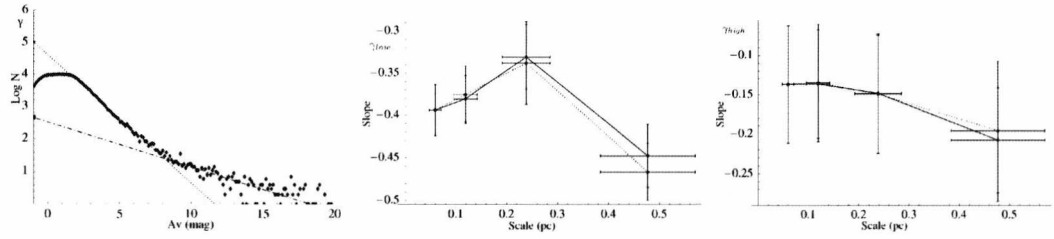

Figure B.45: A histogram showing the log of the number of pixels in each bin against A_V for the Orion B cloud (left panel). Plot showing the variation of slopes γ_{low} (middle panel) and γ_{high} (right panel) for the Orion B cloud. The solid line connects the points obtained using the *con-res* A_V maps and the dotted line connects the points obtained by rebinning the highest resolution map to obtain the remaining three resolutions.

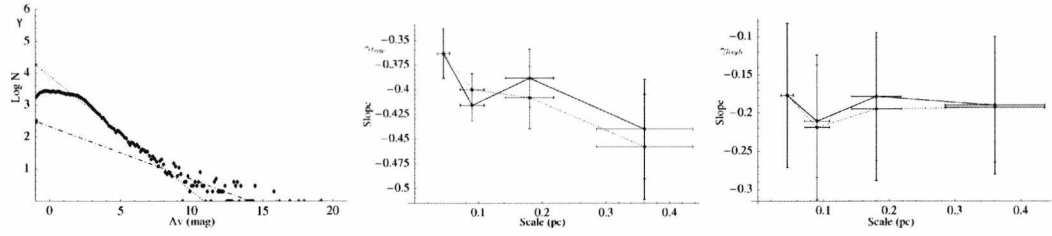

Figure B.46: A histogram showing the log of the number of pixels in each bin against A_V for the Perseus cloud (left panel). Plot showing the variation of slopes γ_{low} (middle panel) and γ_{high} (right panel) for the Perseus cloud. The solid line connects the points obtained using the *con-res* A_V maps and the dotted line connects the points obtained by rebinning the highest resolution map to obtain the remaining three resolutions.

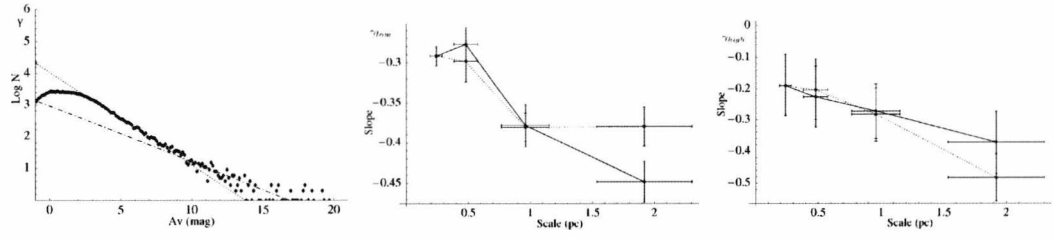

Figure B.47: A histogram showing the log of the number of pixels in each bin against A_V for the Rosette Nebula cloud (left panel). Plot showing the variation of slopes γ_{low} (middle panel) and γ_{high} (right panel) for the Rosette Nebula cloud. The solid line connects the points obtained using the *con-res* A_V maps and the dotted line connects the points obtained by rebinning the highest resolution map to obtain the remaining three resolutions.

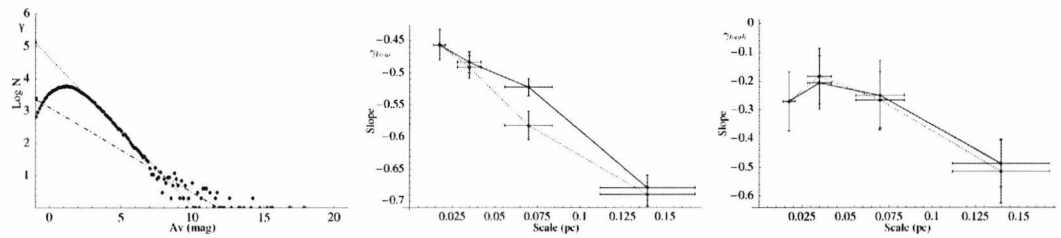

Figure B.48: A histogram showing the log of the number of pixels in each bin against A_V for the Scorpius cloud (left panel). Plot showing the variation of slopes γ_{low} (middle panel) and γ_{high} (right panel) for the Scorpius cloud. The solid line connects the points obtained using the *con-res* A_V maps and the dotted line connects the points obtained by rebinning the highest resolution map to obtain the remaining three resolutions.

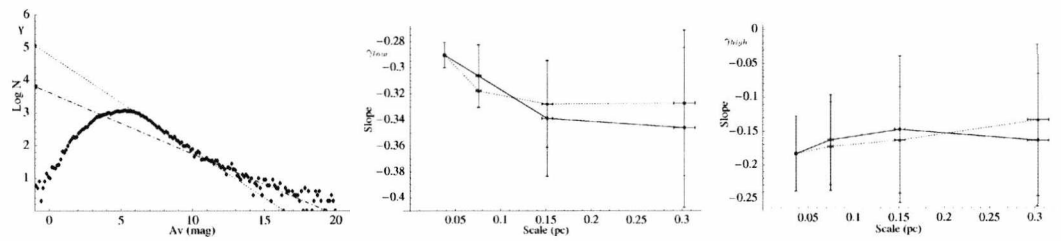

Figure B.49: A histogram showing the log of the number of pixels in each bin against A_V for the Serpens cloud (left panel). Plot showing the variation of slopes γ_{low} (middle panel) and γ_{high} (right panel) for the Serpens cloud. The solid line connects the points obtained using the *con-res* A_V maps and the dotted line connects the points obtained by rebinning the highest resolution map to obtain the remaining three resolutions.

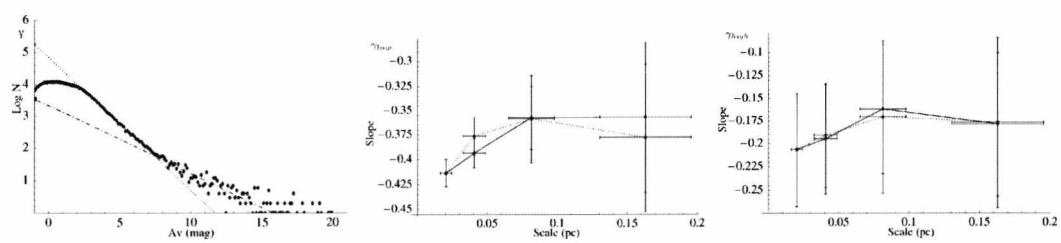

Figure B.50: A histogram showing the log of the number of pixels in each bin against A_V for the Taurus cloud (left panel). Plot showing the variation of slopes γ_{low} (middle panel) and γ_{high} (right panel) for the Taurus cloud. The solid line connects the points obtained using the *con-res* A_V maps and the dotted line connects the points obtained by rebinning the highest resolution map to obtain the remaining three resolutions.

B.1.4 Galactic Plane Plots

The data are displayed for the region by showing the value for each $5^\circ \times 5^\circ$ square as a shade between black and white. The overlaid contours are the 3 mag A_V (outer) and 6 mag A_V (inner) from the nearest 49 star extinction map. This is included to show the position of the central bulk of the Galaxy.

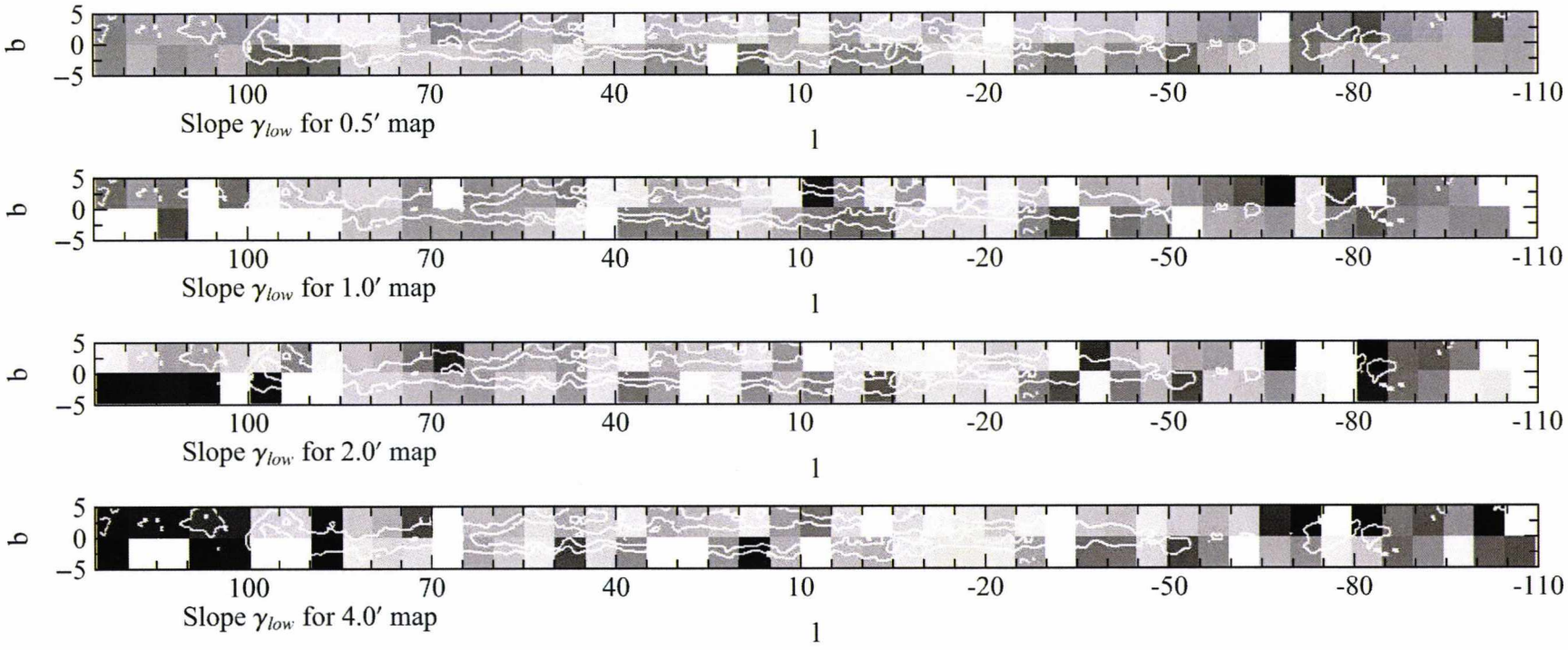

Figure B.51: Visual representation of the slopes γ_{low} obtained in the central Galactic plane. The gradients are scaled linearly from -0.5 (black) to 0.0 (white). The overlaid contours are the 3 mag A_V (outer) and 6 mag A_V (inner) from the nearest 49 star extinction map.

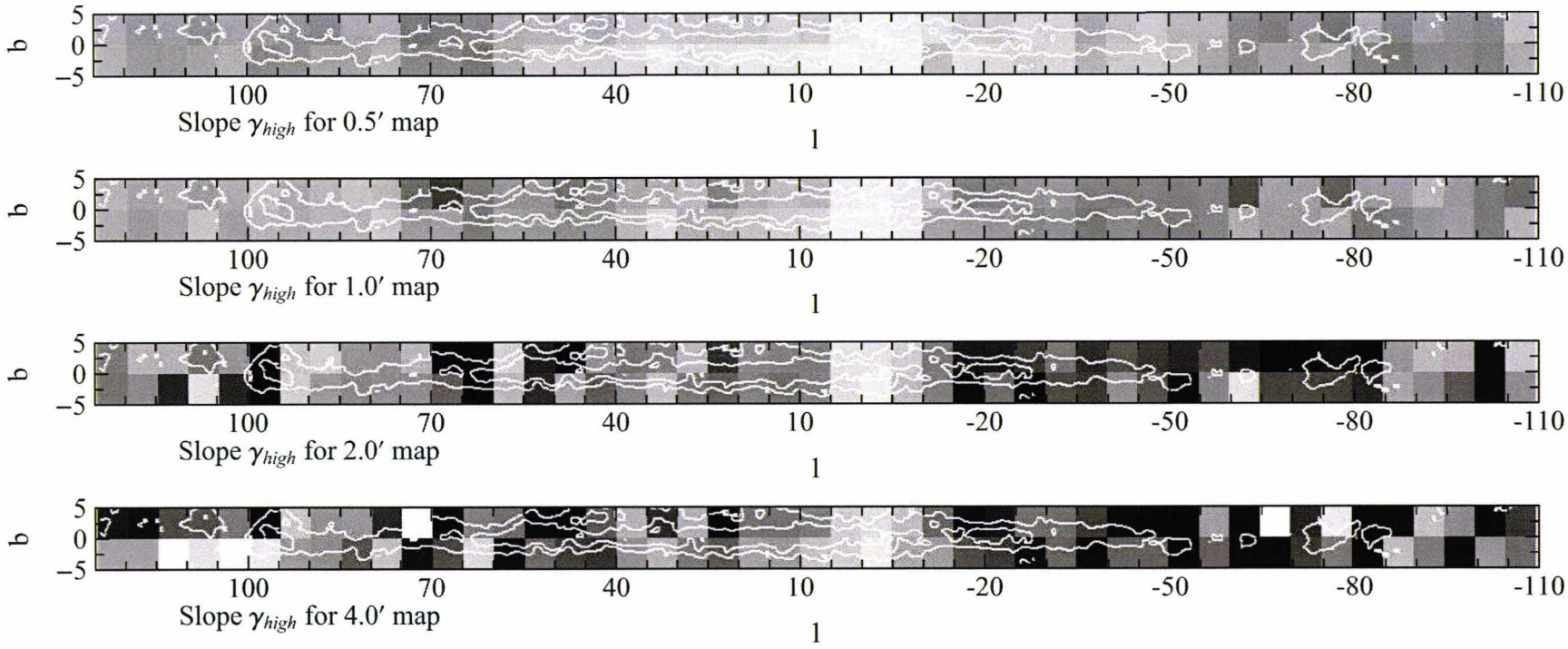

Figure B.52: Visual representation of the slopes γ_{high} obtained in the central Galactic plane. The gradients are scaled linearly from -0.5 (black) to 0.0 (white). The overlaid contours are the 3 mag A_V (outer) and 6 mag A_V (inner) from the nearest 49 star extinction map.

B.2 Mass Distribution

The plots of mass distribution δ_{low} and δ_{high} against scale for the 30 selected clouds are shown here. These were obtained using the method in Section 2.7.3.

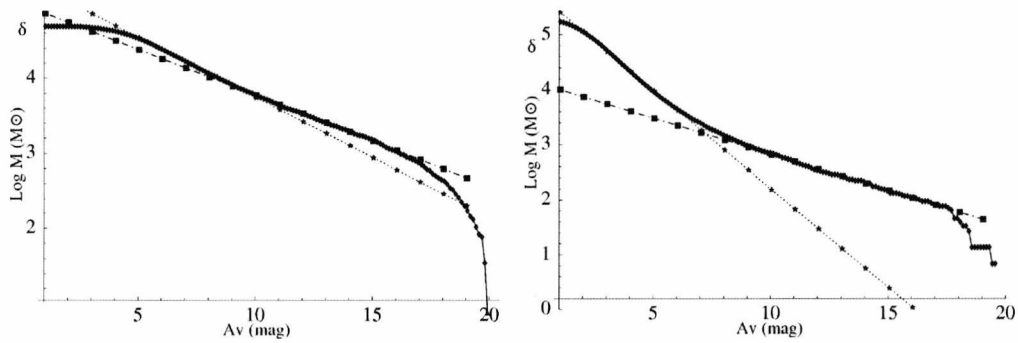

Figure B.53: A plot showing the log of the cumulative mass (integrated from RHS) against A_V for the Aquila Rift cloud (left panel). A plot showing the log of the cumulative mass (integrated from RHS) against A_V for the Auriga 1 cloud (right panel).

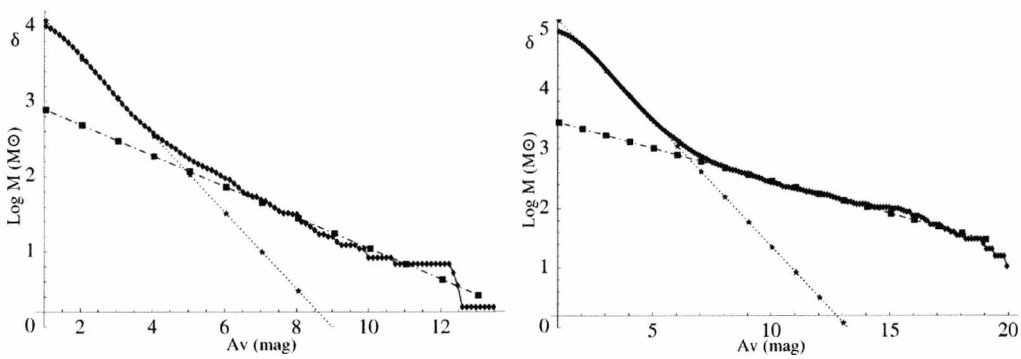

Figure B.54: A plot showing the log of the cumulative mass (integrated from RHS) against A_V for the Auriga 2 cloud (left panel). A plot showing the log of the cumulative mass (integrated from RHS) against A_V for the Cepheus Flare cloud (right panel).

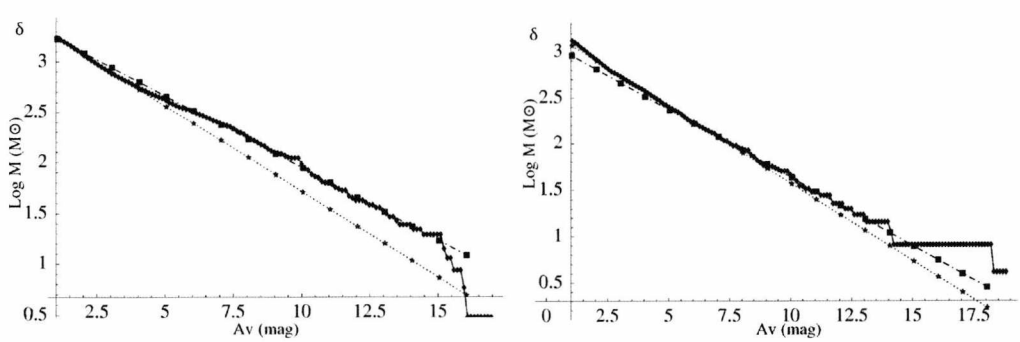

Figure B.55: A plot showing the log of the cumulative mass (integrated from RHS) against A_V for the Chamaeleon I cloud (left panel). A plot showing the log of the cumulative mass (integrated from RHS) against A_V for the Chamaeleon II cloud (right panel).

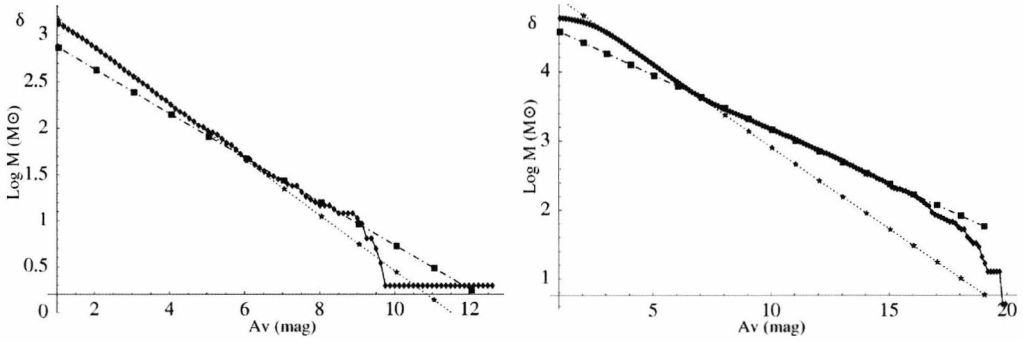

Figure B.56: A plot showing the log of the cumulative mass (integrated from RHS) against A_V for the Chamaeleon II cloud (left panel). A plot showing the log of the cumulative mass (integrated from RHS) against A_V for the Circinus cloud (right panel).

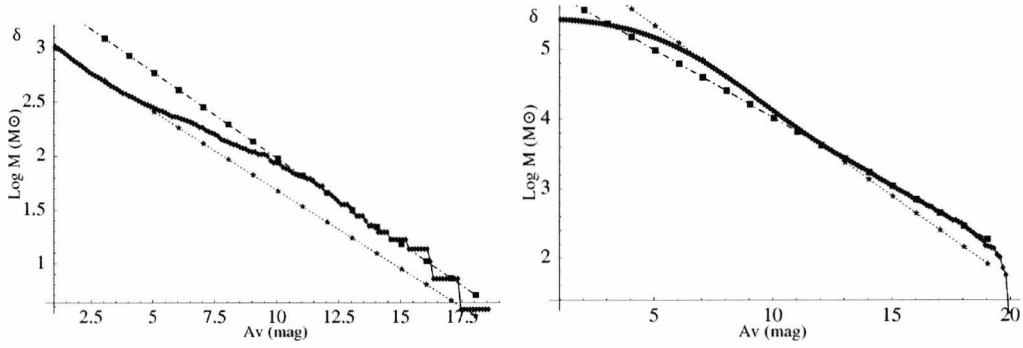

Figure B.57: A plot showing the log of the cumulative mass (integrated from RHS) against A_V for the Corona Australis cloud (left panel). A plot showing the log of the cumulative mass (integrated from RHS) against A_V for the Cygnus OB7 cloud (right panel).

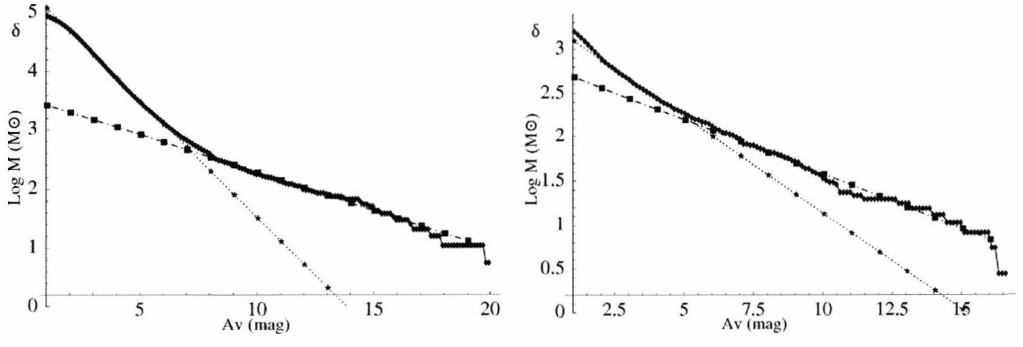

Figure B.58: A plot showing the log of the cumulative mass (integrated from RHS) against A_V for the λ-Ori cloud (left panel). A plot showing the log of the cumulative mass (integrated from RHS) against A_V for the Lupus 1 cloud (right panel).

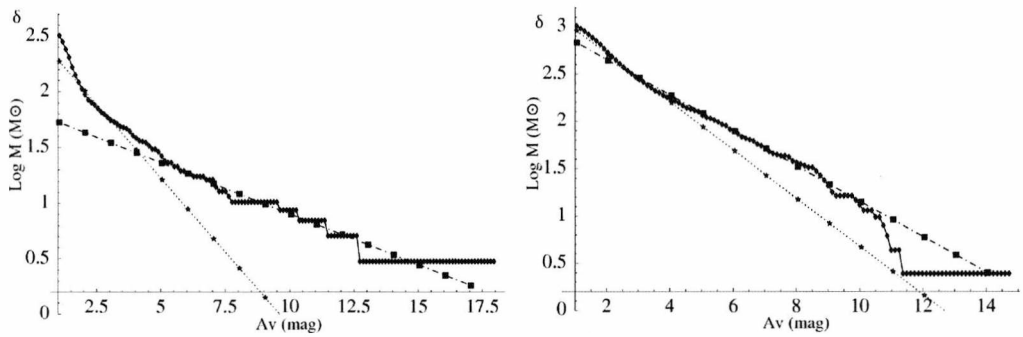

Figure B.59: A plot showing the log of the cumulative mass (integrated from RHS) against A_V for the Lupus 2 cloud (left panel). A plot showing the log of the cumulative mass (integrated from RHS) against A_V for the Lupus 3 cloud (right panel).

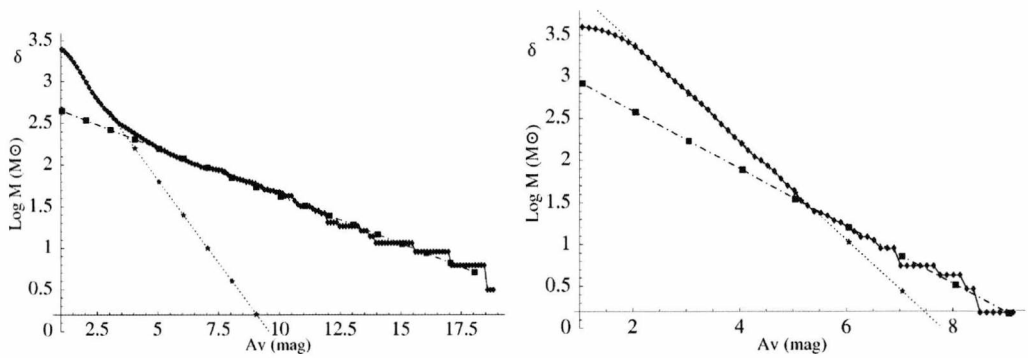

Figure B.60: A plot showing the log of the cumulative mass (integrated from RHS) against A_V for the Lupus 4 cloud (left panel). A plot showing the log of the cumulative mass (integrated from RHS) against A_V for the Lupus 5 cloud (right panel).

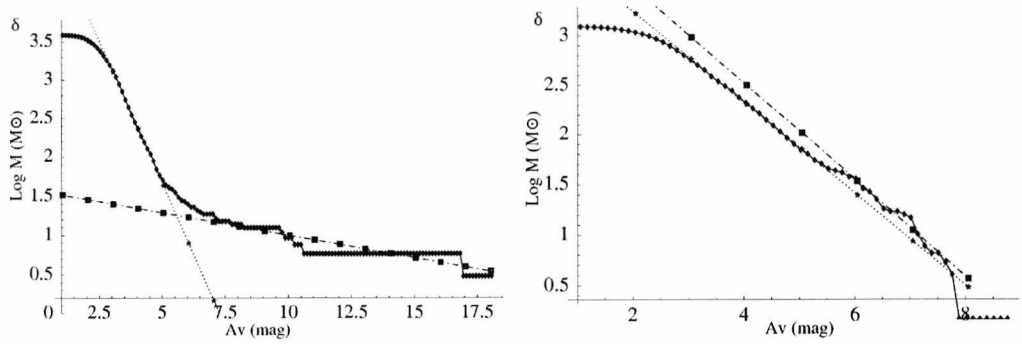

Figure B.61: A plot showing the log of the cumulative mass (integrated from RHS) against A_V for the Lupus 6 cloud (left panel). A plot showing the log of the cumulative mass (integrated from RHS) against A_V for the Lupus 7 cloud (right panel).

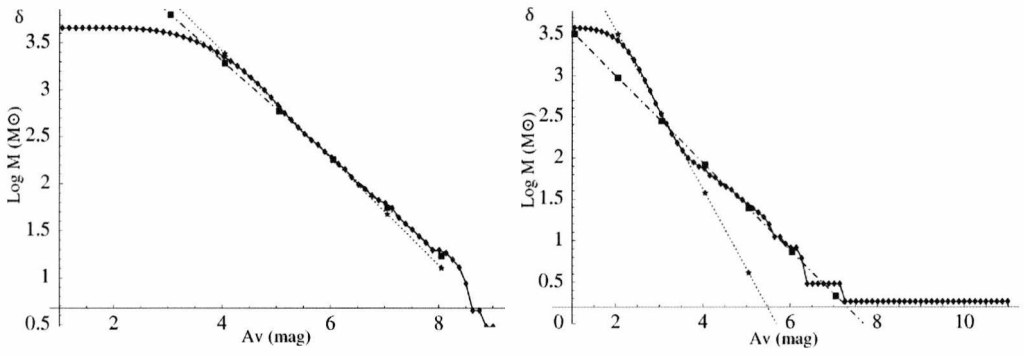

Figure B.62: A plot showing the log of the cumulative mass (integrated from RHS) against A_V for the Lupus 8 cloud (left panel). A plot showing the log of the cumulative mass (integrated from RHS) against A_V for the Lupus 9 cloud (right panel).

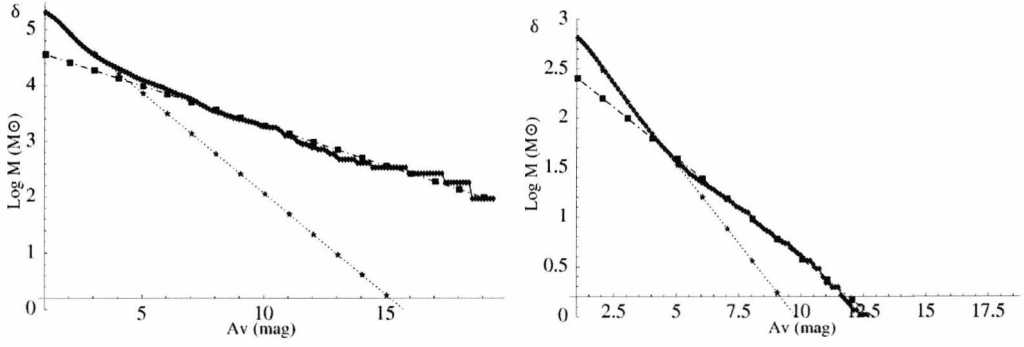

Figure B.63: A plot showing the log of the cumulative mass (integrated from RHS) against A_V for the Monoceros cloud (left panel). A plot showing the log of the cumulative mass (integrated from RHS) against A_V for the Musca cloud (right panel).

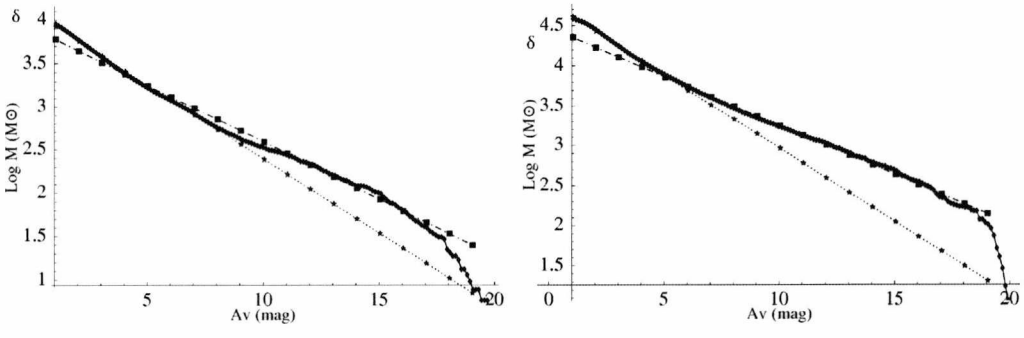

Figure B.64: A plot showing the log of the cumulative mass (integrated from RHS) against A_V for the Ophiuchus cloud (left panel). A plot showing the log of the cumulative mass (integrated from RHS) against A_V for the Orion A cloud (right panel).

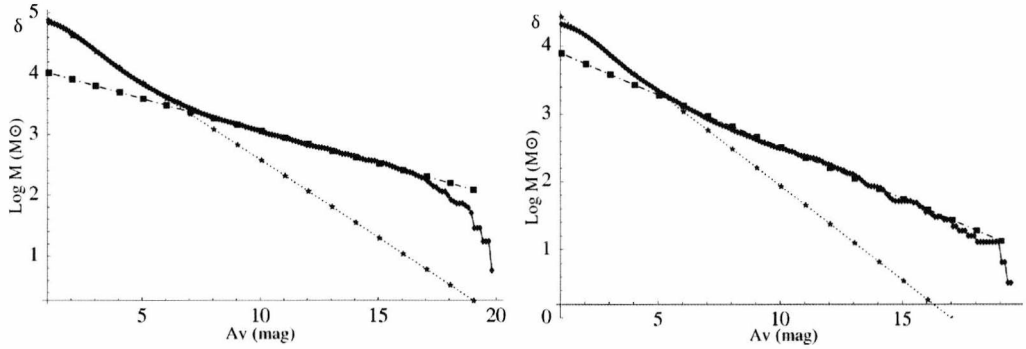

Figure B.65: A plot showing the log of the cumulative mass (integrated from RHS) against A_V for the Orion B cloud (left panel). A plot showing the log of the cumulative mass (integrated from RHS) against A_V for the Perseus cloud (right panel).

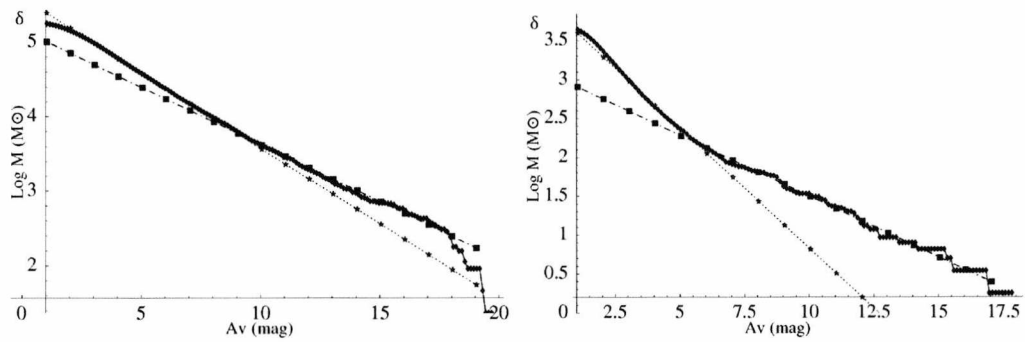

Figure B.66: A plot showing the log of the cumulative mass (integrated from RHS) against A_V for the Rosette Nebula cloud (left panel). A plot showing the log of the cumulative mass (integrated from RHS) against A_V for the Scorpius cloud (right panel).

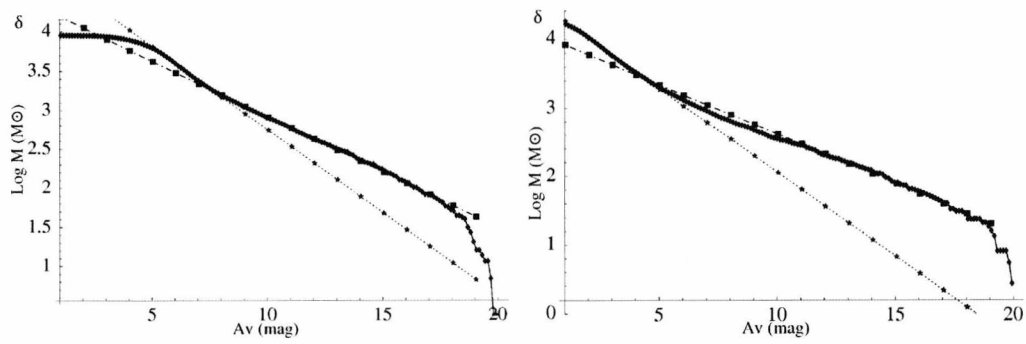

Figure B.67: A plot showing the log of the cumulative mass (integrated from RHS) against A_V for the Serpens cloud (left panel). A plot showing the log of the cumulative mass (integrated from RHS) against A_V for the Taurus cloud (right panel).

Appendix C

Structure of Giant Molecular Clouds

C.1 Structure Functions

C.1.1 Structure Function Plots

The structure function plots for the 30 sample clouds are shown in this section. The data are obtained at the same spatial scales for each cloud - from 0.1 pc to 1.0 pc. Our data (red line) are compared against the models of K41 (solid line), SL94 (dotted line) and B02 (dashed line). The best fit values of Δ, C, β, D and the RMS value are shown. A plot of the difference of the fit from the data against p is also shown. These were obtained using the method in Section 2.8.1.

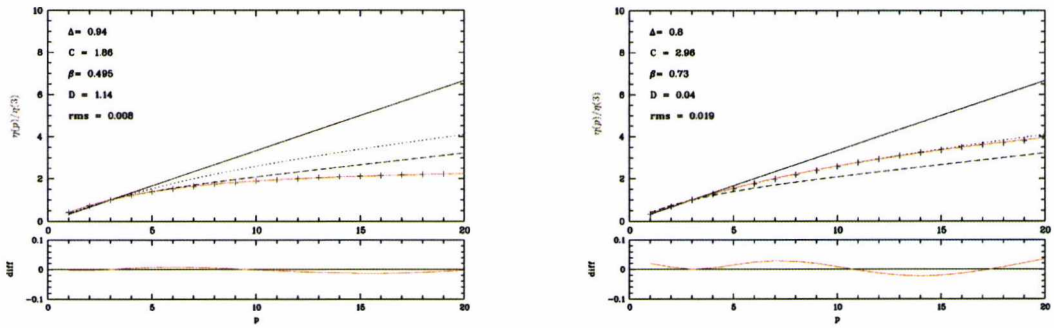

Figure C.1: The structure function plots for the Aquila Rift (left panel) and Auriga 1 clouds (right panel). Our data (red line) are compared against the models of K41 (solid line), SL94 (dotted line) and B02 (dashed line). The best fit values of Δ, C, β, D and the RMS value are shown. A plot of the difference of the fit from the data against p is also shown.

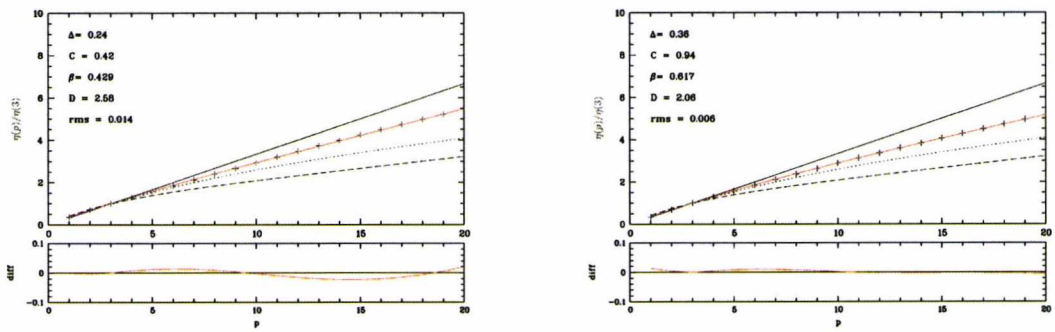

Figure C.2: The structure function plots for the Auriga 2 (left panel) and Cepheus Flare clouds (right panel). Our data (red line) are compared against the models of K41 (solid line), SL94 (dotted line) and B02 (dashed line). The best fit values of Δ, C, β, D and the RMS value are shown. A plot of the difference of the fit from the data against p is also shown.

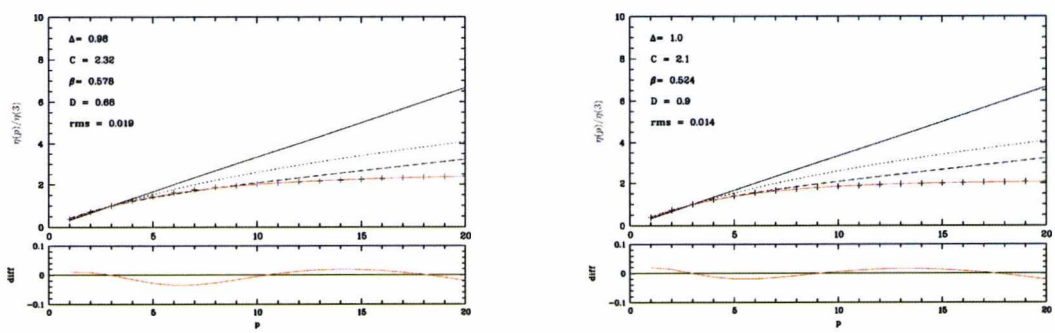

Figure C.3: The structure function plots for the Chamaeleon I (left panel) and Chamaeleon II clouds (right panel). Our data (red line) are compared against the models of K41 (solid line), SL94 (dotted line) and B02 (dashed line). The best fit values of Δ, C, β, D and the RMS value are shown. A plot of the difference of the fit from the data against p is also shown.

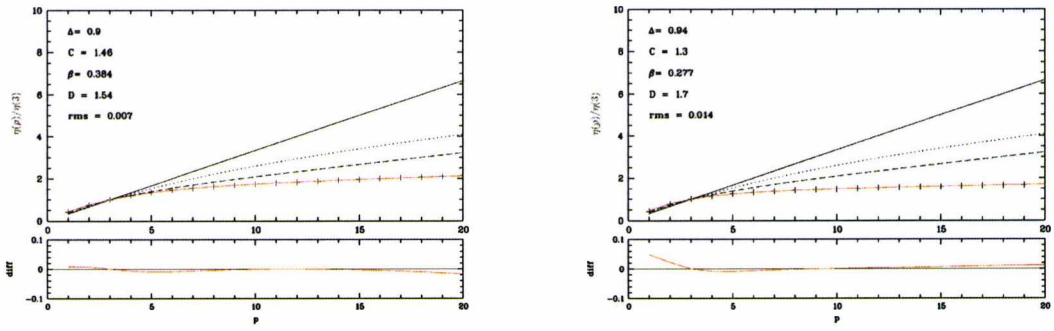

Figure C.4: The structure function plots for the Chamaeleon III (left panel) and Circinus clouds (right panel). Our data (red line) are compared against the models of K41 (solid line), SL94 (dotted line) and B02 (dashed line). The best fit values of Δ, C, β, D and the RMS value are shown. A plot of the difference of the fit from the data against p is also shown.

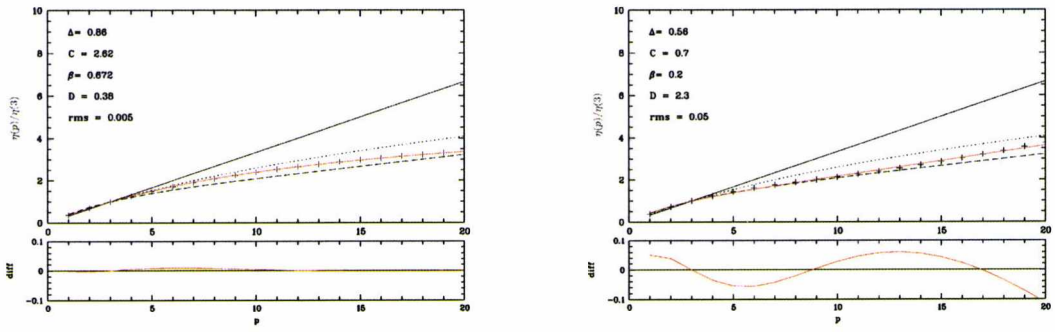

Figure C.5: The structure function plots for the Corona Australis (left panel) and Cygnus OB7 clouds (right panel). Our data (red line) are compared against the models of K41 (solid line), SL94 (dotted line) and B02 (dashed line). The best fit values of Δ, C, β, D and the RMS value are shown. A plot of the difference of the fit from the data against p is also shown.

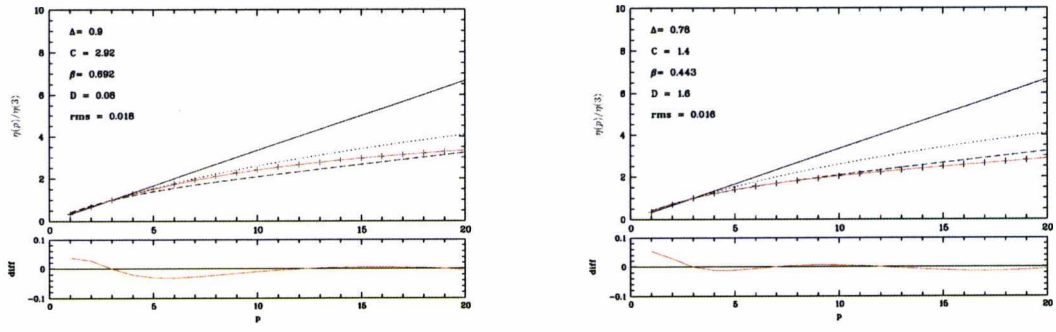

Figure C.6: The structure function plots for the λ-Ori (left panel) and Lupus 1 clouds (right panel). Our data (red line) are compared against the models of K41 (solid line), SL94 (dotted line) and B02 (dashed line). The best fit values of Δ, C, β, D and the RMS value are shown. A plot of the difference of the fit from the data against p is also shown.

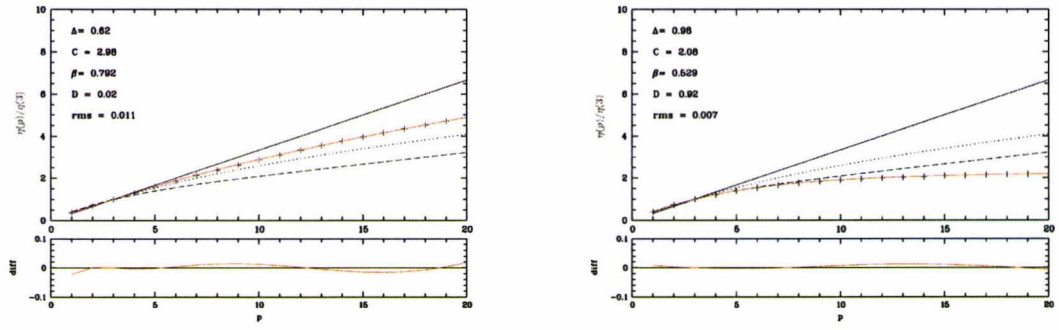

Figure C.7: The structure function plots for the Lupus 2 (left panel) and Lupus 3 clouds (right panel). Our data (red line) are compared against the models of K41 (solid line), SL94 (dotted line) and B02 (dashed line). The best fit values of Δ, C, β, D and the RMS value are shown. A plot of the difference of the fit from the data against p is also shown.

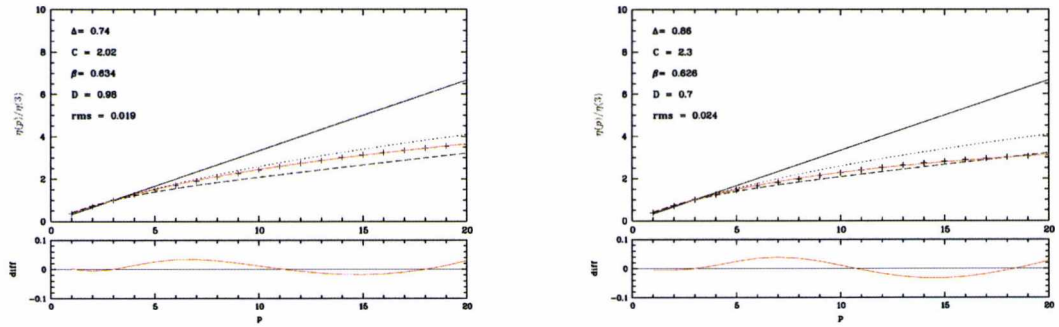

Figure C.8: The structure function plots for the Lupus 4 (left panel) and Lupus 5 clouds (right panel). Our data (red line) are compared against the models of K41 (solid line), SL94 (dotted line) and B02 (dashed line). The best fit values of Δ, C, β, D and the RMS value are shown. A plot of the difference of the fit from the data against p is also shown.

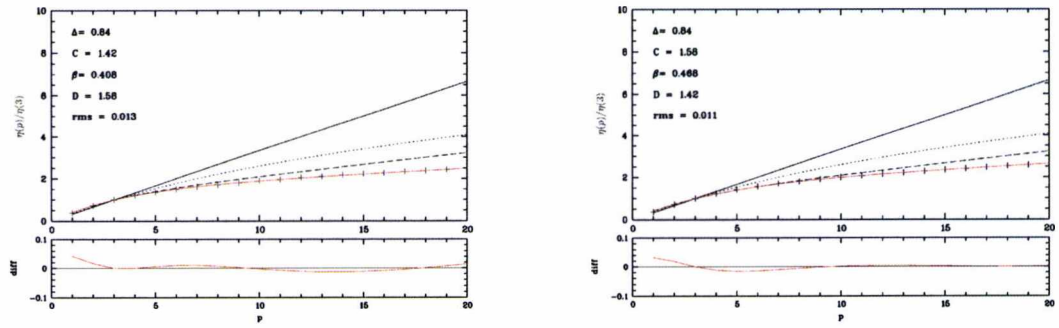

Figure C.9: The structure function plots for the Lupus 6 (left panel) and Lupus 7 clouds (right panel). Our data (red line) are compared against the models of K41 (solid line), SL94 (dotted line) and B02 (dashed line). The best fit values of Δ, C, β, D and the RMS value are shown. A plot of the difference of the fit from the data against p is also shown.

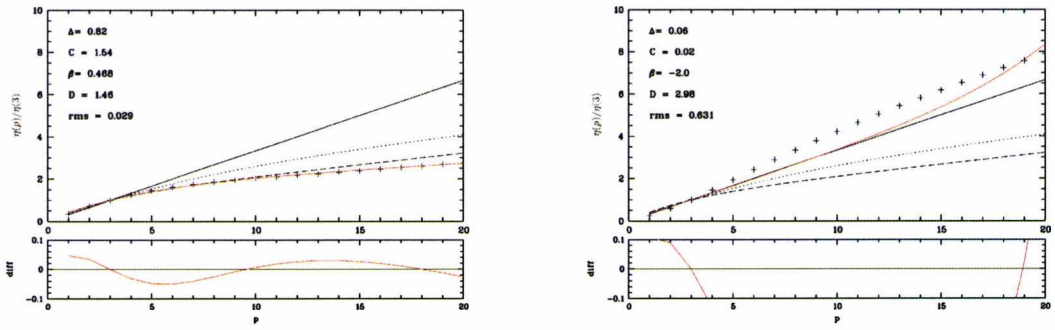

Figure C.10: The structure function plots for the Lupus 8 (left panel) and Lupus 9 clouds (right panel). Our data (red line) are compared against the models of K41 (solid line), SL94 (dotted line) and B02 (dashed line). The best fit values of Δ, C, β, D and the RMS value are shown. A plot of the difference of the fit from the data against p is also shown.

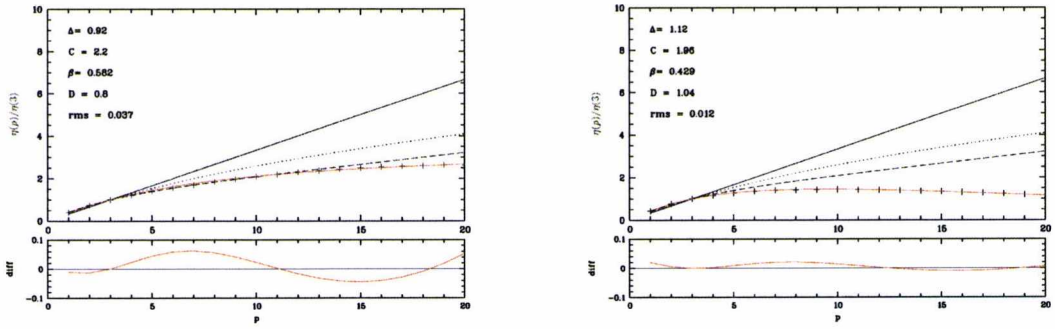

Figure C.11: The structure function plots for the Monoceros (left panel) and Musca clouds (right panel). Our data (red line) are compared against the models of K41 (solid line), SL94 (dotted line) and B02 (dashed line). The best fit values of Δ, C, β, D and the RMS value are shown. A plot of the difference of the fit from the data against p is also shown.

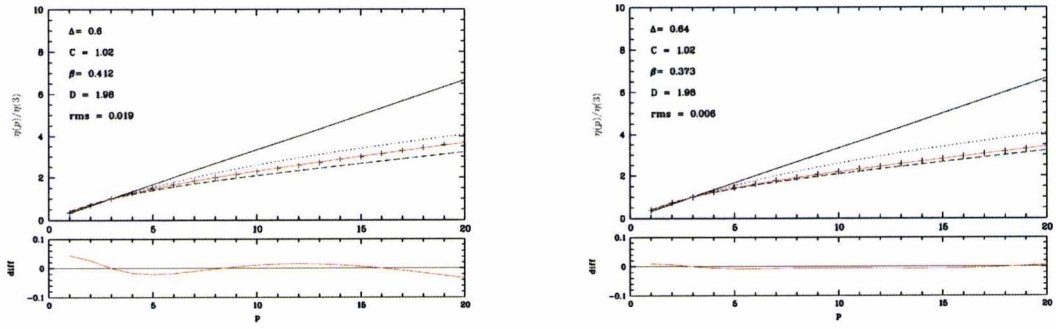

Figure C.12: The structure function plots for the Ophiuchus (left panel) and Orion A clouds (right panel). Our data (red line) are compared against the models of K41 (solid line), SL94 (dotted line) and B02 (dashed line). The best fit values of Δ, C, β, D and the RMS value are shown. A plot of the difference of the fit from the data against p is also shown.

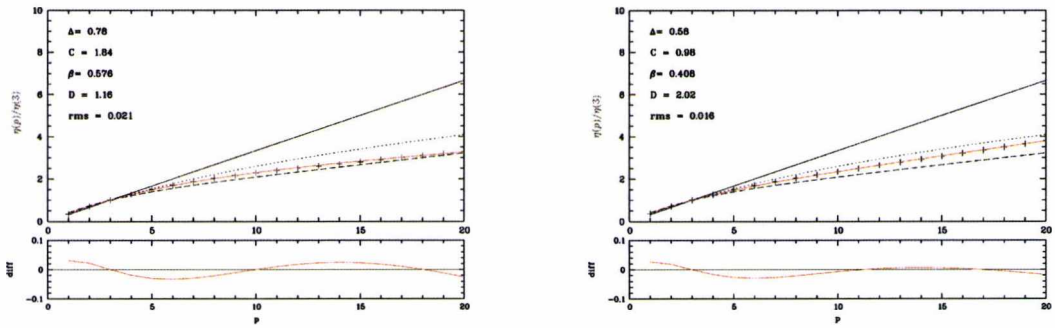

Figure C.13: The structure function plots for the Orion B (left panel) and Perseus clouds (right panel). Our data (red line) are compared against the models of K41 (solid line), SL94 (dotted line) and B02 (dashed line). The best fit values of Δ, C, β, D and the RMS value are shown. A plot of the difference of the fit from the data against p is also shown.

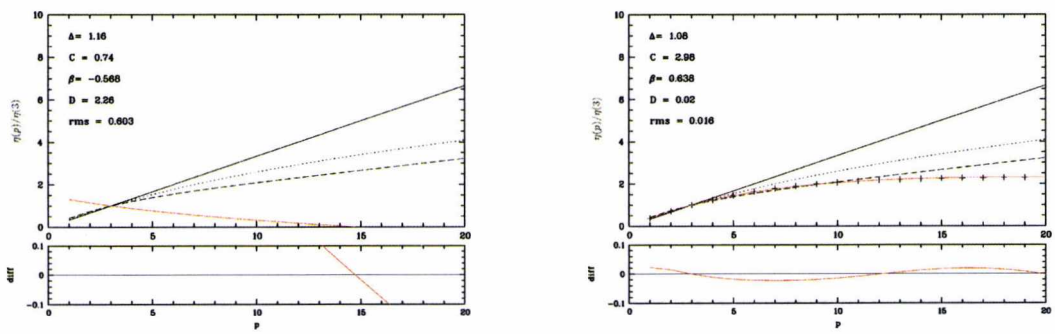

Figure C.14: The structure function plots for the Rosette Nebula (left panel) and Scorpius clouds (right panel). Our data (red line) are compared against the models of K41 (solid line), SL94 (dotted line) and B02 (dashed line). The best fit values of Δ, C, β, D and the RMS value are shown. A plot of the difference of the fit from the data against p is also shown.

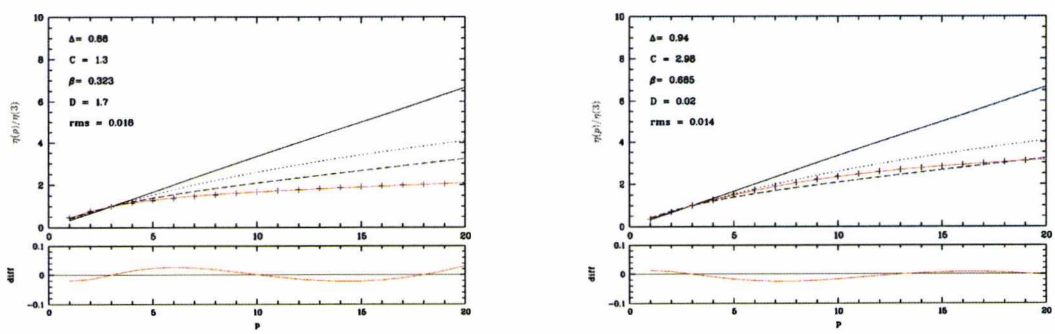

Figure C.15: The structure function plots for the Serpens (left panel) and Taurus clouds (right panel). Our data (red line) are compared against the models of K41 (solid line), SL94 (dotted line) and B02 (dashed line). The best fit values of Δ, C, β, D and the RMS value are shown. A plot of the difference of the fit from the data against p is also shown.

C.1.2 Galactic Plane Plots

The data for the structure function parameters Δ, C, β and D for the Galactic Plane area are displayed here, together with the *rms* of the fit and corresponding standard deviations.

Figure C.16: Visual representation of the parameters Δ and C with standard deviations obtained in the central Galactic plane. The data are scaled linearly (black to white) as follows: Δ 0.0 to 1.0, σ_Δ 0.0 to 0.4, C 0.0 to 2.5, σ_C 0.0 to 1.0. The overlaid contours are the 3 mag A_V (outer) and 6 mag A_V (inner) from the nearest 49 star extinction map.

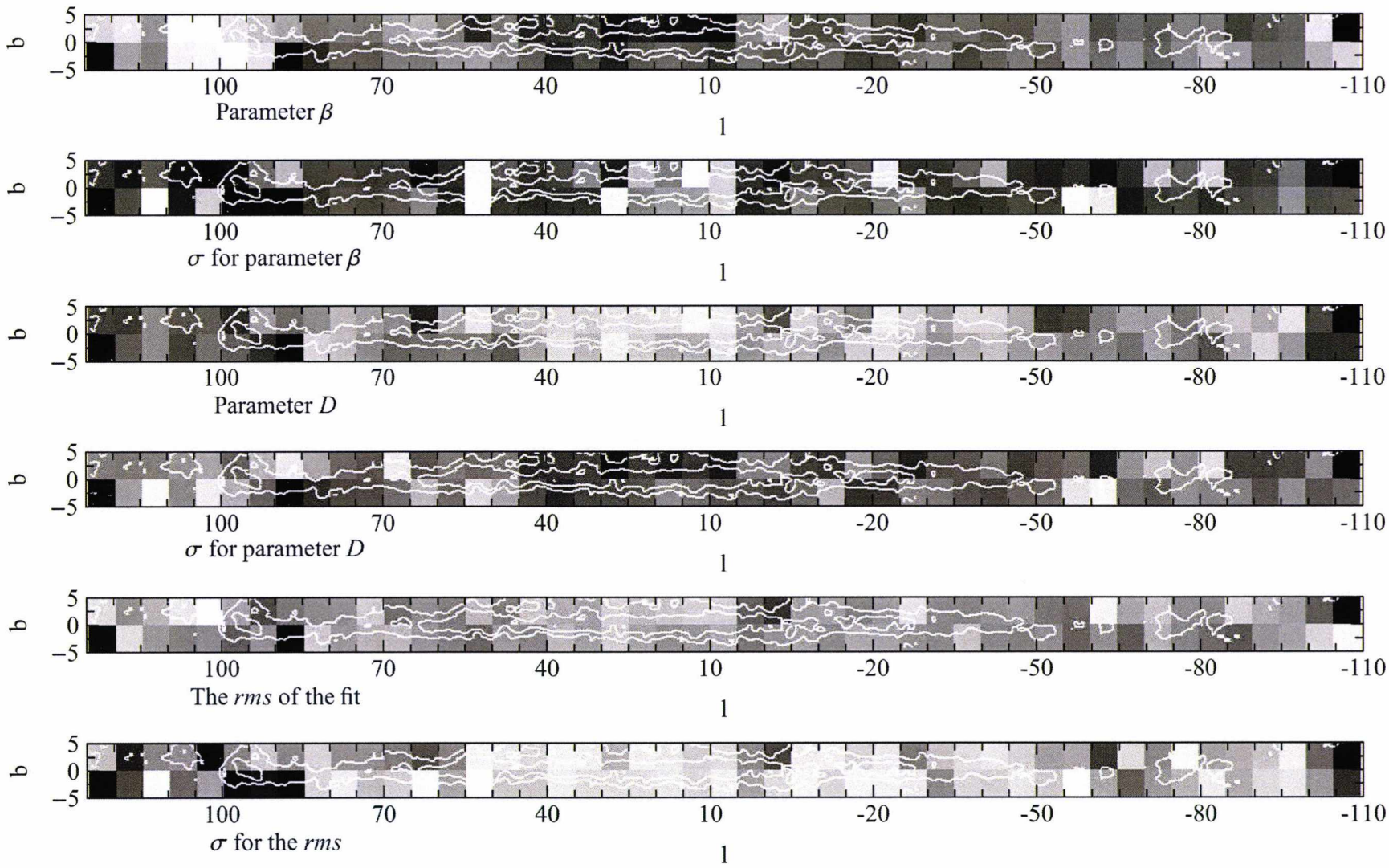

Figure C.17: Visual representation of the parameters Δ and C with standard deviations obtained in the central Galactic plane. The data are scaled linearly (black to white) as follows: β 0.0 to 1.0, σ_β 0.0 to 0.4, D 0.0 to 2.5, σ_D 0.0 to 1.0, *rms* 0.0 to 0.1, σ_{rms} 0.0 to 0.025. The overlaid contours are the 3 mag A_V (outer) and 6 mag A_V (inner) from the nearest 49 star extinction map.

C.2 Δ-variance

This section presents the plots obtained using the Δ-variance analysis, both for the A_V and star density *con-noise maps*. These were made using the method described in Section 2.8.2.

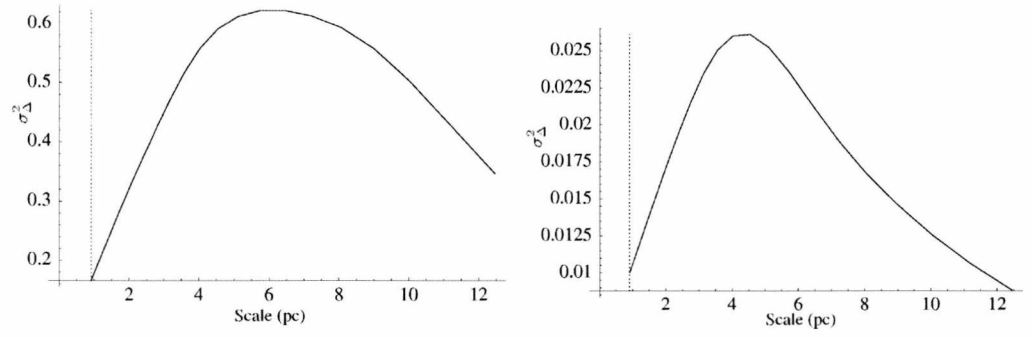

Figure C.18: Δ-variance against scale using the *con-noise* A_V map (**left panel**) and corresponding star density map (**right panel**) for the Aquila Rift cloud, using the 49 nearest star maps. The dashed vertical line on the left of each plot shows the smallest scale at which data can be reliably used while avoiding oversampling due to the spatial resolution of the it con-noise map.

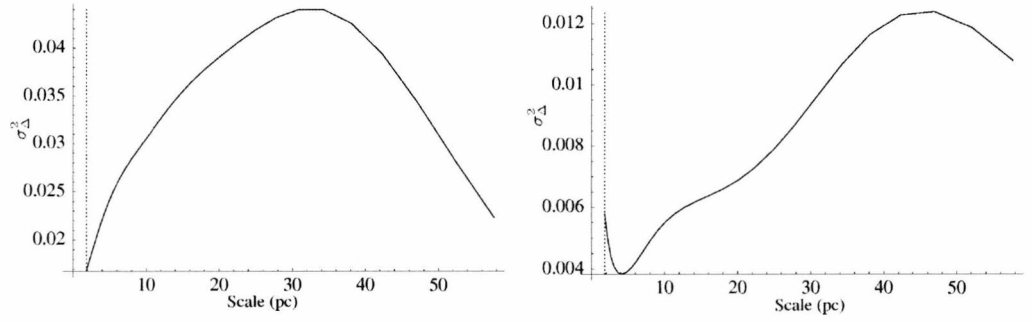

Figure C.19: Δ-variance against scale using the *con-noise* A_V map (**left panel**) and corresponding star density map (**right panel**) for the Auriga 1 cloud, using the 49 nearest star maps. The dashed vertical line on the left of each plot shows the smallest scale at which data can be reliably used while avoiding oversampling due to the spatial resolution of the it con-noise map.

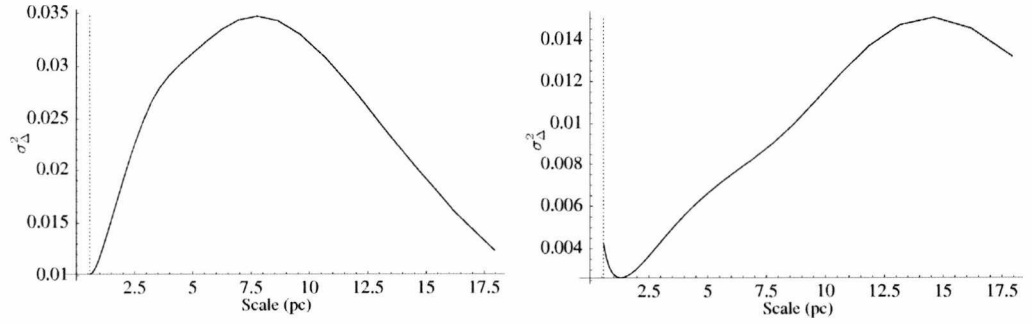

Figure C.20: Δ-variance against scale using the *con-noise* A_V map (**left panel**) and corresponding star density map (**right panel**) for the Auriga 2 cloud, using the 49 nearest star maps. The dashed vertical line on the left of each plot shows the smallest scale at which data can be reliably used while avoiding oversampling due to the spatial resolution of the it con-noise map.

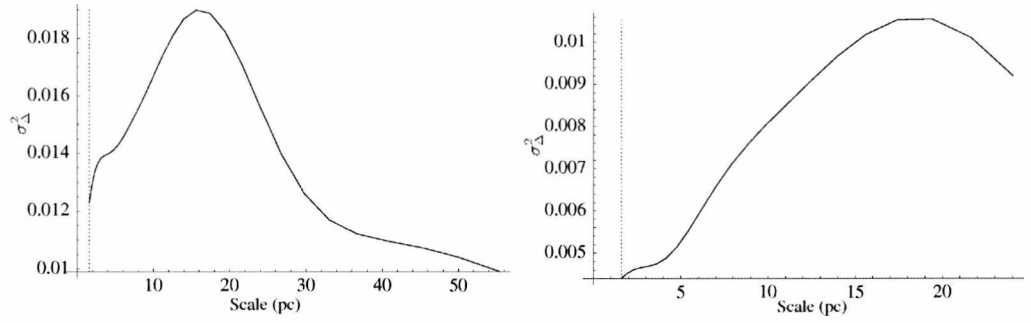

Figure C.21: Δ-variance against scale using the *con-noise* A_V map (**left panel**) and corresponding star density map (**right panel**) for the Cepheus Flare cloud, using the 49 nearest star maps. The dashed vertical line on the left of each plot shows the smallest scale at which data can be reliably used while avoiding oversampling due to the spatial resolution of the it con-noise map.

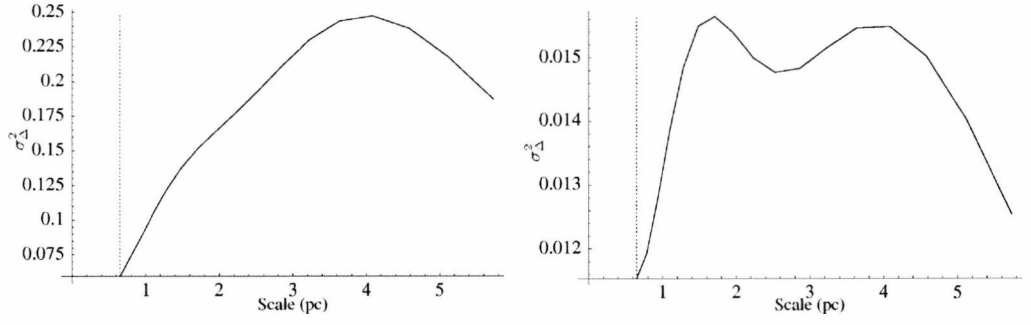

Figure C.22: Δ-variance against scale using the *con-noise* A_V map (**left panel**) and corresponding star density map (**right panel**) for the Chamaeleon I cloud, using the 49 nearest star maps. The dashed vertical line on the left of each plot shows the smallest scale at which data can be reliably used while avoiding oversampling due to the spatial resolution of the it con-noise map.

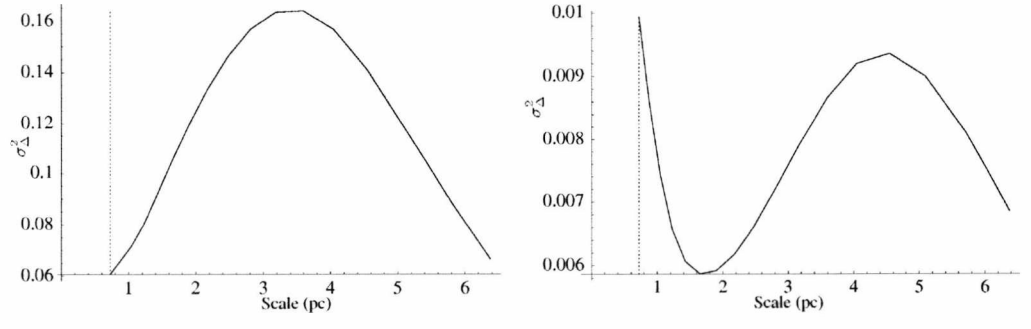

Figure C.23: Δ-variance against scale using the *con-noise* A_V map (**left panel**) and corresponding star density map (**right panel**) for the Chamaeleon II cloud, using the 49 nearest star maps. The dashed vertical line on the left of each plot shows the smallest scale at which data can be reliably used while avoiding oversampling due to the spatial resolution of the it con-noise map.

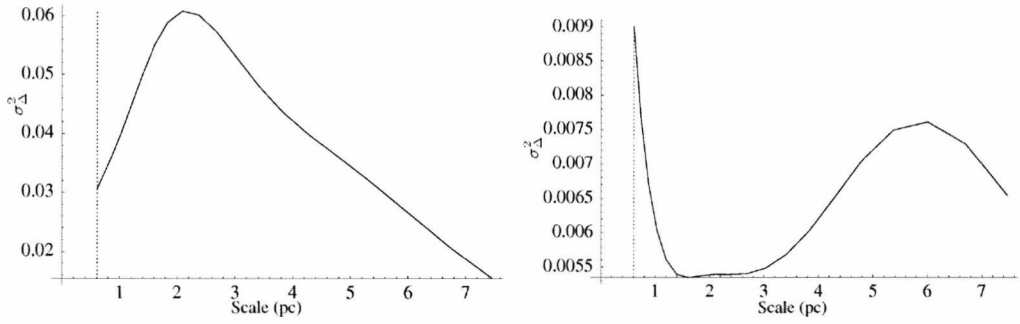

Figure C.24: Δ-variance against scale using the *con-noise* A_V map (**left panel**) and corresponding star density map (**right panel**) for the Chamaeleon III cloud, using the 49 nearest star maps. The dashed vertical line on the left of each plot shows the smallest scale at which data can be reliably used while avoiding oversampling due to the spatial resolution of the it con-noise map.

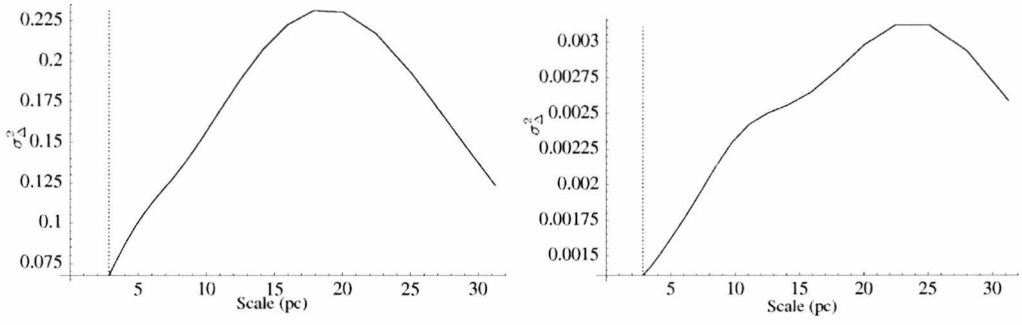

Figure C.25: Δ-variance against scale using the *con-noise* A_V map (**left panel**) and corresponding star density map (**right panel**) for the Circinus cloud, using the 49 nearest star maps. The dashed vertical line on the left of each plot shows the smallest scale at which data can be reliably used while avoiding oversampling due to the spatial resolution of the it con-noise map.

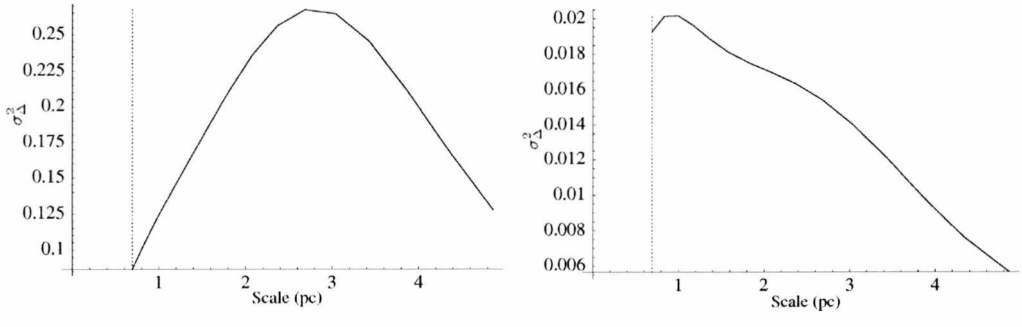

Figure C.26: Δ-variance against scale using the *con-noise* A_V map (**left panel**) and corresponding star density map (**right panel**) for the Corona Australis cloud, using the 49 nearest star maps. The dashed vertical line on the left of each plot shows the smallest scale at which data can be reliably used while avoiding oversampling due to the spatial resolution of the it con-noise map.

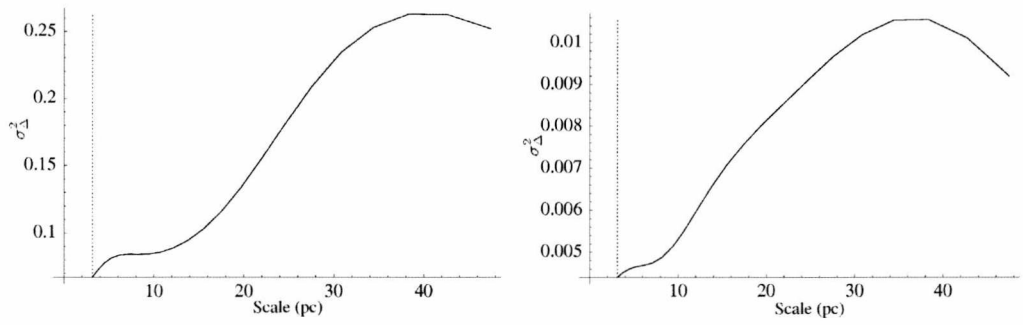

Figure C.27: Δ-variance against scale using the *con-noise* A_V map (**left panel**) and corresponding star density map (**right panel**) for the Cygnus OB7 cloud, using the 49 nearest star maps. The dashed vertical line on the left of each plot shows the smallest scale at which data can be reliably used while avoiding oversampling due to the spatial resolution of the it con-noise map.

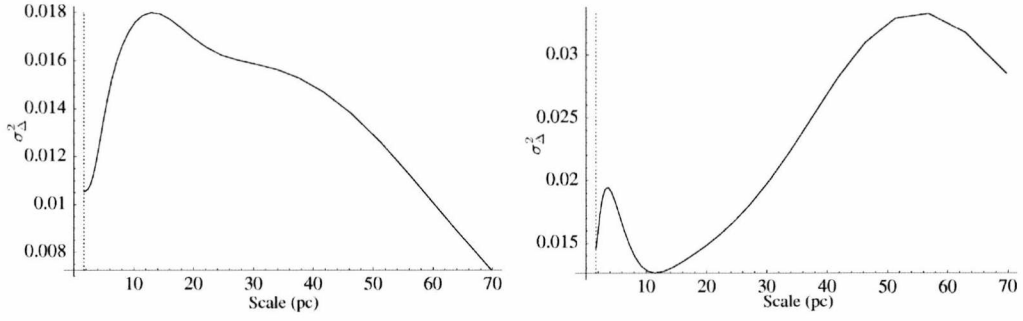

Figure C.28: Δ-variance against scale using the *con-noise* A_V map (**left panel**) and corresponding star density map (**right panel**) for the λ-Ori cloud, using the 49 nearest star maps. The dashed vertical line on the left of each plot shows the smallest scale at which data can be reliably used while avoiding oversampling due to the spatial resolution of the it con-noise map.

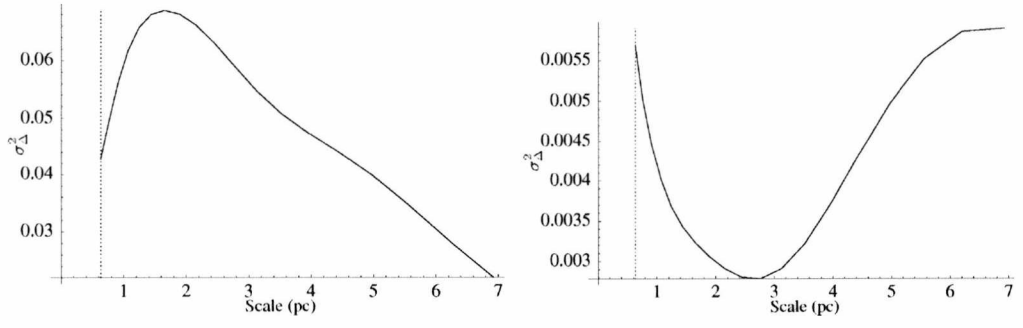

Figure C.29: Δ-variance against scale using the *con-noise* A_V map (**left panel**) and corresponding star density map (**right panel**) for the Lupus 1 cloud, using the 49 nearest star maps. The dashed vertical line on the left of each plot shows the smallest scale at which data can be reliably used while avoiding oversampling due to the spatial resolution of the it con-noise map.

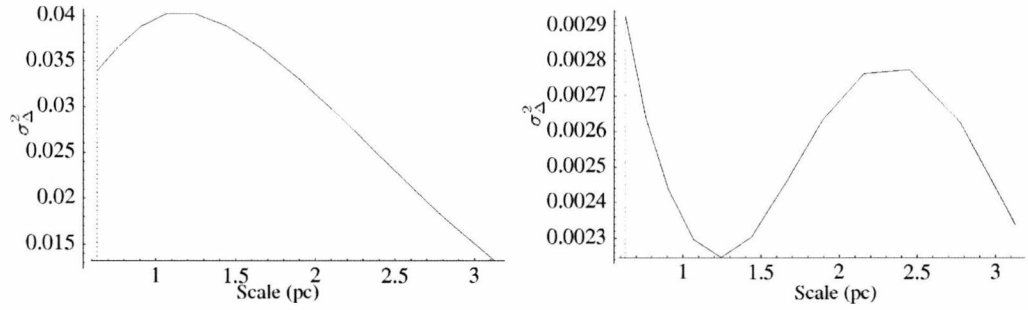

Figure C.30: Δ-variance against scale using the *con-noise* A_V map (**left panel**) and corresponding star density map (**right panel**) for the Lupus 2 cloud, using the 49 nearest star maps. The dashed vertical line on the left of each plot shows the smallest scale at which data can be reliably used while avoiding oversampling due to the spatial resolution of the it con-noise map.

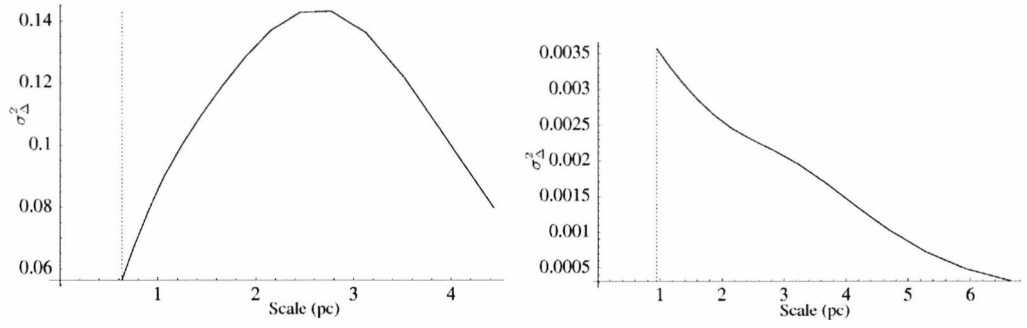

Figure C.31: Δ-variance against scale using the *con-noise* A_V map (**left panel**) and corresponding star density map (**right panel**) for the Lupus 3 cloud, using the 49 nearest star maps. The dashed vertical line on the left of each plot shows the smallest scale at which data can be reliably used while avoiding oversampling due to the spatial resolution of the it con-noise map.

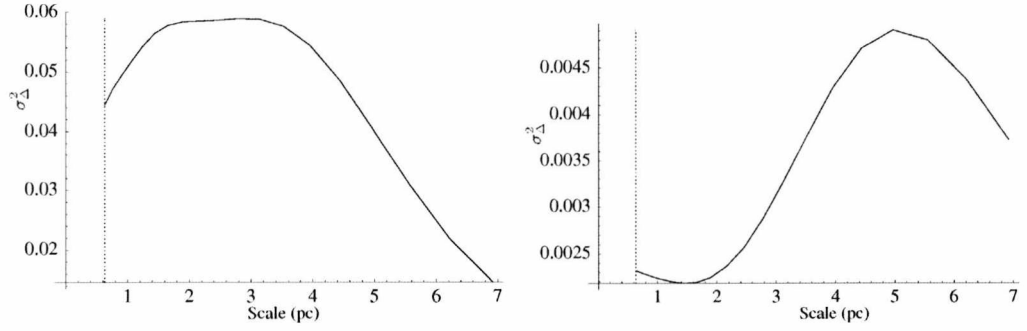

Figure C.32: Δ-variance against scale using the *con-noise* A_V map (**left panel**) and corresponding star density map (**right panel**) for the Lupus 4 cloud, using the 49 nearest star maps. The dashed vertical line on the left of each plot shows the smallest scale at which data can be reliably used while avoiding oversampling due to the spatial resolution of the it con-noise map.

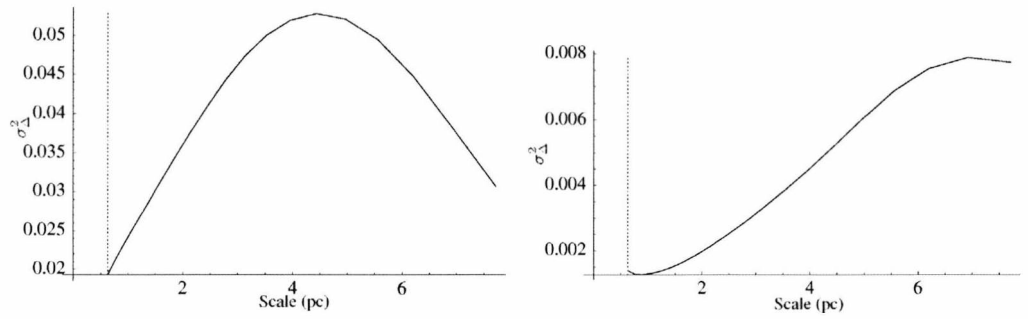

Figure C.33: Δ-variance against scale using the *con-noise* A_V map (**left panel**) and corresponding star density map (**right panel**) for the Lupus 5 cloud, using the 49 nearest star maps. The dashed vertical line on the left of each plot shows the smallest scale at which data can be reliably used while avoiding oversampling due to the spatial resolution of the it con-noise map.

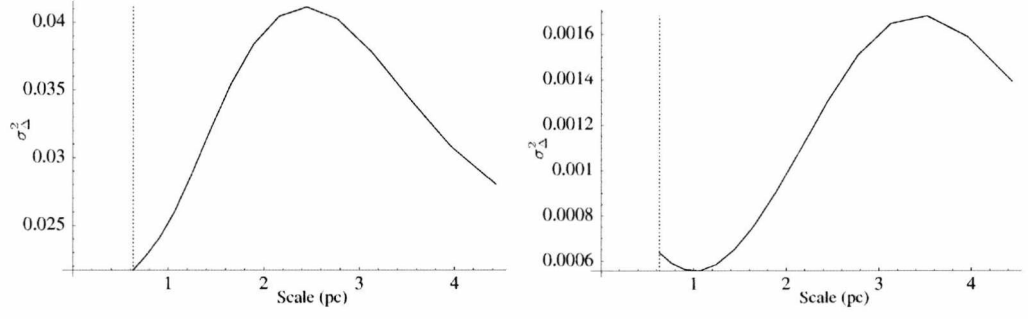

Figure C.34: Δ-variance against scale using the *con-noise* A_V map (**left panel**) and corresponding star density map (**right panel**) for the Lupus 6 cloud, using the 49 nearest star maps. The dashed vertical line on the left of each plot shows the smallest scale at which data can be reliably used while avoiding oversampling due to the spatial resolution of the it con-noise map.

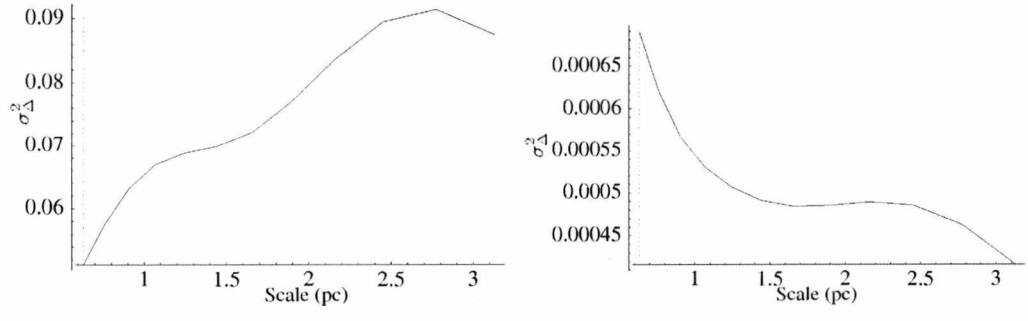

Figure C.35: Δ-variance against scale using the *con-noise* A_V map (**left panel**) and corresponding star density map (**right panel**) for the Lupus 7 cloud, using the 49 nearest star maps. The dashed vertical line on the left of each plot shows the smallest scale at which data can be reliably used while avoiding oversampling due to the spatial resolution of the it con-noise map.

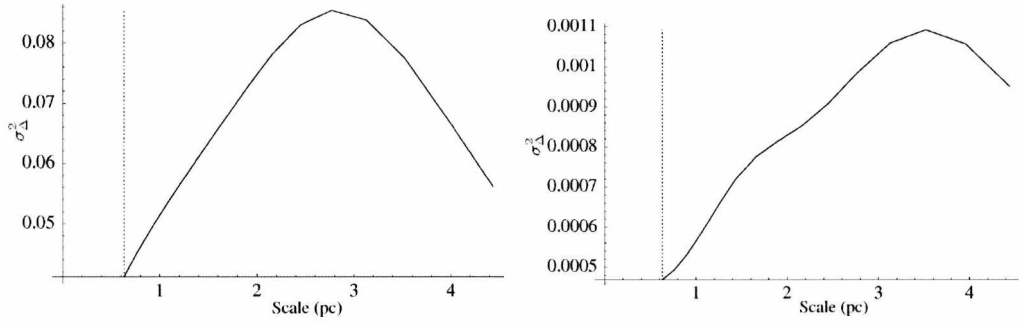

Figure C.36: Δ-variance against scale using the *con-noise* A_V map (**left panel**) and corresponding star density map (**right panel**) for the Lupus 8 cloud, using the 49 nearest star maps. The dashed vertical line on the left of each plot shows the smallest scale at which data can be reliably used while avoiding oversampling due to the spatial resolution of the it con-noise map.

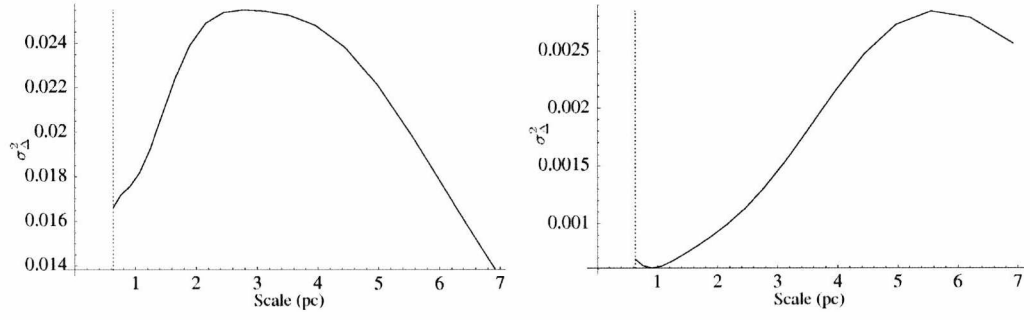

Figure C.37: Δ-variance against scale using the *con-noise* A_V map (**left panel**) and corresponding star density map (**right panel**) for the Lupus 9 cloud, using the 49 nearest star maps. The dashed vertical line on the left of each plot shows the smallest scale at which data can be reliably used while avoiding oversampling due to the spatial resolution of the it con-noise map.

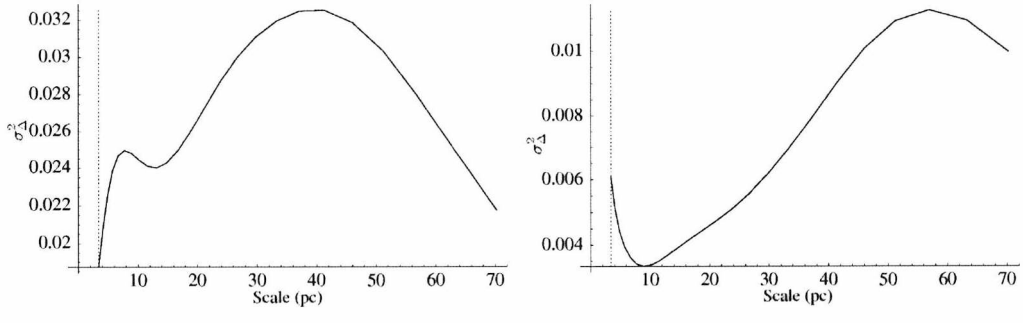

Figure C.38: Δ-variance against scale using the *con-noise* A_V map (**left panel**) and corresponding star density map (**right panel**) for the Monoceros cloud, using the 49 nearest star maps. The dashed vertical line on the left of each plot shows the smallest scale at which data can be reliably used while avoiding oversampling due to the spatial resolution of the it con-noise map.

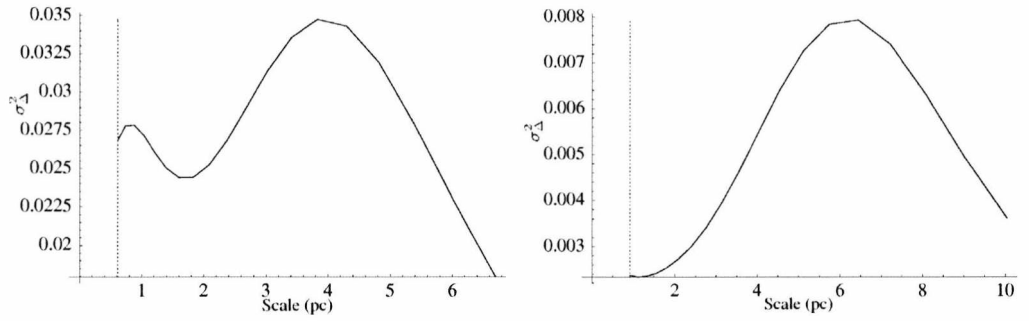

Figure C.39: Δ-variance against scale using the *con-noise* A_V map (**left panel**) and corresponding star density map (**right panel**) for the Musca cloud, using the 49 nearest star maps. The dashed vertical line on the left of each plot shows the smallest scale at which data can be reliably used while avoiding oversampling due to the spatial resolution of the it con-noise map.

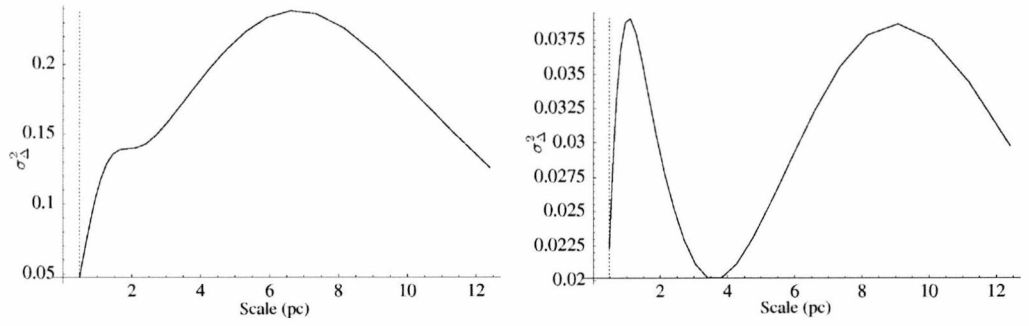

Figure C.40: Δ-variance against scale using the *con-noise* A_V map (**left panel**) and corresponding star density map (**right panel**) for the Ophiuchus cloud, using the 49 nearest star maps. The dashed vertical line on the left of each plot shows the smallest scale at which data can be reliably used while avoiding oversampling due to the spatial resolution of the it con-noise map.

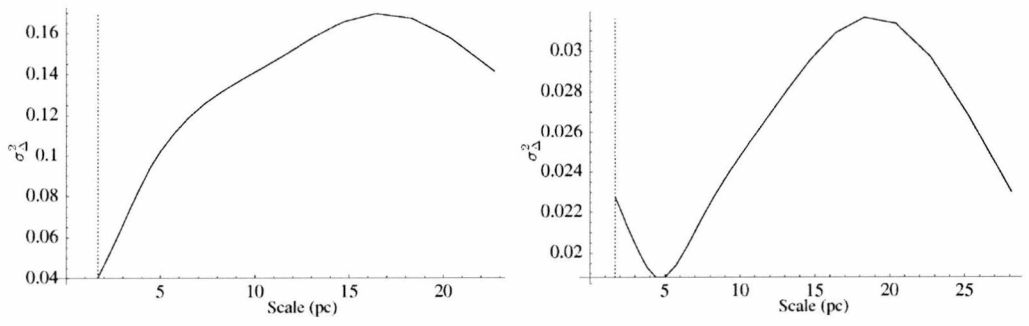

Figure C.41: Δ-variance against scale using the *con-noise* A_V map (**left panel**) and corresponding star density map (**right panel**) for the Orion A cloud, using the 49 nearest star maps. The dashed vertical line on the left of each plot shows the smallest scale at which data can be reliably used while avoiding oversampling due to the spatial resolution of the it con-noise map.

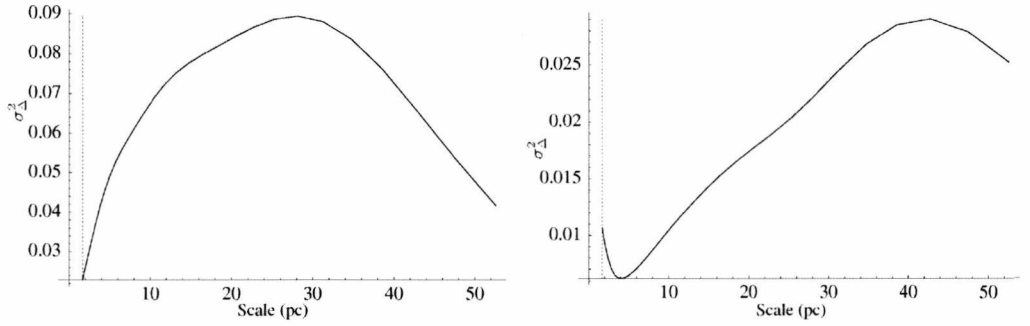

Figure C.42: Δ-variance against scale using the *con-noise* A_V map (**left panel**) and corresponding star density map (**right panel**) for the Orion B cloud, using the 49 nearest star maps. The dashed vertical line on the left of each plot shows the smallest scale at which data can be reliably used while avoiding oversampling due to the spatial resolution of the it con-noise map.

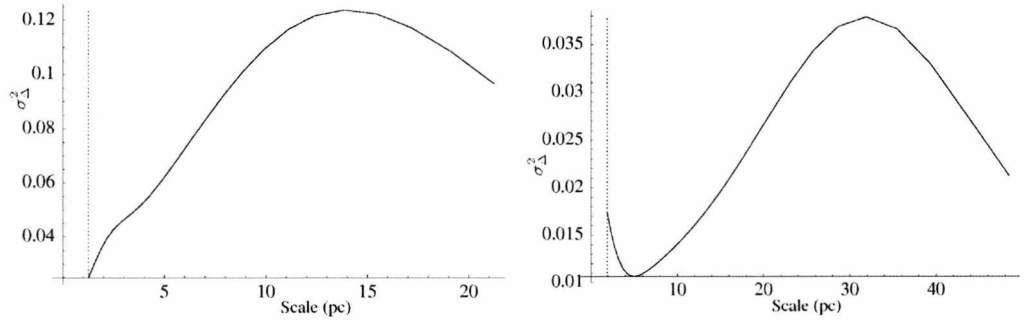

Figure C.43: Δ-variance against scale using the *con-noise* A_V map (**left panel**) and corresponding star density map (**right panel**) for the Perseus cloud, using the 49 nearest star maps. The dashed vertical line on the left of each plot shows the smallest scale at which data can be reliably used while avoiding oversampling due to the spatial resolution of the it con-noise map.

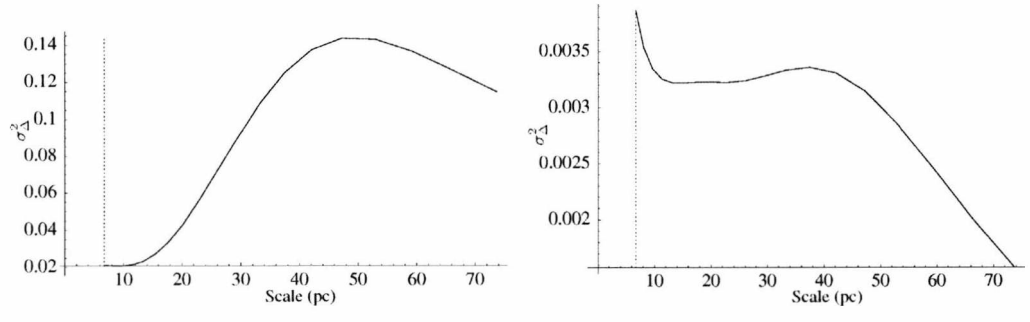

Figure C.44: Δ-variance against scale using the *con-noise* A_V map (**left panel**) and corresponding star density map (**right panel**) for the Rosette Nebula cloud, using the 49 nearest star maps. The dashed vertical line on the left of each plot shows the smallest scale at which data can be reliably used while avoiding oversampling due to the spatial resolution of the it con-noise map.

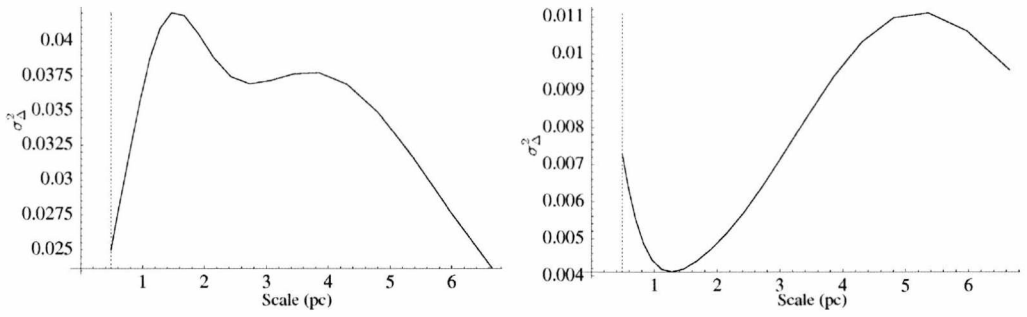

Figure C.45: Δ-variance against scales using the *con-noise* A_V map (**left panel**) and corresponding star density map (**right panel**) for the Scorpius cloud, using the 49 nearest star maps. The dashed vertical line on the left of each plot shows the smallest scale at which data can be reliably used while avoiding oversampling due to the spatial resolution of the it con-noise map.

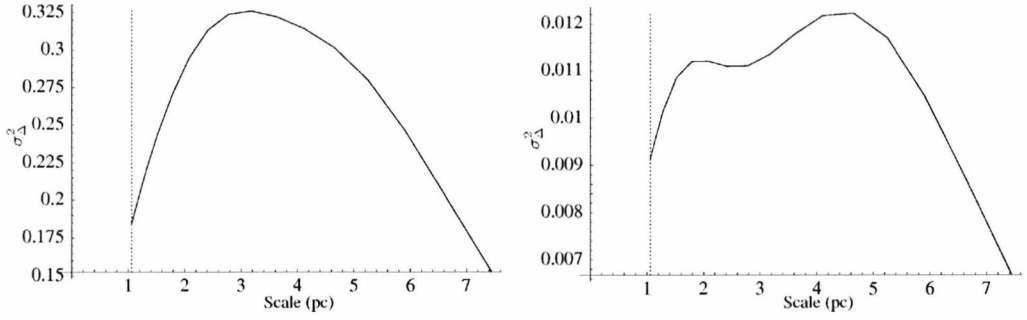

Figure C.46: Δ-variance against scale using the *con-noise* A_V map (**left panel**) and corresponding star density map (**right panel**) for the Serpens cloud, using the 49 nearest star maps. The dashed vertical line on the left of each plot shows the smallest scale at which data can be reliably used while avoiding oversampling due to the spatial resolution of the it con-noise map.

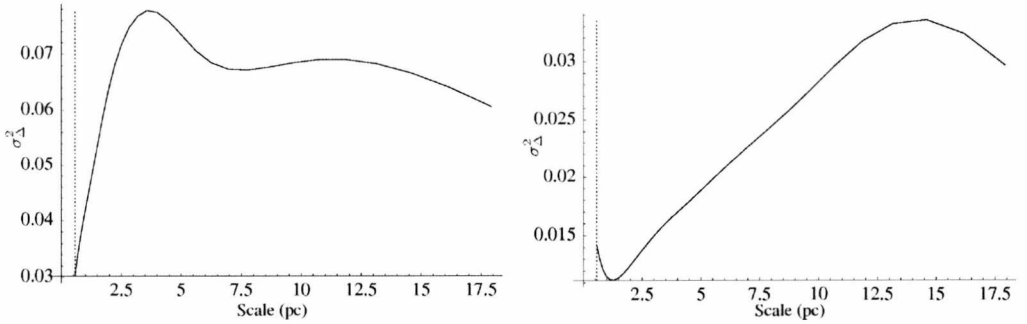

Figure C.47: Δ-variance against scale using the *con-noise* A_V map (**left panel**) and corresponding star density map (**right panel**) for the Taurus cloud, using the 49 nearest star maps. The dashed vertical line on the left of each plot shows the smallest scale at which data can be reliably used while avoiding oversampling due to the spatial resolution of the it con-noise map.